Advances in Swept-Wavelength Interferometry for Precision Measurements

by

Eric D. Moore

B.A., Lawrence University, 1999

M.S., University of Rochester, 2001

A thesis submitted to the

Faculty of the Graduate School of the

University of Colorado in partial fulfillment

of the requirements for the degree of

Doctor of Philosophy

Department of Electrical, Computer, and Energy Engineering

2011

This thesis entitled:
Advances in Swept-Wavelength Interferometry for Precision Measurements
written by Eric D. Moore
has been approved for the Department of Electrical, Computer, and Energy Engineering

Robert R. McLeod

Miloš Popović

Date

The final copy of this thesis has been examined by the signatories, and we find that both the content and the form meet acceptable presentation standards of scholarly work in the above mentioned discipline.

Moore, Eric D. (Ph.D., Electrical, Computer, and Energy Engineering)

Advances in Swept-Wavelength Interferometry for Precision Measurements

Thesis directed by Associate Professor Robert R. McLeod

Originally developed for radar applications in the 1950s, swept-wavelength interferometry (SWI) at optical wavelengths has been an active area of research for the past thirty years, with applications in fields ranging from fiber optic telecommunications to biomedical imaging. It now forms the basis of several measurement techniques, including optical frequency domain reflectometry (OFDR), swept-source optical coherence tomography (SS-OCT), and frequency-modulated continuous-wave (FMCW) lidar. In this thesis, I present several novel contributions to the field of SWI that include improvements and extensions to the state of the art in SWI for performing precision measurements. The first is a method for accurately monitoring the instantaneous frequency of the tunable source to accommodate nonlinearities in the source tuning characteristics. This work extends the commonly used method incorporating an auxiliary interferometer to the increasingly relevant cases of long interferometer path mismatches and high-speed wavelength tuning. The second contribution enables precision absolute range measurements to within a small fraction of the transform-limited range resolution of the SWI system. This is accomplished through the use of digital filtering in the time domain and phase slope estimation in the frequency domain. Measurements of optical group delay with attosecond-level precision are experimentally demonstrated and applied to measurements of group refractive index and physical thickness. The accuracy of the group refractive index measurement is shown to be on the order of 10^{-6}, while measurements of absolute thicknesses of macroscopic samples are accomplished with accuracy on the order of 10 nm. Furthermore, subnanometer uncertainty for relative thickness measurements can be achieved. For

the case of crystalline silicon wafers, the achievable uncertainty is on the same order as the Si-Si bond length, opening the door to potential thickness profiling with single atomic monolayer precision. Thirdly, I demonstrate a novel implementation of SWI in the form of an SS-OCT system for performing quantitative measurements of spatially resolved refractive index contrast. This system relies on the depth-sectioning capability of SWI to isolate Fresnel reflectivity variations at an interface of interest within an optical sample. A motivating application for this quantitative index contrast measurement, volume lithography of photosensitive polymers, is also discussed in detail. This discussion includes the first demonstration of two-dimensional optical waveguide arrays fabricated in photosensitive polymers by means of holographic lithography.

This dissertation is dedicated to my parents,

W. Michael and Katherine L. Moore.

Acknowledgements

First and foremost, I would like to acknowledge and thank my advisor, Bob McLeod. He has been an inexhaustible source of knowledge, insight, advice, and enthusiasm. His support and encouragement gave me the confidence to pursue my own ideas, while at the same time keeping me grounded with sound guidance, objective critiques, and fresh insights. Working with Bob has been fun, exciting, and rewarding, especially because he is always willing to either provide or entertain the next "crazy idea".

I would also like to thank the other members of the McLeod research group, both past and present, especially Amy Sullivan, Matt Grabowski, Sarah Walter, Cotton Anderson, Marty Baylor, Chunfang Ye, Keith Kamysiak, Ben Kowalski, Adam Urness, Darren Forman, and Patrick Wagner. Ben Braker and Max Colice also deserve recognition for insightful conversations regarding swept-wavelength techniques and wavelength chirp measurements. Further thanks are due to Carol Cogswell for the use of the differential interference contrast microscope in her lab, as well as to her former graduate student Sharon King for her patient instruction on how to use the microscope.

The knowledge that I have gleaned regarding the chemistry and practical laboratory production of volume photopolymer materials is principally due to two individuals: Michael Cole and Neil Cramer. Thanks to them for aiding my understanding despite my lack of background in chemistry. The majority of the photopolymer material used in the research documented here was provided by Inphase Technologies, Inc. I'd specifically like to thank David Michaels for fulfilling my many requests for various material formulations and sometimes unusual form factors.

Of course, this work would not have been possible without financial support. I have been the fortunate recipient of two NSF IGERT fellowships while at CU, the first under the Optical Science and Engineering Program (OSEP), and the second under the Computational Optical Sensing and Imaging (COSI) program. This work has also been supported under NSF STTR grant number 0822695 in collaboration with Zenwa, Inc. Jacob Kuykendall, Founder and President of Zenwa, is deserving of special thanks as an enthusiastic and ongoing supporter of my research and professional development. The initial seed funding that launched my work on swept-wavelength interferometry at CU was provided by dBm Optics, Inc.

Contents

List of Tables

List of Figures

Chapter 1

Introduction

1.1 Introduction to swept-wavelength interferometry

Since Young's double slit experiment in the early nineteenth century established the wave nature of light, optical interferometry has been played an essential role in the advancement of scientific understanding and in the development of modern technology. The ability of interferometry to utilize the wavelength of light as a basis for measurement and to convert wavelength-scale characteristics to observable macroscopic phenomena has made optical interferometry an invaluable tool for precision measurements. Historically, perhaps the most famous interferometric experiment was the effort put forth by Albert Michelson and Edward Morley to measure the relative velocity of the Earth and the "luminiferous ether" [1], the hypothetical medium that was postulated to carry the oscillations of propagating light waves (see Fig. 1.1). In this experiment, Michelson and Morley sought to distinguish relative differences in optical path length on the order of 10^{-8} that would indicate a directional dependence in the speed of light. Interferometry is now used to perform precision measurements in a wide array of application areas, including astronomy, spectroscopy, metrology, microscopy, and sensing [2].

The advent of the laser in 1960 [3] brought about ready access to bright, coherent light sources, leading to a revolution in interferometry including new

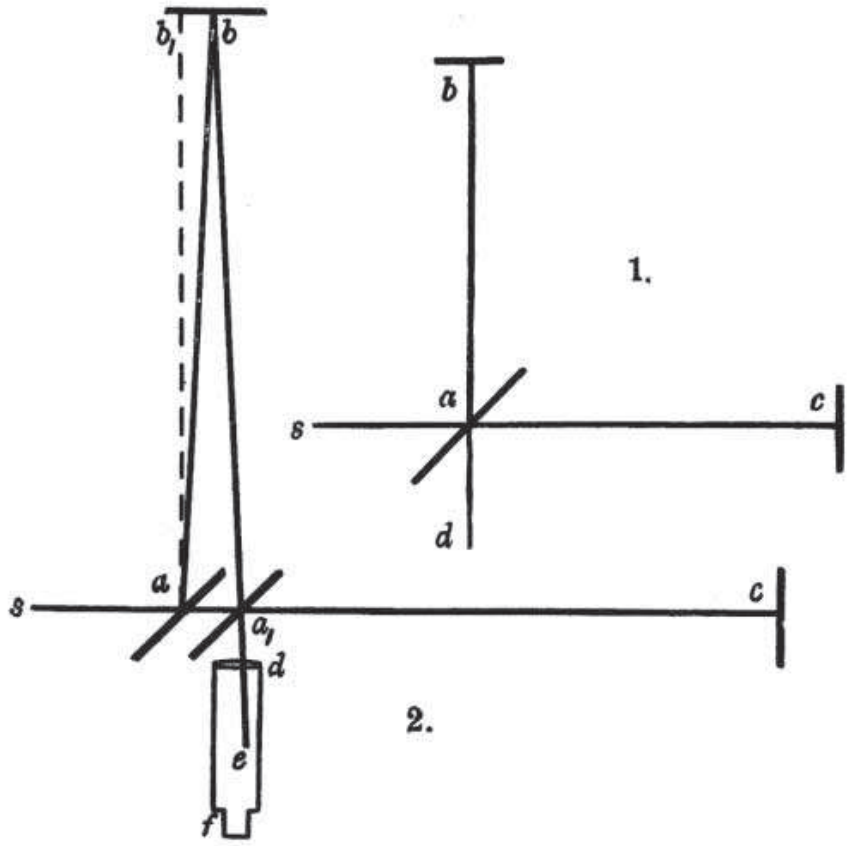

Figure 1.1: A diagram of his namesake interferometer that Albert Michelson, along with Edward Morley, used to describe their experiment for measuring the relative velocity between the Earth and the ether. (Reproduced from the original manuscript [1].)

modes of operation, new applications, and a profusion of commercial interferometric instruments that continues to this day [2]. Among the advancements in laser technology that took place over the course of the ensuing decades, the development of wavelength-tunable laser sources is most noteworthy in the context of this thesis. In particular, the 1980s saw the arrival of semiconductor diode lasers that could be easily tuned using temperature or injection current. These lasers provided a key capability that drove the development of a new form of interferometry based on sweeping of the source wavelength.

Swept-wavelength interferometry (SWI) forms the basis for a variety of mea-

surement techniques utilized in a diverse array of applications. While the details of the implementation may depend on the application, the defining characteristic of all SWI systems is the use of a wavelength tunable source coupled with an interferometer. In contrast to traditional interferometry, where interference fringes are typically observed as a function of a spatial coordinate, the fringe pattern in SWI is acquired as a function of the instantaneous optical frequency of a tunable source. The interferometer may employ various geometries, but all function by splitting the output of the tunable source into two paths, a reference path and a test path. In SWI, the optical path length of the reference path is generally fixed, and the test path may include multiple distinct paths, such as a series of reflecting interfaces. By performing a Fourier transform on the acquired interference pattern data, a measurement of the complex impulse response of the test path may be performed. Depending on the specific implementation, the temporal range of this impulse response measurement, converted to distance units via the speed of light, can vary from a few millimeters to a few kilometers. This ability to perform depth-resolved measurements as a function of delay in the test path has been exploited for a vast array of applications such as telecommunications component testing, distributed sensing, biomedical imaging, microscopic profilometry, and free-space ranging measurements.

The following section provides an overview of the development of SWI and presents a summary of the applications that have driven its development over the past three decades. Section 1.3 follows with an outline of the remainder of this thesis, which includes a number of novel advancements in the field of SWI for performing precision measurements.

1.2 Overview of SWI development

Prior to the appearance of swept-wavelength optical sources, SWI was developed in the radio-frequency (RF) region of the electromagnetic spectrum to perform free-space ranging measurements using the technique known as frequency-modulated continuous-wave (FMCW) radar [4]. The first forays into swept-wavelength interferometry at optical wavelengths were targeted at the measurement of reflections in optical fibers [5–7]. This new method was termed optical frequency domain reflectometry (OFDR), in analogy to optical time domain reflectometry (OTDR), a technique that was already in use [8]. In contrast to OTDR, which employs a measurement of the propagation time delay of short pulses to perform distributed reflection measurements, OFDR performs an analogous measurement in the frequency domain by sweeping the wavelength of a laser source and coherently detecting the reflected signal by mixing it with a copy of the swept-wavelength input. Both methods are still in widespread use; while OTDR provides superior range, OFDR can locate reflectors with better resolution and provides both amplitude and phase information, allowing for spectral measurements in the frequency domain in addition to time domain reflectivity data.

In this thesis, OFDR refers to the method by which the optical carrier frequency of a continuous wave (cw) optical source is modulated and detected coherently in the optical domain. Over the past decade or two this has become the standard usage of the term OFDR, but throughout the 1980s the term was used to describe two different techniques for performing reflective measurements. This ambiguity in terminology is sometimes acknowledged in the literature of the time, but not universally nor always consistently, so the potential for confusion exists in reviews of the relevant literature. In addition to OFDR by modulation of the optical carrier frequency, the term OFDR was also used to refer to

measurement systems that involve sweeping the frequency of a sinusoidal amplitude modulation applied to a single-frequency laser source, henceforth referred to as the modulation-sweep method. This modulated optical signal, after being reflected by the device or system under test, is directly detected and then mixed with the RF modulation signal in the electrical domain [9, 10]. In both methods the location of a reflector can be located to within a resolution that improves with increased range of the frequency sweep [11,12]. At a time when tunable laser diodes were limited to a sweep range on the order of 100 GHz [6], the two methods could achieve similar range resolutions. While wavelength-tunable optical sources have advanced to the point of 50 THz sweep ranges that yield resolutions under 10 μm [13], the modulation-sweep method (like OTDR) is limited to millimeter resolutions by the high-speed electronics required to detect rapidly modulated signals [14]. The advantage of OTDR and the modulation-sweep method is that these techniques can perform long-distance measurements over kilometers or more because they don't rely on optical coherence for coherent detection. On the other hand, it is the coherent aspects of SWI that provide key advantages in terms of resolution, sensitivity, and dynamic range.

The initial development of SWI in the form of OFDR was primarily driven by the need to characterize reflectivity in optical fibers for telecommunication applications. Advances in the sensitivity of OFDR measurements have allowed for detection of the Rayleigh backscatter of optical fibers [15,16], as well as loss measurements of optical network components based on changes in the Rayleigh backscatter level [17]. Sensitivities in excess of -150 dB have been demonstrated [18]. Similarly, research into coherent swept-wavelength sources such as external-cavity diode lasers (ECDLs) has expanded the range of OFDR measurements from a few centimeters to 100 m or more [19, 20]. Telecommunications applications of SWI beyond distributed reflectivity measurements within optical fiber include

measurements of loss in waveguides and optical network components [17, 21–24], measurements of group delay and group velocity dispersion [25–30], fiber Bragg grating characterization [25, 31–37], polarization measurements including polarization mode dispersion and polarization dependent loss [38–43], characterization of multimode [44–46] and specialty [47, 48] fibers, and vector characterization of fiber optic components [49–51].

The ability of SWI to perform precise and accurate measurements over extended lengths of optical fiber makes it an appealing approach for fiber optic sensing applications. Sensor systems employing SWI typically use a calibrated probe in the test arm of the interferometer, such as an air-spaced etalon [52] or fiber Bragg grating [53]. By placing multiple partially reflecting probes in a single fiber, distributed sensing can be accomplished using the ability of SWI to resolve the response from each probe in depth [54]. The sensitivity of SWI allows for distributed sensing in unaltered fiber by detecting changes in the Rayleigh backscatter. This approach has been used for both distributed strain and temperature measurements [55–57]. Furthermore, SWI sensor systems can multiplex the response from multiple probes in disparate spatial locations using multiple sensing paths of different lengths [58].

Whereas telecommunications and sensing applications of SWI are typically concerned with light that is constrained to propagate along one dimension in an optical waveguide, other applications have made use of SWI to perform depth resolved measurements of reflectivity in free space. One such application is the extension of the original SWI work on FMCW radar to the optical spectrum to produce FMCW light detection and ranging (lidar) systems [59, 60]. Ranging of hard targets as well as wind speed measurements have been reported using the FMCW lidar technique [61].

Another major application of SWI is for performing depth-resolved imaging

in two and three dimensions. To produce images using SWI, the typical approach is to make use of a free space probe coupled with a raster scanning system. This technique has been developed primarily in the context of biomedical applications, and within that field it is known by multiple acronyms, including optical frequency domain imaging (OFDI) [62] and swept-source optical coherence tomography (SS-OCT) [63]. More generally, the term optical coherence tomography (OCT), first introduced in 1991 to describe depth resolved imaging using low-coherence interferometry [64], now refers to three related but distinct optical methods. The low-coherence implementation is based on the technique known in the telecommunications field as optical coherence domain reflectometry [65]. In this approach, a broadband source is used in conjunction with an interferometer with a variable reference path delay. Interference occurs only when the reference and test paths of the interferometer are matched to within the coherence length of the source. The envelope of the fringe pattern is observed as a function of reference path delay in order to map out reflectivity as a function of position in the test path. This method yields essentially the same information as SWI, but using a time domain acquisition (as a function of path delay) rather than a frequency domain acquisition (as a function of instantaneous optical frequency of the source). For this reason, this approach is often referred to as time domain (TD-) OCT.

Swept-source OCT employing raster-scanned OFDR is one means for performing OCT in the frequency domain [66]. The other method, termed fourier domain or spectral domain (SD-) OCT,* utilizes a fixed broadband source rather than a tunable laser as the input to an interferometer with a fixed reference path length [67]. The interferometer output is spectrally dispersed using a grating or

*The terminology in the literature is not completely consistent, and SWI approaches to OCT are also sometimes referred to as fourier domain or spectral domain OCT. This is entirely reasonable, but occasionally requires careful inspection by the reader to determine which approach has been employed in a particular paper. In this thesis, SD-OCT refers to OCT using a broadband source with a spectrometer, and SS-OCT refers to OCT using SWI.

some other dispersive element, and detected as a function of wavelength across a linear detector array. There have been a number of papers exploring the relative merits of the different approaches to OCT [68–71]. The frequency domain approaches have been shown to possess a fundamental sensitivity advantage over the time domain approach [68,69], though there is some disagreement on whether or not this advantage can be fully realized in practice [70,71]. Frequency domain approaches are also favored because they utilize interferometers with no moving parts and can achieve faster data acquisition rates than TD-OCT [70]. Because the depth resolution in OCT improves with greater optical bandwidth, TD-OCT and SD-OCT are preferred for applications that require the utmost resolution because broadband sources are available with broader bandwidths than tunable narrow band sources [72–75]. Recent development in the area of high-speed swept-wavelength sources, on the other hand, has made SS-OCT the preferred method for high-speed OCT imaging [76].

Another imaging application of SWI is three-dimensional (3D) imaging of surface profiles [77–86]. In this application area, SWI is often referred to as wavelength-scanning interferometry or wavelength-scanning profilometry in the literature. Whereas OCT imaging is most often performed via scanning either the probe beam or the test sample, implementations of SWI for profilometry often use a full-field approach. Full-field imaging with SWI requires a bulk-optical, free-space interferometer rather than a fiber interferometer, and the detector is a two-dimensional (2D) sensor array such as a charge-coupled device (CCD) or complementary metal-oxide-semiconductor (CMOS) camera. Full-field SS-OCT has also been reported [87,88]. One advantage of full-field imaging with SWI is that the complexity associated with the scanning hardware is eliminated. Another advantage is that data for all points on the object is acquired with the same wavelength sweep, reducing the potential for measurement errors associated with

sweep-to-sweep variations of the source output. The primary drawbacks are the need for a bulk-optic interferometer, which, unlike fiber interferometers, requires precise alignment, and the slow acquisition rates of cameras relative to single-point photodiodes impose a more restrictive design tradeoff between the speed, range, and resolution of the measurement.

The development of optical SWI from its roots in the early 1980s to the present closely follows the development of swept-wavelength sources at optical wavelengths. The source parameters that are most important for SWI are the total sweep bandwidth, the instantaneous line width, and the tuning curve $\nu(t)$ that describes the instantaneous optical frequency ν as a function of time, t. Most early demonstrations of SWI made use of diode lasers that could be tuned by temperature or injection current over a fraction of a nanometer with a coherence length up to a few meters. Broader tuning ranges could be achieved using dye lasers, but with reduced coherence [12]. Development of ECDLs during the 1990s led to the commercial availability of swept sources with mode-hop-free sweep ranges of 100 nm or more and coherence lengths on the order of 1 km by the turn of the century [89]. Imaging applications of SWI involving scanning have necessitated substantial speed improvements over commercial ECDLs targeted at telecommunications applications, which generally offer sweep repetition rates on the order of 1 Hz. Some groups have increased the sweep rate of ECDLs by incorporating high-speed scanning galvanometer mirrors [90–92] and polygonal mirrors [93] into the external cavity. Many orders of magnitude of improvement in sweep rates have been gained by going to fiber laser designs using an electronically addressable intracavity tuning element such as a piezoelectric Fabry-Perot filter at the expense of reduced coherence compared to commercial ECDLs [94–96]. These high-speed swept-wavelength fiber lasers typically use a fiber ring cavity geometry with a semiconductor optical amplifier (SOA) as the gain medium. Within

the past five years, the fiber ring design has led to the introduction of Fourier domain mode-locked lasers (FDMLs) [97], where the intracavity tuning element is tuned at a rate equal to the round trip optical propagation time within the cavity. This results in the cavity mode phases becoming locked such that a complete frequency chirp continually exists within the cavity. Sweep rates up to 370 kHz over a bandwidth of 120 nm have been demonstrated [98]. In addition to increased speed, recent developments in swept sources have endeavored to increase the total sweep bandwidth, as the bandwidth is generally the factor limiting the spatial resolution of SWI measurements. One approach to achieve increased bandwidth is to forgo the use of a laser altogether, and to use a narrow band tunable filter together with a broadband light source, such as a halogen lamp [86] or superluminescent diode [81]. Another approach is to use broadband short pulses from a nonlinear supercontinuum source and stretch them using a dispersive medium to produce long, chirped pulses [13]. Additional bandwidth in an FDML laser has been achieved by incorporating two SOAs with different gain bandwidths within the fiber ring cavity [99].

Another active area of research has been in linearizing the frequency sweep of tunable sources [93, 100, 101]. This is because SWI typically requires sampling of the interferogram at equal increments of optical frequency, and a time-linear frequency sweep provides equal frequency intervals when the sampling is done using a simple temporal clock. A linear sweep is not necessary, however, if the instantaneous optical frequency can be monitored with sufficient resolution throughout the sweep. In 1990 Kobayashi and coworkers [102] first suggested the use of an optical frequency encoder for monitoring the sweep wavelength for SWI, and in 1991 Brinkmeyer and Glombitza first demonstrated this idea experimentally [103]. Their approach, called the frequency sampling method, uses an auxiliary interferometer as a frequency clock for sampling the swept-wavelength

interferogram [22, 104]. Alternatively, the output of an auxiliary interferometer may be used to resample data acquired using a temporal clock onto a grid of equal frequency increments [105]. In a third method, the tuning element in the swept-wavelength source is outfitted with a calibrated encoder that outputs trigger signals at equal frequency intervals [106]. One of the topics addressed in this thesis is the limits under which an auxiliary interferometer may be used for compensation of source tuning rate variations in SWI.

Other recent developments of interest in the field of SWI include vibration-tolerant SWI using time-shearing interferometry [30] and active phase control [86], as well as phase-sensitive SWI. Phase-sensitive approaches to SWI have been demonstrated for performing extremely sensitive measurements of relative displacement and changes in optical path length [107–109], and have been applied to Doppler imaging of fluid flow [110]. Phase-sensitive SWI shows great promise for performing extremely precise distance and displacement measurements with sub-nm sensitivity. Another topic addressed in this thesis is the extension of phase-sensitive SWI beyond purely relative displacement measurements to include absolute range measurements with nanometer-level precision.

1.3 Thesis Outline

This thesis presents several novel improvements and extensions to the field of SWI. These include both general improvements that are applicable to SWI systems across a variety of application areas, and that are not necessarily limited to the optical spectrum, as well as novel application-specific implementations of SWI that demonstrate new measurement capabilities.

Chapter 2 provides the theoretical framework for the presentation of the novel SWI extensions that follow. The fundamentals of swept-wavelength interference are presented together with the theory and practical design considerations

that are required to implement functional optical SWI systems.

Chapter 3 addresses the limitations in the use of an auxiliary interferometer to correct for source tuning rate variations in SWI. In particular, the frequency sampling method is shown to correct for nonlinear tuning only in the case of relatively short interferometer path length mismatches and/or slow source frequency tuning. Historically, this limitation was not a problem due to the limitations in sweep rate and coherence of available swept sources. Recent swept source development, however, has enabled the construction of optical SWI systems where the frequency sampling method is no longer valid, resulting in sampling errors where the increments of the sampled frequency grid are not equal. I show that another source of sampling errors, namely finite delay times in data acquisition hardware, can be used to cancel the sampling errors intrinsic to the frequency sampling method to second order. This allows the frequency sampling method to be used with higher speed swept sources and longer interferometers, enabling faster SS-OCT scanning and longer-distance OFDR measurements while maintaining accuracy.

Chapter 4 presents a novel self-referenced and phase-sensitive approach to performing absolute ranging measurements using SWI. Whereas the range resolution of optical SWI measurements using the traditional amplitude measurement approach is limited to the order of $10\,\mu$m, the use of phase information has been shown to improve the precision by several orders of magnitude for relative displacements. I extend the capability of phase-sensitive SWI to include absolute range measurements with nanometer precision. As an example application, a simultaneous measurement of the group index and thickness of an optical glass sample is presented, achieving an uncertainty on the order of 10^{-6} for the group index and $10^{-8}\,$m in thickness.

Chapter 5 represents somewhat of an aside, in which I present in detail one of

the motivating applications that requires precision measurement capabilities that can be provided by SWI. This application is the characterization of photosensitive volume photopolymers and optical devices fabricated in these materials. Volume photopolymers have the capability to produce 3D refractive index structures distributed throughout a solid volume without the need for any wet processing. This fact makes them appealing as a platform for holographic data storage and for constructing 3D integrated optical devices. Chapter 5 examines the fabrication of one such device type, 2D arrays of optical waveguides, demonstrating successful fabrication of light guiding arrays using holographic lithography.

Chapter 6 describes a novel implementation of SWI for performing quantitative, spatially resolved measurements of refractive index contrast that was directly motivated by the waveguide array fabrication work discussed in Ch. 5. The ability of SWI to resolve reflections is depth is exploited to characterize refractive index structures buried beneath transparent substrates, and the sensitivity intrinsic to coherent detection is used to measure small variations in Fresnel reflectivity to map out spatial variations in index.

Finally, Ch. 7 summarizes the current state of the work presented in this thesis and provides suggestions for future work that could continue to advance the state of the art in SWI measurement capabilities.

Chapter 2

Fundamentals of Swept-Wavelength Interferometry

2.1 Introduction

In this chapter I will provide the background theory necessary to understand the operation of swept-wavelength interferometers and the systems that utilize them. This background is intended to provide a detailed and useful overview of SWI, as well as provide a foundation for the following chapters that present three novel contributions to the field of SWI. Chapter 3 describes a novel improvement applicable to any implementation of SWI where the swept-wavelength source exhibits significant fluctuations in the tuning rate. Chapter 4 presents a new way to utilize the phase information present in SWI data to perform extremely precise absolute ranging measurements. Finally, chapter 6 presents a novel application of SWI in the form of an SS-OCT for performing quantitative, spatially resolved measurements of refractive index contrast for applications such the development of holographic materials and characterization of optical devices such as optical fibers, gradient-index lenses, and polymer optical waveguides and waveguide arrays.

I begin the discussion of SWI in the following sections by analyzing a simplified swept-wavelength interferometer. Depending on the particular application,

SWI systems may be implemented using optical fiber and fiber-coupled components, as a free-space optical system, or using some combination of free-space and fiber optics. For concreteness, the discussion in this chapter uses the context of fiber systems, though the analysis applies equally well to analogous free-space systems. The discussion proceeds by considering the effect of laser tuning characteristics that deviate from perfect linearity. Next, I introduce some measurement capabilities of SWI, including ranging measurements and optical component characterization, along with some functional design considerations for the implementation of these systems. Finally, the chapter concludes with a discussion of noise sources in swept-wavelength interferometers.

2.1.1 A note on terminology and notation

One point of confusion that often accompanies discussions of swept-wavelength interferometry is the terminology used to refer to data acquired in the laboratory domain and data that has had a Fourier transform applied to it. Many people, especially those with electrical engineering backgrounds, are familiar with typical signal applications where data is acquired as a function of time, and the Fourier transform is used to analyze the frequency spectrum of the acquired signal data. Thus, it is common to refer to raw data acquired in the laboratory domain as *time domain* data, while data that has been Fourier transformed is referred to as *frequency domain* data. For reasons that will become clear in subsequent sections, in the context of SWI the roles of the time domain and the frequency domain are reversed relative their typical usage. That is, raw SWI data is often said to be acquired in the frequency domain, and a Fourier transform then produces time domain data. A cursory explanation is that data is generally acquired as (or resampled to be) a function of the instantaneous frequency of the laser source as it sweeps, rather than as a function of time. The fact that the instantaneous

frequency of the source is changing as a function of time only adds to the confusion. In the SWI literature, different authors use both permutations of the time and frequency labels, and still others present the analysis in terms of wavenumber and distance domains. While I would very much like to consistently use a single convention throughout this thesis, that would unfortunately place undue restriction on the presentation of information because there are situations where raw, sampled data is most appropriately described as frequency domain data, and others where describing it as time domain data clearly makes the most sense. In the context of this thesis, the distinction (the reasons for which will hopefully become clear in the sections that follow) is determined by which physical clock signal is used to acquire SWI fringe pattern data. In the analysis that follows, I will attempt to distinguish between time domain and frequency domain data acquisitions using the following notation. When data is acquired using a temporal clock and the laboratory domain corresponds to the time domain, I will use the independent variables t in the time domain and f in the spectral domain. For frequency domain acquisitions, I will use the independent variables ν in the (laboratory) frequency domain and τ in the (transformed) time domain.

2.2 Swept-wavelength interference

2.2.1 Simple interferometer, linear frequency tuning

The simplest SWI system for the purposes of theoretical analysis consists of a coherent optical source capable of a time-linear frequency sweep, an interferometer with two fixed paths of different lengths, and a means for detecting the optical signal at the output of the interferometer. The electric field of the laser output is expressed as

$$\mathbf{E}(t) = E_0 e^{2\pi j[\nu_0 + (\gamma/2)t]t} \hat{\boldsymbol{\varrho}} \tag{2.1}$$

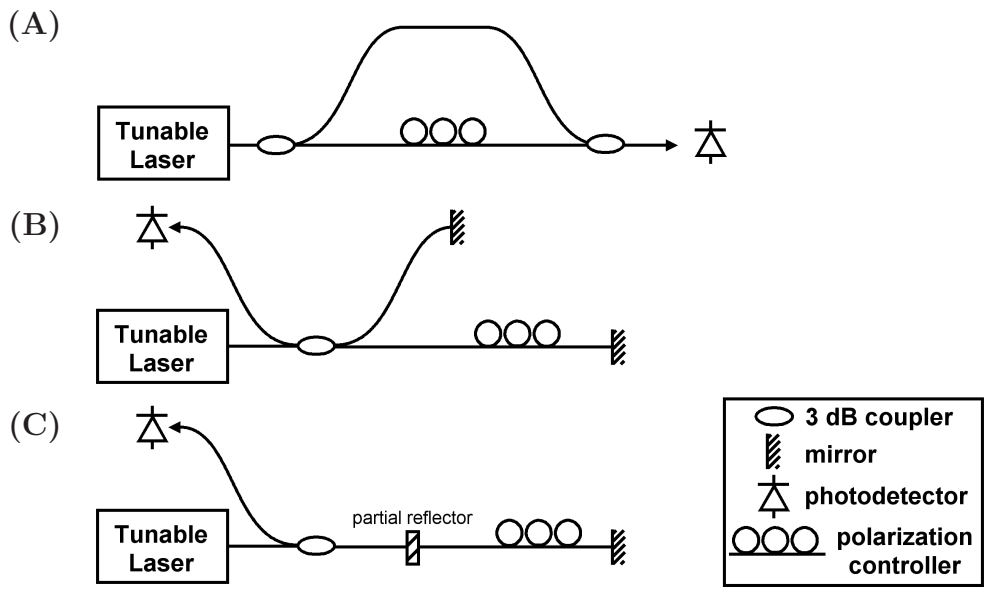

Figure 2.1: Three swept wavelength interferometers implemented in single mode optical fiber based on (A) Mach-Zehnder, (B) Michelson, and (C) Fabry-Perot geometries.

where E_0 is a constant amplitude, $\hat{\boldsymbol{\varrho}}$ is a unit polarization vector, and $\nu(t) = \nu_0 + \gamma t$ is the instantaneous optical frequency at time t. The interferometer may use one of several possible geometries, three of which are depicted in Fig. 2.1. In each case, the laser field is split into two components that travel different distances before being recombined and detected. For convenience I take the splitting ratio to be unity.

I denote the group delays corresponding to the two interferometer paths as τ_1 and τ_2. When the two components of the optical field are recombined, interference results in a detector voltage given by

$$U(t) = U_0[1 + \cos(2\pi\gamma t\tau_0 + \psi)], \tag{2.2}$$

where $\tau_0 = \tau_2 - \tau_1$, ψ is a constant phase, and $U_0 = \sigma E_0^2$. The constant σ depends on the detector sensitivity. Here I have assumed that the contributions from the two interferometer paths are copolarized when they are combined at the

interferometer output. If the two contributions are not copolarized, polarization fading of the interference fringes will occur. Polarization fading is discussed in Sec. 2.4.

Equation (2.2) represents the primary result for the case of a simple interferometer with linear laser frequency tuning. The importance of this result is that it demonstrates a sinusoidal output for a fixed-path-length interferometer. This result will later be used in conjunction with a Fourier transform to separate AC and DC components of interferometer fringe patterns, as well as separate contributions from multiple interferometers in more complex optical networks. In the context of SWI, however, it is often more convenient to write Eq. (2.2) as a function of the instantaneous optical frequency rather than as a function of time:

$$U(\nu) = U_0[1 + \cos(2\pi\nu\tau_0 + \xi)], \tag{2.3}$$

where $\xi = \psi - 2\pi\nu_0\tau_0$.

2.2.2 Simple interferometer, nonlinear tuning

In the practical application of SWI, it is not generally possible to ensure that the frequency tuning characteristics of the laser source are perfectly linear. Historically, the problem of nonlinear laser tuning has been dealt with in three ways. One is to focus on the design and execution of a tunable laser source with a tuning curve that is linear in time [19,21,93,100,101,111]. Depending on the laser source, this approach can be difficult or impossible and, in general, is less convenient than the other options. Rather than linearizing the laser sweep, a second technique uses an auxiliary interferometer to measure the laser tuning rate as it changes throughout a wavelength sweep. This information is then used to resample the fringe data from a grid of equal time intervals to a grid of equal frequency intervals [34, 36, 105, 112]. The third technique, the frequency-sampling method,

also uses an auxiliary interferometer, but avoids the potentially large number of interpolations required for resampling by using the interferometer output as a clock signal to trigger data acquisition [22, 103, 113–115].

To account for arbitrary nonlinear tuning mathematically, Eq. (2.1) is replaced by

$$\mathbf{E}(t) = E_0 e^{j\phi(t)} \hat{\boldsymbol{\varrho}}, \tag{2.4}$$

where $\phi(t)$ is an arbitrary time-varying phase. In this case the instantaneous optical frequency is given by

$$\nu(t) = \frac{1}{2\pi}\frac{d\phi}{dt}, \tag{2.5}$$

and the generalized version of Eq. (2.2) for the voltage at the photodetector becomes

$$U(t) = U_0 \left\{1 + \cos\left[\phi(t) - \phi(t-\tau_0) + \psi\right]\right\}, \tag{2.6}$$

where again I have assumed copolarization. For convenience, this expression reflects a shift in the origin of the variable t by an amount equal to the propagation time through one arm of the interferometer. Equation (2.6) can be simplified if we expand $\phi(t-\tau_0)$ in a Taylor series as

$$\phi(t-\tau_0) = \sum_{n=0}^{\infty} \frac{(-\tau_0)^n}{n!}\phi^{(n)}(t). \tag{2.7}$$

Here the notation $\phi^{(n)}(t)$ refers to the n^{th} derivative of ϕ with respect to t. Writing the zero- and first-order terms of the sum explicitly and using Eq. (2.5) yields

$$\phi(t) - \phi(t-\tau_0) = 2\pi\nu(t)\tau_0 - 2\pi\sum_{n=2}^{\infty}\frac{(-\tau_0)^n}{n!}\nu^{(n-1)}(t). \tag{2.8}$$

The higher order terms of this expansion are negligible when the condition

$$\tau_0^2\frac{d\nu}{dt} \ll 1 \tag{2.9}$$

is satisfied. This is true for many practical SWI systems, and can be interpreted physically to mean that the instantaneous laser frequency does not change appreciably over a time interval equal to the relative delay between the interferometer

paths. The case where inequality 2.9 is not satisfied will be treated in Chapter 3. For now I will drop the higher order terms and take

$$\phi(t) - \phi(t - \tau_0) = 2\pi\nu(t)\tau_0. \tag{2.10}$$

Note that this phase difference is no longer an explicit function of time, but rather a function of the instantaneous optical frequency. Therefore, when this expression is substituted back into Eq. (2.6) the detector voltage becomes a function of optical frequency, yielding

$$U(\nu) = U_0[1 + \cos(2\pi\nu\tau_0 + \xi)] \tag{2.11}$$

where, as before, $\xi = \psi - 2\pi\nu_0\tau_0$. This expression is identical to Eq. (2.3), but more care must be taken in its application in the case of nonlinear tuning. In the case of linear tuning, the fringe pattern is periodic in both time and optical frequency, whereas in the case of nonlinear tuning the fringe pattern is periodic in optical frequency, but not in time. This has two important implications for SWI:

1. When sampling a fringe pattern with the intention of performing a Fourier transform using the FFT algorithm, it is necessary to sample at equal intervals of optical frequency. If the laser tuning is nonlinear, this means that a time-synchronous clock may not be used for data acquisition without resampling onto a grid of equal frequency increments. Rather, a signal that is periodic in optical frequency must be used to trigger the acquisition of data points in order to avoid the need for resampling.

2. Because the fringe pattern output by a simple interferometer is periodic in optical frequency regardless of the tuning characteristics of the laser [within the constraints of inequality (2.9)], such a fringe pattern can serve as the required frequency clock for sampling the fringe pattern of another interferometer.

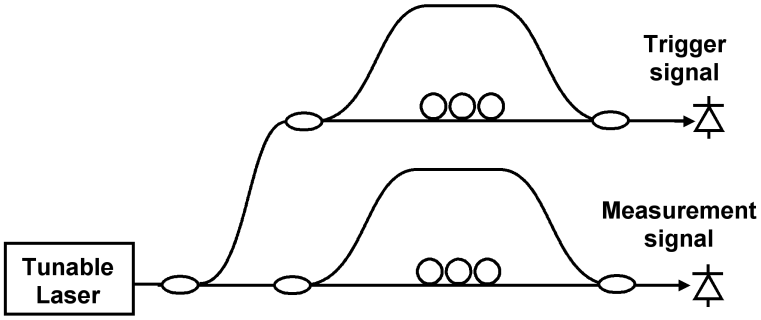

Figure 2.2: Hardware configuration for swept-wavelength interferometry (SWI) incorporating a trigger interferometer to accommodate nonlinear frequency tuning of the laser source. While Mach-Zehnder interferometers are shown, Michelson and Fabry-Perot geometries are equally applicable for both the trigger and measurement interferometers.

Consideration of the above points leads to an interferometer configuration such as that shown in Fig. 2.2 as the most basic configuration necessary for SWI using a nonlinearly tuned laser source. If the relative delay between the two paths in the trigger interferometer is τ_t, then Eq. (2.11) indicates that the period of fringe pattern output by the trigger interferometer will be $\Delta\nu = 1/\tau_t$. Using this signal as an external clock to sample the fringe pattern output by the measurement interferometer allows sampling at equal optical frequency increments $\Delta\nu$, provided inequality 2.9 holds. Alternatively, the trigger signal output can be used to measure the varying laser sweep rate throughout an acquisition, providing the sweep rate data required to perform a resampling step. For the experimental work presented in this thesis, the frequency sampling method has been used in lieu of resampling for dealing with laser tuning rate fluctuations. For this reason, the remaining theoretical analysis will proceed with the assumption of interferometric triggering of fringe data acquisition. Going forward, the auxiliary interferometer used to provide the frequency clock signal will generally be referred to as the *trigger interferometer*. The primary interferometer used to perform SWI measurements will be called the *measurement interferometer*.

2.3 Group delay or phase delay?

In introducing the concept of swept-wavelength interference, I stated that the important parameter describing the interferometer paths is the group delay associated with optical transmission through the path. Here I will demonstrate why it is the group delay, and not the phase delay, that is the proper parameter to consider.

Begin by expressing the input electric field to a swept-wavelength interferometer in terms of the Fourier transform of its frequency spectrum:

$$E(t;0) = \int_{-\infty}^{\infty} \mathcal{E}(\nu) e^{-j2\pi\nu t} d\nu. \tag{2.12}$$

When this field traverses a path of physical length z, it will advance in phase by an amount determined by the propagation constant β along the path, which may be a function of ν. Thus the field exiting the path, having traveled a distance z, will be

$$E(t;z) = \int_{-\infty}^{\infty} \mathcal{E}(\nu) e^{-j\beta(\nu)z} e^{-j2\pi\nu t} d\nu. \tag{2.13}$$

Next approximate the function $\beta(\nu)$ to first order by expanding about a frequency ν_0 as

$$\beta(\nu) = \beta(\nu_0) + \beta'(\nu_0)(\nu - \nu_0), \tag{2.14}$$

where the prime indicates differentiation with respect to ν. Then substitute $\beta = 2\pi n/\lambda = 2\pi n\nu/c$, where n is the index of refraction, yielding

$$\beta(\nu) = 2\pi n(\nu_0)\frac{\nu_0}{c} + \frac{d}{d\nu}\left[2\pi n(\nu)\frac{\nu}{c}\right]_{\nu_0}(\nu - \nu_0), \tag{2.15}$$

$$= 2\pi n(\nu_0)\frac{\nu_0}{c} + 2\pi\frac{\nu - \nu_0}{c}\left[n(\nu_0) + \nu_0 n'(\nu_0)\right]. \tag{2.16}$$

Note here that the quantity in brackets in Eq. (2.16) is the group refractive index [116], n_g. Therefore,

$$\beta(\nu) = 2\pi n\frac{\nu_0}{c} + 2\pi n_g\frac{\nu - \nu_0}{c}. \tag{2.17}$$

Equation (2.17) can now be used to evaluate the integral in Eq. (2.13). Making the substitution for $\beta(\nu)$ and dropping unimportant constant phase factors, the output field after traversing the optical path becomes

$$E(t;z) = \int_{-\infty}^{\infty} \mathcal{E}(\nu) e^{-j2\pi n_g \nu z/c} e^{-j2\pi\nu t} d\nu. \tag{2.18}$$

In this expression, the quantity $n_g z/c$ can be identified as the group delay, τ_g, associated with optical propagation along the physical path length z. The term that includes the phase delay nz/c has been dropped because it does not depend on ν and therefore contributes only a constant phase factor to the output field. Finally, the Fourier shift theorem [117] is invoked to arrive at the result

$$E(t;z) = E(t - \tau_g; 0), \tag{2.19}$$

to within a constant phase factor. Constant phase factors can be neglected in swept-wavelength interferometry because they do not affect either the amplitude or oscillation frequency of the interference term when two delayed fields are summed and the resulting square amplitude is computed. Thus, when representing propagation through various paths within a swept-wavelength interferometer as a delay applied to the input field, the appropriate delay to use is the group delay associated with the physical length of the path.

2.4 Polarization fading

In the preceding sections, I assumed that the light traversing the two interferometer paths was copolarized at the point where the two paths recombine. This will not be the case in general, especially in single-mode fiber systems where each length of fiber acts as a random wave plate. When the two field contributions are not copolarized at the interferometer output, Eq. (2.11) becomes

$$U(\nu) = U_0[1 + |\hat{\boldsymbol{\varrho}}_m \cdot \hat{\boldsymbol{\varrho}}_r^*| \cos(2\pi\nu\tau_0 + \varphi)], \tag{2.20}$$

where $\hat{\boldsymbol{\varrho}}_m$ and $\hat{\boldsymbol{\varrho}}_r$ are the polarization vectors of the fields exiting the measurement arm and the reference arm of the interferometer, respectively, * denotes complex conjugate, and $\varphi = \xi + \arg(\hat{\boldsymbol{\varrho}}_m \cdot \hat{\boldsymbol{\varrho}}_r^*)$. When the two interfering fields are not copolarized, the dot product of the two polarization vectors leads to polarization fading of the interference term. That is, when the dot product is less than one, the amplitude of the interference term will be reduced, and for orthogonal polarizations the interference term disappears altogether.

Several approaches may be employed to combat polarization fading. In a free-space implementation, the polarization may be preserved in each interferometer arm so no special action may be needed to avoid polarization fading. Similarly, fiber systems may be constructed using polarization-maintaining (PM) fiber and components to ensure copolarization at the interferometer output. In a singe-mode fiber implementation, a polarization controller may be used in one arm to align the polarizations and maximize the fringe amplitude. Polarization fading can be avoided in a Michelson geometry using single-mode fibers if the reflectors in each arm are Faraday rotator mirrors, which utilize the non-reciprocal Faraday effect to rotate the state of polarization by $\pi/2$ radians upon reflection causing polarization variations experienced on the forward pass to be reversed on the return pass. These approaches all assume a measurement arm with a known effect on the source polarization that is constant over the wavelength range of the tunable laser source. A more versatile solution to the problem of polarization fading that does not require *a priori* knowledge of the measurement arm is polarization-diverse detection.

A network layout implementing polarization diverse detection is illustrated in Fig. 2.3. A polarization beam splitter (PBS) is added to the output of the measurement interferometer and two photodetectors are used to measure the light intensity at the two outputs of the PBS, labeled S and P. Additionally, a polar-

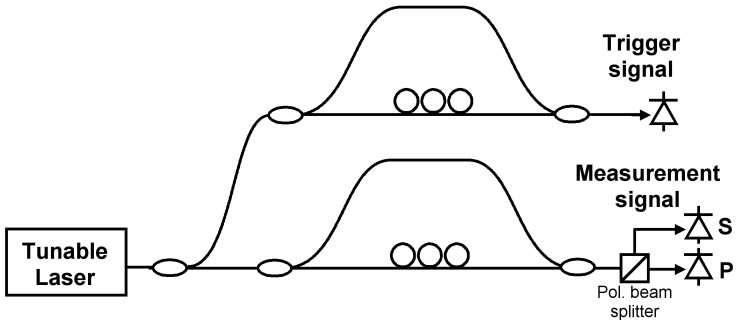

Figure 2.3: An SWI system incorporating polarization diverse detection.

ization controller is required in the reference arm of the interferometer. For this network, the output signals at the S and P detectors are given by

$$U_s(\nu) = U_0 \left[|\hat{\boldsymbol{s}} \cdot \hat{\boldsymbol{\varrho}}_m|^2 + |\hat{\boldsymbol{s}} \cdot \hat{\boldsymbol{\varrho}}_r|^2 + |(\hat{\boldsymbol{s}} \cdot \hat{\boldsymbol{\varrho}}_m)(\hat{\boldsymbol{s}} \cdot \hat{\boldsymbol{\varrho}}_r)^*| \cos\left(2\pi\nu\tau_0 + \varphi_s\right) \right] \tag{2.21}$$

and

$$U_p(\nu) = U_0 \left[|\hat{\boldsymbol{p}} \cdot \hat{\boldsymbol{\varrho}}_m|^2 + |\hat{\boldsymbol{p}} \cdot \hat{\boldsymbol{\varrho}}_r|^2 + |(\hat{\boldsymbol{p}} \cdot \hat{\boldsymbol{\varrho}}_m)(\hat{\boldsymbol{p}} \cdot \hat{\boldsymbol{\varrho}}_r)^*| \cos\left(2\pi\nu\tau_0 + \varphi_p\right) \right], \tag{2.22}$$

where $\hat{\boldsymbol{s}}$ and $\hat{\boldsymbol{p}}$ are unit vectors describing the principal polarization states of the PBS and φ_s and φ_p are constant phase terms. Here the measurement arm polarization state $\hat{\boldsymbol{\varrho}}_m$ is unknown, while the reference arm polarization state $\hat{\boldsymbol{\varrho}}_r$ can be controlled using the polarization controller. Because $\hat{\boldsymbol{s}}$ and $\hat{\boldsymbol{p}}$ are orthogonal, it is not possible for polarization fading to null the fringes at both outputs of the PBS simultaneously since this would require the dot products $\hat{\boldsymbol{s}} \cdot \hat{\boldsymbol{\varrho}}_m$ and $\hat{\boldsymbol{p}} \cdot \hat{\boldsymbol{\varrho}}_m$ to both be zero. Therefore, as long as at least one of the dot products incorporating the reference arm polarization are nonzero, a measurable interference signal is assured. Since the reference arm polarization can be controlled, we are free to set the value of $\hat{\boldsymbol{\varrho}}_r$. The best choice for $\hat{\boldsymbol{\varrho}}_r$ to maximize the signal level is to adjust the polarization controller such that the light in the reference path is split evenly at the PBS. In this case, $|\hat{\boldsymbol{s}} \cdot \hat{\boldsymbol{\varrho}}_r| = |\hat{\boldsymbol{p}} \cdot \hat{\boldsymbol{\varrho}}_r| = 1/\sqrt{2}$. Depending on the application (e.g., ranging or reflectivity measurements in the time domain or spectral characterization of

optical devices), the polarization diverse signals are more appropriately combined in either the time domain or in the frequency domain following digital filtering in the time domain [29]. In either case, the terms in Eqs. (2.21) and (2.22) that oscillate as a function of the laser frequency ν are the only terms of importance. If the unknown polarization unit vector $\hat{\boldsymbol{\varrho}}_m$ is cast as a general Jones vector in the form

$$\hat{\boldsymbol{\varrho}}_m = \begin{bmatrix} \sin\theta e^{-j\zeta/2} \\ \cos\theta e^{j\zeta/2} \end{bmatrix}, \tag{2.23}$$

then combination of the oscillating portion of the polarization diverse signals, $\tilde{U}_s$ and $\tilde{U}_p$, is accomplished in software post-processing via

$$\begin{aligned} \left(\tilde{U}_s^2 + \tilde{U}_p^2\right)^{1/2} &= \frac{U_0}{2}(\sin^2\theta + \cos^2\theta)\cos\left(2\pi\nu\tau_0 + \xi\right) \\ &= U_0\cos\left(2\pi\nu\tau_0 + \xi\right), \end{aligned} \tag{2.24}$$

where a constant phase has been absorbed in the term ξ. Note that this is now the same as the oscillating portion of Eq. (2.11), and does not depend on the unknown polarization state in the measurement arm of the interferometer.

2.5 Range measurements

One of the most common uses of SWI is for performing reflectivity measurements as a function of distance. This capability forms the basis of the majority of applications of SWI, including reflectometry, FMCW lidar for free space ranging, SS-OCT imaging, and wavelength-scanning profilometry. Range measurements using SWI typically employ a Michelson geometry, as illustrated in Fig. 2.4. Range information is contained in Eq. (2.20) in the factor τ_0, which is the group delay difference between the two interferometer paths. The range to an unknown reflector in one path, referred to as the *test path*, is determined relative to the other interferometer path, called the *reference path*. Once the interference

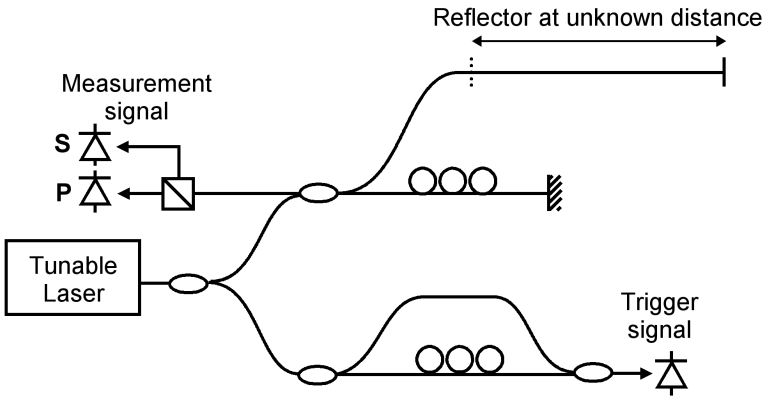

Figure 2.4: A schematic illustration of a swept-wavelength interferometer for performing range measurements.

fringe data has been acquired as function of the instantaneous laser frequency, an FFT is applied yielding a time domain plot such as the one shown in Fig. 2.5. Assuming copolarization for simplicity, the Fourier transform of Eq. (2.20) is

$$\mathcal{U}(\tau) = U_0 \left[\delta(\tau) + \delta(\tau - \tau_0) + \delta(\tau + \tau_0)\right], \tag{2.25}$$

where δ denotes the Dirac delta function. In Fig. 2.5, the positive frequency peak is located at the delay τ_0, while the negative frequency peak shows up at $\Delta\tau - \tau_0$ due to the periodicity of the FFT, where $\Delta\tau$ is the full range of the time domain data set. Thus by performing a Fourier transform of the interference fringes and identifying the peaks in the time domain corresponding to the interference term, the relative delays between the interferometer arms can be discerned. If the length of the reference arm is known, then a range measurement to the reflector in the measurement arm is accomplished.

I will reiterate here the message of Sec. 2.1.1, namely that the roles of the time and frequency domains are reversed in the context of SWI relative to their more traditional roles as taught in introductory signal processing courses. Data is acquired as an oscillating interferogram as a function of the instantaneous laser frequency, ν; thus the raw measured signals are spectral domain functions. A

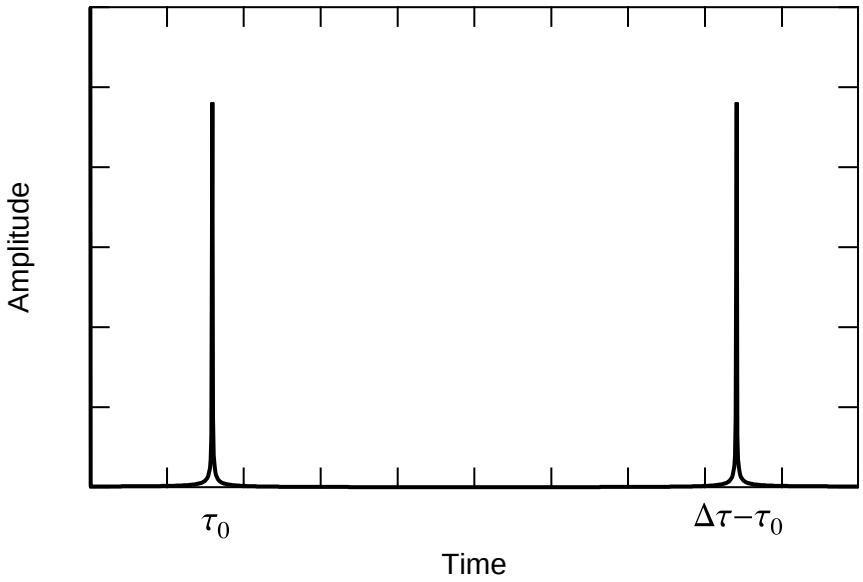

Figure 2.5: A plot of the Fourier transform of the fringe pattern output by a swept-wavelength interferometer. τ_0 is the relative delay between the two interferometer arms, and $\Delta\tau$ is the total time domain range given by the reciprocal of the frequency sampling interval.

Fourier transform converts this data to the time domain, where each oscillatory component in the spectral domain is observed to correspond to a peak located at a particular time, or delay, τ. The time axis in the Fourier domain directly corresponds to the delay relative to the interferometer reference path.

This distinction between time and frequency domain data acquisition is especially important in the presence of laser tuning rate variations. Fig. 2.6 illustrates the effect of sampling a swept-wavelength interferogram using a temporal clock when the laser tuning rate is not constant. Instead of sharp δ-functions in the time domain, the peaks are broadened considerably.

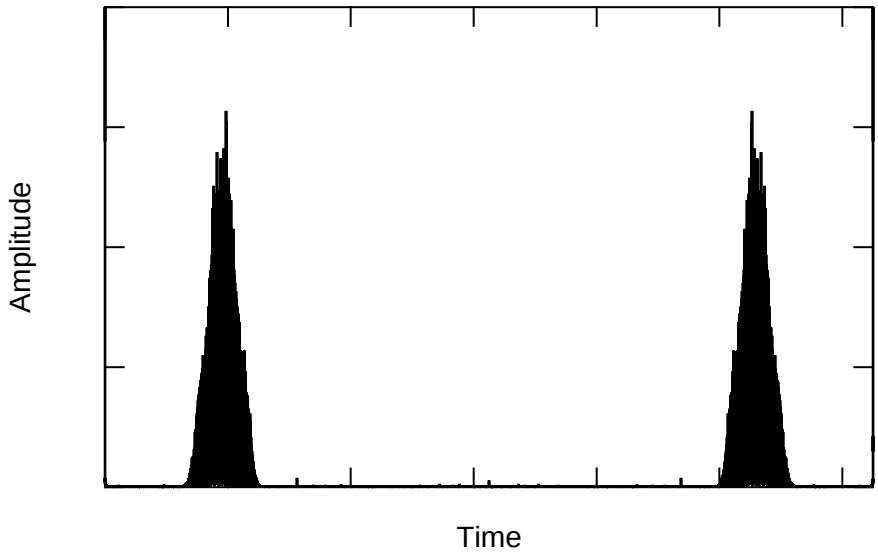

Figure 2.6: A plot of the amplitude of the Fourier transform of a swept-wavelength interferogram sampled with a temporal clock in the presence of nonlinear laser tuning.

2.5.1 Range measurement metrics

2.5.1.1 Maximum measurable range

For SWI data sampled using an external frequency clock as described in Sec. 2.2.2 and shown in Fig. 2.4, there will be a reciprocal relationship between the sampling interval in the frequency domain, $\delta\nu$, and the range spanned by the time domain data, $\Delta\tau$. According to Eq. (2.11), the frequency domain output of the trigger interferometer is

$$U_t(\nu) = U_{t0}\left[1 + 2\cos\left(2\pi\nu\tau_t + \xi_t\right)\right], \tag{2.26}$$

where the t subscripts indicate parameters specifically associated with the trigger interferometer. This signal is the clock signal used to sample the fringe pattern output by the measurement interferometer. The period of the trigger signal is the sampling interval in the frequency domain, $\delta\nu$, and is equal to the reciprocal of

the relative delay between the two arms of the trigger interferometer:

$$\delta\nu = \frac{1}{\tau_t}. \tag{2.27}$$

I will refer to the quantity τ_t as the *trigger delay*. Because the range measurement is performed in the time domain by performing a discrete Fourier transform on fringe data acquired in the frequency domain, the range of the time domain data will be the reciprocal of the sampling interval in the frequency domain. Therefore, the full range of the time domain data will be $\Delta\tau = \tau_t$. The dynamic range of the range measurement, however, is $\tau_t/2$, or half of the trigger delay. This is because the real sinusoidal component to the fringe pattern produced by each remote reflector will contribute both a positive and negative delay peak in the time domain, so only half of the time domain range is available for unambiguous measurements. Equivalently, sampling theory requires at least two samples per period of the fringe pattern in order to represent the measurement signal faithfully without aliasing, so the measurement interferometer can have a relative delay that is at most half of the trigger delay.

I have shown that for a given optical network, the maximum measurable range is determined by the trigger delay, τ_t, but so far I have not described what limits constrain the value of the trigger delay. When using highly coherent sources, the upper limit on the allowable trigger delays will be determined by the tuning rate of the laser and the speed of the data acquisition hardware. To see that this is the case, note that for a mean frequency tuning rate $\overline{\gamma} = \overline{d\nu/dt}$, the mean time interval $\overline{\Delta t}$ between samples will be

$$\overline{\Delta t} = \frac{1}{\overline{\gamma}\tau_t}. \tag{2.28}$$

Thus, the mean sampling rate $\bar{S}$ is

$$\overline{S} = \frac{1}{\overline{\Delta t}} = \overline{\gamma}\tau_t. \tag{2.29}$$

In fact, it is not the mean frequency tuning rate, but the maximum tuning rate $\gamma_{\max}$ that will determine the limit on τ_t, along with the maximum sampling rate $S_{\max}$ that the hardware can achieve. Here $\gamma_{\max}$ is the maximum tuning rate (in frequency units) that is reached as the laser tuning rate varies over the course of a frequency sweep. The trigger delay will be limited to a maximum value $\tau_{t,\max}$ given by

$$\tau_{t,\max} = \frac{S_{\max}}{\gamma_{\max}}. \tag{2.30}$$

In cases where the relative interferometer delays in an SWI system approach the coherence length of the source, the maximum measurable range will be limited by the source coherence length. A detailed analysis of this scenario is given in Sec. 2.9.3.

2.5.1.2 Temporal resolution

Because range measurement using SWI is fundamentally a delay measurement, the spatial resolution of the range measurement is determined by the temporal resolution of the delay measurement and the speed of light in the media present in the test path of the interferometer. As with the dynamic range, the temporal resolution is governed by the Fourier transform relationship between the time domain data used to determine the range, and the raw data acquired in the frequency domain. The range of frequencies $\Delta\nu$ over which the laser sweeps is

$$\Delta\nu = N\delta\nu, \tag{2.31}$$

where N is the total number of acquired data points. When a discrete Fourier transform is applied to the acquired frequency domain data, the resulting time domain data set will have a range, $\Delta\tau$, as described in the preceding section, and a step size $\delta\tau$ given by

$$\delta\tau = \frac{1}{\Delta\nu}. \tag{2.32}$$

In this way, the total frequency sweep range $\Delta\nu$ determines the fundamental temporal resolution of the measurement. The actual two-point resolution τ_{res} will depend on the resolution criteria being employed, as well as any windowing function used to multiply the frequency domain data prior to the discrete Fourier transform. In general,

$$\tau_{\text{res}} = C\frac{1}{\Delta\nu} \tag{2.33}$$

where C is a constant on the order of unity.

2.5.1.3 Temporal accuracy

Because range measurements are performed by locating a peak in a time domain data set, the accuracy of the range measurement will be determined by the uncertainty in the time domain sampling interval, δt. The time domain extends from a delay of zero up to the trigger delay, τ_t, as discussed in Sec. 2.5.1.1. Since $\delta\tau = \tau_t/N$ for a data set with N points, the uncertainty in $\delta\tau$, $u(\delta\tau)$, will be

$$u(\delta\tau) = \frac{u(\tau_t)}{N}, \tag{2.34}$$

where $u(\tau_t)$ is the uncertainty in the determination of the trigger delay. The question of the accuracy of the range measurement thus becomes a question of the quality of the calibration of the trigger delay. Because the calibration of the trigger delay involves a single measurement of length or delay, there are numerous approaches to calibration that will result in varying degrees of uncertainty. Consider, for example, a trigger interferometer with a length mismatch between the two arms of approximately 10 m of single mode fiber. With some care, one may be able to measure this mismatch using a ruler to within an uncertainty of perhaps 1 cm. This translates to an uncertainty in τ_t of approximately 50 ps. In Sec. 4.2.2 I describe an alternate method of trigger interferometer calibration that yields an uncertainty of approximately 1 ps.

Note that the uncertainty in $\delta\tau$ does not follow a normal distribution from point to point throughout the time domain data set. Rather, an error in the measurement of the trigger delay will yield a single value of $\delta\tau$ that is either too small or too large by the same relative magnitude as the error in τ_t. Therefore, a range measurement with a measured delay τ_m performed by locating a peak at index m in the time domain data array will have an uncertainty $u(\tau_m)$ given by

$$u(\tau_m) = mu(\delta t) = \frac{m}{N}u(\tau_t). \tag{2.35}$$

Thus, the relative error in the range measurement will equal the relative error in the calibration of the trigger interferometer.

2.6 Scalar device characterization

Thus far the analysis has assumed that the amplitude and phase responses of the interferometer paths do not exhibit any spectral variation. This is generally a valid assumption for interferometer paths comprising only single-mode fiber and/or free-space propagation. Now I will introduce a device under test (DUT) to the test path of the measurement interferometer, as shown in Fig. 2.7, and demonstrate the device characterization capabilities of SWI. The scalar characterization described in this section includes both the amplitude and phase responses of the DUT. The amplitude response yields a measurement of the loss associated with the device, and the phase response provides a measure of the group delay and chromatic dispersion of the device.

To show how SWI can be used to measure properties of a device, take the general input electric field described by Eq. (2.4) and launch it into a measurement interferometer with a device in the test path. As before, the laser output is split, but now the light propagating down the test path is modified by the DUT, while the light in the reference path is not. The DUT can be represented by its transfer

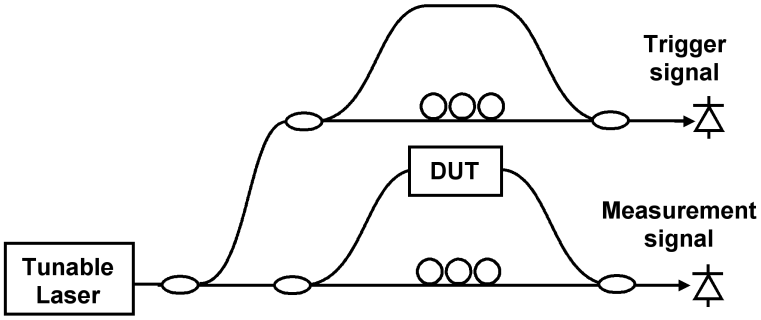

Figure 2.7: SWI system for characterizing the scalar response of a device under test (DUT).

function, $\mathbf{H}(\nu)$, which in general is a 2×2 complex matrix. This matrix multiplies an arbitrary input electric field vector, $\mathbf{E}_{\text{in}}(\nu)$ to produce an output electric field vector, $\mathbf{E}_{\text{out}}(\nu) = \mathbf{H}(\nu)\mathbf{E}_{\text{in}}(\nu)$. The resulting interferometer output is a detector voltage given by

$$U(t) = U_0 \left| \hat{\boldsymbol{\varrho}}_1 e^{j\phi(t-\tau_1)} + \mathbf{H}\hat{\boldsymbol{\varrho}}_2 e^{j\phi(t-\tau_2)} \right|^2 \tag{2.36}$$

$$\Rightarrow \quad U(\nu) = U_0 \left[1 + \left| \mathbf{H}(\nu)\hat{\boldsymbol{\varrho}}_2 \right|^2 + 2\Re\{\hat{\boldsymbol{\varrho}}_1 \cdot \mathbf{H}(\nu)\hat{\boldsymbol{\varrho}}_2\} \cos\left(2\pi\nu\tau_0 + \psi\right) \right], \tag{2.37}$$

where $\tau_0 = \tau_2 - \tau_1$ is again the group delay difference between the two interferometer paths and ψ is a constant phase. Here the veracity of inequality (2.9) has been assumed to make the transition from $U(t)$ to $U(\nu)$.

There are several things to note about the expression in Eq. (2.37). First note that the transfer function $\mathbf{H}(\nu)$ is projected on to the polarization vector $\hat{\boldsymbol{\varrho}}_2$ of the light in the device path, and the resulting vector is further projected on the polarization vector of the reference path, $\hat{\boldsymbol{\varrho}}_1$. This means that the full matrix $\mathbf{H}(\nu)$ cannot be measured with this system. At best, this system can measure one matrix element, i.e., the matrix element that couples $\hat{\boldsymbol{\varrho}}_2$ to $\hat{\boldsymbol{\varrho}}_1$. Because of this limitation of the measurement to a single matrix element, this type of device characterization is referred to as scalar device characterization, and the quantity $H(\nu) = \hat{\boldsymbol{\varrho}}_1 \cdot \mathbf{H}(\nu)\hat{\boldsymbol{\varrho}}_2$ is called the *scalar transfer function*. In contrast, the matrix

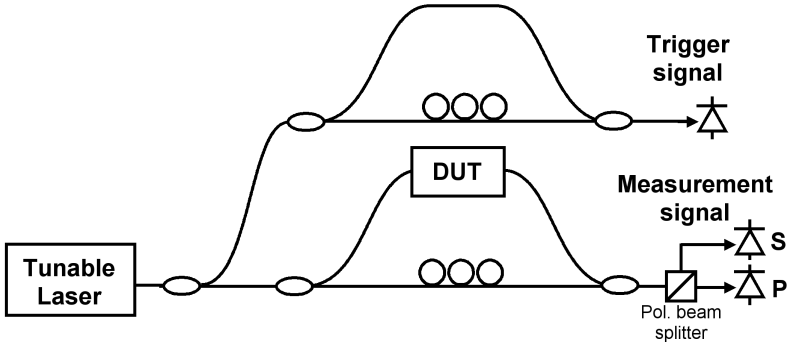

Figure 2.8: SWI system for characterizing the scalar response of a DUT utilizing polarization diverse detection.

$\mathbf{H}(\nu)$ is known as the *vector transfer function*.

Second, because the DUT may rotate the polarization $\hat{\boldsymbol{\varrho}}_2$ in an arbitrary fashion, it is impossible to use a polarization controller in the reference arm to select a polarization state $\hat{\boldsymbol{\varrho}}_1$ that is guaranteed to avoid polarization fading of the interference fringes for an unknown device. One way to deal with this problem is to perform multiple measurements using various settings of $\hat{\boldsymbol{\varrho}}_1$. If, for example, the DUT is a polarizer, an effective measurement can be achieved by orienting $\hat{\boldsymbol{\varrho}}_1$ such that the fringe amplitude is maximized. A better method to avoid polarization fading is to use polarization diverse detection as described in Sec. 2.4. This involves the addition of a polarization beam splitter at the output of the measurement interferometer and an additional photodetector, as shown in Fig. 2.8. In this case, the single photodetector at the output of the measurement interferometer has been replaced with two photodetectors, labeled S and P. The output signals at these detectors are given by

$$U_s(\nu) = U_0 \left[\left| \hat{\boldsymbol{s}} \cdot \hat{\boldsymbol{\varrho}}_1 \right|^2 + \left| \hat{\boldsymbol{s}} \cdot \mathbf{H}(\nu) \hat{\boldsymbol{\varrho}}_2 \right|^2 + 2\Re\{(\hat{\boldsymbol{s}} \cdot \hat{\boldsymbol{\varrho}}_1)(\hat{\boldsymbol{s}} \cdot \mathbf{H}(\nu) \hat{\boldsymbol{\varrho}}_2)\} \cos\left(2\pi\nu\tau_0 + \psi\right) \right] \tag{2.38}$$

and

$$U_p(\nu) = U_0 \left[|\hat{\boldsymbol{p}} \cdot \hat{\boldsymbol{\varrho}}_1|^2 + |\hat{\boldsymbol{p}} \cdot \mathbf{H}(\nu)\hat{\boldsymbol{\varrho}}_2|^2 + 2\Re\{(\hat{\boldsymbol{p}} \cdot \hat{\boldsymbol{\varrho}}_1)(\hat{\boldsymbol{p}} \cdot \mathbf{H}(\nu)\hat{\boldsymbol{\varrho}}_2)\} \cos\left(2\pi\nu\tau_0 + \psi\right) \right]. \tag{2.39}$$

Now, instead of projecting the output of $\mathbf{H}(\nu)\hat{\boldsymbol{\varrho}}_2$ onto a single vector as in Eq. (2.37), we have two signals that contain projections of $\mathbf{H}(\nu)\hat{\boldsymbol{\varrho}}_2$ onto two orthogonal vectors, $\hat{\boldsymbol{s}}$ and $\hat{\boldsymbol{p}}$, which are the polarization basis state vectors of the polarization beam splitter. The orthogonality of $\hat{\boldsymbol{s}}$ and $\hat{\boldsymbol{p}}$ prevent polarization fading from nulling out both projections simultaneously. As in Sec. 2.4, using the polarization controller in the reference arm to split the reference arm output evenly between the S and P detectors ensures that the dot products $\hat{\boldsymbol{s}} \cdot \hat{\boldsymbol{\varrho}}_1$ and $\hat{\boldsymbol{p}} \cdot \hat{\boldsymbol{\varrho}}_1$ also do not cause fading of the fringe visibility.

The third and final important characteristic to note in Eq. (2.37), as well as in Eqs. (2.38) and (2.39), is the distinction between the AC and DC components of the voltage signal. The scalar transfer function appears in the AC portion, whereas its square appears as a DC term. In order to perform both amplitude and phase measurements of the DUT, a data processing algorithm must be applied that isolates the AC component on the signal where the scalar transfer function appears unsquared. This data processing algorithm utilizes a Fourier transform and digital filtering in the Fourier domain. The algorithm steps are illustrated in Fig. 2.9. First, the fringe pattern is acquired in the frequency domain at equal intervals of optical frequency. This is shown in Fig. 2.9(A) for a simulated data set of 512 points using a trigger interferometer delay of 100 ns and a start wavelength of 1550 nm. The relative delay of the measurement interferometer is 10 ns. This data is then converted to the time domain using a Fourier transform. The time domain version of the measured fringe pattern is shown in Fig. 2.9(B). The AC portion of the fringe pattern produces two peaks in the time domain: the "positive delay peak" at 10 ns and the "negative delay" peak at -10, or equivalently 90, ns,

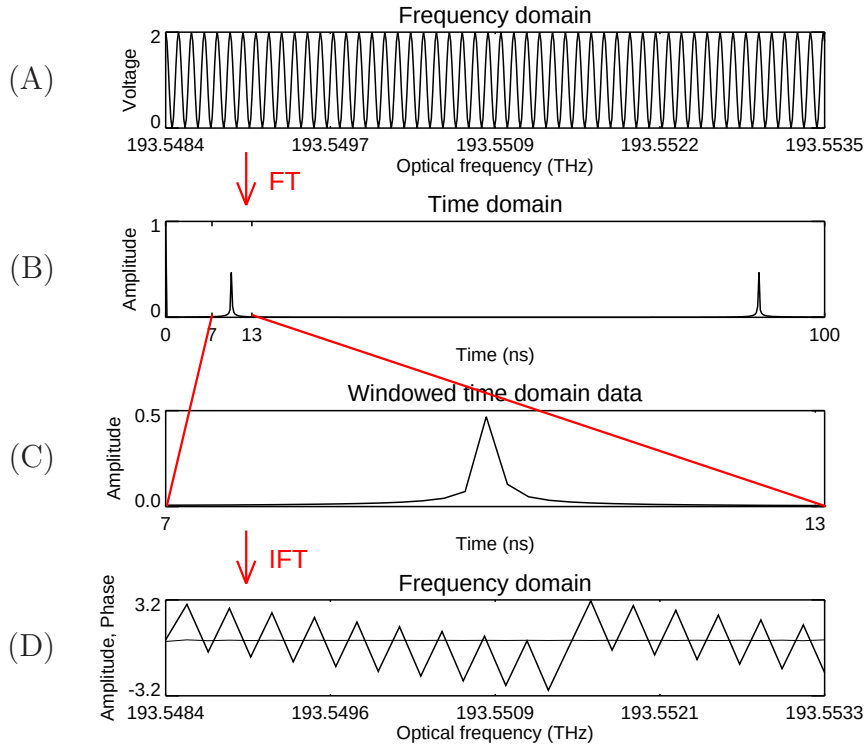

Figure 2.9: The process of extracting the AC component of a measured fringe pattern. (A) The measured fringe pattern in the frequency domain. (B) The Fourier transform (FT) of the measured fringe pattern, showing positive and negative frequency sidebands in the time domain. (C) Selection of the positive sideband using a digital filter. (D) An inverse Fourier transform (IFT) returns the data to the frequency domain. The filtered frequency domain data is complex with both amplitude and phase information.

since the Fourier domain is periodic. These two peaks correspond to the positive and negative complex exponential functions that, when summed, produce the cosine term of the fringe pattern. In the next step, a digital filter is used to select only the positive delay peak, as shown in Fig. 2.9(C). When just this portion of the data is transformed back to the frequency domain via an inverse Fourier transform [Fig. 2.9(D)], the result is a complex function of frequency that represents only the positive complex exponential of the cosine, along with any complex multipliers. In this way, the fringe pattern described by Eq. (2.37) (or by Eqs. 2.38 and 2.39) may

be digitally processed in software to produce a filtered complex data set $U^f(\nu)$ given by

$$U^f(\nu) = 2U_0[H(\nu)e^{j(\pi\nu\tau_w)}], \tag{2.40}$$

where τ_w is the duration of the digital filter window, which I have taken to be centered on the positive frequency peak. Thus a measurement of the scalar transfer function of the device under test has been performed, to within a constant amplitude and a linear phase factor. For the purposes of evaluating the performance of a device, this is equivalent to a measurement of the exact scalar transfer function because a reference measurement can be used to scale the overall amplitude, and the linear phase factor is equivalent to a delay.

Note that while the optical frequency spacing of the data points in the original data set was $1/\tau_t$, the sample spacing is now $1/\tau_w$. This down-sampling is an effect of selecting only a portion of the data set in the time domain.

With a measurement of the scalar transfer function in hand, the group delay and chromatic dispersion of the device under test can be obtained through straightforward calculations. The group delay of an optical device is defined as the derivative of the phase of the transfer function with respect to angular frequency, $\omega = 2\pi\nu$:

$$\mathrm{GD} = \frac{d\Theta}{d\omega}, \tag{2.41}$$

where $\Theta = \arg[H(\nu)]$. This basic definition, applied to the case of an SWI measurement of the scalar transfer function using polarization diverse detection, leads to the following expression for the average group delay over output polarization states:

$$\mathrm{GD}(\nu) = \frac{\arg\left\{U_s^f(\nu)U_s^{f*}(\nu+\delta\nu) + U_p^f(\nu)U_p^{f*}(\nu+\delta\nu)\right\}}{2\pi\delta\nu}. \tag{2.42}$$

Here U_s^f and U_p^f are the analogs of U^f in Eq. (2.40) for the case of polarization diverse detection as described above.

Chromatic dispersion can be defined as the derivative of the group delay with respect to either frequency or wavelength, λ. Here I will use the definition involving λ, since this yields chromatic dispersion units of ps/nm, which is the most commonly used unit in telecommunications applications. In this case,

$$\mathrm{CD} = \frac{d(\mathrm{GD})}{d\lambda}. \tag{2.43}$$

The insertion loss of the DUT can also be found from the scalar transfer function, provided a reference measurement is available, which can be performed using a standard single mode fiber or a known reflector as the device under test. The reference measurement yields a reference scalar transfer function, $H_r(\nu)$. The insertion loss of the DUT is then given by

$$\mathrm{IL}(\nu) = \frac{|H(\nu)|^2}{|H_r(\nu)|^2}. \tag{2.44}$$

Polarization information is not available from the scalar transfer function, because the scalar transfer function contains information about the device response to only a single input polarization state. To measure the polarization response of a device using SWI, it is necessary to perform a measurement of the complete vector transfer function of the device under test. The next section demonstrates this capability of SWI.

2.7 Vector device characterization

In the preceding section I described how SWI can be used for scalar device characterization, resulting in a measure of a device response to a single input polarization state. For devices that respond similarly to all input polarization states, a scalar measurement may be sufficient. Oftentimes, however, devices respond very differently to different input polarization states. Both the amplitude and phase response of a device can vary with polarization. Changes in the amplitude

response are commonly referred to as polarization dependent loss (PDL), while changes in the phase response are characterized as birefringence, differential group delay (DGD), or polarization mode dispersion (PMD) depending on context. In the context of discrete optical devices, PMD is generally defined as the difference in propagation delay between the two principal polarization states. It is therefore equivalent to the DGD, and the two terms are often used interchangeably. This is in contrast to PMD in the context of fiber transmission lines, in which case there is not a single set of well-defined principal polarization states. Rather, the principal states change in a random manner along the length of the fiber. Therefore the DGD becomes a statistical quantity, and PMD is defined as the average DGD [118]. Because of the finite length limitation for SWI measurements, the technique is better suited for device characterization than for fiber measurements, which often involve fiber length of many kilometers. Therefore, in this thesis I use the terms PMD and DGD interchangeably.

There are multiple possible approaches to polarization measurements using SWI. One method would be to perform multiple measurements of the device scalar transfer function, as described in the previous section, for multiple input polarization states. While a brute force scan over a multitude of input states to identify the maximum and minimum group delays, for example, could work given enough measurements, it is possible to acquire all necessary information using just two measurements if polarization diverse detection is used. The requirement here is that the two measurements must use input polarization states that are orthogonal to one another.

An alternative method trades a small amount of added complexity to both the system hardware and the data processing algorithm for the ability to measure the polarization response of a device using a single measurement scan [49, 51]. For reasons of ease, speed, and stability, this is the preferred method for polar-

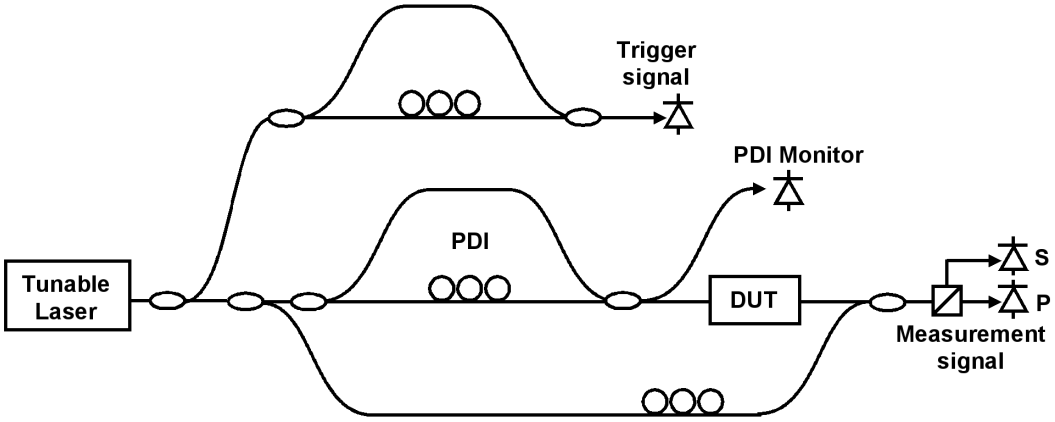

Figure 2.10: An optical network for performing vector device characterization using SWI. Additional features beyond those present for the scalar system include the polarization delay interferometer (PDI) located within the measurement interferometer just prior to the DUT, as well as a photodetector to monitor the PDI fringe amplitude.

ization measurements using SWI. A schematic diagram of the optical system for single-scan vector device characterization appears in Fig. 2.10. In this system an additional interferometer, called the polarization delay interferometer (PDI), has been included within the measurement interferometer, just prior to the device under test. An additional photodetector has also been added at the output of the PDI. The effect of the PDI is to produce two orthogonal polarization states that are separated in time by the relative delay of the PDI, τ_p. These are the two orthogonal input states necessary for a measurement of the vector transfer function, but instead of using two measurement scans, differential delay in the time domain is used to separate out the different matrix elements of $\mathbf{H}(\nu)$. To produce orthogonal states, the polarization controller in the PDI is aligned such that the amplitude of the fringe pattern observed on the PDI monitor detector is minimized.

To fully analyze the optical system for vector device characterization, I will

start by defining the Jones vectors

$$\hat{\boldsymbol{\varrho}}_{p1} = \begin{bmatrix} 1 \\ 0 \end{bmatrix}, \qquad \hat{\boldsymbol{\varrho}}_{p2} = \begin{bmatrix} 0 \\ 1 \end{bmatrix} \tag{2.45}$$

to describe the orthogonal states in the two arms of the PDI. If the field entering the PDI is given by Eq. (2.4), then the field at the output of the PDI is

$$\mathbf{E}_{\text{PDI}} = \frac{E_0}{\sqrt{2}} \begin{bmatrix} e^{j\phi(t)} \\ e^{j\phi(t-\tau_p)} \end{bmatrix} \tag{2.46}$$

to within a constant phase factor. This field then encounters the device under test, which has the effect of multiplication by the vector transfer function of the device:

$$\mathbf{H}(\nu)\frac{E_0}{\sqrt{2}} \begin{bmatrix} e^{j\phi(t)} \\ e^{j\phi(t-\tau_p)} \end{bmatrix}. \tag{2.47}$$

Prior to encountering the beam splitter, the field through the device is combined with the field from the reference arm of the measurement interferometer. The polarization of the reference arm signal should be adjusted using the polarization controller to be split evenly by the polarization beam splitter, as described in the Sec 2.4. At this point, a problem with the representation of fields arises because the polarization basis states of the polarization beam splitter do not match the basis states of the PDI. Therefore, we introduce a polarization rotation matrix, $\mathbf{R}$, that has the effect of transforming the PDI basis states into the beam splitter basis states:

$$\hat{\boldsymbol{s}} = \mathbf{R}\hat{\boldsymbol{\varrho}}_{p1}; \qquad \hat{\boldsymbol{p}} = \mathbf{R}\hat{\boldsymbol{\varrho}}_{p2}. \tag{2.48}$$

The functional form of $\mathbf{R}$ is identical to a matrix that describes lossless propagation in an optical fiber. To this point I have neglected the polarization rotations that result from transmission through fiber, though each section of fiber, including the fiber leads of the device under test, produce such rotations. These rotations

can be ignored because they do not affect the amplitude or phase response of the device. Stated another way, the device properties (e.g., loss, group delay, chromatic dispersion, PDL, PMD) calculated using the matrix product $\mathbf{RH}(\nu)$ are identical to the device properties calculated from $\mathbf{H}(\nu)$. Therefore I can define a new vector transfer function $\mathbf{H}_R(\nu) = \mathbf{RH}(\nu)$ that contains the necessary basis transformation within it. I will subsequently drop the R subscript since this new vector transfer function is functionally identical to the original vector transfer function for the purposes of the measurement. The effect of this transformation is equivalent to the inclusion of a specific fiber pigtail leading to the device under test. Since the polarization rotation associated with a specific physical pigtail is arbitrary and changes each time the pigtail is moved, I am free to choose the value of the polarization rotation matrix $\mathbf{R}$ that simplifies the data analysis. The end result of this discussion of polarization rotation and basis states is that the field incident on the beam splitter may be expressed as

$$\mathbf{E}_{\mathrm{PBS}} = \frac{E_0}{\sqrt{2}} \left\{ \mathbf{H}(\nu) \begin{bmatrix} e^{j\phi(t)} \\ e^{j\phi(t-\tau_p)} \end{bmatrix} + \begin{bmatrix} 1 \\ 1 \end{bmatrix} e^{j\phi(t-\tau_r)} \right\}, \tag{2.49}$$

where all polarization vectors are written in terms of the beam splitter basis states. Note that the second term, corresponding to light traversing the reference path, contains a linear phase factor with a slope equal to τ_r, the relative delay between the reference path and a path through one arm of the PDI and the device under test. Again, a constant phase factor has been dropped.

The function of the beam splitter is to separate its polarization basis states by directing them in two different directions. To express this mathematically, we must first write $\mathbf{H}(\nu)$ explicitly in terms of its complex matrix elements,

$$\mathbf{H}(\nu) = \begin{bmatrix} a & b \\ c & d \end{bmatrix}, \tag{2.50}$$

and multiply this matrix by the polarization vector in the first term of Eq. (2.49). This yields

$$\mathbf{E}_{\mathrm{PBS}} = \frac{E_0}{\sqrt{2}} e^{2\pi j\nu t} \begin{bmatrix} ae^{j\phi(t)} + be^{j\phi(t-\tau_p)} + e^{j\phi(t-\tau_r)} \\ ce^{j\phi(t)} + de^{j\phi(t-\tau_p)} + e^{j\phi(t-\tau_r)} \end{bmatrix}. \tag{2.51}$$

The measured voltage signals at the S and P detectors are then proportional to the square-modulus of the two polarization vector components:

$$U_s(t) = U_0 \left[1 + |a|^2 + |b|^2 + 2\Re\left\{ a^* b e^{j[\phi(t)-\phi(t-\tau_p)]} + a e^{j[\phi(t)-\phi(t-\tau_r)]} + b e^{j[\phi(t-\tau_r)-\phi(t-\tau_p)])} \right\}\right],$$

$$U_p(t) = U_0 \left[1 + |c|^2 + |d|^2 + 2\Re\left\{ c^* d e^{j[\phi(t)-\phi(t-\tau_p)]} + c e^{j[\phi(t)-\phi(t-\tau_r)]} + d e^{j[\phi(t-\tau_r)-\phi(t-\tau_p)])} \right\}\right].$$

Finally, we use three distinct implementations of the slow tuning approximation to convert from function of time to functions of instantaneous optical frequency. The implication of this step is that τ_p, τ_r, and $\tau_r - \tau_p$ must all satisfy inequality (2.9). The result is

$$U_s(\nu) = U_0 \left[1 + |a|^2 + |b|^2 + 2\Re\left\{ a^* b e^{2\pi j\nu\tau_p} + a e^{2\pi j\nu\tau_r} + b e^{2\pi j\nu(\tau_r-\tau_p)} \right\}\right], \tag{2.52}$$

$$U_p(\nu) = U_0 \left[1 + |c|^2 + |d|^2 + 2\Re\left\{ c^* d e^{2\pi j\nu\tau_p} + c e^{2\pi j\nu\tau_r} + d e^{2\pi j\nu(\tau_r-\tau_p)} \right\}\right]. \tag{2.53}$$

Equations (2.52) and (2.53) represent the primary theoretical result that allows for vector device characterization via SWI using a single laser sweep. The salient feature of this result is that the four matrix elements of the vector transfer function appear in independent terms, with two per detector channel. Within the signal on a single channel, two matrix elements appear in terms that oscillate at different frequencies. Therefore, using a digital filtering process similar to that described in Section 2.6 for scalar device characterization, the four matrix elements can be

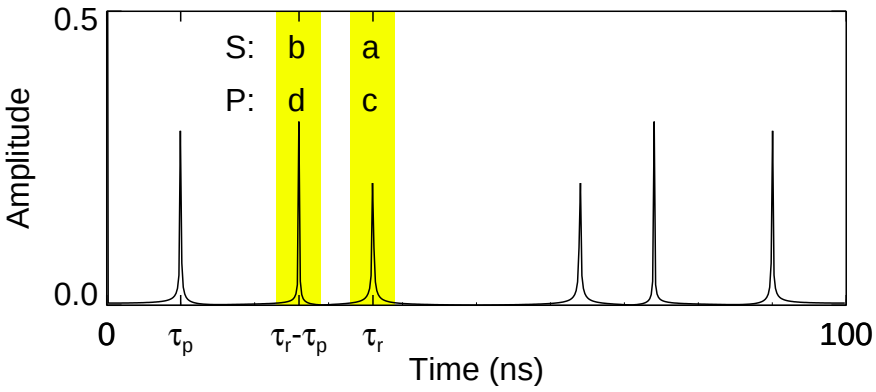

Figure 2.11: Time domain data for a single data channel of a vector SWI system. The peaks at τ_r and $\tau_r - \tau_p$ on the S channel represent the a and b elements of the vector transfer function of the device under test. The peaks at the same locations on the P channel represent c and d. On both channels, the peaks corresponding to transfer function matrix elements are selected using a digital filter, shown here as the shaded yellow regions.

separated in the time domain. This filtering process is illustrated in Fig. 2.11, which shows the Fourier transform of a simulated data set from either the S or P detector. The shaded yellow regions represent the two filter windows required for each data set to select the peaks that occur at the delays τ_r and $\tau_r - \tau_p$. The third peak, which appears at the delay τ_p, contains a combination of two matrix elements and is not used in the measurement. The DC component is also not used.

After digital filtering and an inverse Fourier transform, the four resulting data sets constitute a measurement of the four elements of the vector transfer function, $\mathbf{H}(\nu)$. In principle, this information allows the calculation of any linear parameter of the device under test. It also allows for direct calculation of the device output given an arbitrary input field. In order to realize the full utility of a vector transfer function measurement, however, additional effort must be directed towards calibration of the system in order to remove the effects of imperfect net-

work components, such as the couplers, polarization controllers, etc. In the present analysis, we have assumed all components to be lossless and dispersionless. For a system designed for phase measurements this is a reasonable approximation, because the amount of dispersion and PMD present in the network components are generally below the noise floor of the instrument. The network components can, however, exhibit appreciable loss, so the use of a transfer function measurement for loss measurements requires additional calibration.

With vector transfer function data in hand, the group delay of the device under test may be calculated in a manner analogous to Eq. (2.42). Because the group delay can change with polarization, a useful definition for the group delay is to define it as an average group delay over all input polarization states weighted by the amplitude response of the device [51]:

$$\mathrm{GD}(\nu) = \frac{\arg\left\{\sum_{ij} \mathbf{H}(\nu)\mathbf{H}^*(\nu+\delta\nu)\right\}}{2\pi\delta\nu}. \tag{2.54}$$

This definition provides intuitively correct results for the group delay, even for devices like arbitrary polarizers, where the group delay for the device would generally be understood as the group delay for the transmitted principal polarization state. Polarization-averaged chromatic dispersion then follows from Eq. (2.54) according to Eq. (2.43).

PMD is calculated from the vector transfer function using [119]

$$\mathrm{PMD}(\nu) = \left|\frac{\arg\left(\beta_1/\beta_2\right)}{2\pi\delta\nu}\right|, \tag{2.55}$$

where β_1 and β_2 are the eigenvalues of $\mathbf{H}(\nu)$.

2.8 Functional design considerations

When designing an SWI system for a particular application, various design choices involve tradeoffs between such factors as cost, performance, and ease of

use. In this section tradeoffs involving the laser tuning rate and measurable device length, polarization control, and transmission and reflection measurement capability are presented.

2.8.1 Laser sweep rate and measurable device length

As discussed in Sec. 2.5.1, the maximum range that can be measured using an SWI system with an interferometric trigger is limited to half of the trigger interferometer delay, τ_t. For device characterization applications, the maximum device length including leads is subject to the same limitation. For SWI systems utilizing modern commercial ECDLs developed for telecom applications, the coherence length is rarely the limiting factor in choosing the trigger delay, with the sampling speed of the data acquisition system typically imposing the upper length limit.

The required sampling speed is determined not only by the trigger delay, but also by the maximum laser sweep rate according to Eq. (2.30). Therefore a longer trigger delay may be used if the laser sweep rate is reduced. Generally speaking, however, reducing the laser sweep rate will also increase the measurement noise due to environmental coupling. In fiber systems, vibrations, temperature fluctuations, and air currents can all cause small changes to the phase and polarization of light in the fiber. These noise sources lead to phase and amplitude noise in the sampled interferogram. A fast laser sweep excludes noise sources that occur on timescales longer than the laser sweep. By slowing the laser sweep, lower frequency environmental noise sources can couple into the measurement. Therefore, because of environmental noise factors, high wavelength sweep rates will generally provide better system performance than lower sweep rates. This potential performance degradation must be considered when evaluating a choice to reduce the laser sweep rate in order to achieve larger range and device length capabili-

ties. For ECDLs, tuning rates are typically limited to a few tens up to 100 nm/s. With these sources, the maximum tuning rate should generally be used for SWI measurements.

The alternative method for increasing the range capabilities of an SWI system is to increase the speed of the data acquisition system. This route is primarily a tradeoff between performance and cost. The capability to measure longer devices requires faster, more expensive data acquisition systems. Also, increasing the measurable device length through the use of a longer trigger interferometer results in a smaller frequency spacing between data points, and therefore yields larger data set sizes for a given wavelength range. As an example, a 1 μs trigger delay, which allows for a 100 m measurement range in fiber, results in a 1 MHz sampling interval. For a 100 nm sweep about a center wavelength of 1550 nm, this results in approximately 12.5 million data points per channel. Therefore maintaining a desired total measurement time may also require higher cost computational resources to manage the large data set sizes and the associated processing.

2.8.2 Polarization control

Polarization control is a necessary component in any SWI system to ensure adequate fringe contrast. A variety of means to accomplish polarization control exist, and the decision of which to use must balance the concerns of cost, ease of use, and ease of construction. Performance should be consistent among suitable means of polarization control, provided they are implemented in an appropriate manner.

The primary issue with regard to ease of use is whether polarization control is accomplished automatically, or if it requires user interaction. Paying the cost of user interaction simplifies both hardware and software designs and requires less expensive components. A straightforward means for manual polarization control

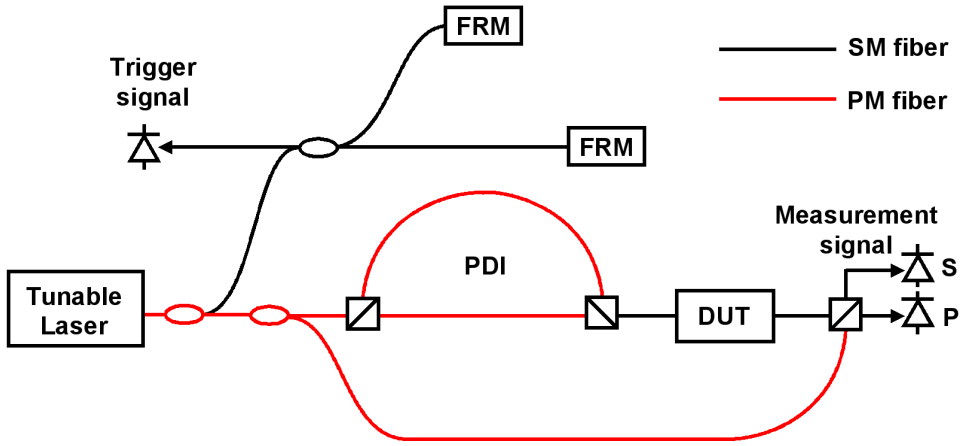

Figure 2.12: An optical network for performing vector device characterization in which polarization controllers have been eliminated. The trigger interferometer uses a Michelson geometry with singe mode (SM) fiber and Faraday rotator mirrors (FRMs). The measurement network is built primarily from polarization maintaining (PM) fiber and utilizes three polarization beam splitter/combiners.

is to use inexpensive LeFevre loop polarization controllers. Automatic polarization control can be accomplished either actively or passively. Active polarization control requires programmable polarization controllers, such as motorized LeFevre loops or waveplates in motorized rotation mounts. One type of polarization controller to avoid is the type that uses mechanical fiber stress to control the polarization, usually by means of a piezoelectric transducer that squeezes an optical fiber. This process generally induces unacceptable levels of polarization dependent loss for accurate vector device characterization using SWI.

Passive polarization control can be accomplished using polarization maintaining (PM) fiber and components. An example of an SWI network for vector device characterization using all passive polarization control is shown in Fig. 2.12. Good fringe visibility in a simple interferometer, such as one used for triggering, can be achieved without PM fiber or a polarization controller if a Michelson geometry is used with a Faraday rotator mirror (FRM) terminating each arm. In

the measurement network, PM fiber in conjunction with polarization beam splitter/combiners is required if the necessary PDI output is to be produced without a polarization controller. An added benefit of this design is that a photodetector to monitor the PDI fringe amplitude is no longer necessary. PM fiber can also be used to ensure the reference arm light is split evenly at the polarization beam splitter just prior to the detectors. In this network all PM inputs to polarization beam splitters must be oriented such that the input is split evenly between the two outputs.

While passive polarization control eliminates both the need for user interaction and software control of active polarization controllers, it requires more costly components to implement, and construction of the PM network is significantly more difficult than construction of an SM network because of the need for precise alignment and orientation of PM fiber and components.

2.8.3 Transmission and Reflection measurements

As mentioned in Section 2.2.1, an SWI system can be based on a variety of different interferometer geometries. A Mach-Zehnder geometry is suitable for performing transmission measurements, whereas Michelson and Fabry-Perot configurations are suited for reflection measurements. Depending on the specific device under test, the desired measurement may be a transmission measurement, reflection measurement, or both. The most versatile measurement system is one that is capable of performing both reflection and transmission measurements simultaneously. Such a system is also more complex and requires more resources than a system that can only perform one type of measurement, or one that is capable of both types of measurements, but not simultaneously.

The system presented in Fig. 2.10 is capable of transmission measurements only. Reflection measurement capability can be added using one additional 3 dB

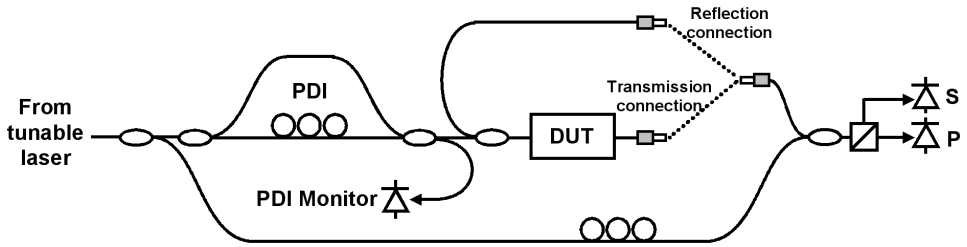

Figure 2.13: An SWI system capable of sequential transmission and reflection measurements. The user must reconfigure one fiber optic connection to change between transmission and reflection modes. Alternatively, the mode transition process could be automated using a fiber optic switch.

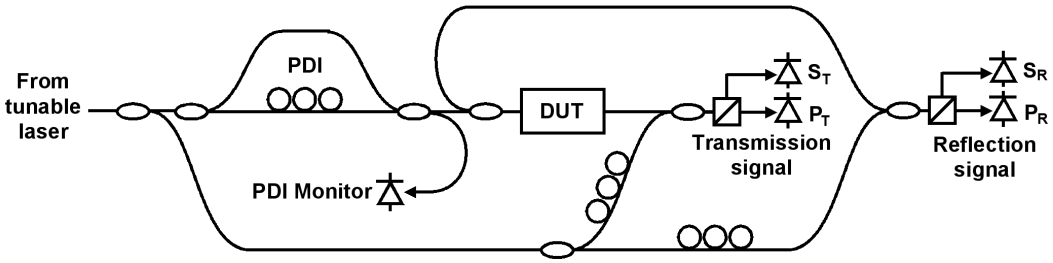

Figure 2.14: An SWI system capable of simultaneous transmission and reflection measurements. This system requires additional components, including two photodetectors and two data acquisition channels beyond what is necessary for the sequential system.

coupler as shown in Fig. 2.13. This system requires the user to change one fiber connection to switch back and forth between transmission and reflection mode. This process could also be automated using a fiber optic switch. To perform reflection and transmission measurements simultaneously, a system such as that shown in Fig. 2.14 is necessary. The drawback to simultaneous measurements is the need for an additional polarization beam splitter, polarization controller, and two additional photodetectors. This system also requires a data acquisition system with two extra input channels compared to the previously described systems.

2.9 Noise in swept-wavelength interferometers

The signal to noise ratio that can be achieved in swept-wavelength interferometers will be degraded by a variety of noise sources. In this section I will analyze the noise floor of SWI systems by considering the signal level to be the peak amplitude of the time domain response corresponding to a specific test path. The noise floor is the ambient time domain signal level for delays where no test path exists. In the following analysis I derive the noise contributions from four sources: shot noise in the detected photocurrent, and relative intensity noise (RIN) and phase noise of the laser source, and quantization noise due to digitization of the analog interference signal.

2.9.1 Shot noise

Shot noise, also known as quantum noise, is present in both optical and electronic signals due to the fact that both the optical electromagnetic field and electrical current are not continuously divisible, but rather quantized with minimum quanta known as photons and electrons, respectively.

To analyze the shot noise contribution to the signal to noise ratio in SWI measurements, we will consider the simplified optical network shown in Fig. 2.1(A), consisting of a wavelength tunable optical source that is split between a reference or local oscillator path and a test path. After traversing these two paths, the light is recombined and interferes at a single photodetector.

For high sensitivity measurements performed using SWI, it is typically the case that the local oscillator power, P_{lo}, is much greater than the power reflected or transmitted by the test path, P_d. In this case, the mean number of photons $\bar{n}$ incident on the photodetector during a measurement time T can be written in

terms of the local oscillator power only:

$$\bar{n} = \frac{P_{lo}T}{h\bar{\nu}}, \tag{2.56}$$

where h is Planck's constant and $\bar{\nu}$ is the average optical frequency. For a photodetector with a quantum efficiency η, the resulting mean photocurrent $\bar{i}$ will be

$$\bar{i} = \frac{e}{T}\eta\bar{n} = \frac{e\eta}{h\bar{\nu}}P_{lo}, \tag{2.57}$$

where e is the fundamental electron charge. Because the arrival of photons at the photodetector obeys Poissonian statistics, the variance of the photon number, σ_n^2, is equal to the mean number of photons, $\bar{n}$. This leads to a variance σ_{iq}^2 of the detected photocurrent due to shot noise given by

$$\sigma_{iq}^2 = \left(\frac{e}{T}\right)^2 \eta\bar{n} = \frac{2e^2\eta P_{lo}B}{h\bar{\nu}}, \tag{2.58}$$

where $B = 1/(2T)$ is the power equivalent bandwidth of the measurement [120].

In SWI systems, the optical source is a frequency tunable laser with a an output electric field $E(t) = E_0 \exp\phi(t)$. The instantaneous laser frequency is

$$\omega(t) = \frac{d\phi}{dt} \tag{2.59}$$

and the frequency tuning rate, which in general will vary during a measurement, is

$$\gamma(t) = \frac{d\omega}{dt} = \frac{d^2\phi}{dt^2}. \tag{2.60}$$

The measurement takes place over a frequency range $\Delta\omega = \omega_2 - \omega_1$. Over this range, the tuning rate has a mean value

$$\bar{\gamma} = \frac{1}{\Delta\omega}\int_{\omega_1}^{\omega_2} \gamma(\omega)\, d\omega \tag{2.61}$$

which can be used to define the total measurement time T as

$$T = \frac{\Delta\omega}{\bar{\gamma}}. \tag{2.62}$$

For the present analysis, I will assume that the swept-wavelength interferogram is sampled over the measurement time T at equal increments of optical frequency using, for example, an interferometric trigger under the slow tuning approximation. In other words, the frequency interval for the m^{th} sample $\delta\omega_m = \delta\omega$ for all m. If the laser tuning rate is not constant, the measurement time δt_m for the m^{th} sample will differ for each sample. The corresponding effective bandwidth B_m for each sampled point will also differ, given by

$$B_m = \frac{1}{2\delta t_m}. \tag{2.63}$$

For such single-point measurements, the variance of the detected photocurrent due to shot noise is given by Eq. 2.58 using the single-point bandwidth B_m. SWI measurements are rarely concerned only with the sampled frequency domain interferogram, however, and generally include post-acquisition data processing beginning with a discrete Fourier transform of the acquired data set. For many SWI measurements, such as optical frequency domain reflectometry (OFDR), the transformed timed-domain data set is the goal. For these measurements, the single-point variance of the detected photocurrent in the frequency domain is not of interest so much as the contribution of the shot noise to the noise floor of the time-domain reflectogram. The time domain variance σ_{Iq} due to shot noise can be determined using Parseval's theorem for discrete Fourier transforms:

$$\frac{1}{N}\sum_{m=0}^{N}\left|\sigma_{iq,m}\right|^2 = \sum_{k=0}^{N}\left|\sigma_{Iq}\right|^2. \tag{2.64}$$

Because many samples are taken over the course of a measurement, we can replace $\sigma_{iq,m}$ with its mean value $\bar{\sigma}_{iq}$ and take it outside of the sum. This yields

$$\sigma_{Iq}^2 = \frac{\bar{\sigma}_{iq}^2}{N}, \tag{2.65}$$

or

$$\sigma_{Iq}^2 = \frac{2e^2\eta P_{lo}\bar{B}}{Nh\bar{\nu}}, \tag{2.66}$$

where $\bar{B}$ is the mean value of B_m. Thus the shot noise floor for time domain measurements is reduced by a factor of the number of sampled points, N, compared to single-point frequency domain measurements. One can also arrive at this result by observing that each point in the time domain data set is acquired over the full frequency scan range $\Delta\omega$, or equivalently over the entire measurement time T. Therefore the effective bandwidth for time domain data points is $1/2T = 1/2N\bar{\delta}t$ instead of $1/2\delta t_m$ for frequency domain data points.

While the shot noise is determined by the average power at the photodetector and is dominated by the local oscillator power, the measured signal is the AC portion of the total optical power at the photodetector. The amplitude of the signal photocurrent i_s is therefore given by

$$\begin{aligned} i_s &= 2\frac{e\eta}{h\bar{\nu}}\sqrt{P_{lo}P_d} \\ &= 2\frac{e\eta}{h\bar{\nu}}\sqrt{R_{lo}R_d}P_{in} \end{aligned} \tag{2.67}$$

where the R_{lo} and R_d represent the reflectivity or transmissivity of the local oscillator and test paths, respectively, depending on the physical implementation of the network, and P_{in} is the laser power at the input to the SWI system. To determine the shot-noise-limited measurable reflectivity $R_d = R_{min,q}$ we set the signal amplitude equal to the time domain standard deviation of the photocurrent due to shot noise [104]:

$$2\frac{e\eta}{h\bar{\nu}}\sqrt{R_{lo}R_{min,q}} = \sqrt{\frac{2e^2\eta P_{lo}B}{Nh\bar{\nu}}}. \tag{2.68}$$

Simplification yields

$$R_{min,q} = \frac{h\bar{\nu}\bar{B}}{2\eta N P_{in}}. \tag{2.69}$$

Interestingly, the reflectivity (or transmissivity) of the local oscillator cancels out and does not affect the shot noise floor of the measurement. This is because both the signal interference term and the shot noise level scale as the square root of the

local oscillator power. As shown in the next section, however, the local oscillator power level does play a role in determining the contribution of classical intensity noise to the noise floor of the measurement.

To put the result in Eq. 2.69 in the context of a real system, we will calculate the shot noise limit for typical parameters for the experimental SWI systems described in the following chapters. Representative values are:

$$\begin{aligned} P_{in} &= 1 \text{ mW} \\ \eta &= 0.9 \\ N &= 2^{16} \\ \bar{\nu} &= c/(1550\,\text{nm}) = 1.935 \times 10^{14} \text{ Hz} \\ h &= 6.626 \times 10^{-34} \text{ J} \cdot \text{s} \\ \bar{B} &= 320\,\text{kHz} \end{aligned}$$

which yield a shot-noise limited reflectivity floor of

$$R_{min,q} = -155\,\text{dB}. \tag{2.70}$$

2.9.2 Relative intensity noise

In addition to intrinsic quantum fluctuations in the output power due to shot noise, lasers in general exhibit classical intensity noise due to a variety of sources, such as cavity vibration and pump noise. The noise power is generally proportional to the laser output power, so relative intensity noise (RIN) is defined as the noise power over the laser output power, and as such remains constant with changes in laser power. RIN typically exhibits $1/f$ character at low frequencies, and levels off to a constant value for high frequencies.

The noise floor due to RIN for time domain SWI measurements will occur for a test path reflectivity (or transmissivity) $R_{min,R}$ where the amplitude of the

signal photocurrent in Eq. 2.67 is equal to the time domain standard deviation of the photocurrent σ_{RIN}:

$$2\frac{e\eta}{h\bar{\nu}}\sqrt{R_{lo}R_{min,R}}P_{in} = \sigma_{RIN}. \tag{2.71}$$

For the experimental SWI systems described in later chapters, the laser source is an Agilent 81680A tunable laser with a specified RIN power spectral density of $\mathcal{S}_{RIN} = -145$ dB/Hz. Determination of the standard deviation of the detected photocurrent due to RIN from this value depends on the laser power and the measurement bandwidth. As for shot noise, the effective bandwidth for time domain measurements is $\bar{B}/N$, and the total optical power is well approximated by the local oscillator power, $P_{lo} = R_{lo}P_{in}$. Thus,

$$\sigma_{RIN} = \sqrt{\frac{\mathcal{S}_{RIN}\bar{B}}{N}}R_{lo}P_{in}. \tag{2.72}$$

Substituting Eq. 2.72 into Eq. 2.71 yields

$$R_{min,R} = \frac{\mathcal{S}_{RIN}\bar{B}R_{lo}}{4N}. \tag{2.73}$$

For a representative transmission local oscillator path that includes three 3 dB couplers, $R_{lo} = (0.5)^3 = 0.125$, and

$$R_{min,R} = -153\,\text{dB} \tag{2.74}$$

is the noise floor due to classical laser intensity noise.

2.9.3 Coherence and phase noise

The effect of laser phase noise in interferometric systems has been presented in the literature for both general interferometric systems [121, 122], as well as for the specific cases of FMCW lidar [123] and frequency domain reflectometers [7, 23, 104, 124]. The theoretical analyses of laser phase noise in swept-wavelength interferometers presented in the literature all incorporate the assumption of linear optical frequency tuning. A rigorous analysis accounting for tuning

rate variations requires knowledge of the specific laser tuning characteristics. As shown below, however, the result of laser phase noise in coherent swept-wavelength interferometers is a broad, flat, amplitude noise spectrum in the time domain that depends on the strength and location of reflections (or transmission paths) in the test path. Since the effect of laser tuning rate variations is generally to broaden time domain features (as shown in Fig. 2.6), the effect on the phase noise spectrum will be minimal and the analysis for linear tuning provides an adequate model for determining the noise floor due to laser phase noise. The analysis presented here is modeled after that of Venkatesh and Sorin [124].

For this analysis, begin with a generalized expression for the input electric field:

$$E(t) = E_0 e^{j\phi(t)}. \tag{2.75}$$

Here I will assume copolarized fields and neglect polarization unit vectors. To account for a finite laser linewidth, recast the optical phase $\phi(t)$ as

$$\phi(t) = \phi_d(t) + \phi_r(t), \tag{2.76}$$

where $\phi_d(t)$ is the deterministic portion of the phase and $\phi_r(t)$ is the stochastic variation in the optical phase that leads to broadening of the quasimonochromatic line width. The input electric field is launched into a single-mode interferometer with a reference path and a test path. For convenience, I will take the reference path to be lossless, and the fractional power loss through the test path is R. The detected signal at the interferometer output is then

$$\begin{aligned} U(t) &= U_0 \left| E(t) + \sqrt{R} E(t - \tau_0) \right|^2 \\ &= U_0 \left\{ 1 + R + 2\sqrt{R} \cos\left[\phi_d(t) - \phi_d(t - \tau_0) + \phi_r(t) - \phi_r(t - \tau_0) \right] \right\} \end{aligned} \tag{2.77}$$

where τ_0 is the relative group delay difference between the measurement path and the reference path. As before, the constant σ depends on the detector sensitivity,

and $U_0 = \sigma|E_0|^2$. Invoking the slow tuning approximation for the deterministic part of the output signal phase allows us to write

$$U(t) = U_0 \left\{ 1 + R + 2\sqrt{R} \cos\left[\omega(t)\tau_0 + \phi_r(t) - \phi_r(t - \tau_0)\right] \right\}, \tag{2.78}$$

where $\omega(t) = 2\pi\nu(t)$ is the instantaneous angular frequency of the optical field. Next, assuming that the stochastic phase variation over a time interval τ is stationary with a mean of zero, then the relationships [122]

$$\langle \cos[\Delta\phi_\tau] \rangle = e^{-(1/2)\langle \Delta\phi_\tau \rangle} \tag{2.79}$$

$$\langle \sin[\Delta\phi_\tau] \rangle = 0 \tag{2.80}$$

may be used, where $\Delta\phi_\tau \equiv \phi(t) - \phi(t - \tau)$ and the angled brackets denote a time average. Furthermore, if the source lineshape is a Lorentzian with a full-width-at-half-maximum (FWHM) linewidth of $\Delta\nu_{\mathrm{FWHM}}$, then [124]

$$\Delta\phi_\tau^2 = 2\pi|\tau|\Delta\nu_{\mathrm{FWHM}} = \frac{2\tau}{\tau_c}, \tag{2.81}$$

where $\tau_c = 1/(\pi\Delta\nu_{\mathrm{FWHM}})$ is the source coherence time. Recasting Eq. (2.78) through the use of a trigonometric identity and Eqs. (2.80) and (2.81) yields

$$U(t) = U_0 \left\{ 1 + R + 2\sqrt{R} \cos\left[\omega(t)\tau_0\right] e^{-|\tau_0|/\tau_c}. \right\} \tag{2.82}$$

This equation demonstrates that the effect of finite source linewidth reduces the magnitude of the oscillating interference term by a factor that depends exponentially on the interferometer delay, τ_0. Thus for path imbalances that approach the laser coherence time, the signal level will be significantly reduced. The coherence time of the source therefore represents an upper limit on measurable path length differences using SWI. Equation (2.82) is general and applies for arbitrary frequency tuning.

While Eq. (2.82) is useful for describing the effect of phase noise on the signal level, it is also important to understand how laser phase noise affects the noise

floor of SWI measurements. Since SWI measurements involve a Fourier transform of the sampled interferogram to produce a Fourier domain data set, the effect of laser phase noise on the measurement noise floor will be determined by the power density due to the phase fluctuations in Fourier domain. The Weiner-Khintchin theorem states that the power spectral density of a wide-sense stationary process is given by the Fourier transform of its autocorrelation. Starting from Eq. (2.78), the normalized autocorrelation $R_U(T)$ of the interferometer output signal is given by

$$\begin{aligned} R_U(T) &= \frac{1}{U_0^2}\langle U(t)U(t+T)\rangle \\ &= (1+R)^2 + 2(1+R)\sqrt{R}\langle\cos\left[\omega(t)\tau_0 + \phi_r(t) - \phi_r(t-\tau_0)\right]\rangle \\ &\quad + 2(1+R)\sqrt{R}\langle\cos\left[\omega(t+T)\tau_0 + \phi_r(t+T) - \phi_r(t+T-\tau_0)\right]\rangle \\ &\quad + 4R\langle\cos\left[\omega(t)\tau_0 + \phi_r(t) - \phi_r(t-\tau_0)\right] \\ &\quad \cdot \cos\left[\omega(t+T)\tau_0 + \phi_r(t+T) - \phi_r(t+T-\tau_0)\right]\rangle. \end{aligned} \tag{2.83}$$

The second and third terms in this expression will be driven to zero by the time average. The product of cosines in the fourth term can be rewritten using the identity $\cos u \cos v = (1/2)[\cos(u-v) + \cos(u+v)]$, and the resulting cosine sum term also averages to zero, leading to

$$\begin{aligned} R_U(k) = (1+R)^2 + 2R\langle\cos\left[\omega(t)\tau_0 - \omega(t+T)\tau_0\right. \\ \left. + \phi_r(t) - \phi_r(t-\tau_0) - \phi_r(t+T) + \phi_r(t+T-\tau_0)\right]\rangle. \end{aligned} \tag{2.84}$$

At this point the assumption of linear tuning allows us to use $\omega(t) - \omega(t+T) = \gamma T$,

where $\gamma = d\omega/dt$, in order to rewrite Eq. (2.84) as

$$\begin{aligned} R_U(k) = (1+R)^2 \\ &+ 2R\cos(\gamma\tau_0 T)\left\langle\cos\left[\phi_r(t) - \phi_r(t-\tau_0) - \phi_r(t+T) + \phi_r(t+T-\tau_0)\right]\right\rangle \\ &- 2R\sin(\gamma\tau_0 T)\left\langle\sin\left[\phi_r(t) - \phi_r(t-\tau_0) - \phi_r(t+T) + \phi_r(t+T-\tau_0)\right]\right\rangle. \end{aligned} \tag{2.85}$$

Equation (2.85) can now be solved for to distinct cases:

Case (1) for $|T| \leq \tau_0$:

$$R_U(T) = (1+R)^2 + 2R\cos(\gamma\tau_0 T)\, e^{-2|T|/\tau_c}. \tag{2.86}$$

Case (2) for $|T| \geq \tau_0$:

$$R_U(T) = (1+R)^2 + 2R\cos(\gamma\tau_0 T)\, e^{-2\tau_0/\tau_c}. \tag{2.87}$$

To arrive at these expressions Eqs. (2.79) and (2.81) have been employed. Equations (2.86) and (2.87) represent the desired result for the autocorrelation of the interferometer output signal, and this result is plotted in Fig. 2.15. The plot shows a transition at the interferometer delay τ_0 from an exponentially decaying sinusoid to a sinusoid with constant amplitude. Some intuition into the behavior of the system can be gleaned by considering the limiting cases of complete coherence and complete incoherence. These cases can be understood by taking $\tau_0 = 0$ and $\tau_0 \to \infty$, respectively. For complete coherence, the autocorrelation is a constant sinusoid, which is equivalent to the mathematical development presented earlier in this chapter where the effect of laser phase noise is neglected. In this case the Fourier transform of the autocorrelation function yields delta functions at the positive and negative beat frequency, $\gamma\tau_0$. In the incoherent case, there is no transition point and the autocorrelation is an exponentially decaying sinusoid, with a Lorentzian Fourier transform centered at $\gamma\tau_0$.

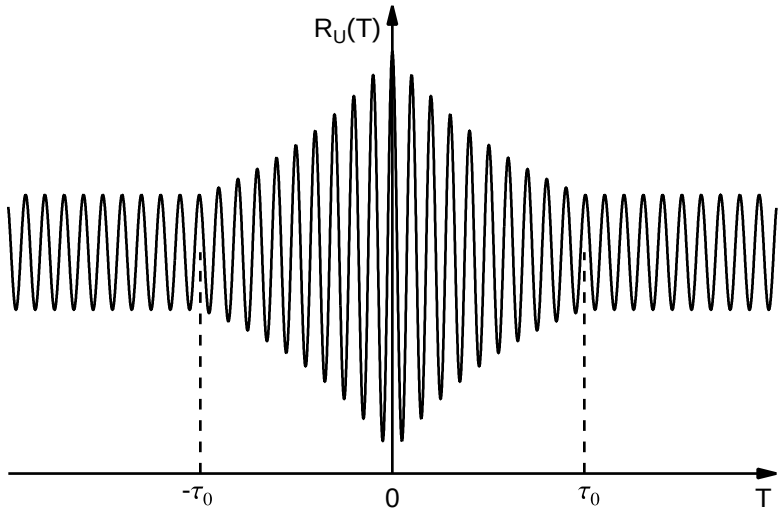

Figure 2.15: The autocorrelation of the swept-wavelength interferometer output signal. Figure adapted from Ref. [124].

A general expression for the spectral density $\mathcal{S}_U(f)$ of the interferometer output signal is given by its Fourier transform:

$$\begin{aligned}\mathcal{S}_U(f) &= \int_{-\infty}^{\infty} R_U(T) e^{-2\pi j f T} dT \\ &= \int_{-\tau_0}^{\tau_0} [(1+R)^2 + 2R\cos(\gamma\tau_0 T) e^{-2|T|/\tau_c}] e^{-2\pi j f T} dT \\ &\quad + \int_{\tau_0}^{\infty} [(1+R)^2 + 2R\cos(\gamma\tau_0 T) e^{-2\tau_0/\tau_c}] e^{-2\pi j f T} dT \\ &\quad + \int_{-\infty}^{-\tau_0} [(1+R)^2 + 2R\cos(\gamma\tau_0 T) e^{-2\tau_0/\tau_c}] e^{-2\pi j f T} dT. \end{aligned} \tag{2.88}$$

Evaluating the integrals yields the final expression for the spectral density [124]:

$$\begin{aligned}\mathcal{S}_U(f) = (1+R)^2\delta(f) + Re^{-2\tau_0/\tau_c}\delta(f \pm f_b) + \frac{T\tau_c}{1+\pi^2\tau_c^2(f \pm f_b)^2} \\ \cdot \left(1 - e^{-2\tau_0/\tau_c}\left\{\cos[2\pi(f \pm f_b)\tau_0] + \frac{\sin[2\pi(f \pm f_b)\tau_0]}{\pi\tau_c(f \pm f_b)}\right\}\right), \end{aligned} \tag{2.89}$$

where $f_b = \gamma\tau_0/2\pi$. The third term in this expression gives the amplitude noise spectrum in the Fourier domain that results from phase noise in the laser source. The first two terms containing delta functions correspond to the DC and oscillating

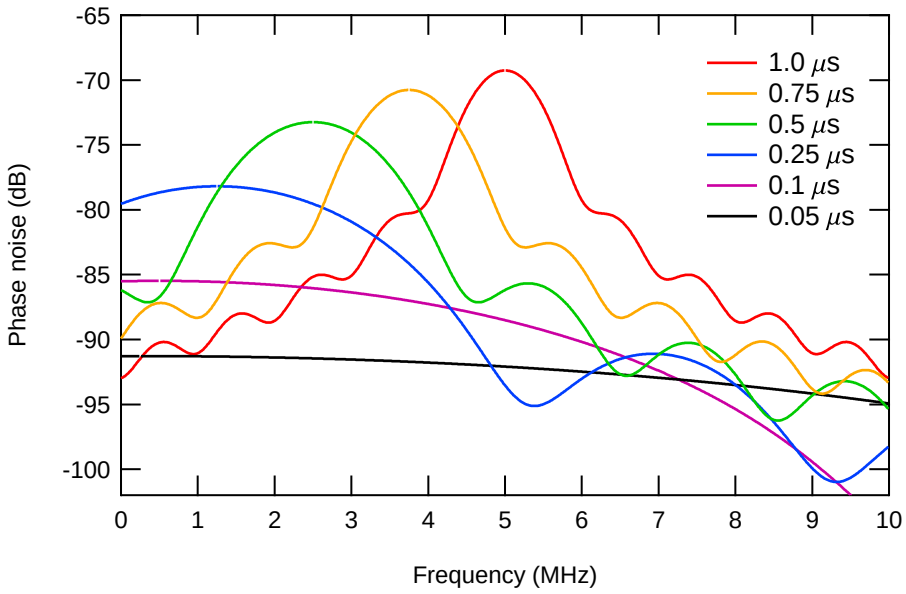

Figure 2.16: Noise power spectral density for swept-wavelength interferometers with various path length differences for an instantaneous source linewidth of 250 kHz assuming a measurement path reflectivity of 4%.

components of the output interferogram. Note that the noise floor due to laser phase noise depends on the strength of the signal (described by R) as well as the length of the test path (described by f_b).

The phase noise spectrum is plotted in Fig. 2.16 for an instantaneous laser linewidth of 250 kHz and a test path reflectivity of 4% for a range of interferometer path length differences. The black curve corresponding to $\tau_0 = 50\,\text{ns}$ is representative of the typical system configuration used for the experimental work presented in the following chapters. This represents the case of a highly coherent system, where the noise spectrum is an extremely broad Lorentzian centered at f_b. As the interferometer path length difference increases, the peak of the phase noise spectrum grows and modulation becomes apparent.

Practically speaking, the noise floor due to laser phase noise for coherent swept-wavelength interferometers is well approximated by the peak value of the phase noise spectrum. This value is plotted in Fig 2.17 for a 4% measurement

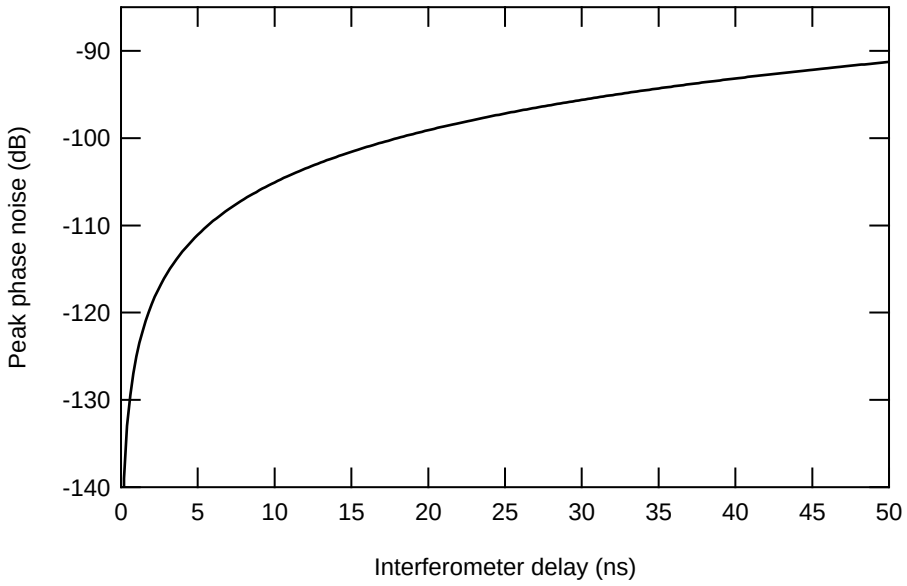

Figure 2.17: The peak value of the Fourier domain noise spectrum due to laser phase noise versus relative interferometer path delay for a 250 kHz instantaneous laser linewidth and a 4% measurement path reflectivity.

path reflection and relative delays up to 50 ns, a range that encompasses the experimental swept-wavelength interferometers presented later in this thesis.

These results for the Fourier domain noise floor imposed by laser phase noise have two practical consequences that must be considered when designing SWI systems. These considerations are generally most important for reflection systems, since they often have multiple simultaneous optical paths. Transmission systems typically have a single path, though it is certainly possible for transmission systems to have multiple paths as well. The first important consideration is that the existence of a single strong reflection, such as a cleaved fiber end facet, will raise the noise floor throughout the time domain reducing the system's ability to detect weak reflections. Therefore, when detection of weak reflections is the goal, strong reflectors must be eliminated, for example through bend-loss fiber termination or by immersion of the fiber end facet in index matching fluid. Second, the contribution of a reflector to the phase noise floor increases for longer path

length mismatches. Therefore, small spurious reflections within an SWI system network may have a strong influence on the noise floor if they result from long path delays, even if they appear to result from short delays due to aliasing.

2.9.4 Quantization noise

In the case of the experimental SWI systems presented later in this thesis, the noise source that limits the sensitivity of the measurement is quantization noise associated with the process of converting the analog interferogram to a set of digital data. Inevitably, this process of analog-to-digital conversion (ADC) introduces error into the sampled data set. In general, two types of error can occur. The first is clipping error, which happens if the detected interference signal $U(\nu)$ lies outside the minimum and maximum input voltage settings for the data acquisition (DAQ) hardware, denoted here as V_{lo} and V_{hi}, respectively. This type of error is generally avoided by adjusting the photodetector amplifier gains and the DAQ hardware settings so that $U(\nu)$ always lies in the range $V_{\mathrm{lo}} \leq U \leq V_{\mathrm{hi}}$. The second type of error is the granular error that results in quantization noise. This error arises because the continuous variable U is converted to one of a finite set of possible values over the input voltage range of the DAQ. The number of possible values, or quantization levels, Q, is given by the number of bits b used in the ADC process according to $Q = 2^b$. The spacing Δ between the levels is then

$$\Delta = \frac{V_{\mathrm{hi}} - V_{\mathrm{lo}}}{Q}. \tag{2.90}$$

When the interference signal $U(\nu)$ is sampled at a given value of ν, the analog value U is converted to a quantized value $\hat{U}_i$, where the index i runs from zero to $Q - 1$ and gives the specific quantization level used. The error ε in this process is

$$\varepsilon(U) = U - \hat{U}_i. \tag{2.91}$$

In general, the distribution of values that $\varepsilon(U)$ can take on is signal-dependent. A common approximation is made by assuming $\varepsilon(U)$ is a uniform random variable over the range $[-\Delta/2, \Delta/2]$. As such, it has a probability density function f_ε given by [125]

$$f_\varepsilon(\varepsilon) = \begin{cases} 1/\Delta, & -\Delta/2 \leq \varepsilon \leq \Delta/2 \\ 0, & \text{otherwise} \end{cases}. \tag{2.92}$$

The variance σ_ε^2 then follows as

$$\begin{aligned} \sigma_\varepsilon^2 &= \int_{-\infty}^{\infty} \varepsilon^2 f_\varepsilon(\varepsilon) d\varepsilon \\ &= \int_{-\Delta/2}^{\Delta/2} \frac{\varepsilon^2}{\Delta} d\varepsilon \\ &= \frac{\Delta^2}{12}. \end{aligned} \tag{2.93}$$

In an SWI system, the signal amplitude is proportional to the electric field amplitude in the measurement arm. Thus, the photodetector amplifiers together with the DAQ hardware settings can be configured such that a desired maximum electric field amplitude corresponds to a signal spanning the full input voltage range of the DAQ. For example, in a reflection system where the hardware is configured for a maximum power reflectivity of R_{max}, the quantization level is effectively $\Delta = \sqrt{R_{max}}/Q$ and standard deviation of the quantization noise is

$$\sigma_\varepsilon = \frac{\sqrt{R_{max}}}{\sqrt{12}Q}. \tag{2.94}$$

The minimum reflectivity $R_{min,Q}$ that can be detected in the presence of quantization noise is then found when the corresponding amplitude reflectivity $(R_{min,Q})^{1/2}$ is equal to the standard deviation of the quantization noise. Thus, the noise floor due to quantization is

$$R_{min,Q} = \frac{R_{max}}{12Q^2}. \tag{2.95}$$

For the experimental SWI systems presented in this thesis, the DAQ hardware employs 12-bit ADC and the maximum reflectivity in the measurement arm

is typically 4%. In order that multiple reflections do not increase the signal level to the point that clipping errors occur, the signal level is adjusted so that a single 4% reflection spans 11 bits. These values result in a system sensitivity of

$$R_{min,Q} = -91\,\mathrm{dB}. \tag{2.96}$$

2.10 Summary and conclusions

This chapter has provided an overview of the fundamentals of SWI, beginning with the basics of swept-wavelength interference and working through the practical aspects of SWI system implementation, including laser tuning nonlinearities, polarization variations, and noise sources. In addition, the theoretical framework for performing measurements of distance as well as scalar and vector device transfer functions has been presented. This chapter is by no means a complete introduction to SWI, but hopefully it provides a sufficient foundation for understanding the SWI systems described in the following chapters.

Chapter 3

Sampling Error Correction

3.1 Introduction

The preceding chapter presented the fundamentals of SWI, beginning with the case of linear frequency tuning of the laser source, and quickly introducing the concept of frequency sampling to deal with variations in the laser tuning rate during a wavelength sweep. Provided the average laser tuning rate is slow enough and the interferometer path length difference is small enough that inequality (2.9) (the slow tuning approximation) is satisfied, then a trigger interferometer may be used to provide a clock signal for sampling data at equal increments of optical frequency. Alternatively, such an interferometer output can be used to resample data acquired at equal time increments onto a grid of equal frequency increments. Both of these approaches rely on the interferometer output signal to be periodic in optical frequency, which is true to first order. When Brinkmeyer and Glombitza first described OFDR using an interferometric trigger in 1991 [103], they were concerned with characterizing small integrated optic devices ($\tau_0 < 1\,\text{ns}$) using temperature-tuned laser diodes with sweep rates on the order of 100 GHz/s. In this case, $\tau_0^2(d\nu/dt) \sim 10^{-7}$. As highly coherent tunable lasers with rapid tuning capabilities have become available, however, it is increasingly easy to construct an SWI system for which the slow tuning approximation is not valid. For exam-

ple, commercially available tunable lasers from several manufacturers now offer tuning rates on the order of 100 nm/s with instantaneous linewidths of around 100 kHz. Tuning at 100 nm/s in the C telecommunication band corresponds to a $d\nu/dt$ of 1.25×10^{13} Hz/s, which violates the slow tuning approximation for only a few tens of meters of fiber. The coherence length, however, permits high visibility interference fringes over path mismatches an order of magnitude larger, and there is interest in telecom and sensing applications for SWI measurements performed over multiple km [126,127]. Another class of swept-wavelength sources that are pushing the limits of the slow tuning approximation are the extremely high speed swept sources now being developed for SS-OCT applications, particularly FDML lasers, which have been demonstrated with frequency sweep rates up 7.4×10^{18} Hz/s [109]. While the coherence length of these high-speed swept sources is typically on the order of a centimeter, an interferometer with a centimeter path length difference would yield $\tau_0^2(d\nu/dt) \sim 1$ at these high sweep rates. These and other developments in the area of high speed, high coherence swept wavelength sources will drive demand for SWI measurement capabilities in regimes where the slow tuning approximation does not apply.

In this chapter I explore the potential capability of performing SWI measurements using the frequency sampling method outside of the limitations of the slow tuning approximation. I approach this problem in the framework of SWI systems using commercially available tunable lasers designed for telecommunications testing applications. In general these lasers exhibit significantly nonlinear tuning that can lead to sampling errors when using an interferometric clock. In this context, the term *sampling errors* refers to undesired variations in the sampling interval that arise when using a particular clock to trigger the sampling of an experimental data set. The motivation for the frequency sampling method is that the interference fringes at the output of the trigger interferometer provide a

clock signal that is periodic in optical frequency. Sampling errors occur when the frequency intervals between data points in the acquired data set are not in fact equal. I will use the term *fringe periodicity errors* to refer to the more general phenomenon where the optical frequency interval over which the phase of a fringe pattern changes by 2π varies with time and wavelength across the fringe pattern.

Sampling errors can arise due to fringe periodicity errors, as well as from other causes. This chapter will focus specifically on two sources of sampling errors. The first is intrinsic to the frequency-sampling method because the frequency spacing of the output fringes is uniform only to first order [22]. The approximation of uniform frequency spacing breaks down as both interferometer path length mismatches and average laser tuning rates increase. The resulting fringe periodicity errors lead to sampling errors when the interferometer output is used as a frequency clock for sampling swept-wavelength data sets. The second source of sampling error exists in practical SWI systems employing nonideal data acquisition (DAQ) hardware in which finite optical and electronic propagation delays cause the sampled data to lag behind the clock signal by a small time interval. These delays coupled with a nonlinear laser frequency sweep leads to a sampling grid with unequal frequency increments [34].

I begin in the following section by demonstrating the problem of laser tuning rate fluctuations by presenting tuning rate measurements for several commercial tunable lasers. Thus motivated, I derive analytic expressions for two sources of sampling error present in SWI systems that use the frequency-sampling method. Section 3.3.1 describes sampling errors intrinsic to interferometric triggering, and Sec. 3.3.2 analyzes errors do to nonzero signal propagation delays in DAQ hardware. Furthermore, I show that the optical system can be configured such that the two error sources cancel one another to second order. This error correction results in greater applicability of the frequency-sampling method for long interferometers

and fast laser tuning. In principle, this error correction technique can be applied to any SWI system. Section 3.4 presents experimental verification of sampling error correction using a general swept-wavelength interferometer implemented in optical fiber.

3.2 Measurement of laser tuning rate variations

If the frequency tuning characteristics of a tunable laser source are sufficiently linear, then no interferometric trigger is needed and SWI systems can use a temporal clock as described in Sec. 2.2.1. If a tunable laser exhibits tuning rate variations but the mean sweep rate and interferometer delays are configured such that the slow tuning approximation is valid, an interferometric trigger as described in Sec. 2.2.2 eliminates the problem of sampling errors. SWI systems with laser tuning rate variations in the presence of faster tuning and/or longer interferometer delays require attention to the analysis of the following sections. When sampling errors are present, their magnitude will be related to the derivatives of the tuning rate, as will be shown in Sec. 3.3.1. Therefore, to determine if an interferometric trigger is needed, and whether one will provide sufficient mitigation of sampling errors, it is important to have a method for precise measurements of the tuning characteristics of tunable lasers. Accurate measurement of the tuning rate throughout a laser sweep allows an SWI system designer to plan for the appropriate level of sampling error compensation, ranging from none for sufficiently linear tuning, to the use of an interferometric trigger for nonlinear tuning within the regime of the slow tuning approximation, to higher-order sampling error correction as described in this chapter. In this section I describe a means for measuring laser tuning rates, and I present measurements for four commercially available tunable lasers (three current models from different manufacturers, and one discontinued model that is still widely available on the used market).

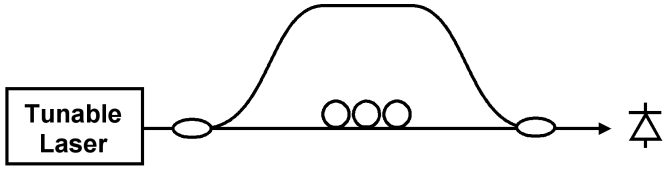

Figure 3.1: A schematic diagram of an optical layout used to measure the sweep rate of a tunable laser source.

The method I will present for measuring the sweep rates of tunable lasers is based on the use of an interferometer with a fixed path length difference coupled with digital filtering of the interference fringe data in the Fourier domain. Ahn and co-workers have described a similar measurement approach for tuning rate measurement using a Hilbert transform [128]. One suitable optical hardware configuration for the tuning rate measurement is shown in Fig. 3.1. A Mach-Zehnder geometry is shown, though other interferometer geometries, such as the Michelson geometry, are also suitable. While a polarization controller is shown in one arm of the interferometer, in practice precise polarization control is not necessary because 100% fringe visibility is not required. If fringe visibility is poor, flipping the coil of fiber in one arm of the interferometer usually provides sufficient coarse polarization control to give adequate fringe visibility.

To outline the steps of the Fourier domain filtering method for characterizing laser frequency sweeps, I will refer to experimental data shown in Fig. 3.2 for an Agilent 81680A tunable laser. To produce this data, the laser wavelength was swept at a nominal tuning rate of 40 nm/s. The group delay mismatch between the two arms of the interferometer was $\tau_0 = 13.2$ ns*. The interferogram was detected using an amplified InGaAs PIN photodetector (Thorlabs PDA10CS) and sampled at 1.0 MS/s using a National Instruments PCI-6115 data acquisition card. Note

*A means for precisely and accurately determining relative interferometer delays is presented in Ch. 4

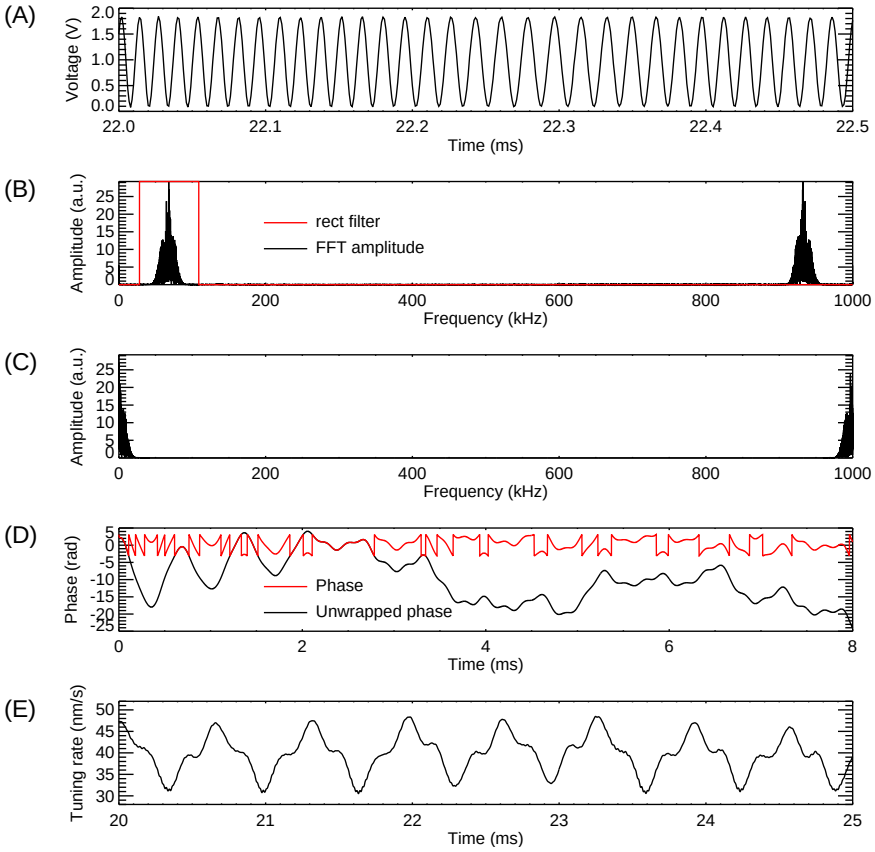

Figure 3.2: (Measured data and processing steps for characterizing nonlinear laser frequency sweeps using the Fourier domain filter method. Note that different sections of the 65 ms measurement are shown in the time domain plots. (A) Measured interference fringes for an Agilent 81680A laser swept at a nominal rate of 40 nm/s using a relative path delay of 13.2 ns. (B) Fourier transform of the fringe pattern and the digital filter function. (C) The filtered data is shifted so the selected sideband occupies the DC location in the data array. (D) The phase of the inverse FFT of the shifted filtered data before and after unwrapping. (E) Measured laser tuning rate as a function of time.

that this sampling is performed using a temporal clock, so the laboratory domain is the time domain for this measurement.

Figure 4.1(A) is a plot of the interference fringes measured during a frequency sweep. Because the differential group delay between the two paths of the interferometer is chosen such that the slow tuning approximation is satisfied, this fringe pattern is well-described by the following expression from Sec. 2.2.2:

$$U[\nu(t)] = U_0 \left\{1 + 2\cos\left[2\pi\nu(t)\tau_0 + \xi\right]\right\}, \tag{3.1}$$

where the time dependence of the optical frequency is now noted explicitly. The goal of the following data processing steps is to isolate the quantity $\nu(t)$ from the phase of this expression. The first step is to perform an FFT, which transforms the time domain fringe pattern to the frequency domain and results in positive and negative sidebands corresponding to $\exp\left[\pm j2\pi\nu(t)\tau_0\right]$ as shown in Fig. 4.1(B). Next, a digital filter is used to select a single sideband through multiplication by the rect function overlaid on Fig. 4.1(B). Before transforming back to the time domain via an inverse FFT, the filtered data is shifted such that the selected sideband occupies the DC location in the data array, as shown in Fig. 4.1(C). According to the shift theorem of Fourier transforms [117], this shift in the frequency domain is equivalent to a multiplication by a linear phase factor in the time domain. When the selected sideband is off of DC in the frequency domain, the phase of the time domain data includes a linear phase factor with a slope proportional to the displacement of the peak from DC. By shifting the peak to DC, this steep linear slope is removed from the time domain data. This processing step allows for straightforward unwrapping of the time domain phase; without removing the steep slope, the phase experiences rapid wrapping between 0 and 2π making phase unwrapping difficult to perform reliably. When an inverse FFT is applied to the filtered and shifted frequency domain data, the resulting time domain data set

corresponds to a single complex exponential. The phase of this complex data set is then straightforward to extract, and it is plotted in red in Fig. 4.1(D). This phase is then unwrapped by simply noting 2π discontinuities and adding integer multiples of 2π, as shown in black in Fig. 4.1(D). After unwrapping, the linear phase must be added back to compensate for the shift according to the Fourier shift theorem. The linear phase corresponds to the mean sweep rate of the laser, while the residual phase after shifting and unwrapping provides the measurement of the tuning rate variations about the mean. The result is a complex processed time domain data set $U^p(t)$ described by

$$U^p(t) = U_0 e^{2\pi j \nu(t) \tau_0}. \tag{3.2}$$

Taking the phase of this data set and dividing by $2\pi\tau_0$ yields a measurement of $\nu(t)$. A numerical derivative may then be performed to get the instantaneous tuning rate at each point throughout the sweep.

I used the process described above to measure the tuning rates of several commercially available tunable lasers operating in and around the optical telecommunications C-band (1530–1565 nm). These lasers include the following manufacturers and models: Agilent 81680A and 81600B, Yokogawa AQ2200-136, and Yenista Tunics T100R. Results of measurements for a 10 nm sweep from 1520 nm to 1530 nm for each of these lasers are presented in Figs. 3.3–3.6. Each measurement was performed using the maximum wavelength sweep rate supported by the laser. For each measurement, two plots are shown: one showing the tuning rate over the entire sweep, and one showing the sweep rate over a 5 ms interval. The latter plots are included because all four lasers were found to exhibit rapid variations in the sweep rate, the structure of which cannot be discerned in a plot of an entire 10 nm sweep. Note that these tuning rate oscillations for both Agilent models occur about a local mean that is consistently close to the nominal tuning

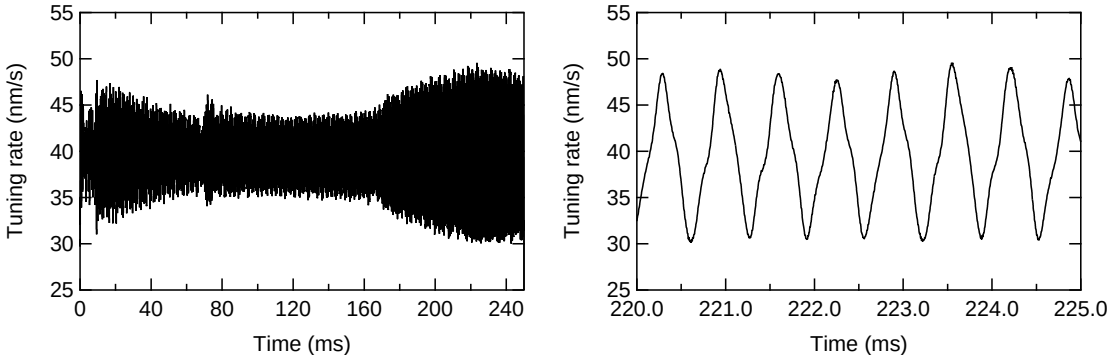

Figure 3.3: Measured tuning rate for an Agilent 81680A tunable laser for a wavelength scan from 1520 nm to 1530 nm (left) and a 5 ms portion of the same scan showing the fine structure of the tuning rate variations (right). The nominal wavelength tuning rate setting was 40 nm/s.

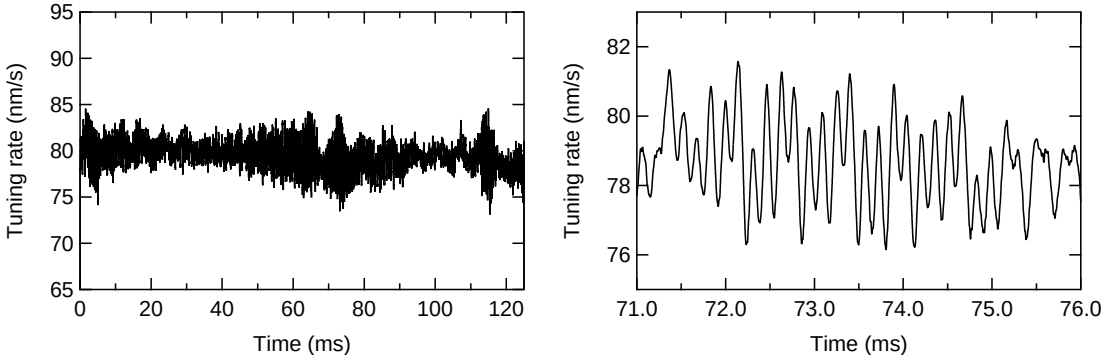

Figure 3.4: Measured tuning rate for an Agilent 81600B tunable laser for a wavelength scan from 1520 nm to 1530 nm (left) and a 5 ms portion of the same scan showing the fine structure of the tuning rate variations (right). The nominal wavelength tuning rate setting was 80 nm/s.

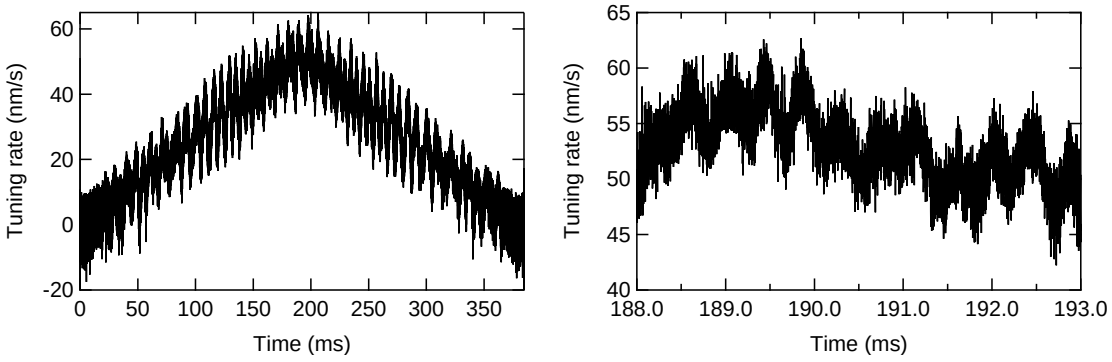

Figure 3.5: Measured tuning rate for a Yokogawa AQ2200-136 tunable laser for a wavelength scan from 1520 nm to 1530 nm (left) and a 5 ms portion of the same scan showing the fine structure of the tuning rate variations (right). The nominal wavelength tuning rate setting was 50 nm/s.

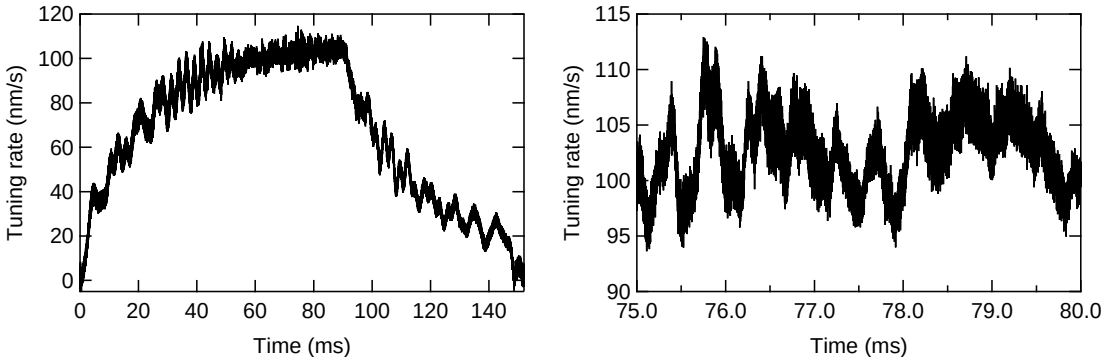

Figure 3.6: Measured tuning rate for a Yenista Tunics T100R tunable laser for a wavelength scan from 1520 nm to 1530 nm (left) and a 5 ms portion of the same scan showing the fine structure of the tuning rate variations (right). The nominal wavelength tuning rate setting was 100 nm/s.

rate setting throughout the sweep, whereas the Yokogawa and Yenista lasers exhibit marked periods of acceleration and deceleration at the beginning and end of the sweep. In all cases the tuning rate fluctuations are significant, indicating that none of these lasers can be used for SWI without performance degradation due to sampling errors if an interferometric trigger or other means to compensate for nonlinear frequency tuning is not employed.

3.3 Sampling errors in swept-wavelength interferometry

Measurements performed using SWI generally rely on the ability to convert between the time and frequency domains by means of a Fourier transform. In practice, this is typically accomplished using the FFT algorithm or a related algorithm for performing discrete Fourier transforms that operates based on the assumption that data points lie on a grid with equal intervals of the independent variable. Other algorithms for performing discrete Fourier transforms that don't utilize an assumption of equal sampling intervals may be used, but then the size each sampling interval must be recorded and used to accurately perform the transform. When using a transform algorithm that requires equal sample intervals, any deviation from equality in the sample intervals across the data set will result in measurement errors.

The ultimate effect of sampling errors on the transformed data depends on the nature of the data being Fourier transformed. For example, consider sampling a function $f(x)$ at the points x_i, where $x_{i+1} - x_i = \delta x + \eta_i$. Here δx is the size of a nominal spacing that is the same for all sample intervals, and η_i is the sampling error on the i^{th} interval. If $f(x)$ is a constant function, then sampling errors will have no effect at all, since the value of the sampled function is the same at $x_i + \eta_i$ as it is at x_i. On the other hand, if $f(x)$ varies with x, then the sampled value of $f(x_i + \eta_i)$ will differ from the value of $f(x_i)$ that was intended to be

acquired. If $f(x)$ represents a swept-wavelength interferogram, then sampling errors will manifest as fluctuations in the phase of the fringe pattern. In an SWI system, such an interferogram may include a device transfer function multiplying the sinusoidal fringe pattern; because the device transfer function will generally vary much more slowly with wavelength than the fringe pattern, the dominant effect of sampling errors in SWI systems is phase errors in the final measurement.

In the following analysis I derive theoretical expressions for two sources of sampling errors in SWI systems: sampling errors intrinsic to interferometric triggers, and sampling errors due to finite propagation delays in data acquisition hardware. While the discussion is framed in terms of the frequency sampling method, the same phenomena will lead to measurement errors regardless of whether the auxiliary interferometer output is used to trigger data acquisition or resample a time-synchronously sampled data set.

3.3.1 Sampling errors intrinsic to interferometric triggering

To understand how intrinsic sampling errors can arise through the use of an interferometric trigger, I will again derive the output of a single swept wavelength interferometer in the presence of nonlinear laser frequency tuning. This analysis is similar to that in Sec. 2.2.2 but without simplifying assumption of inequality (2.9). I begin again by defining the electric field at the input of the interferometer in terms of a complex function with a completely general time-varying phase:

$$E(t) = E_0 e^{j\phi(t)}. \tag{3.3}$$

The amplitude, E_0, of the electric field will in general vary with time as well, but since the variability of the optical phase is what leads to sampling errors, I will treat the amplitude as constant for convenience. It is convenient to recall that with this definition of the electric field, the instantaneous optical frequency of the

laser is given by

$$\nu(t) = \frac{1}{2\pi}\frac{d\phi}{dt}. \tag{3.4}$$

The interferometer will split the input laser field along two paths, and the two parts are recombined after traveling different distances. I take the splitting ratio to be unity for convenience; the phase of the resulting fringe pattern is of primary interest, and other splitting ratios will only affect the fringe visibility of the resulting interference pattern. Also for convenience I define zero delay as the group delay through the shorter of the two interferometer paths and denote the group delay[†] mismatch between the two paths as τ. With these definitions in place, a photodetector placed at the output of the interferometer will register a voltage given by

$$\begin{aligned} U(t) &= \sigma|E(t) + E(t+\tau_0)|^2 \\ &= U_0\left\{1 + \cos\left[\phi(t+\tau_0) - \phi(t)\right]\right\}, \end{aligned} \tag{3.5}$$

where σ is a constant of proportionality that depends on the detector sensitivity, and $U_0 = 2\sigma|E_0|^2$. Next, Taylor expand the function $\phi(t+\tau_0)$ about t:

$$\phi(t+\tau_0) = \sum_{n=0}^{\infty} \frac{\tau_0^n}{n!}\phi^{(n)}(t). \tag{3.6}$$

Writing the zero- and first-order terms of the sum explicitly and using Eq. (3.4) yields an expression for the phase of the output fringe pattern:

$$\phi(t+\tau_0) - \phi(t) = 2\pi\nu(t)\tau_0 + 2\pi\sum_{n=2}^{\infty}\frac{\tau_0^n}{n!}\nu^{(n-1)}(t). \tag{3.7}$$

This is the point in the analysis where in Sec. 2.2.2 the approximation

$$\tau_0^2\frac{d\nu}{dt} \ll 1 \tag{2.9}$$

[†]Reference [22] demonstrates why it is appropriate to use the group delay rather than the phase delay.

allowed the higher order terms of the Taylor expansion to be dropped leading to an output fringe pattern that is periodic in optical frequency with a period $\delta\nu = \tau_0^{-1}$. This approximation is not always valid, however, and when the higher-order terms in Eq. (3.7) are retained, the fringe pattern output by the interferometer is no longer periodic in optical frequency. When the interferometer is used as a frequency clock for data acquisition, deviations from periodicity result in nonuniform frequency intervals between data acquisition events. In this case, the i^{th} interval will depart from τ_0^{-1} by some amount η_i^I, i.e., $\delta\nu_i = \tau_0^{-1} + \eta_i^I$. The superscript I denotes that the sampling error derived here is the intrinsic error present in the frequency-sampling method, distinct from sampling errors due to delays in the DAQ hardware, which are treated in the next section.

To derive an expression for the sampling error η_i^I, consider the set of times t_i at which trigger events occur. These times are each separated by one period of the fringe pattern described by Eq. (3.5). The phase of the fringe pattern, represented in Eq. (3.7), will experience a change of 2π between t_i and t_{i+1}. To express the evolution of a single period mathematically, subtract the right side of Eq. (3.7) at time t_i from the same expression at time t_{i+1}, yielding

$$2\pi\tau_0[\nu(t_{i+1}) - \nu(t_i)] + 2\pi\sum_{n=2}^{\infty}\frac{\tau_0^n}{n!}[\nu^{(n-1)}(t_{i+1}) - \nu^{(n-1)}(t_i)] = 2\pi. \tag{3.8}$$

Rearranging terms, the change in optical frequency from one trigger event to the next can be expressed as

$$\delta\nu_i \equiv \nu(t_{i+1}) - \nu(t_i) = \tau_0^{-1} + \eta_i^I, \tag{3.9}$$

where

$$\eta_i^I = -\sum_{n=2}^{\infty}\frac{\tau_0^{n-1}}{n!}[\nu^{(n-1)}(t_{i+1}) - \nu^{(n-1)}(t_i)]. \tag{3.10}$$

Here η_i^I represents a fringe periodicity error intrinsic to swept wavelength interferometers and a sampling error intrinsic to the frequency sampling method that

depends on the interferometer path mismatch and the derivatives of the tuning rate. The sampling error couples to the final SWI measurement through the Fourier transform, leading to both amplitude and phase errors. These errors impose a limit on the interferometer path length differences allowable in an SWI system for a given laser that exhibits nonlinear frequency tuning. This limit can be extended, however, by using sampling errors due to delays in the DAQ hardware to cancel the intrinsic sampling errors to second order. These sampling errors due to data acquisition delays are treated next.

3.3.2 Sampling errors due to data acquisition delays

Even when the slow tuning approximation is valid, uniform frequency intervals between interferometrically triggered data points are still not ensured because of a second source of sampling errors: finite propagation delays in the DAQ hardware. Like the intrinsic sampling errors, sampling errors due to DAQ delays occur only when the optical frequency sweep of the laser source is not linear in time.

To derive an expression for the sampling errors due to the DAQ delays, begin with a detected optical trigger signal $\tilde{U}$ that varies as a simple cosine in frequency (as is the case when intrinsic sampling errors can be neglected):

$$U_t(t) = U_{t0}\{1 + \cos[2\pi\nu(t)\tau_0]\}. \tag{3.11}$$

Because this signal is periodic in frequency, it produces a set of trigger times t_i that correspond to sampling intervals of equal optical frequency:

$$\nu(t_{i+1}) - \nu(t_i) = \tau_0^{-1}. \tag{3.12}$$

Next define a fixed delay τ_D that includes two components: the differential optical delay between the trigger signal and the sampled signal, and the electronic delay between a trigger event and the moment a voltage value is recorded by the data

acquisition hardware. I will refer to the quantity τ_D as the DAQ delay. Such a finite delay will necessarily exist because of optical and electronic transmission delays if the analog clock and data channels are not carefully path-matched. Because of this delay, the data are not sampled at the times t_i, but rather at the set of times $t_i + \tau_D$. The effect of this delay is to perturb each frequency interval of the sampled data by an amount η_i^D according to

$$\nu(t_{i+1} + \tau_D) - \nu(t_i + \tau_D) = \tau_0^{-1} + \eta_i^D. \tag{3.13}$$

Here η_i^D is the sampling error due to the DAQ delay for the i^{th} sample. If the laser tuning rate is constant, the change in frequency over each τ_D will be the same and $\eta_i^D = 0$ for all i. But if the tuning rate of the laser is changing, the frequency change over each τ_D will be different, and the frequency spacing between acquired data points will no longer be uniform. To account for changes in tuning rate, expand $\nu(t + \tau_D)$ as

$$\nu(t + \tau_D) = \sum_{n=0}^{\infty} \frac{\tau_D^n}{n!} \nu^{(n)}(t). \tag{3.14}$$

Substituting Eq. (3.14) into Eq. (3.13) and explicitly writing the first term of the sums yields

$$\nu(t_{i+1}) - \nu(t_i) + \sum_{n=1}^{\infty} \frac{\tau_D^n}{n!} \nu^{(n)}(t_{i+1}) - \sum_{n=1}^{\infty} \frac{\tau_D^n}{n!} \nu^{(n)}(t_i) = \tau^{-1} + \eta_i^D. \tag{3.15}$$

Subtracting Eq. (3.12) from Eq. (3.15) results in an expression for the sampling error due to the data acquisition delay:

$$\eta_i^D = \sum_{n=1}^{\infty} \frac{\tau_D^n}{n!} [\nu^{(n)}(t_{i+1}) - \nu^{(n)}(t_i)]. \tag{3.16}$$

Generally speaking, the data acquisition delay τ_D can be controlled by adding a delay line to either the trigger channel or the measurement channel of the combined optical and electronic system. Since τ_D is the relative delay between a trigger event and the acquisition of the corresponding datum, it can be increased

by adding delay in the measurement portion of the network, or decreased by either removing delay from the measurement channel or by adding delay to the trigger channel. Thus it is possible to force $\eta_i^D = 0$ by appropriately path-matching the system such that $\tau_D = 0$. This strategy does not always yield the best system performance, however. Instead, a nonzero sampling error due to the relative DAQ delay can be used to cancel the intrinsic sampling errors derived in Sec. 3.3.1 through a prudent choice of τ_D.

3.3.3 Correcting sampling errors

So far I have derived expressions for sampling errors due to two sources: (1) errors intrinsic to interferometric triggering due to laser tuning rate fluctuations, given by Eq. (3.10), and (2) errors that are due to delays in DAQ hardware in the presence of laser tuning rate fluctuations, given by Eq. (3.16). When both of these errors are present, data is acquired at the times $t_i + \tau_D$, and the frequency spacing between acquisitions is

$$\begin{aligned}\delta\nu_i &= \tau_0^{-1} + \eta_i^I + \eta_i^D \\ &= \tau_0^{-1} - \sum_{n=1}^{\infty} \frac{\tau_0^n}{(n+1)!}[\nu^{(n)}(t_{i+1}) - \nu^{(n)}(t_i)] \\ &\quad + \sum_{n=1}^{\infty} \frac{\tau_D^n}{n!}[\nu^{(n)}(t_{i+1}) - \nu^{(n)}(t_i)],\end{aligned} \tag{3.17}$$

where the summation index for η_i^I has been converted from n to $n-1$ in order to start the summation at $n = 1$. In general, the sampling errors due to the first-order terms of the two sums will dominate. In this case the higher-order terms can be neglected, and the frequency spacing becomes

$$\delta\nu_i = \tau_0^{-1} + [\tau_D - \tau_0/2][\nu'(t_{i+1}) - \nu'(t_i)]. \tag{3.18}$$

As mentioned in the preceding section, τ_D may be controlled using delay lines in the system hardware. Therefore, one can set $\tau_D = \tau_0/2$, which will drive the

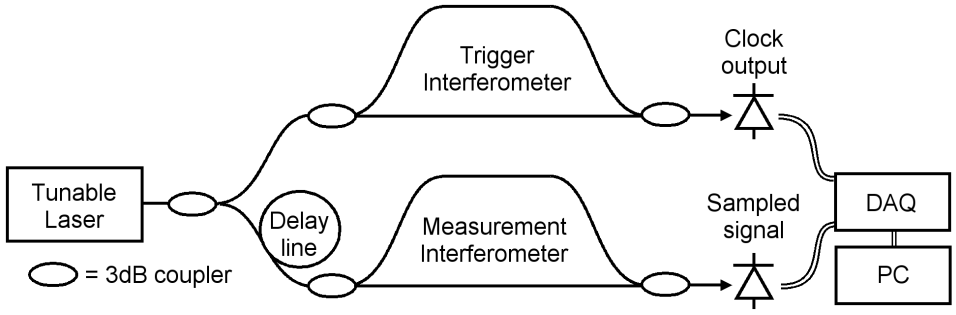

Figure 3.7: Simplified schematic diagram of the SWI system used for experimental verification of sampling error correction.

error term to zero and result in a cancelation of the sampling errors, thus restoring equal frequency intervals so that $\delta\nu_i = \tau_0^{-1}$ for all i. This approach yields error-free sampling to second order in $\phi(t)$ and is valid as long as $\tau_0^3(d^2\nu/dt^2) \ll 1$.

I have shown the cancelation of the first-order error term, but it is also possible to cancel any individual term in the series representing the total sampling error. Only one term in the series may be canceled in a given system because each successive term in the sums that constitute η_i^I and η_i^D differs by a factor of $1/n$. Therefore, there is no value of the relative DAQ delay that will cause the sampling error to be identically zero, but cancelation of any single term in the error expansion is possible through the proper choice of τ_D. The required value of τ_D will be different depending on which term in the series is to be canceled. In general, to drive the n^{th} order term of the sampling error to zero, the relative DAQ delay must be $\tau_D = \tau_0(n+1)^{-1/n}$.

3.4 Experimental sampling error correction

To experimentally verify the method for correcting sampling errors described theoretically in the preceding section, I constructed the SWI system is shown schematically in Fig. 3.7. The system was built using single-mode optical fiber and components designed for use in the C telecommunications band. Not shown

in the figure are polarization control and a tap that directs 2% of the laser output to an $H^{13}CN$ wavelength reference. The bulk of the laser output is split by a 3 dB fiber coupler, sending half of the light to the trigger interferometer and half to the measurement interferometer. The trigger interferometer provides the frequency clock signal for sampling the output of the measurement interferometer at equal intervals of optical frequency. The detectors at both interferometer outputs are Thorlabs PDA10CS amplified InGaAs photodetectors. The output of the trigger interferometer is routed to the external clock input of a National Instruments PCI-6115 DAQ card. The output of the measurement interferometer is sampled by the DAQ card on one of the card's four analog input channels.

The trigger interferometer uses a Mach-Zehnder geometry with a group delay difference of $\tau_t = 516$ ns between the two paths. This delay is chosen to be much less than the coherence length of the laser to avoid fringe fading due to coherence effects, but large enough such that the slow tuning approximation is violated. The laser wavelength is swept at a nominal rate of 40 nm/s, so for this combination of tuning rate and relative interferometer delay, $\tau_t^2(d\nu/dt) \approx 1.3$.

The measurement interferometer also uses a Mach-Zehnder geometry. The group delay difference between the two paths of this interferometer is $\tau_m = 13.2\,\text{ns}$. This interferometer satisfies the slow tuning approximation, since $\tau_m^2(d\nu/dt) \approx 10^{-3}$ for a mean sweep rate of $40\,\text{nm/s}$. Therefore the sampled fringe pattern is well described by Eq. (3.11) in the absence of sampling errors. Because the measurement interferometer comprises single mode fiber only, without any wavelength selective element, the amplitude of the output fringe pattern will be constant except for any amplitude variations of the laser input power as a function of wavelength. Overall, this means that the amplitude of the measurement interferometer output will be constant, or at most a slow function of wavelength. The phase of the measurement interferometer output, on the other hand, will

vary rapidly with wavelength. The relative path delay of 13.2 ns leads to a fringe period of $\delta\nu = 75.8$ MHz, or approximately 600 fm at a nominal wavelength of 1550 nm. This corresponds to a mean temporal period of around 15 μs for an average wavelength sweep rate of 40 nm/s. Therefore, the effect of sampling errors on the sampled measurement interferometer fringe pattern will primarily manifest as phase errors. In the absence of sampling errors, the measured phase $\Phi(\nu)$ should be a linear function of frequency, i.e.,

$$\Phi(\nu) = 2\pi\nu\tau_0. \tag{3.19}$$

Sampling errors will cause the phase of the sampled fringe pattern to deviate from linearity as a function of optical frequency.

For the first portion of this experiment, the SWI system was constructed without attention to the overall delays of the system, other than the differential delays between interferometer arms. These differential interferometer delays were determined using a $H^{13}CN$ gas cell according to the method described in Ch. 4. The fringe pattern output by the measurement interferometer was sampled by the PCI-6115 DAQ card using the fringe pattern output by the trigger interferometer as an analog clock. The laser wavelength was swept from 1530 to 1538 nm at a nominal rate of 40 nm/s. To produce a plot of the phase of the sampled interferogram as a function of optical frequency, I applied the following data processing steps. First, the fringe data is transformed to the time domain using the FFT algorithm. Second, a digital bandpass filter selects a 4 ns segment of the data centered on the positive delay sideband in the time domain. Third, the selected subset of the time domain data is shifted such that the peak of the sideband occupies the DC location of the 4 ns data array. Fourth, the rotated data segment is converted back to the frequency domain using an inverse FFT, resulting in complex frequency domain data. Lastly, the phase of this data is unwrapped and a

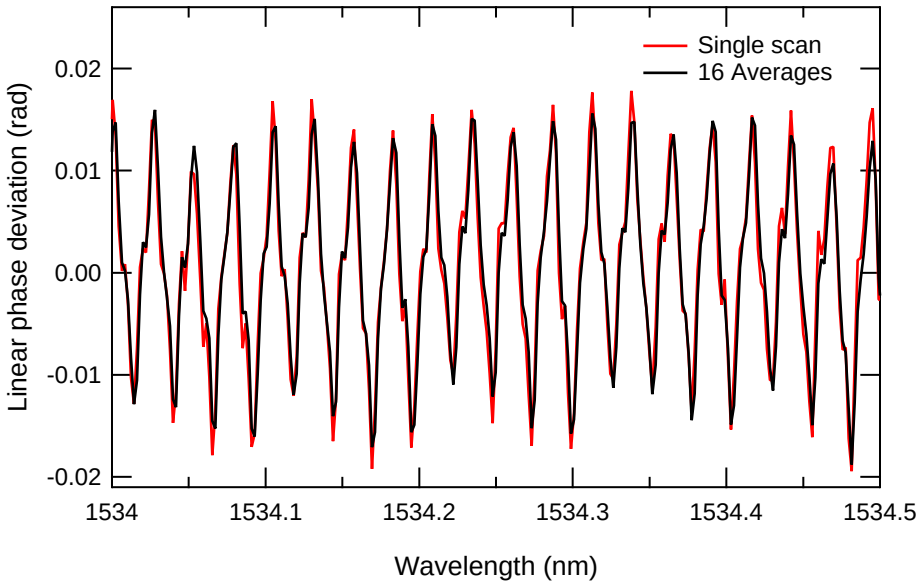

Figure 3.8: Measured linear phase deviation data for a swept-wavelength interferometer using the frequency-sampling method. The nonzero deviation from linear phase results is due to sampling errors resulting from unmatched system delays. These errors affect both single-scan and averaged data. The red curve is the linear phase deviation for a single measurement, and the black curve is the average of 16 measurements.

linear fit is subtracted. The resulting measurement of the deviation from linear phase appears in Fig. 3.8. The large deviation is equally present in single scan and averaged data, showing the sampling errors to be systematic in nature. The data plotted in Figure 3.8 shows both a single scan measurement as well as the average linear phase deviation for 16 measurements.

For the second portion of the experiment, I implemented the method described in Sec. 3.3.3 to correct the sampling errors. To do so, the first step is to measure the delays associated with each optical path in the system, as well as the electronic delay between a trigger event on the analog clock channel of the DAQ card and the acquisition of the corresponding datum on the analog input channel.

Optical delays were measured by incorporating the optical paths into an external Mach-Zehnder interferometer using two 3 dB couplers, as shown in Fig. 3.9.

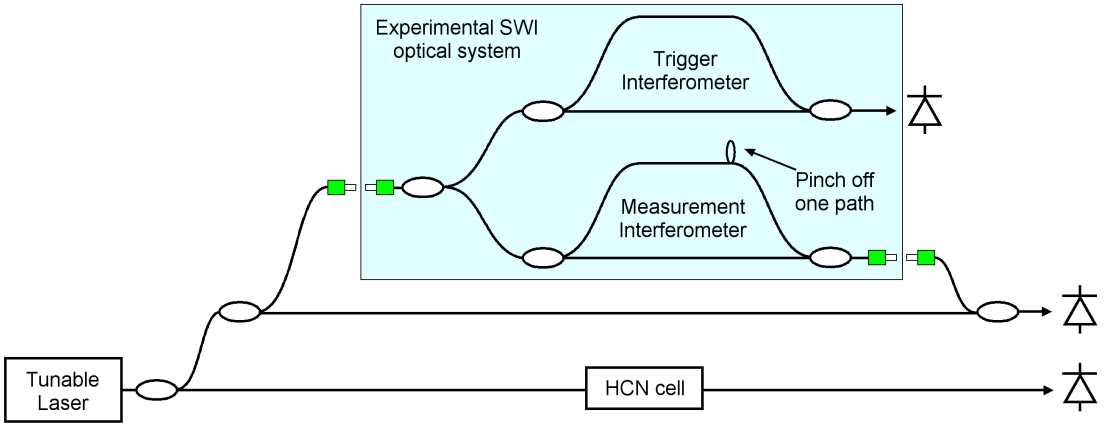

Figure 3.9: Optical layout for measuring the optical path lengths of the experimental SWI system for verifying sampling error correction.

The method of Sec. 4.2.2 incorporating an $H^{13}CN$ wavelength reference was used to measure the relative delay of the external interferometer. A baseline delay measurement was performed first, by closing the external interferometer path without any additional length between the connectors. Then the interferometer was connected to the experimental SWI system and the four optical path delays were measured sequentially. To measure a single path of either the measurement or trigger interferometer, the other path can be disconnected or simply pinched off to prevent optical transmission. By allowing only a single transmission path, the length of that path is measured unambiguously without the need to identify additional time domain peaks. The increase in the measured interferometer delay relative to the baseline measurement represents the length of the optical path. It is important to ensure that the external interferometer path that will include the path to be measured is longer than the other path of the external interferometer when it is closed without additional length. Otherwise, the change in measured interferometer delay will not be equal to the introduced path length. This method for measuring the relative delay of an interferometer generally relies on the validity of the slow tuning approximation that yields periodic fringes in optical frequency.

But because the tuning rate fluctuations exhibited by the Agilent 81680A tunable laser are oscillatory (as shown in Fig. 3.3), variations in the fringe period cancel out over a large number of samples. Expressed another way, while the sample spacing is not equal due to fringe periodicity errors, the average sample spacing will be τ_0^{-1} because the fringe periodicity errors average to zero for the given laser tuning characteristics.

The electronic delay associated with the DAQ hardware was measured by splitting a sinusoidally modulated laser signal and sending equal parts to the trigger detector and the measurement detector. By sampling the same signal that is used for triggering, the difference between the sampled voltage and the trigger threshold voltage determines the electronic component of the DAQ delay τ_{De} according to

$$\tau_{De} = \frac{\sin^{-1} V/A}{2\pi f}, \tag{3.20}$$

where V is the sampled voltage level, A is the amplitude of the modulated signal, and f is the modulation frequency. The modulation frequency of 2.58 MHz was chosen to correspond to the average sampling frequency that results from using the trigger interferometer with $\tau_t = 516$ ns and a laser tuning rate of 40 nm/s.

Measurement of all system delays determined that before correction the overall relative DAQ delay for the system was 567 ± 5 ns. The uncertainty associated with this value is dominated by the uncertainty in the measurement of the electronic delay. Since a value of $\tau_t/2 = 258$ ns is necessary to correct sampling errors, and addition of delay to the measurement path contributes negative delay to τ_D, 309 ± 5 ns must be added to the measurement path.

Next I modified the experimental SWI system to incorporate a delay line as shown in Fig. 3.7. I took repeated measurements of the fringe pattern at the output of the measurement interferometer for delay lines of various lengths ranging from zero to 445 ns. For each measurement I recorded the standard deviation of

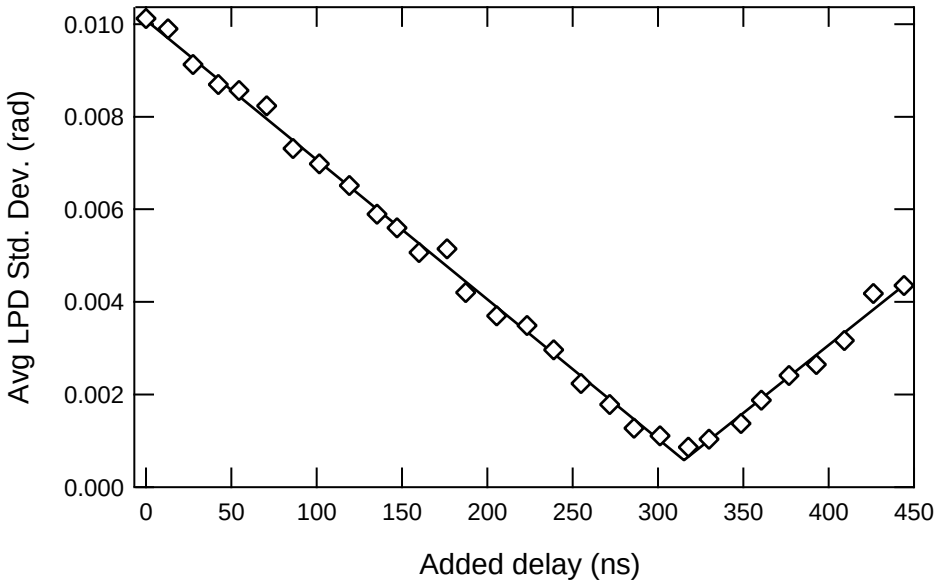

Figure 3.10: Standard deviation of the linear phase deviation of the measured fringe pattern as a function of added delay. The open diamonds represent measured data and the solid line is a piecewise linear fit.

the deviation from linear phase. The uncertainty in these data was ± 0.2 mrad, due primarily to external vibration coupling into the measurement. The results are plotted in Fig. 3.10. The intersection of a piecewise linear fit locates the minimum error at an added delay of 315 ± 14 ns, which is in good agreement with the calculated value of 309 ± 5 ns. Single-scan and averaged linear phase deviation data for the optimally corrected case is shown as the red and blue curves in Fig. 3.11, respectively. Over the wavelength range shown in this plot, the standard deviation of the uncorrected linear phase deviation is 8.6 mrad for 16 averages; when sampling error is employed it is reduced to 0.75 mrad for a single scan, and to 0.42 mrad for 16 averages.

3.5 Summary and conclusions

In this chapter, I have derived analytic expressions for two sources of sampling errors that can occur when using the frequency-sampling method to trigger

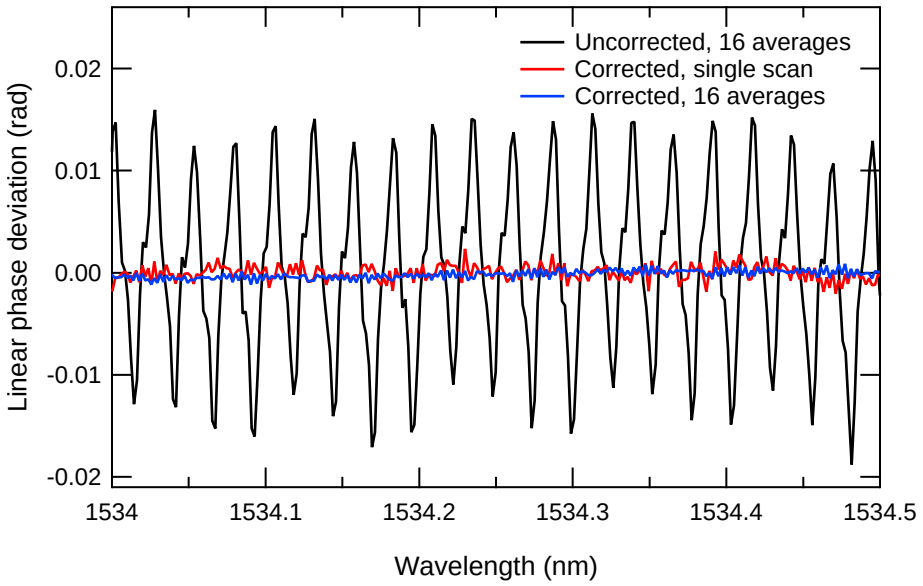

Figure 3.11: Measured linear phase deviation data for a swept-wavelength interferometer with and without sampling error correction. The black curve shows significant deviation from linear phase due to sampling errors for a system with unmatched system delays. The red curve shows a corrected single-scan measurement of linear phase deviation using an optical delay line for sampling error correction. The blue curve demonstrates further reduction in the linear phase deviation by averaging, indicating that the residual error is not systematic in nature.

data acquisition in swept-wavelength measurements when the laser tuning rate is not constant. One source is intrinsic in the physics of a swept-wavelength interferometer when the path length difference and average laser tuning rate are large enough such that the slow tuning approximation $\tau_0^2(d\nu/dt) \ll 1$ is not valid. The second source can be present even for small path length differences and slow tuning rates and is due to transmission delays in data acquisition hardware. Furthermore, introducing an optical delay line into the swept-wavelength measurement system, these errors can effectively cancel one another to second order. This eases the restrictions on the interferometer delay and laser tuning curve necessary for using the frequency-sampling method from $\tau_0^2(d\nu/dt) \ll 1$ to $\tau_0^3(d^2\nu/dt^2) \ll 1$. In the case where intrinsic sampling errors are negligible, errors due to DAQ delays can

be removed by using the delay line to match the measurement channel path length to the trigger channel path length. Correction of sampling errors was experimentally verified, showing an order of magnitude improvement in the phase error of the sampled interferogram.

Chapter 4

Precision Ranging

4.1 Introduction

One of the most common uses of SWI is measurement of distance to a reflecting object or interface. This capability is the foundation of OFDR measurements for network testing and fiber optic sensing, FMCW lidar for free-space range measurements and remote sensing, and SS-OCT for noninvasive, depth-resolved imaging for a variety of biological and medical applications. While all of these applications can benefit from improved range resolution, microscopic imaging performed using OCT is most concerned with reflectivity variations on small length scales. With variations based on both low-coherence [65] and swept-wavelength interferometry [62,66], OCT provides measurements of optical reflectivity as function of depth (A-scans) within the sample under test. By laterally scanning either the probe beam or the sample under test, depth-resolved 2- and 3-dimensional images can be produced. The high axial resolution offered by these measurements provide a unique ability to image subsurface biological structures based on the level of scattering returned by underlying tissues. For both low-coherence and swept-source OCT, the axial resolution is inversely proportional to the frequency bandwidth of the optical source [129]. Axial resolutions on the order of $1\,\mu$m have been achieved with low-coherence approaches using extremely broadband

supercontinuum sources [72]. For SS-OCT, the axial resolution is typically limited to the order of 10 μm due to the more limited spectral breadth available from swept-wavelength sources.

Axial displacement sensitivities greatly exceeding the axial resolution of OCT systems have been demonstrated by numerous groups using phase-sensitive frequency-domain OCT techniques [87, 107, 109, 110, 130, 131]. These frequency-domain approaches include both low-coherence interferometry using spectrally dispersed detection as well as swept-wavelength interferometry. Both modes detect spectral interferograms as a function of optical frequency and produce *A*-scan data by applying a Fourier transform to the acquired fringe patterns. Small displacements of discrete reflectors can be detected by noting changes in the phase of the complex-valued *A*-scan data at the location in the data array corresponding to the reflector. These phase measurements provide a relative displacement measurement from scan to scan, and have been applied to surface profiling [87], phase imaging [130], and Doppler flow measurements [110,131]. In all of these cases, the submicron displacements measured via phase have been relative to an arbitrary zero point within a single depth bin defined by the source-spectral-width-limited axial resolution of the system. In this chapter, I present a novel implementation of phase-sensitive swept-source OCT where phase information is used to perform measurements of lengths and thicknesses spanning multiple resolution-limited depth bins to nanometer precision. Additionally, I present a means for accurate calibration of the time (or, equivalently, spatial) domain sampling grid, leading to highly accurate macroscopic optical path length measurements.

As an example application, I demonstrate the proposed phase-sensitive SS-OCT system for simultaneous measurements of group refractive index and physical thickness of optical samples. The technique employed was first introduced by Sorin and Gray [132] using low-coherence interferometry, and there has been

renewed interest in the method recently using low-coherence interferometry in both the time domain [133] and spectral domain [134]. Here I present what is to my knowledge the first swept-source demonstration of simultaneous group index and thickness measurement, as well as the first implementation to utilize phase information for improved performance. The use of phase-sensitive self-referenced SS-OCT provides resolution improvements of up to two orders of magnitude for both group index and thickness over previously published works.

4.2 Principles of precision ranging with SWI

In swept-source OCT, each A-scan performs an axial reflectivity measurement using optical frequency domain reflectometry (OFDR) [66]. As described in Ch. 2, in this technique the output of a wavelength-tunable source is split into a fixed-length reference path and a test path, which are then recombined allowing the light traversing each path to interfere prior to detection. As the source optical frequency is swept over a range $\Delta\nu$ about a central frequency ν_c, a fringe pattern is observed at the interferometer output. The frequency of the fringe pattern indicates the differential group delay between the reference path and the sample path. For a sample with K distinct reflectors distributed axially, the oscillating portion of the photodetector voltage at the interferometer output is given by

$$\tilde{U}(\nu) = 2U_0 \sum_{i=1}^{K} |r_i| \cos\left(2\pi\nu\tau_i + \psi_i\right) \tag{4.1}$$

where ν is the instantaneous frequency of the laser source, τ_i is the group delay difference between the i^{th} reflection in the sample path and the reference path, and ψ_i is a constant phase offset. The factor r_i is the effective reflection coefficient of the i^{th} reflection [22]. To avoid limitations in the axial resolution of the scan due to nonlinearity of the optical frequency sweep, the fringe pattern must be sampled on a grid of equal optical frequency increments. This can be accomplished

using an auxiliary interferometer to provide either instantaneous frequency data throughout the sweep in order to resample the interferogram [112], or by using the auxiliary interferometer output as a frequency clock to trigger acquisition of the fringe pattern data [115]. The equal-frequency sampling allows the sampled frequency-domain fringe pattern data to be converted to a time domain data set $\mathcal{U}(\tau)$ via a fast Fourier transform (FFT):

$$\mathcal{U}(\tau) = \mathcal{F}[\tilde{U}(\nu)], \tag{4.2}$$

where $\mathcal{F}$ denotes the Fourier transform. In the time domain, the portion of the signal due to the i^{th} reflector is

$$\mathcal{U}_i(\tau) = U_0|r_i|\,\Delta\nu\,\text{sinc}[\Delta\nu(\tau-\tau_i)]e^{j(2\pi\nu_c\tau-\xi_i)} \tag{4.3}$$

where $\xi_i = \psi_i + 2\pi\nu_0\tau_i$ and $\text{sinc}(x) = \sin(\pi x)/(\pi x)$. Here the sinc function arises due to the assumption of a constant amplitude over the spectral range $\Delta\nu$. Other spectral shapes (or the application of a windowing function prior to the Fourier transform) will change the shape of the time domain response. The width $\Delta\tau_w$ of this response function determines the axial resolution of an A-scan, and this width will generally be $\Delta\tau_w \approx 1/\Delta\nu$ for most spectra. Note also that $\delta\tau = 1/\Delta\nu$ will be the sample spacing of the time domain data, so that in the best case the axial resolution will be equivalent to one temporal bin. If there are two reflectors spaced by $\delta\tau$ or less, they will not be resolvable. For an isolated reflector, however, the location of the reflector, described by τ_i, can be determined to within a small fraction of $\delta\tau$ by analyzing the phase of the reflector's contribution to the time domain reflectogram.

4.2.1 Phase slope measurements for improved range precision

To illustrate the process of performing highly precise range measurements using phase sensitive SS-OCT, refer to the simulated A-scan data shown in Fig. 4.1.

For this simulated data, the total sweep range was 1520 to 1570 nm, or 6.28 THz, resulting in a time domain step size of 159 fs. The total data set size was 4096 samples, yielding a frequency domain sampling interval of 1.53 GHz and a time domain range of 0.644 ns. The group delay difference τ_0 between the reference path and a single reflector in the test path was chosen to be exactly 0.14 ns.

From the sampled time domain data shown in Fig. 4.1(a), a coarse determination of τ_0 is accomplished by noting the location $\tau_{0,q}$ of the reflection peak in the time domain data array. Here the subscript q denotes that $\tau_{0,q}$ is a coarse approximation of the true reflector position τ_0 to within a precision of approximately $\delta\tau$, or one temporal bin. The true value of τ_0 lies between sampled points. This offset between the location $\tau_{0,q}$ of the peak value in the time domain data array and the true value of τ_0 can be found by applying the shift theorem of Fourier transforms [117] to a subset of time domain data surrounding the i^{th} peak. The shift theorem states that a translation in the time domain is accompanied by a corresponding linear phase factor in the frequency domain. Thus, determination of the offset between the exact value of τ_0 and the location of the sampled peak maximum can be accomplished through a linear phase measurement in the frequency domain. For an isolated reflection peak, the corresponding phase contribution in the frequency domain can be found by windowing out the single peak using a digital filter and then performing an inverse FFT on the windowed data subset. Figure 4.1(b) is a plot of the amplitude of the windowed reflection peak selected by applying a digital filter to the positive delay peak in Fig. 4.1(a). The phase of the resulting frequency domain data set will wrap rapidly between 0 and 2π unless the time domain subset is rotated such that the amplitude maximum occupies the first (DC) index location in the data array. Performing this rotation prior to the inverse FFT results in a slowly-varying frequency domain phase that can be straightforwardly unwrapped by noting discontinuities and adding

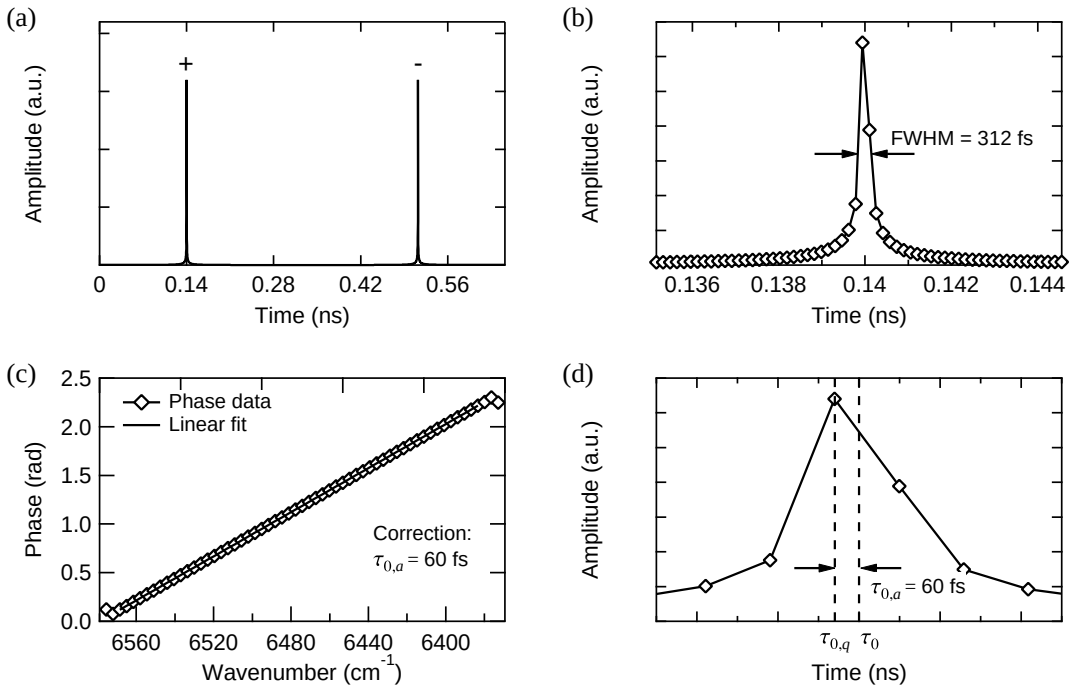

Figure 4.1: Plots illustrating the processing steps for precision range measurements using phase-sensitive swept-source optical coherence tomography. (a) Simulated *A*-scan data for a single reflector at a relative group delay of exactly $\tau_0 = 0.14\,\text{ns}$, corresponding to a path length difference between the reference and sample arms of approximately 4.2 cm. Both the positive- (+) and aliased negative-delay (-) peaks are shown. (b) The digitally filtered reflection peak with a maximum value located at $\tau_{0,q} = 0.13994\,\text{ns}$, yielding an error in the axial location of $9.0\,\mu$m in air. (c) The frequency domain phase for the filtered subset. Prior to the inverse Fourier transform, a Hanning window was applied to reduce truncation effects and the peak was shifted to the DC location in the data array. The linear fit excluded data points at the extremities due to residual truncation effects. The resulting slope of the linear fit corresponds to a group delay correction of $\tau_{0,a} = 0.00006\,\text{ns}$, which is the precise correction needed to recover the exact value of $\tau_0 = 0.14\,\text{ns}$ as shown in (d).

integer multiples of 2π. Fitting a line to the unwrapped phase $\phi(\nu)$, as shown in Fig. 4.1(c), and extracting the slope $d\phi/d\nu$ yields a group delay correction $\tau_{0,p}$ given by

$$\tau_{0,p} = \frac{1}{2\pi}\frac{d\phi}{d\nu}. \tag{4.4}$$

This quantity represents a fine adjustment to the coarse group delay measurement $\tau_{i,q}$, resulting in a high precision determination of the reflector location, τ_0, according to

$$\tau_0 = \tau_{0,q} + \tau_{0,p}. \tag{4.5}$$

The precision of the resulting measurement of the reflector position as determined by the standard deviation over multiple measurements will be limited by a variety of factors, including the repeatability of the wavelength sweep, the magnitude of τ_0 relative to the coherence length of the laser, and drift of the interferometer with changes in environmental conditions. Because measurement errors due to sweep-to-sweep variations in the optical source will be correlated for multiple reflections within a single A-scan, measurement precision can be significantly improved by performing a relative group delay measurement using one reflector within the A-scan as a reference [134]. For fiber systems with a free space probe, the fiber end facet in the test arm makes a convenient reference reflector.

4.2.2 Sampling grid calibration for accurate absolute ranging

The accuracy with which a reflector can be located depends not only on the precision of the group delay measurement, but also the accuracy of the time domain sampling grid that is used to perform the coarse group delay measurement, $\tau_{i,q}$. Because of the discrete Fourier transform relationship between the acquired frequency domain fringe pattern and the time domain A-scan, the time domain step size of the A-scan, $\delta\tau$, is given by the reciprocal of the frequency domain sweep range, $\Delta\nu$. For an N-point A-scan, where the frequency domain step size is $\delta\nu$, the

time domain step size is therefore $\delta\tau = (N\delta\nu)^{-1}$. As mentioned above, the interval $\delta\nu$ separating frequency domain samples must remain constant throughout the data set, and is determined through the use of a frequency clock to trigger data acquisition or by monitoring the instantaneous frequency of the source throughout a sweep and resampling the fringe data in post-processing. Thus the uncertainty in the time domain step size depends on the accuracy with which the instantaneous optical frequency can be determined during a wavelength sweep.

The most common way to monitor the instantaneous optical frequency of a swept source is through the use of an auxiliary interferometer. Provided that the differential group delay τ_t between the auxiliary interferometer paths and the mean laser sweep rate $\gamma = \mathrm{d}\nu/\mathrm{d}\,t$ are chosen such that $\Gamma = \tau_t^2\gamma \ll 1$, then the output fringe pattern will be a periodic function of optical frequency with a period of $1/\tau_t$ [115]. If the fringe data is sampled or resampled at this period so that the frequency domain step size $\delta\nu$ is equal to $1/\tau_t$, then τ_t will be the full range of the dual-sided time domain data set, and the Nyquist-limited measurable group delay will be $\tau_t/2$. The accuracy of the time and frequency domain sampling grids then depend on the accuracy with which τ_t (or its reciprocal) can be measured. Note that once τ_t has been determined, the uncertainty in the time domain step size $\delta\tau = \tau_t/N$ does not follow a normal distribution from point to point throughout the time domain data set. Rather, an error in the measurement of the trigger delay will yield a single value of $\delta\tau$ that is either too small or too large by the same relative magnitude as the error in τ_t. Therefore, a range measurement with a measured delay τ_i performed by locating a peak at a fractional index m in the time domain data array will have an uncertainty given by

$$u(\tau_{i,q}) = m\,u(\delta\tau) = \frac{m}{N}u(\tau_t), \tag{4.6}$$

where $u(x)$ is used to denote the uncertainty in the quantity x. Thus, the relative

error in the range measurement will equal the relative error in the calibration of the auxiliary interferometer.

As described in Sec. 2.5.1.3, a simple way to calibrate the relative delay of the trigger interferometer would be to measure the length of fiber in both arms and then take the difference. This relative length difference can then be converted to a delay value using the effective index of the guided fiber mode and the speed of light. A more precise calibration can be accomplished by counting the number of fringe periods between well-characterized spectral features, such as molecular absorption lines. Wavelength references based on molecular absorption lines can be accurate to ±0.01 pm [135], and commercial gas cells with wavelength accuracies as good as ±0.05 pm are available in multiple spectral bands. These specifications yield a known uncertainty between two spectral features that span a frequency range $\Delta\nu_c$. For a given auxiliary interferometer with a differential group delay τ_t, the number of periods over the range $\Delta\nu_c$ will be $p = \Delta\nu_c\,\tau_t$. Using this relationship to determine τ_t, there will be contributions to the uncertainty due to the quality of the wavelength reference $u(\Delta\nu_c)$, as well an uncertainty in the determination of p to a fraction of a fringe. Therefore, the total uncertainty in τ_t is

$$u(\tau_t) = u\left(\frac{p}{\Delta\nu_c}\right) = \frac{p}{\Delta\nu_c}\left[\left(\frac{u(p)}{p}\right)^2 + \left(\frac{u(\Delta\nu_c)}{\Delta\nu_c}\right)^2\right]^{1/2}. \tag{4.7}$$

When this interferometer is used to trigger data acquisition during a frequency sweep over a range $\Delta\nu$, the number of samples N will be $N = \Delta\nu\,\tau_t$, and the uncertainty in the time domain step size will be $u(\delta\tau) = u(\tau_t)/N$. Figure 4.2 is a plot of $u(\delta\tau)$ for some representative values over a range of interferometer path imbalances spanning five orders of magnitude from 1 mm to 100 m. This range covers typical SS-OCT imaging systems on the short end, and typical OFDR systems designed for fiber sensing and telecommunications system testing on the upper end. The frequency sweep range is $\Delta\nu_c = 3.49$ THz, corresponding to

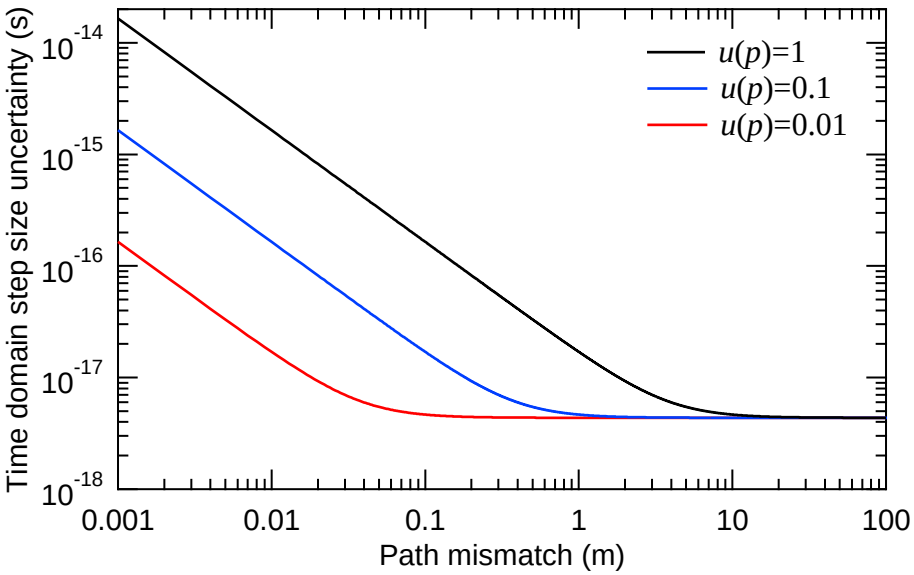

Figure 4.2: Uncertainty in the *A*-scan sampling grid as a function of path length difference for an interferometer calibrated using the R20 and P20 absorption lines of a 100-Torr $H^{13}CN$ wavelength reference. The three curves correspond to fringe counting uncertainties of 1, 0.1, and 0.01.

the spectral separation between the R20 and P20 absorption lines of $H^{13}CN$ at 100 Torr, a common wavelength reference material for the range between 1528 and 1562 nm. The absorption spectrum of a 100 Torr $H^{13}CN$ cell manufactured by dBm Optics is shown in Fig. 4.3, and Table 4.1 lists the wavelengths corresponding to each of the 51 characterized absorption lines. The R20 and P20 lines are located at 1530.3061 nm and 1558.0329 nm, respectively, and the uncertainties in their locations are ±0.3 pm. The three curves in Fig. 4.2 represent the uncertainty in the time domain step size for three values of the uncertainty in the number of fringes between the absorption lines. The asymptotic value of 4.4 as is reached when the uncertainty of the wavelength reference dominates. Interestingly, this plot shows that an extremely high degree of temporal accuracy can be achieved over a range of interferometer length imbalances spanning several orders of magnitude. For short interferometers, such as those typically used for SS-OCT, more care must be taken

Table 4.1: Absorption line wavelengths for a dBm Optics model WA-1528-1562 100 Torr $H^{13}CN$ wavelength reference. Accuracy is ±0.3 pm except for wavelengths marked with an asterisk (*), which are known to ±0.6 pm.

R Branch		P Branch	
Line no.	Wavelength (nm)	Line no.	Wavelength (nm)
25	1528.0541	1	1543.1148*
24	1528.4862*	2	1543.8094
23	1528.9271	3	1544.5147
22	1529.3762	4	1545.2314*
21	1529.8376*	5	1545.9563*
20	1530.3061	6	1546.6902
19	1530.7856	7	1547.4354
18	1531.2764*	8	1548.1904
17	1531.7738	9	1548.9554*
16	1532.2825	10	1549.7302*
15	1532.8024*	11	1550.5149*
14	1533.3291	12	1551.3106
13	1533.8671	13	1552.1157
12	1534.4159*	14	1552.9308
11	1534.9723	15	1553.7560
10	1535.5401*	16	1554.5892*
9	1536.1170*	17	1555.4346*
8	1536.7034*	18	1556.2919
7	1537.2997*	19	1557.1573
6	1537.9069	20	1558.0329
5	1538.5224*	21	1558.9185
4	1539.1494	22	1559.8143
3	1539.7855	23	1560.7185*
2	1540.4314	24	1561.6344*
1	1541.0872	25	1562.5625
0	1541.7529		

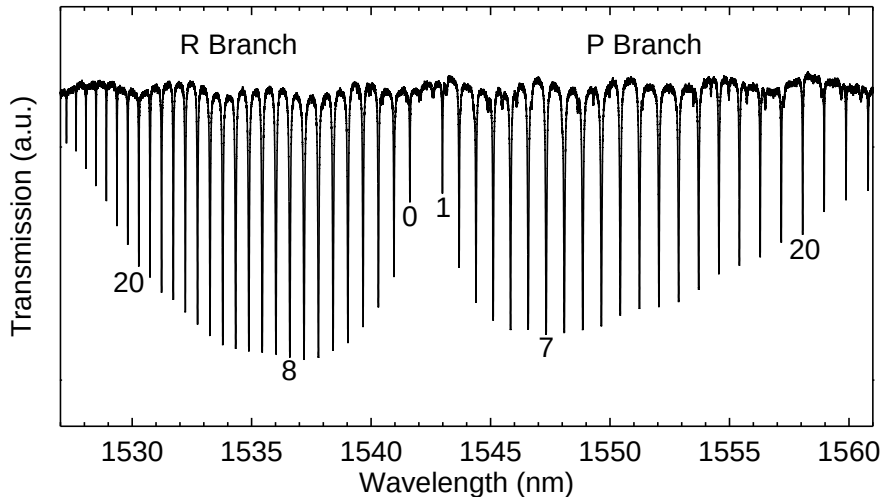

Figure 4.3: The absorption spectrum of a dBm Optics model WA-1528-1562 100 Torr $H^{13}CN$ wavelength reference showing the absorption line numbering scheme.

to accurately determine the number of periods between the absorption lines to a fraction of a fringe. This is typically accomplished by fitting a Lorentzian curve to the sampled absorption line data. For longer interferometers, high temporal accuracy can be achieved without the need for fractional fringe counting.

4.3 Experimental phase-sensitive SS-OCT system

A schematic diagram of the experimental phase-sensitive SS-OCT system for demonstrating precision ranging is shown in Fig. 4.4. The tunable laser is an Agilent 8160A with a sweep range of 1460 to 1580 nm. The measurement interferometer employs a transmissive reference path and a reflective test path. Polarization diverse detection ensures good fringe visibility regardless of the polarization state in the test path. As described in Sec. 2.4, the polarization controller in the reference path is set to split the reference path light equally between the two output channels. The auxiliary trigger interferometer utilizes a Mach-Zehnder

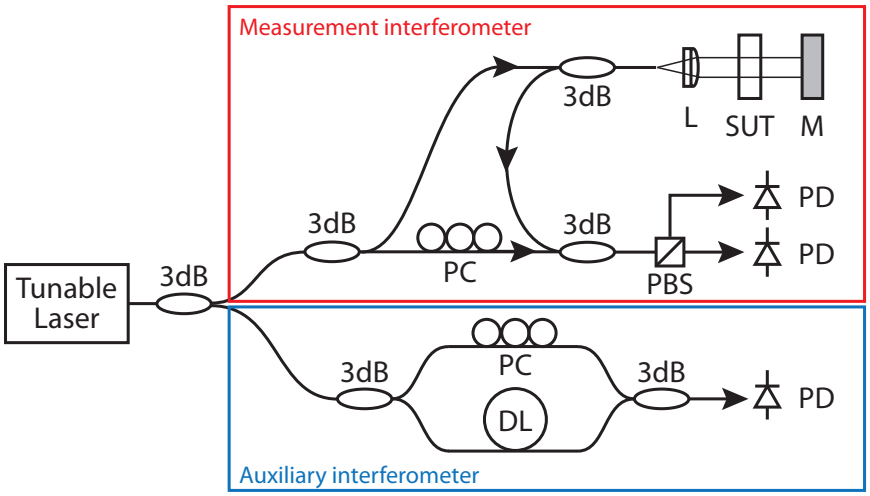

Figure 4.4: Schematic diagram of the experimental phase-sensitive swept-source optical coherence tomography system. 3dB, 3dB fiber coupler; DL, fiber delay line; L, collimation lens; M, mirror; PBS, polarization beam splitter; PC, polarization controller; PD, photodetector; SUT, sample under test.

geometry, and its output is used to provide an analog clock signal to trigger sampling of the measurement interferometer fringe data using a National Instruments PCI-6115 DAQ card.

The trigger interferometer was calibrated using an $H^{13}CN$ wavelength reference as described in the preceding section. The trigger interferometer calibration step utilized the optical network shown in Fig. 4.5. The trigger interferometer output is used as an analog clock signal to sample transmission data through the wavelength reference as the wavelength of the optical source is swept. As long as the values for the laser sweep rate and the interferometer delay satisfy the slow tuning approximation ($\Gamma \approx 0.02$ for this system), the $H^{13}CN$ absorption spectrum is sampled at constant optical frequency intervals, $\delta\nu$, equal to the reciprocal of the unknown trigger interferometer delay, τ_t. Recall this is because the interferometer output as a function of optical frequency is given by

$$U(\nu) = U_0[1 + \cos(2\pi\nu\tau_t + \xi)]. \tag{4.8}$$

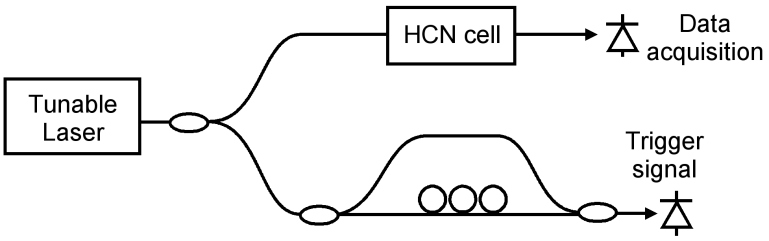

Figure 4.5: Optical network for calibrating the relative delay of an interferometer using a hydrogen cyanide gas cell wavelength reference.

Within the resulting data array, each array index corresponds to an increment of $\delta\nu$. Since the spectral locations of the absorption features are known, determining the number of data points p separating two chosen absorption lines separated by $\Delta\nu_c$ yields a measurement of $\delta\nu = \Delta\nu_c/p$. Determination of the location of the two chosen absorption lines typically requires a curve fit of the absorption data for one of two reasons. For short interferometers, accurate calibration requires the fringe counting between the two absorption features to be accurate to a fraction of a fringe, as shown in Fig. 4.2 above. In this case a curve fit is required to locate the absorption line minimum between array data points. For long interferometers, the absorption data will be densely sampled, so noise in the measurement can lead to errors if a simple local minimum identification is used.

This calibration method has been implemented as a LabVIEW software utility designed to interface with the optical network shown in Fig. 4.5. This utility performs the following functions:

- It sweeps the Agilent 81680A tunable laser source over the range 1525–1565 nm covering the full $H^{13}CN$ absorption spectrum.
- It uses the National Instruments PCI-6115 data acquisition card and an external clock signal provided by the trigger interferometer output to sample transmission data through the $H^{13}CN$ as a function of optical frequency.

- It provides a graphical interface for a user to specify which absorption lines to use for the calibration and their approximate location in the data array using graph cursors.
- It performs a curve fit of the absorption line data in the neighborhood of the graph cursors to locate the chosen absorption lines to within a fraction of an array index.
- It uses the calculated absorption line locations to determine the separation between the chosen absorption lines to within a fraction of a fringe.
- It calculates the interferometer delay from the number of data points separating the absorption lines along with a lookup table containing the absorption line wavelengths given in Table 4.1.

The user interface of this utility is shown in Fig. 4.6. This utility was used to calibrate the trigger interferometers used in the experimental phase-sensitive SS-OCT system described in this chapter as well as the experimental SWI systems described elsewhere in this thesis. For the phase-sensitive SS-OCT system described here, the trigger interferometer yields $p = 222,918.07$ points separating the R20 and P20 lines of the $H^{13}CN$ cell. The standard deviation of repeated measurements is 0.1 points. Converting values in Table 4.1 to frequency units gives the separation $\Delta\nu_{R20,P20}$ between the R20 and P20 lines to be

$$\Delta\nu_{R20,P20} = 3.486306\,\text{THz} \pm 53\,\text{MHz}, \tag{4.9}$$

so the frequency interval of the data acquisition is

$$\frac{3.48631\,\text{THz}}{222,918.07} = 15.6394\,\text{MHz}, \tag{4.10}$$

and the interferometer delay is $\tau_t = (15.6394\,\text{MHz})^{-1} = 63.9410\,\text{ns}$. The uncertainty in this calibration is dominated by the uncertainty in the locations of the

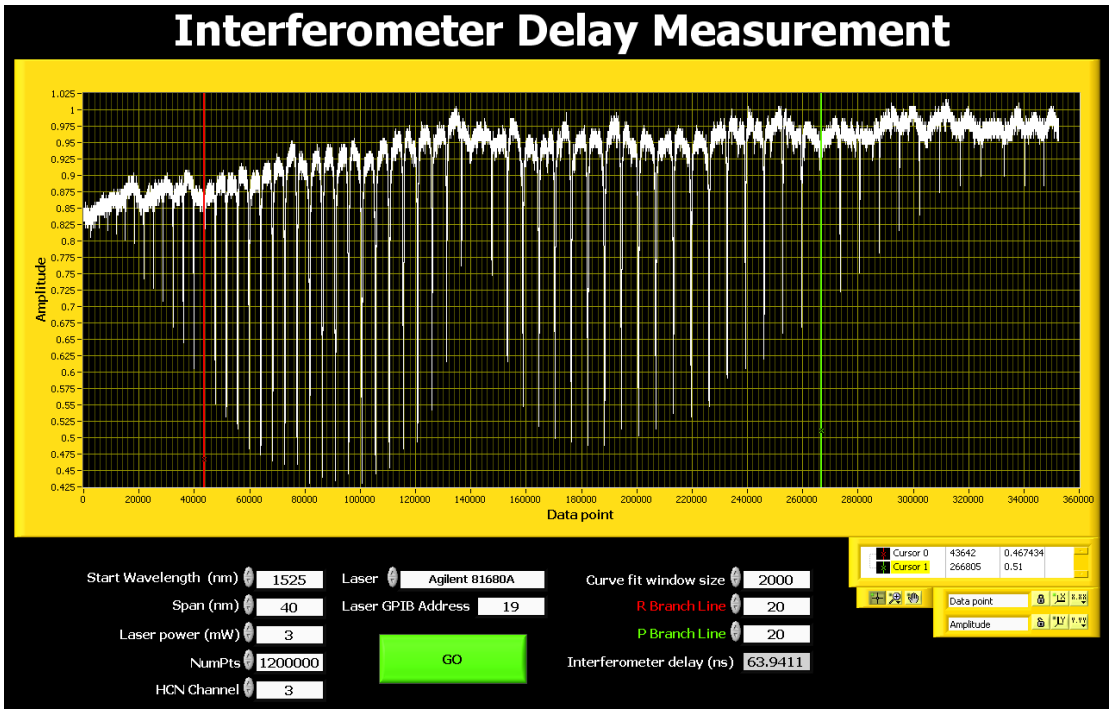

Figure 4.6: User interface for a utility implementing interferometer calibration using an $H^{13}CN$ wavelength reference artifact.

absorption lines in the $H^{13}CN$ wavelength reference. This fact is evident when the quotient rule for propagating uncertainties is applied:

$$u(\tau_t) = \tau_t \sqrt{\left(\frac{u(p)}{p}\right)^2 + \left(\frac{u(\Delta\nu_{R20,P20})}{\Delta\nu_{R20,P20}}\right)^2} \tag{4.11}$$
$$= 0.973\,\text{ps}.$$

If the uncertainty in p is neglected, $u(\tau_u)$ only drops to ± 0.972 ps. This uncertainty calculation is one specific case of the general trend illustrated by Fig. 4.2.

4.4 Results and discussion

With the trigger interferometer calibrated, I used the SS-OCT system shown in Fig. 4.4 to perform simultaneous measurements of group refractive index and physical thickness of an optical sample as an example application of highly precise

optical range measurements. The AC-coupled output of the trigger interferometer was used as an analog clock to trigger data acquisition on the polarization-diverse outputs of the measurement interferometer using the National Instruments PCI-6115 data acquisition card. Measurements were performed by sweeping the Agilent 81680A tunable laser at a nominal sweep rate of 40 nm/s over the range from 1500 to 1564.17 nm. This sweep range coupled with the frequency domain step size of $1/\Delta\tau = 15.6395$ MHz yields A-scans comprising 524,288 data points. The sample under test (SUT) was a fused silica plate with a nominal thickness of 3 mm. A reference mirror was positioned several millimeters behind the SUT. To minimize scan-to-scan drift in the position of the reference mirror, the entire system was enclosed and the test plate was mounted on a motorized translation stage so it could be inserted into and removed from the measurement path without opening the enclosure.

A-scan data acquired with the SUT present and absent are plotted in Fig. 4.7. The labeled reflection peaks in the figure correspond to the following optical interfaces: the test arm fiber end facet, located at τ_0; the front facet of the fused silica test plate at τ_1; the back of the fused silica plate at τ_2; the reference mirror when the fused silica plate is absent at τ_3; and the reference mirror when the fused silica plate is present at τ_4. Note that the physical location of the reference mirror does not change when the fused silica plate is inserted or removed, but the round trip group delay to the reference mirror changes with the introduction of the optically dense test plate.

The physical thickness L of the plate is determined from relative group delay measurements according to

$$L = \frac{c}{n_g}\frac{\tau_{21}}{2} \tag{4.12}$$

where c is the speed of light in vacuum and n_g is the group index of the SUT,

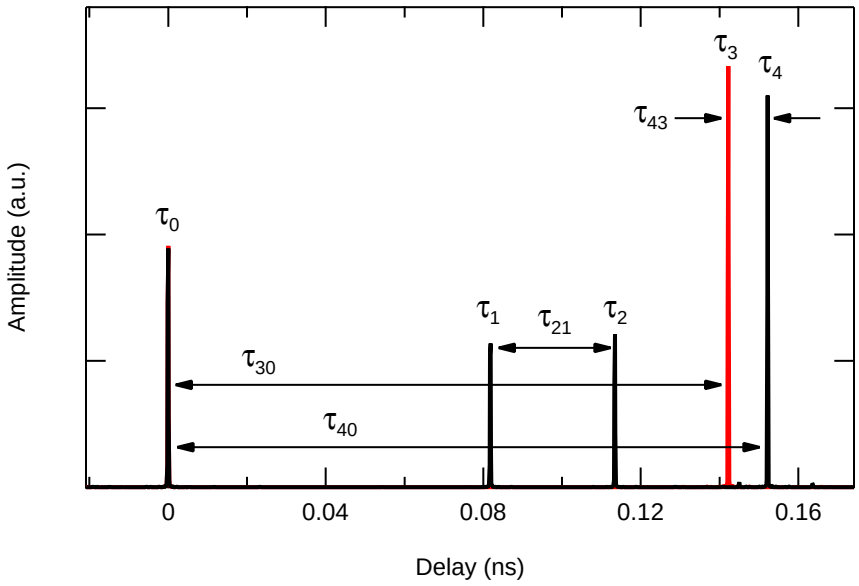

Figure 4.7: *A*-scans with (black) and without (red) the fused silica test plate in place. The reflection peaks correspond to the fiber end facet (τ_0), the front (τ_1) and rear (τ_2) of the fused silica test plate, and the reference mirror (τ_3 and τ_4). Zero delay has been defined to correspond with the fiber end facet.

which is found using

$$n_g = \frac{\tau_{21}}{\tau_{21} - \tau_{43}} n_{g,\mathrm{air}}, \tag{4.13}$$

where $\tau_{21} = \tau_2 - \tau_1$ and $\tau_{43} = \tau_4 - \tau_3$. I employed the model described by Ciddor and Hill [136, 137] to determine the group refractive index of air to be $10^6(n_{g,\mathrm{air}} - 1) = 2184 \pm 1$ at the center sweep wavelength for the atmospheric conditions present during the experiment. The details of the implementation of this model are presented in Appendix . The relevant environmental conditions present during the experiment are summarized in Table 4.2. The value of τ_{21} is found directly in a single scan, so noise due to environmental fluctuations and scan-to-scan variations in the laser sweep cancel. Determination of τ_{43} requires two *A*-scans, one with the SUT present and one without. By referencing the mirror range measurement to the reflection from the fiber end facet (τ_0 in Fig. 4.7), scan-

Table 4.2: Measured environmental parameters used to determine the group refractive index of air.

Parameter	Value	Uncertainty
Temperature	25° C	±1° C
Pressure	83.5 kPa	±0.1 kPa
Relative humidity	20%	±5%

to-scan variations largely cancel, and the measurement noise of τ_{43} approaches that of τ_{21}. This process involves calculating $\tau_{40} = \tau_4 - \tau_0$ and $\tau_{30} = \tau_3 - \tau_0$ for each scan, and then taking $\tau_{43} = \tau_{40} - \tau_{30}$.

To illustrate the level of measurement noise in each group delay measurement, plots of 50 repeated measurements of referenced and unreferenced group delays defined in Fig. 4.7 are shown in Fig. 4.8. Note that the curves for the unreferenced group delays τ_0 and τ_4 are nearly identical, with a standard deviation of 4.4 fs. This illustrates the high degree of correlation in the measurement noise between different reflection peaks within a single scan. Self-referencing removes this correlated noise, resulting in standard deviations for self-referenced group delay measurements as small as 5.2 as for τ_{21}, where the relative measurement involved two facets of a single glass plate. This group delay standard deviation value corresponds to a distance of 780 pm in air.

Using the measurement data shown in Fig. 4.8, I determined the group refractive index of the fused silica plate to be 1.462905±0.000002. The uncertainty in this measurement includes the standard deviation of τ_{21} shown in Fig. 4.8, as well as an increased uncertainty in τ_{43} due to drift in the position of the reference mirror during the process of inserting or removing the fused silica test plate. I estimated this uncertainty to be a factor of 2 greater than the standard deviation based on the repeated measurements of τ_{40} and τ_{30} shown in Fig. 4.8. Because the group index measurement is a relative measurement (apparent from Eq. (4.13)),

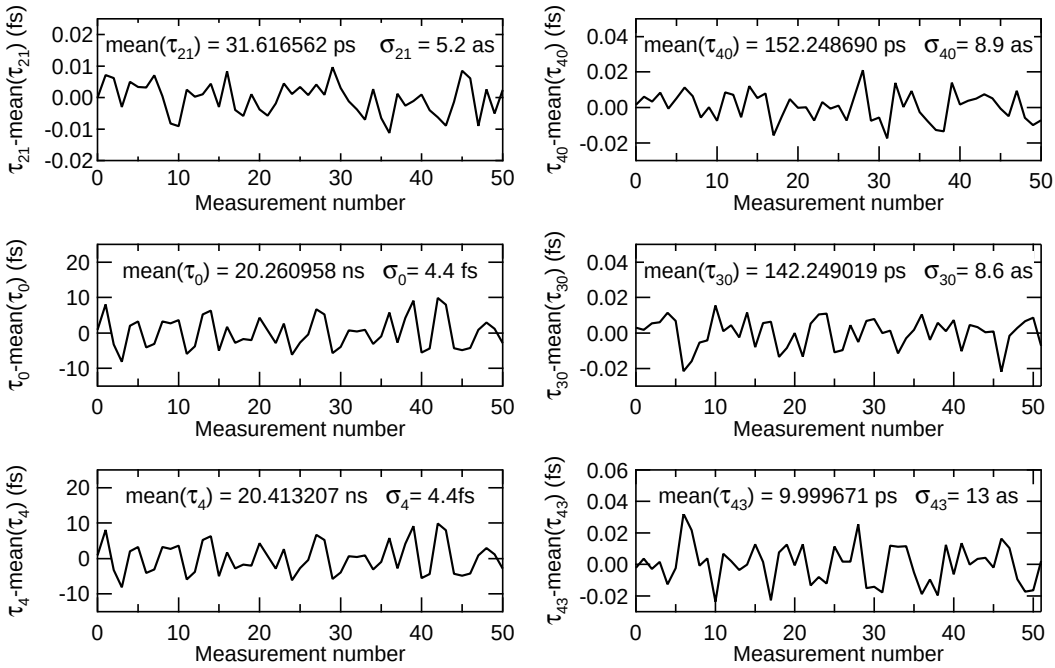

Figure 4.8: Repeated measurements of relative group delays defined in Fig. 4.7. Note that the standard deviations for the unreferenced group delays, τ_0 and τ_3 (presented in units of fs $= 10^{-15}$s), are three orders of magnitude larger than the standard deviations for the referenced group delays (presented in units of as $= 10^{-18}$s)

the value of the time domain step size falls out of the measurement and does not affect the final uncertainty.

To validate the group index measurement, I compared the measured value to a calculation of the group index of fused silica based on a temperature-dependent Sellmeier model. This model utilized Sellmeier coefficients provided by the manufacturer (Schott AG) along with an interpolated value for the thermo-optic coefficient based on data reported by Leviton and Frey [138] (see Appendix B for details of the implementation). The resulting calculated value for the group index of fused silica at the center sweep wavelength is 1.462893 ± 0.00002. The accuracy of this model is an order of magnitude less than the uncertainty of the group index measurement, and is limited by the accuracy of the Sellmeier coefficients. The

measured value for the group index of fused silica shows excellent agreement with the calculated value.

The thickness of the test plate found using Eq. (4.12) was 3.239584 mm ± 61 nm. This is in good agreement with the value of 3.240 ± 0.001mm found by measuring the thickness of the test plate using a mechanical micrometer. The uncertainty in the interferometric thickness measurement is dominated by the uncertainty in the calibration of the relative group delay of the auxiliary interferometer, which results in an uncertainty in the time domain step size of $u(\delta\tau) = 2.3\,\text{as}$. Because τ_{21} is determined by the sum of an integer number of time domain samples and an adjustment of a fraction of a sample determined by the phase slope, the total uncertainty in the absolute determination of τ_{21} is given by

$$u(\tau_{21}) = \left\{ \left[\text{int}\left(\frac{\tau_{21}}{\tau_t} N \right) u(\delta\tau) \right]^2 + \sigma_{21}^2 \right\}^{1/2}, \tag{4.14}$$

where the function int() denotes rounding to the nearest integer. For macroscopic thicknesses, the uncertainty in the time domain step size dominates, and the total uncertainty can be approximated as

$$u(\tau_{21}) \approx \frac{\tau_{21}}{\tau_t} u(\tau_t). \tag{4.15}$$

If $u(\tau_t)$ is independent of the magnitude of τ_t (as it is for the auxiliary interferometer calibration routine utilized here), Eq. 4.15 reveals that the accuracy of relative distance measurements can be improved by increasing the total time domain range of the system beyond simply that which is necessary to measure the distances of interest. The overall limitation on τ_t is generally imposed by either the coherence length of the laser or the speed capability of the data acquisition system.

While the absolute accuracy of thickness measurements is determined as described in the previous paragraph, it is worth noting that the sensitivity of

the measurement is significantly better than the overall uncertainty in τ_{21} suggests. This is because the uncertainty in the time domain step size is constant for any given set of measurements. This can be exploited for highly precise relative measurements, such as thickness variations from sample to sample or within a single sample. In this case $u(\delta\tau)$ can be ignored, and the uncertainty in the relative thickness measurement now becomes dominated by the determination of the group index. To illustrate this case, taking $u(\delta\tau) = 0$ for the experimental thickness measurement of the fused silica plate, the uncertainty is reduced to $\pm 4.5\,\mathrm{nm}$. Furthermore, for relative measurements on the same sample where the group index doesn't change, or if the group index were known exactly (for example, in a measurement of the variation in thickness of a region of vacuum between reflectors), the uncertainty is further diminished. Neglecting the group index uncertainty for the fused silica test sample results in a thickness uncertainty of $\pm 530\,\mathrm{pm}$. For monocrystalline silicon, the refractive index of 3.481 at 1550 nm would yield a thickness uncertainty of 224 pm, less than half of the crystal lattice spacing of 543 pm and comparable to the Si-Si bond length of 235 pm. These results therefore open the door to thickness profiling of macroscopic samples with single atomic monolayer resolution.

4.5 Summary and conclusions

In this chapter have presented a method for absolute ranging using phase sensitive swept-source interferometry yielding self-referenced group delay measurements with attosecond-level precision. This corresponds to sub-nanometer sensitivities for relative distance measurements. I have shown that the accuracy of absolute range measurements depends not only on the measurement noise floor, but also on accurate calibration of the time domain sampling interval. For macroscopic distance measurements, the uncertainty in this calibration dominates over

the uncertainty due to measurement noise. The contribution to the uncertainty due to the sampling calibration can be reduced by increasing the time domain range of the measurement, or equivalently by sampling on a finer grid in the frequency domain. This has important implications for practical swept-wavelength interferometry systems for performing absolute ranging, because it means that improved performance can be achieved by increasing the range of the depth measurement, even when the increased range is not required for the specific types of samples that the system is intended to image. This also provides another driver for improvements in the coherence length of high-speed swept-wavelength sources to enable these extended-range interferometers. The concepts presented and demonstrated here—phase-slope determination, self-referencing, and accurate sampling grid calibration—enable measurements of optical path length with extremely high accuracy.

Chapter 5

Optical Waveguide Arrays in Volume Photopolymers

This chapter represents somewhat of an aside from the primary thrust of this thesis, namely improvements and extensions to measurement techniques employing SWI. The work presented in this chapter, however, is in large part the motivating application for all the rest of the SWI work presented in this thesis. Volume photopolymers are material systems that enable the creation of 3D refractive index structures distributed within thick volumes of solid material. Initially developed for holographic data storage applications, these materials have been the subject of research as an integrated optics platform for only the past several years. While the volumetric nature of these materials and their associated processing technologies enable new types of optical devices, they also present a challenge for the characterization of the resulting refractive index structures. Investigations into SWI motivated by the desire to characterize volumetric index structures led to the recognition that there is still much room for extension and innovation in the field of SWI, despite the fact that first optical incarnations date back to the late 1970's and the underlying principles were used in radar systems for decades prior to that.

This chapter presents an overview of one specific application of volume pho-

topolymers that benefits from the measurement capabilities of SWI: optical waveguide array fabrication. Linear arrays of optical waveguides have long been fabricated using traditional planar lithographic methods, but 2D arrays of waveguides (with the direction of propagation representing the third dimension) are much more challenging to fabricate. This chapter begins with a discussion of the motivating applications for 2D waveguide arrays and the techniques that have been used for 2D waveguide array fabrication to date. The subsequent section presents an introduction to volume photopolymer materials, including a simplified model for the mechanism of index structure formation. Full understanding of index structure formation in volume photopolymers is an ongoing area of research, and one that will benefit from new measurement capabilities of SWI. Next, I introduce three methods of waveguide array fabrication in volume photopolymers: direct write lithography, projection lithography, and holographic lithography. Holographic lithography is the most promising approach for fabricating large, dense arrays of optical waveguides, and therefore is the subject of in-depth experimental investigation. An experimental holographic lithography system is described, and results from waveguide arrays written with this system are presented.

5.1 Introduction to optical waveguide arrays

5.1.1 Applications

Research into fabrication methods for 2D optical waveguide arrays is driven by a diverse set of applications. Perhaps the most common application of optical waveguide arrays is endoscopic imaging [139]. In recent years, 2D optical waveguide arrays have largely replaced rigid relay lens systems for endoscopic medical imaging. Most commonly, 2D optical waveguide arrays are outfitted with an objective lens that collects an image onto the input facet of the array. The array then relays the image to a camera or an eyepiece by discretely sampling the im-

age intensity at each waveguide pixel. The imaging properties of the array are largely determined by the refractive index distribution that defines the core and cladding regions of each individual waveguide. These properties include resolution, fill factor, and coupling efficiency, which is determined by the waveguide NA. Endoscopic arrays have also been used to expand the capabilities of microscopy techniques that have traditionally relied on single-point scanning, such as confocal microscopy [140, 141], OCT [142, 143], and near-field microscopy [144].

Another common application for optical waveguide arrays is for optical data channel interconnections for short-distance data communication applications, such as from board-to-board or from chip-to-chip in electronic devices [145]. A variety of free-space optical interconnection architectures have been developed, but waveguide architectures are often necessary due to mechanical constraints. The quest for higher data throughput, as well as the emergence of low-cost vertical-cavity surface-emitting laser (VCSEL) arrays, has driven research in optical waveguide interconnects beyond the capabilities of traditional planar lithographic techniques to include 2D optical waveguide arrays. Waveguide arrays for optical interconnects generally require significantly smaller total guide counts than arrays for imaging applications, with typical channel counts of 16 to 512 channels. Interconnect applications, however, present additional challenges with respect to connectorization, cost, and reliability.

A third application of optical waveguide arrays is as a medium for scientific study of wave propagation in periodic media. In recent years, arrays of coupled optical waveguides have become a fertile ground for the discovery of new physics, as well as a means for studying inaccessible physical systems by analogy [146, 147]. Light traveling in coupled waveguide arrays exhibits propagation behavior fundamentally different than in free space. For example, in homogeneous, isotropic media, propagation of optical waves is governed by the Helmholtz equation, which

results in a dispersion relation

$$k_z = (k^2 - k_x^2 - k_y^2)^{1/2} \tag{5.1}$$

that relates the magnitude and Cartesian components of the wavevector **k** to one other. The amount of beam spreading due to diffraction is determined by the curvature of the **k**-surface, which in homogeneous, isotropic media is a sphere. In contrast, optical propagation in an array of coupled waveguides is governed by coupled mode theory, which in the case of a one-dimensional (1D) array of identical waveguides yields an alternative dispersion relation [148]

$$k_z = \beta - 2k\cos(k_x d), \tag{5.2}$$

where β is the propagation constant for the fundamental mode of a single guide and d is the separation distance between waveguides. Thus discrete propagation exhibits diffraction that depends on the direction of propagation, unlike isotropic diffraction observed in free space. Discrete propagation exhibits other anomalous diffractive and refractive effects relative to continuous media as well [149]. Initially studied in 1D systems, discrete diffraction has also been observed in 2D arrays of coupled waveguides [150]. Furthermore, nonlinear behavior has been widely studied in discrete coupled-waveguide systems. Discrete solitons have been observed in both 1D [151] and 2D [152] waveguide arrays. Interest is such discrete nonlinear behavior is driven by the fact that nonlinear periodic lattices occur in a wide variety of systems, from biological molecules [153] to Bose-Einstein condensates [154], but often cannot be directly addressed and studied. Coupled nonlinear optical waveguide arrays provide an experimental platform for studying discrete nonlinear systems by analogy, where the physics of optical propagation often mimics the physics of other discrete systems. This is because the mathematics that describe coupling between optical waveguides is identical to that which describes the tunneling of a quantum mechanical particle between adjacent potential wells. This

fact has made coupled waveguide arrays a key tool for experimental explorations of quantum systems [147]. Additionally, nonlinear interactions in coupled waveguide arrays have been proposed and studied as a means for performing all-optical switching and routing of signals [155, 156].

5.1.2 Fabrication methods

2D optical waveguide arrays have been fabricated using a variety of techniques. Certain fabrication methods are often more well suited than others to meet the specific requirements for particular applications of 2D waveguide arrays. Endoscopic imaging, for example, requires long arrays on the order of 1 m, with minimal coupling among adjacent guides. For these reasons, modern endoscopes are dominated by 2D waveguide arrays based on optical fibers. These image-transmitting fiber bundles are referred to as fiber image guides (FIGs) or coherent fiber bundles, where in this context coherence refers to the consistent spatial arrangement of fibers from one end of the device to the other. This is in contrast to fiber bundles with randomly distributed cores that are used for broad area illumination rather than imaging. Fiber-based arrays are currently the only 2D waveguide array technology that can provide lengths on the order of a meter or more. Standard fiber manufacturing begins with a glass preform, which is a large, solid, composite glass cylinder that contains core and cladding regions with the same relative dimensions as the manufactured fiber [118]. The preform is heated and drawn, reducing its cross-sectional area and increasing its length by many orders of magnitude. Coherent fiber bundles are made by extending basic fiber manufacturing techniques using one of two methods. The first involves simple stacking of individual fibers to create a bundle, which is straightforward in principle, but in practice it is difficult to maintain the relative positions of each fiber throughout the length of the array. Much of the cladding of each fiber is

sometimes etched away to allow for closer packing of the guiding cores [142]. The second method is the so-called "stack-and-draw" technique [157], where primary preforms are drawn once, and then a secondary preform is made by stacking drawn segments made from the primary preforms. The secondary preform is then drawn a second time. During fabrication, steps are generally undertaken to ensure some variation from guide to guide in the array in order to suppress crosstalk between guides, though some level of crosstalk nevertheless occurs [158]. This core-to-core variation means that while coherent fiber bundles generally work well for imaging applications, they are generally not suitable as discrete media where waveguide coupling is required, though discrete diffraction has been demonstrated in a drawn fiber array [159]. The arrays can be quite high resolution, with core diameters on the order of a few μm. One disadvantage of fiber bundles is that the array layout is generally hexagonal because of the natural ordering of stacked cylindrical rods. This means that the full resolution of the array cannot be exploited when interfacing to devices the utilize square arrays, such as CCD and CMOS sensor arrays. Also, as the size of the array increases, flexibility decreases since the fiber bundle is essentially a glass rod. Dark pixels can also form when individual cores in the array break within the bundle. Commercial fiber bundles are now available with as many as 100,000 guiding cores*. In addition to imaging applications, coherent fiber bundles have also been used for establishing interconnects in optical circuit boards [160, 161] and for coupling to VCSEL arrays [162, 163].

Another method for producing 2D waveguide arrays is the extension of planar lithography to multilayer structures [164]. This approach to 2D waveguide array fabrication is primarily targeted at optical interconnect applications. The primary advantage is that it takes advantage of highly mature existing planar

*E.g., Fujikura FIGH-100-1500N Image Fiber has a nominal pixel count of 10^5 within a 1.5 mm fiber diameter.

lithography technology. Extending planar processes in depth is challenging, however, and structures are generally limited to a small number of layers.

Discrete optical propagation studies require a much higher degree of uniformity throughout the waveguide array than the other applications discussed here. This is because complete coupling of light between guides requires that all guides have a fundamental modes with identical propagation constants. In 2002 it was first suggested that 2D discrete solitons may be observed in 2D waveguide arrays formed by illuminating a photorefractive crystal with a four-beam interference pattern [165]. Experimental observation of 2D discrete solitons in such a photorefractive array was reported the following year [152]. Like volume photopolymers, photorefractive crystals respond to incident illumination with local changes in index of refraction, though the mechanism of index structure formation is different. Whereas index structure in volume photopolymers arise due to mass transit of monomer, index structures in photorefractives occur due to excitation of mobile conduction band electrons which leave behind stationary holes, resulting in a space-charge field that gives rise to refractive index variations through the electro-optic effect. Around the same time as the first demonstration of interference-based photorefractive waveguide arrays, an alternative method for forming 2D waveguide arrays in photorefractive crystals was reported. This method relies on an array of spatial solitons formed by illuminating the input facet of a photorefractive crystal with an array of incoherent spots [166]. Discrete solitons have been observed using a spatial light modulator to create a reconfigurable 2D waveguide array using this method [167]. Photorefractive waveguide arrays can be fixed permanently [168], but typically they are temporary structures that dissipate when the writing light is turned off.

Another fabrication method that provides sufficient uniformity from guide to guide for high coupling efficiency is direct write lithography in glass using fem-

tosecond laser pulses [169]. In this method, high-power laser pulses are focused into bulk glass samples causing localized damage to the glass resulting in photoinduced refractive index changes. By translating the glass sample relative to the laser beam focus, a line of increased index is drawn, forming an optical waveguide. Serializing this process allows for the creation of 2D waveguide arrays in bulk glass samples [150,170]. While direct write lithography in glass can produce highly uniform waveguide arrays with arbitrary guide configurations, the total guide count is limited because of long exposure times for large arrays associated with the serial nature of the process. Since high laser powers are required to produce the index changes, it is not generally possible to parallelize the process to fabricate multiple features at once. Also, directly written waveguide arrays are limited in length, since they require precise 3D translation stages to translate the glass sample during fabrication.

Volume lithography of photopolymers offers a promising alternative to existing waveguide array fabrications techniques. Photopolymer materials can be inexpensive, and their high sensitivity allows for large numbers of refractive index features to be written simultaneously. Because the photopolymer material begins as a liquid, it can be cast together with other components built from other material systems, yielding hybrid integrated optical systems. 2D waveguide arrays fabricated in such hybrid systems are promising candidates for robust optical interconnects. Like photorefractives, volume photopolymers can be patterned holographically, but the resulting index structures are permanent, and the photopolymer material is less costly and more robust than photorefractive crystals. The next section provides an introductory overview of these versatile optical materials, followed by a discussion of lithographic methods that can be used to fabricate 2D optical waveguide arrays.

5.2 Diffusion-mediated optical photopolymers

5.2.1 Introduction

Diffusion-mediated optical photopolymers, also referred to as volume photopolymers, are a class of materials that are an active area of research as media for holographic data storage [171] and hybrid integrated optics applications. These materials have the capability to form 3D volumetric refractive index structures through localized exposure to optical radiation. This process of index structure formation requires no thermal or wet processing [172–174]. This is in stark contrast to traditional photopolymers such as photoresists, which are used to fabricate planar structures using an optical exposure followed by material removal via solvent wash. Wet processing of this type makes photoresists inappropriate for the fabrication of 3D index structures where solvent access is impossible.

Volume photopolymers offer numerous characteristics making them an appealing choice for holographic data storage and hybrid integrated optics applications [174,175]. Because they begin as a mixture of liquid precursors, they can be cast into thick geometries or spun to form thin films. The material formulations can be engineered to have low optical absorption and scatter in the final sample following flood cure. High sensitivity allows index structures to be written using low power, continuous wave lasers. By careful chemical design, the recording process can occur with less than 0.1% polymerization shrinkage, minimizing stress and dimensional changes [174]. Index changes are comparable to inorganics at $\sim 10^{-2}$, and this can be increased at the expense of greater shrinkage.

5.2.2 Index structure formation

The volume photopolymer materials used in this work comprise two independent and compatible polymerizable systems: one forms a solid but perme-

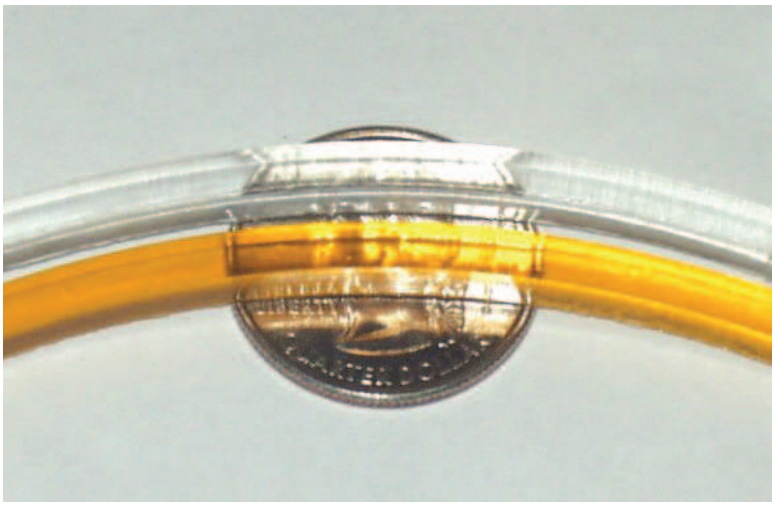

Figure 5.1: Flexible polymer "rods" of 4×4 mm cross-section on a U.S. quarter coin, fabricated by casting the liquid precursors in a slot mold. The top, clear, sample is matrix only (no writing monomer or initiator), while the bottom, colored, sample is fabricated from the complete photosensitive mixture.

able matrix polymer that provides a mechanical scaffold, and the other is made up of mobile monomers that act as refractive index "carriers" and function as the agent of refractive index structure formation. Other volume photopolymer systems achieve similar behavior through an initial partial cure of a single photopolymer, leaving an uncured fraction of the original precursors available for the formation of photoinduced index structures. Another essential component is a photoinitiator that absorbs incident optical energy and initiates polymerization. Figure 5.1 shows matrix-only and complete photosensitive samples of HDS-3000, a volume photopolymer material system manufactured by InPhase Technologies. While the exact mechanism of index structure formation in these materials is an active area of research [176–179], the predominant view is that index structures are formed primarily through diffusion of a small molecular weight species such as monomer. In preparing a volume photopolymer sample, the matrix precursors are polymerized *in situ* in the desired sample format, typically through an optical or

thermal cure. The monomers remain dissolved and unreacted until the sample undergoes localized illumination by optical radiation with a wavelength compatible with the photoinitiator absorption spectrum. Optical excitation of the photoinitiator species initiates polymerization of the monomer in the illuminated regions, while in dark regions the monomer remains unreacted. This spatially selective polymerization locally depletes the monomer concentration, leading to monomer diffusion from the surrounding volume into the illuminated regions. The result is an increased density in the illuminated regions and a corresponding increase in index of refraction. The resulting index structures may be due to increased density only, in the case where the matrix and monomer have similar refractive indices, or increased index contrast may be achieved by choosing the component chemical systems such that the monomer has a higher refractive index than the matrix. Following monomer diffusion, the index structure may be "fixed" through a flood exposure, whereby the entire sample is uniformly illuminated, bleaching all remaining photoinitiator and crosslinking all remaining monomer in place without introducing additional concentration gradients.

In order to optimize photopolymer material performance, a quantitative model of index structure formation is required to describe the functional dependence of recorded index structures on the optical irradiance pattern within the photopolymer sample. While such a model is important for all applications of volume photopolymers, it is of particular importance for hybrid integrated optics applications, where precise index structures are required to produce desired functionality in integrated optical components. Examples of such applications include engineered waveguide dispersion for dispersion-managed waveguides and adiabatic guided mode conversion in tapered waveguides. While holographic applications would also benefit from a detailed understanding of index structure formation, holography in volume photopolymers is generally performed in the Bragg regime,

so nonlinearities in the recording process lead to higher harmonics that are not Bragg-matched during readout. This means that nonlinearities result in an overall decrease in dynamic range, but do not generally affect the achievable fidelity of the readout process. Also, because holography has been the dominant application for volume photopolymers, the existing models have been developed within the context of holographic exposures and tested using measurements of diffraction efficiency rather than direct measurement of the index contrast. This is largely due to the fact that techniques for directly measuring the precise shape of micron-scale, volumetric index structures have not been available. Integrated optics applications for volume photopolymers are now driving the development of quantitative, spatially resolved index measurement techniques. Quantitative index measurement using SS-OCT is one such measurement technique. The quantitative index contrast measurements enabled by this technique hold the potential to help develop and verify detailed models of index structure formation, taking into account chemical, optical, environmental, and process variables to yield a robust exposure process design tool for precise index structure fabrication.

I will now present an example of a simplified model of index structure formation in volume photopolymers that could be expanded with the help of direct index contrast measurements. This model assumes that the resulting index contrast is proportional to the amount of polymer formed through local illumination, or, equivalently, the amount of monomer consumed. It is presented in the context of radical-initiated chain photopolymerization [180], though the simple rate-equation approach can be applied to other initiation mechanisms, such as cationic initiation, as well.

When a volume photopolymer sample is illuminated, the first step in the resulting radical chain polymerization process is the dissociation of an initiator

molecule I to form a pair of radicals $R\bullet$:

$$I \rightarrow 2R\bullet. \tag{5.3}$$

The second step in the initiation process is for the primary radical $R\bullet$ to react with a monomer molecule M to produce a chain initiating radical $M\bullet$, according to

$$R\bullet + M \rightarrow M_1\bullet, \tag{5.4}$$

where the subscript indicates the number of monomer units. Polymerization then proceeds via chain growth with successive addition of monomer units, which can be generally expressed as

$$M_n\bullet + M \rightarrow M_{n+1}\bullet. \tag{5.5}$$

The polymerization reaction propagates according to Eq. (5.5) until the reaction terminates, which can occur by one of several mechanisms. Two polymer chains can terminate each other by coupling, resulting in a single "dead polymer" chain, or two chains can terminate by the process of disproportionation resulting in two unlinked dead polymer chains. Both of these mechanisms are examples of bimolecular termination, whereby two radical centers annihilate one another. An alternative termination pathway is unimolecular termination, where the propagating radical center is terminated by a species that acts as an inhibitor or retarder of the polymerization reaction. The kinetics of bimolecular versus unimolecular termination yield very different relationships between index contrast and irradiance. To see that this is the case, consider the rates at which the initiation, polymerization, and termination steps occur. For initiation via photo-dissociation of initiator molecules, the initiation rate $\mathcal{R}_i$ will be given by

$$\mathcal{R}_i = 2\varphi\mathcal{I}_0, \tag{5.6}$$

where $\mathcal{I}_0$ is proportional to the irradiance in the case of monochromatic illumination, and describes the incident optical radiation in units of photons per second

per volume. The parameter φ is the quantum yield, i.e., the number of initiated polymer chains per photon. The factor of 2 indicates that each cleaved photoinitiator molecule produces a pair of radicals. The polymerization step involves the reaction of a monomer molecule with a radical center, and as such the polymerization rate $\mathcal{R}_p$ will be proportional to the concentrations of radicals and monomer:

$$\mathcal{R}_p = \kappa_p[M\bullet][M], \tag{5.7}$$

where κ_p is the kinetic rate constant of the polymerization reaction, $[M\bullet]$ is the radical concentration, and $[M]$ is the monomer concentration. For the case of bimolecular radical termination, where each termination event involves two propagating radical centers, the termination rate $\mathcal{R}_t$ is

$$\mathcal{R}_t = 2\kappa_t[M\bullet]^2, \tag{5.8}$$

where κ_t is the kinetic rate constant for termination. In the steady state where the concentration of radicals is assumed to be constant, the initiation rate equals the termination rate. This results in a radical concentration given by

$$[M\bullet] = \left(\frac{\varphi\mathcal{I}_0}{\kappa_t}\right)^{1/2}, \tag{5.9}$$

and the overall polymerization rate is

$$\mathcal{R}_p = \kappa_p[M]\left(\frac{\varphi\mathcal{I}_0}{\kappa_t}\right)^{1/2}. \tag{5.10}$$

Thus the polymerization rate is proportional to the square root of the incident irradiance for the case of bimolecular termination. For unimolecular termination, on the other hand, the termination rate is given by

$$\mathcal{R}_t = \kappa_z[M\bullet][Z], \tag{5.11}$$

where $[Z]$ is the concentration of the inhibiting species and κ_z is the kinetic constant for the inhibition reaction. In this case, the steady state solution yields

$$[M\bullet] = \frac{2\varphi}{\kappa_z[Z]}\mathcal{I}_0, \tag{5.12}$$

and the polymerization rate is

$$\mathcal{R}_p = \frac{2\kappa_p[M]\varphi\mathcal{I}_0}{\kappa_z[Z]}. \tag{5.13}$$

So in the case where the dominant termination pathway is unimolecular, the polymerization rate is directly proportional to the incident irradiance. In both of the aforementioned cases, the assumptions of a constant polymerization rate and a resulting index contrast proportional to monomer consumption lead to an index contrast δn given by

$$\delta n \propto \mathcal{R}_p T, \tag{5.14}$$

where T is the duration of the optical exposure. Thus, for the case of bimolecular termination,

$$\delta n = C_2 \mathcal{I}_0^{1/2} T, \tag{5.15}$$

where C_2 is a constant of proportionality that depends on κ_p, κ_t, $[M]$, and φ, while for unimolecular termination

$$\delta n = C_1 \mathcal{I}_0^{1/2} T, \tag{5.16}$$

where C_1 depends on κ_p, κ_z, $[M]$, $[Z]$, and φ. This difference in the functional dependence of the index contrast on the incident irradiance has a deep impact on the fabrication of index structures in volume photopolymers. To illustrate this effect, consider two potential optical exposure methods: (1) flash exposure of an isolated voxel via a focused laser beam, and (2) exposure by an interference pattern formed by two plane waves. Figure 5.2(A) shows an xz irradiance cross section of a focused Gaussian beam propagating in the z direction. For a polymer system with purely unimolecular termination, exposing polymer sample with this pattern would result in an index structure with precisely the same shape. For a sample exhibiting purely bimolecular termination on the other hand, exposure with the focused Gaussian beam would yield an index structure with a shape like

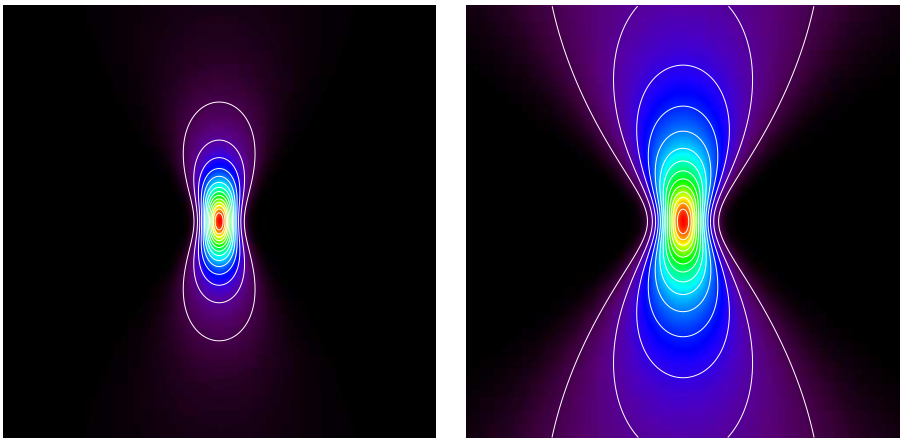

(A) (B)

Figure 5.2: (A) A cross section parallel to the optical axis of the normalized irradiance of a focused Gaussian beam. (B) The normalized square root of the irradiance pattern shown in (A). Both plots contain 14 equally distributed contour lines.

the square root of the Gaussian irradiance pattern. An xz cross section of this structure is shown in Fig. 5.2(B). From this plot, it is apparent that the square root dependence of index contrast on irradiance leads to significantly reduced localization of the photoinduced index change relative to a linear response. The largest impact is in the direction parallel to the propagation axis of the Gaussian beam, where the irradiance fall-off is quadratic rather than exponential, as it is in the transverse directions.

Figure 5.3 illustrates the difference in resulting index structures between polymer systems with different termination kinetics for a plane wave holographic exposure. Whereas the linear kinetics of unimolecular termination leads to a reproduction of the cosine irradiance pattern, bimolecular termination leads to a sub-linear material response, broadening the peaks and narrowing the valleys of the periodic pattern.

In general, a photopolymerization reaction will include both bimolecular and unimolecular pathways. A common approximation to describe this general

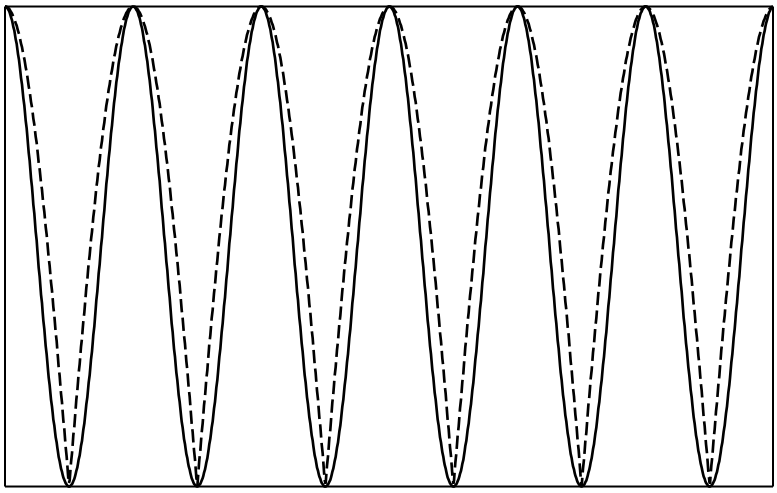

Figure 5.3: Normalized raised cosines to the first (solid) and one-half (dashed) power, illustrating the broadening of peaks and narrowing of valleys for the case of the square root.

case is to model the polymerization rate as depending on the incident irradiance raise to a power α, which takes on a value between 0.5 and 1. While this model is qualitatively useful for understanding photopolymer behavior, it rests on numerous assumptions that may not be valid for all exposure conditions. These assumptions include the steady-state assumption of constant radical concentration, non-depletion of molecular species such as the monomer M and termination agent Z, uniform irradiance throughout the polymer volume, a lack of other species or intermediate states that absorb incident photons, and reaction rate constants that are truly constant and don't, for example, change with increased temperature due an exothermic polymerization reaction. Violations of these and other assumptions can lead to values of α that are less than 0.5 or greater than 1. For designing integrated optical devices using volume photopolymers, a more complete model of index structure formation would allow more reliable design and fabrication processes to produce the precise index structures that are required. Development

of more sophisticated models requires the ability to measure quantitative index contrasts in order to test the validity of the model for specific experimental conditions. The SS-OCT system presented in Ch. 6 is one approach to provide the needed quantitative index contrast measurements.

Among the applications for volume photopolymers, optical waveguide arrays in particular are interesting for multiple reasons. First, they are an active area of research driven by application needs as described in the preceding section. The high sensitivity and mechanical flexibility of volume photopolymers, along with their ability to be cast into hybrid systems, offers unique capabilities to produce high-channel-count arrays that can be integrated with other optical components to form useful systems. Additionally, 2D waveguide arrays provide an ideal test target for developing methods for quantitative index contrast measurements needed for further research into photopolymer material models. The feature sizes in optical waveguide arrays are on the order of a few to a few tens of microns, which is the size regime relevant to integrated optics applications. But unlike isolated waveguides, 2D arrays are broad area structures that are easy to locate within large material volumes. The following sections discuss the variety of lithographic methods that can be used to create optical waveguide arrays in volume photopolymers.

5.3 Direct-write lithography

Direct-write lithography is the method of producing physical features by spatially addressing a photosensitive material one point at a time using a focused laser beam. This technique has been widely employed for writing refractive index structures in bulk glasses using high-energy-density femtosecond laser pulses [181]. Direct-write lithography has also been demonstrated as a promising approach for producing hybrid integrated optical circuits [175, 182] and polymer waveguides

for optical interconnect applications [183] using volume photopolymer materials. Because of the high sensitivity of volume photopolymers, high-power mode-locked lasers are not required to produce index structures as they are in glass and exposure can be accomplished using low-power continuous wave (cw) lasers. Also, because of the high sensitivity and low-order kinetics of volume photopolymers, direct-write lithography in photopolymers can produce index structures that in some cases are quite different than those that can be achieved with direct-write lithography in glass. For example, the approach has been used to fabricate gradient index lenses and lens arrays [184] in volume photopolymers, whereas direct-write lithography in glass requires highly focused beams to achieve the necessary energy density to produce index features, and thus cannot be used to create broad-area index structures. Other optical devices structures that can take advantage of the low-order kinetics of volume photopolymers are tapered waveguides [185] and low-loss waveguide bends [186].

5.3.1 Direct-write geometries

Optical waveguide fabrication via direct-write lithography can utilize either of two primary writing geometries: perpendicular or parallel. The distinction between the two is based on the direction of material translation relative to the optical axis of the writing beam, as shown in Fig. 5.4. Both approaches have advantages and limitations in terms of waveguide properties and geometries that can be achieved. The perpendicular writing geometry has no intrinsic limitation on the length of the waveguides that can be fabricated, and it can be used to make complete optical connections by "drawing" waveguides between independent points within the sample volume, such as the input or output facets of embedded micro-optic components. The major drawback of the perpendicular geometry for fabricating optical waveguides, especially in the context of volume photopolymers

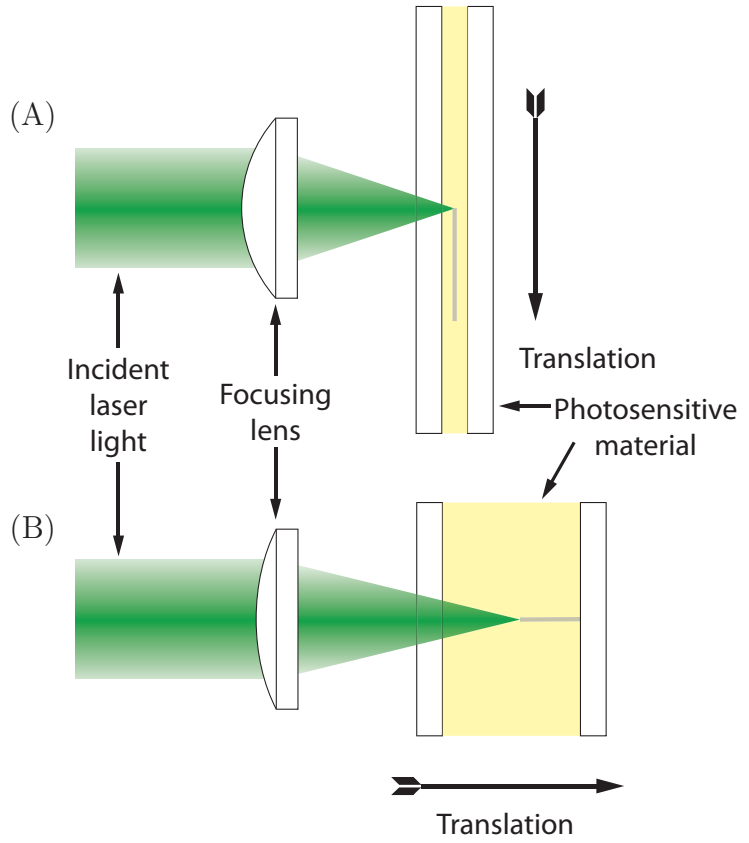

Figure 5.4: Writing geometries for direct-write lithography. (A) Perpendicular writing. (B) Parallel writing.

with linear or sub-linear index responses, is the high degree of ellipticity of the resulting index structures (see Fig. 5.2) and their corresponding optical modes [187]. This ellipticity arises due to the fact that the Raleigh range z_0 of a focused Gaussian beam, which essentially defines the axial extent of the spatially localized optical power distribution at the focus, is given by [188]

$$z_0 = \frac{\pi n w_0^2}{\lambda_0}, \tag{5.17}$$

where w_0 is the beam waist, λ_0 is the free-space wavelength, and n is the refractive index of the medium. Depending on the specific material response characteristics and exposure geometry, the size of the beam waist will typically be chosen to be approximately equal to the transverse size of the desired index structure. The

required waveguide size is determined by the desired modal properties of the waveguides and the achievable index contrast of the polymer material. To get an order-of-magnitude estimate of waveguide size, the normalized frequency, or V-number, is a useful parameter to consider. The V-number is defined as [118]

$$V = l\frac{2\pi}{\lambda_0}(n_2^2 - n_1^2)^{1/2} \tag{5.18}$$

$$\approx l\frac{2\pi}{\lambda_0}(2n_1\,\Delta n)^{1/2} \tag{5.19}$$

where l is the width of the waveguide, n_1 is the cladding or background material index, n_2 is the peak refractive index of the waveguide core, and $\Delta n = n_2 - n_1$. A waveguide will support a single mode for $V \sim 1$, and become increasingly multimode for larger values of V. The exact value of V that represents the single mode cutoff condition depends on the specific cross-sectional index distribution of the waveguide. For example, for a cylindrical step-index waveguide cross-section, the single-mode cutoff condition is $V < 2.405$. For a 1D "$1/\cosh^2$" index profile described by

$$n(x) = n_1 + \frac{\Delta n}{\cosh^2(2x/l)}, \tag{5.20}$$

the single-mode condition is $V < 4.899$ [189]. Thus, considering that typical index contrasts available in volume photopolymers are on the order of 10^{-3} to 10^{-2}, and assuming that the waveguides fabricated by direct-write lithography in volume photopolymers are designed for a V-number of a few at visible or near-infrared wavelengths yielding single- or few-moded operation, the required spatial scales are on the order of a few to a few tens of microns.

In a perpendicular writing geometry, this spatial scale is straightforwardly achieved in the transverse dimension determined by the waist of the focused beam, but in the orthogonal cross-sectional dimension the waveguide size is determined by the Rayleigh range of the beam, which can be much larger. For example, exposure using 532 nm light focused to a waist of 2.5 μm results in a Rayleigh range

that is over 50 μm in extent. This problem can be overcome for femtosecond direct writing in glass through the use of beam shaping methods [190], but adequate beam shaping is much more challenging in materials with a linear or sublinear response. Using a higher numerical aperture (NA) focusing optic decreases the amount of asymmetry but does not eliminate it, and it yields transverse waveguide dimensions that are too small for good mode confinement given the available index contrasts that are typically achievable in volume photopolymers. Also, increasing the NA also generally involves sacrificing working distance, which decreases the depth of the addressable sample volume for fabricating 3D structures.

The parallel writing geometry has the benefit of intrinsically producing symmetric waveguide profiles with a cross-sectional radius that roughly matches the writing beam waist. A drawback is that the parallel geometry cannot be used to form a waveguide interconnect between two distinct surfaces in a single sample. Also, for most sample geometries, the length of the resulting waveguides are limited by the working distance of the writing lens. Unlike the perpendicular writing geometry, where the entire waveguide length can be written at a constant depth in the material, the parallel write geometry requires varying transmission depths throughout the writing process. Since the photoactivation process of the initiator requires optical absorption, this means that the irradiance reaching the focus will vary during the writing process if steps are not undertaken to equalize the optical dose at different writing depths. This equalization process can include, for example, varying the laser power or the translation speed of the polymer sample during writing.

5.3.2 Sensitivity variation and precure

The preceding discussion was primarily focused on the fabrication of single waveguides, but an additional problem arises when considering sequential direct

write lithography of dense waveguide arrays. This problem is that the material response can change between exposures. One common mechanism for this change in material sensitivity is the consumption of an inhibiting chemical species. Atmospheric oxygen acts as an inhibitor for many radical chain polymerization reactions, and because volume photopolymers are designed to be permeable on the molecular level to allow monomer diffusion to form refractive index structures, oxygen is also free to diffuse into photopolymer samples if the utmost care isn't taken to eliminate its presence. The existence of oxygen within a photopolymer sample will reduce the material sensitivity until the oxygen is consumed by cleaved photoinitiator radicals. Once the oxygen has been exhausted, it can be replenished by diffusion if the sample is open to the atmosphere, but this process can take a significant amount of time depending on the distance that the atmospheric oxygen must traverse. The result is a transient period of inhibition during early exposures leading to a low level of material sensitivity, followed by increasing sensitivity as the inhibitor is consumed. This means that for sequentially written waveguides, the index contrast resulting from early exposures can be significantly smaller than the contrast arising from later exposures. This effect is illustrated in Fig. 5.5 for two sets of sequential exposures using direct-write lithography into 1 mm HDS 3000 coupons. Figure 5.5(A) shows a hexagonal arrangement of six waveguide exposures produced using the parallel writing geometry of Fig. 5.4(B), while Fig. 5.5(B) shows two hexagonal rings totalling 18 exposures. The images were taken using a differential interference contrast (DIC) microscope resulting in an image contrast roughly proportional to the gradient of the refractive index [191]. From these images, it is clear that sequential writing of individual waveguides leads to substantial nonuniformity among the guides.

One way to mitigate the problem of transient inhibition is to consume some or all of the inhibiting species using a short uniform exposure prior to any litho-

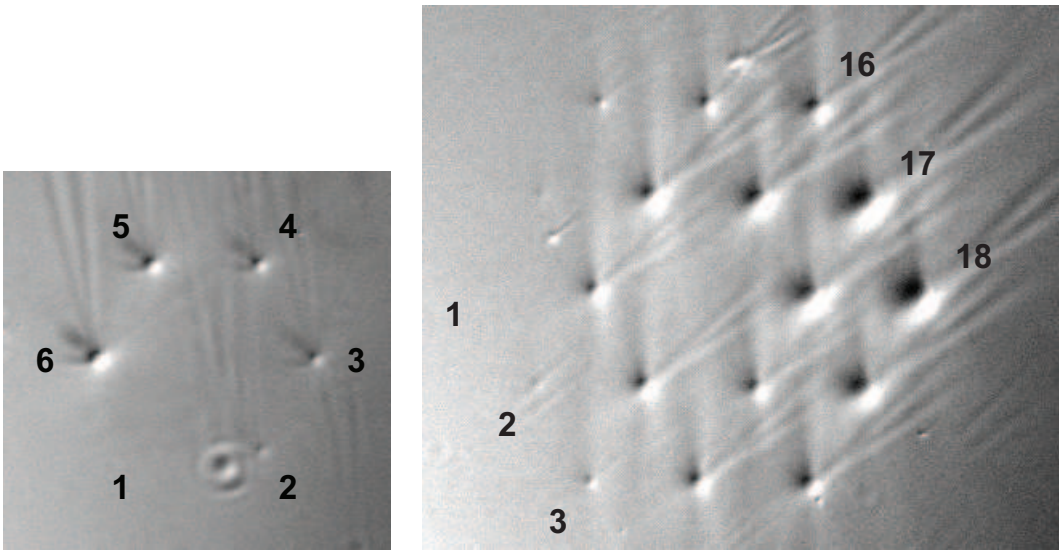

(A) (B)

Figure 5.5: Phase contrast microscope images of sequential direct-write lithography exposures in 1 mm-thick photopolymer. (A) A single hexagonal ring of waveguide exposures with the exposure sequence indicated. (B) A double hexagonal ring of waveguide exposures with the exposure sequence indicated.

graphic exposures intended to produce index structures. This type of precure can work well for thin samples where it is relatively straightforward to provide the entire sample volume with a uniform flood exposure. Waveguide array fabrication often has the additional complication of requiring thick polymer samples, where the smallest linear dimension may be a cm or more. For such thick samples, a uniform precure exposure does not provide the entire volume with a uniform energy dose because of material absorption. Small-signal absorption in photopolymers follows the Beer-Lambert law, which states that the optical power P propagating in an absorbing medium will decrease exponentially with distance:

$$P(z) = P_0 e^{-az}, \tag{5.21}$$

where a is the absorption coefficient and P_0 is an initial power value. Since the precure is meant to only consume inhibitor and maintain material sensitivity, the

small signal assumption is generally valid. For longer exposures (or higher energy doses) the photoinitiator will bleach, resulting in a time- or dose-dependent absorption coefficient. For InPhase HDS 3000 photopolymer material with half the standard initiator concentration, the absorption coefficient was measured to be $0.0908\,\mathrm{mm}^{-1}$ by measuring the transmission through a sample with a standard photoinitiator concentration but without writing monomer. Transmission measurements for the full formulation are difficult due to rapid index structure formation, which rapidly begins to diffract incident light so that it is difficult to collect on a detector. This value represents the initial absorption; bleaching of the photoinitiator causes the absorption to decrease over the course of an exposure.

The effect of absorption on the precure exposure distribution in the sample can be straightforwardly modeled by summing exponentially decaying irradiance distributions that represent illumination of the sample from different directions. The ability to provide a uniform precure exposure throughout the sample volume depends greatly on the sample form factor, as well as the material absorption. A convenient form factor for the thick polymer samples required for waveguide array fabrication is a $1 \times 1 \times 3\,\mathrm{cm}$ fluorimetry cell. The geometry of such a cell along with a reference coordinate system is illustrated in Fig. 5.6(A). If this cell is filled with HDS 3000 photopolymer material and subjected to a precure exposure where the sample is illuminated with uniform, incoherent radiation from the $\pm x$ and $\pm y$ directions, then a yz cross section of the resulting precure dose will be that shown in Fig. 5.6(B). This plot indicates that the center of the sample receives nearly 10% less energy than the outer corners, which receive the highest dose.

It is possible to make the distribution of optical energy more uniform throughout the volume by spatially apodizing the precure illumination. A Gaussian apodization along the z direction for light incident from the $\pm y$ directions, and along the y direction for light incident from the $\pm z$ directions, is sufficient to

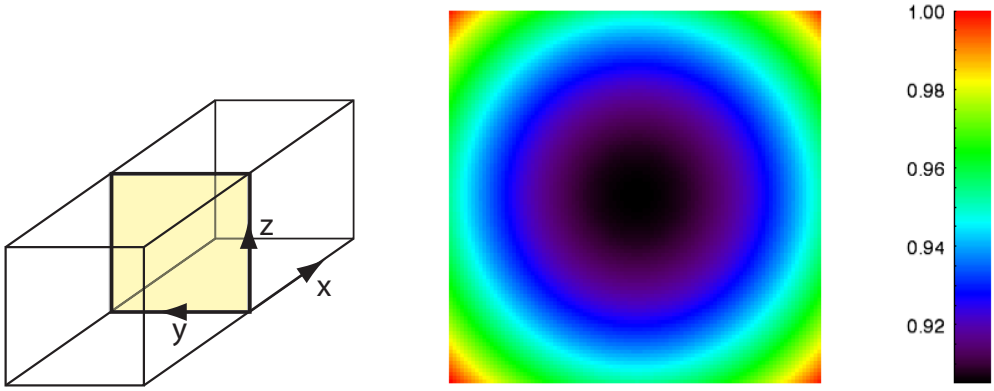

(A) (B)

Figure 5.6: (A) The geometry of a $1 \times 1 \times 3\,\text{cm}$ fluorimetry cell used for volume photopolymer sample preparation. (B) Cross section of the normalized optical energy dose along the yz plane defined in (A) for a uniform optical exposure incident along the $\pm y$ and $\pm z$ directions.

make the dose uniform to better than 1% throughout the usable sample volume, as shown in Fig. 5.7. The size of the optimal Gaussian intensity profile depends on the amount of absorption in the material. For HDS 3000, the optimal Gaussian profile has a $1/e$ half-width equal to 1.50 cm for a $1\,\text{cm}^2$ fluorimetry cell. If the absorption is increased to $0.1\,\text{mm}^{-1}$, for example, the width of the optimal Gaussian profile is reduced to 1.35 cm.

5.3.3 Other considerations for directly written waveguide arrays

Another important consideration for writing dense arrays of waveguides using sequential direct-write lithography is the accumulation of out-of-focus optical exposure to the sample volume. This problem exists for projection lithography as well, and will be treated in more detail in the following section.

Lastly, a major factor driving the consideration of alternatives to direct-write lithography for waveguide array fabrication in volume photopolymers is the overall exposure time. For sequential waveguide writing, the total exposure time scales linearly with the number of guides in the array. For applications that re-

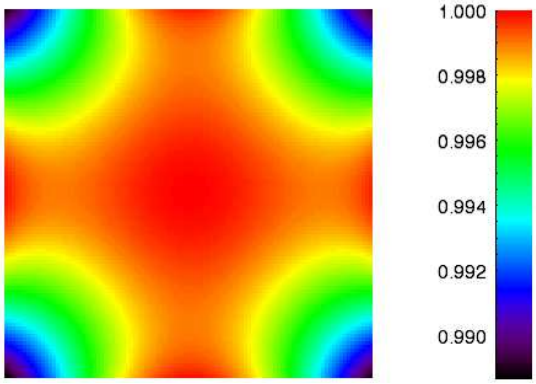

Figure 5.7: Distribution of equalized precure dose by Gaussian apodization of the illumination. The plot geometry is identical to Fig. 5.6.

quire 2D arrays of waveguides, the number of guides can lead to inconveniently long exposure times. For example, if megapixel-level resolution is desired for an imaging waveguide array where the required exposure time is 1 s per guide, the total fabrication time would be greater than 11.5 days. The fact that index structures can be fabricated in volume photopolymers using low optical power densities allows for the use of alternate exposure methods for broad area index structures. Two potential means for broad-area exposure are projection lithography and holographic lithography.

5.4 Projection lithography

5.4.1 Introduction

Because the typical optical power required to write a solitary index structure in a volume photopolymer material can be on the order of 10^{-6} W [175], a single, moderate-power cw laser can be used to simultaneously write a large number of distinct index features. Projection lithography, which uses full-field patterned illumination to perform the optical exposure, is one method that exploits the sensitivity of volume photopolymers to create potentially large numbers of index

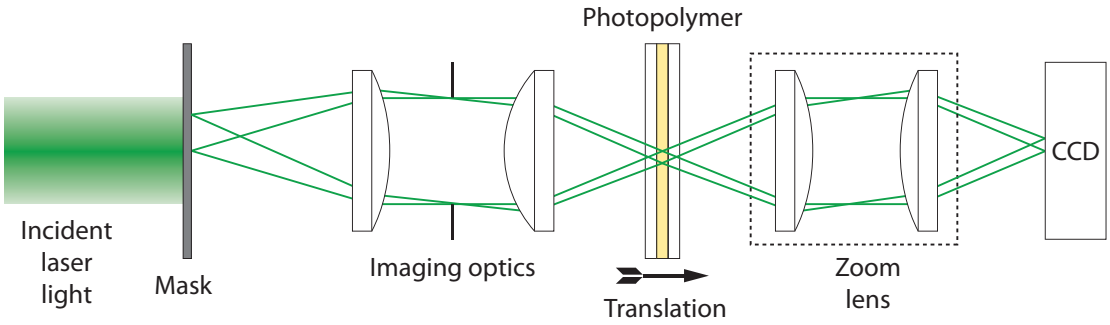

Figure 5.8: A projection lithography system for use with volume photopolymer materials.

structures in parallel. The approach is similar to mask-based lithography used for patterning photoresists in traditional semiconductor processing, but instead of exposing a single, planar layer, volume structures are created by moving a thick photopolymer sample through a broad-area irradiance distribution, such as a conjugate image plane of an amplitude mask.

5.4.2 Proof of principle

An example of a basic projection lithography system for producing relatively short waveguide arrays in volume photopolymer is shown in Fig. 5.8. This system was used to establish proof-of-principle fabrication of index structure arrays using mask projection to expose InPhase HDS 3000 photopolymer material. This material is designed for exposure using 532 nm light. The source is a diode-pumped Nd:YAG laser that is frequency doubled to produce 532 nm output. The spatially filtered and collimated output beam illuminates a chrome-on-glass mask. The mask has an array of holes arranged to match the desired waveguide array distribution. The mask is then imaged into the photopolymer material, and the material is translated through the exposure region. The depth of material and the overall length of the waveguide array is limited by both the working distance of the projection optics, and their ability to create a high-quality image at

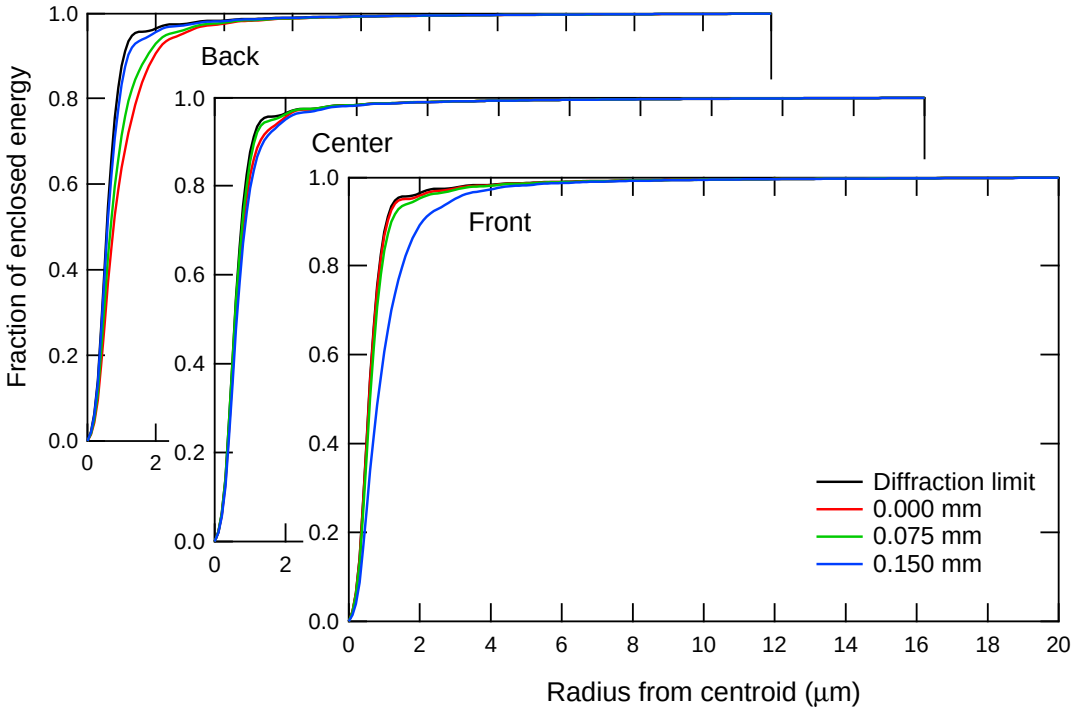

Figure 5.9: Zemax calculations of encircled energy as a function of radius from the centroid for imaging depths of 1 mm (front), 1.5 mm (center), and 2 mm (back), compared to diffraction limited performance for image space field points on axis as well as 75 μm and 150 μm off axis.

varying material depths. This can be a challenge since the amount of spherical aberration present in the system changes for differing material depths. Nearly diffraction-limited image quality can be achieved over a depth range variation of 1 to 2 mm at an NA of 0.25 over a 300 μm field through the use of commercial off-the-shelf molded aspheric optics, as shown in Fig. 5.9. This figure shows the expected performance of the optics used in the proof-of-principle system calculated using Zemax[†] optical system modeling software. This optical system used a combination of two aspheric lenses with focal lengths of 11 mm and 4 mm (Geltech 350220 and 350340, respectively) in order to project an image of the mask into the photopolymer material with 2.75× demagnification. The photopolymer

[†]Zemax is a trademark of Zemax Development Corporation.

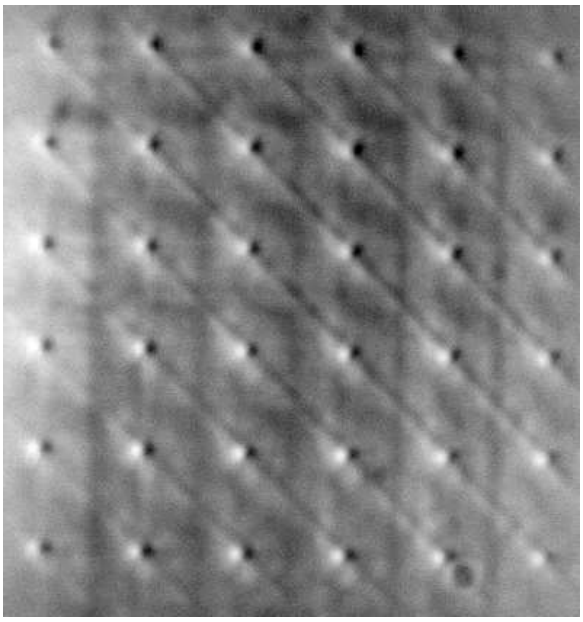

Figure 5.10: A phase-contrast micrograph of an array of index structures formed by projection lithography into a 1 mm-thick sample of volume photopolymer. Artifacts due to coherent interference of out-of-focus exposure are apparent.

was packaged as a 1 mm-thick layer between two 1 mm glass substrates. Both the glass and the polymer have a bulk index of refraction of approximately 1.5, so the polymer region corresponds to imaging depths of 1 to 2 mm within the total volume defined by the combined polymer and glass sample. The exposure requires a physical translation of the sample by 0.66 mm to move the focus from the rear polymer/glass interface to the front polymer/glass interface. To ensure that the image of the mask is in focus at the desired axial location relative to the polymer sample, relay optics are employed to reimage the spot array pattern onto a CCD camera.

The result of an exposure using this system is shown in Fig. 5.10. For this exposure, the incident laser power on the mask was 12.0 mW. The beam was collimated and oversized so that entire mask region experienced relatively constant incident irradiance. The mask was a 10×10 square array of 6.4 μm holes

with a center-to-center separation distance of 67 μm. Initially, prior to opening a shutter and exposing the sample to the laser light, the polymer sample was positioned such that the image plane was at the back glass/air interface. Computer control was used to simultaneously open the shutter and begin moving the sample along the optical axis in the direction away from the projection optics using a motorized translation stage. The polymer sample moved at a rate of 0.1 mm/s for a distance of 2.0 mm. This ensured that the image plane began completely outside of the polymer material, completely traversed the material, and ended completely outside of the material again. The result shown in Fig. 5.10 was taken with a DIC microscope using the entire 1 mm polymer sample and glass substrates. The apparent diagonal lines in this image are due to coherent interference between the individual beamlets that form each individual array component. At the focal plane they do not overlap, but the polymer sample is also translated through out-of-focus regions where pattern components overlap and interfere, leading to artifacts in the recorded index structure. This image demonstrates the ability of projection lithography to create arrays of index structures in volume photopolymer materials.

The projection lithography approach has several advantageous features. As mentioned already, it allows the exposure of multiple index structures simultaneously, speeding the fabrication process relative to direct-write lithography and avoiding difficulties associated with changing material sensitivity. Also, the waveguide array geometry can be arbitrarily selected through the design of the mask. This can include regular or irregular arrays, as well as arbitrary guide sizes and spacings. It is also possible to modify the exposure conditions during the exposure itself, both through changes in laser power and sample translation velocity as in direct-write lithography, as well as by manipulating the mask. For example, in principle one could fabricate in image-inverting waveguide array by rotating the

mask by 180° as the polymer sample is translated, though this would require a depth range longer than the 1 mm capability of the system described here because of the limited bend radius of the waveguides.

The proof-of-principle projection lithography system as described here has several limitations that can be improved upon. First, the use of a transmission mask with a 2D array of holes and a 10% duty cycle in each dimension means that at least 99% of the laser power is wasted. For waveguide arrays with a small total guide count this can be tolerated, but for larger arrays the available laser power will limit the total number of guides that can be written simultaneously. An alternative approach to an amplitude mask is to use a phase mask that produces the desired illumination pattern in the far field via diffraction, such as a lenslet array or computer generated hologram (CGH). Another severe limitation of this system is the $\sim$1 mm depth range, imposed by both the variable spherical abberation that occurs due to sample translation, as well as the limited working distance of the projection optics. The projection optics also limit the minimum guide size and the spatial extent of the resulting array due to the fact that the variable spherical aberration can be compensated only for a limited NA and over a limited field.

The problems associated with variable spherical abberation can be overcome through a more sophisticated optical design. One approach would be to include a second element with variable spherical aberration in the optical train to actively compensate for the aberration variation during sample translation. A second approach is to enable polymer translation without changing the overall depth of material between the projection optics and the exposure plane. The latter approach also holds the potential to eliminate the depth range limitation imposed by the working distance of the projection optics by taking advantage of the mechanical flexibility of volume photopolymer materials. A diagram of a system

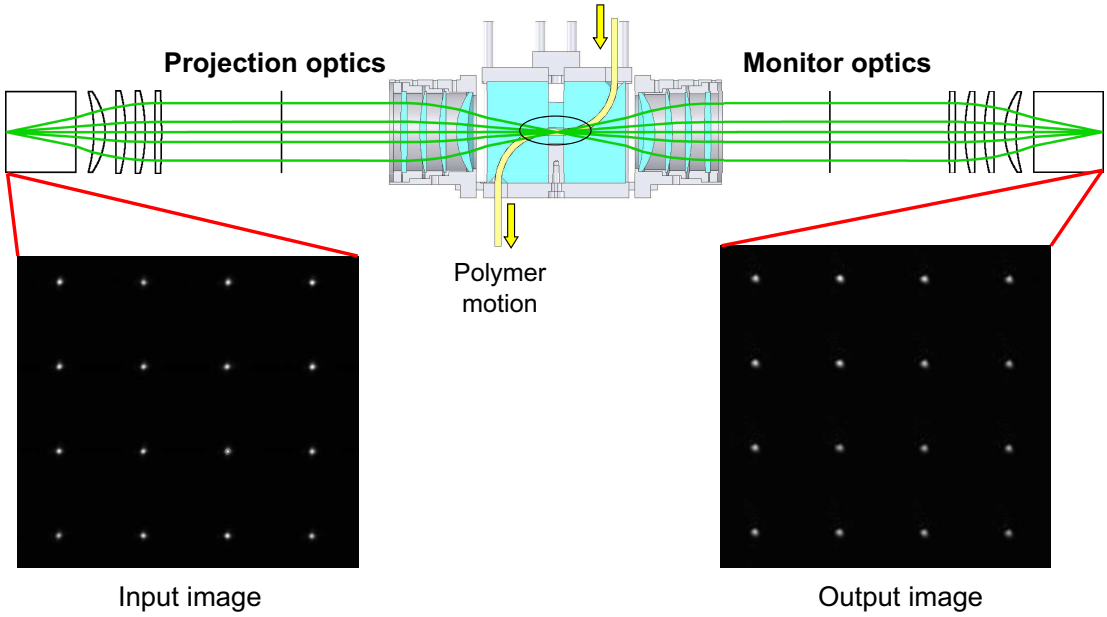

Figure 5.11: A projection lithography system for creating arbitrarily long waveguide arrays. The optical system was verified using index matching fluid in place of the polymer in the central chamber.

implementing this approach is shown in Fig. 5.11, where a cast or extruded photopolymer cable is fed along a curved path through the exposure region. However, projection lithography has one other significant drawback that prevents the fabrication of large, dense waveguide arrays using this approach. This is the problem of out-of-focus exposure.

5.4.3 Out-of-focus exposure

Perhaps the most problematic obstacle for dense waveguide array fabrication in volume photopolymers using projection lithography (and using direct-write lithography as well) is integration of out-of-focus light. Unlike direct-write lithography in glass, where the exposure process has a strong threshold and therefore occurs exclusively at the beam focus, optical exposure in volume photopolymers occurs throughout the illuminated volume due to the low-order kinetics of the ma-

terial response. Direct-write and projection lithography techniques endeavor to concentrate the exposure energy in the desired pattern, but because of diffraction, the desired patterns exist only within a finite depth of focus. For a Gaussian beam propagating in the $+z$ direction, the spatial irradiance distribution $I_G(x, y, z)$ is given by [188]

$$I_G(x, y, z) = I_0 \left(\frac{w_0}{w(z)} \right)^2 \exp \left[-\frac{2\rho^2}{w^2(z)} \right], \tag{5.22}$$

where

$$\rho = (x^2 + y^2)^{1/2}, \tag{5.23}$$

$$w(z) = w_0 \left[1 + \left(\frac{z}{z_0} \right)^2 \right]^{1/2}, \tag{5.24}$$

$$z_0 = \frac{\pi n w_0^2}{\lambda_0}, \tag{5.25}$$

and I_0 is the peak irradiance of the beam. During exposure, the photopolymer sample is translated through the irradiance distribution. For an axial exposure geometry where the sample is translated along the z-axis at a constant velocity v, the stationary laboratory coordinate system (x, y, z) and the moving sample coordinate system (x', y', z') and are related by

$$x = x' \tag{5.26}$$

$$y = y' \tag{5.27}$$

$$z = z' + vt. \tag{5.28}$$

The total energy per unit area $\mathcal{V}$ incident at each point in the sample volume is then

$$\mathcal{V}(x', y', z') = \int_0^T I_G(x', y', z' + vt) dt, \tag{5.29}$$

where T is the total exposure time. For symmetric motion about the focus, the total incident energy will be independent of z'. This integration of irradiance throughout the sample volume leads to index structure formation that is due to

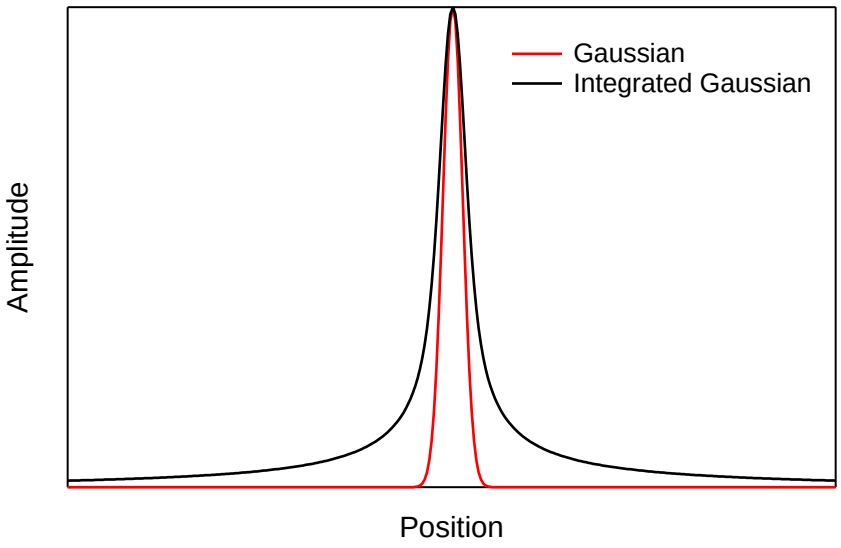

Figure 5.12: Comparison of a Gaussian profile (black) and a the profile of a Gaussian beam integrated along the direction of propagation (red).

the out-of-focus light as well as the light at the focus. Figure 5.12 illustrates the effect of this integration for a Gaussian beam. This figure shows normalized cross-sectional plots of the translationally invariant integrated irradiance distribution along with the irradiance distribution at the Gaussian waist. For this figure, the integration distance is approximately $1000w_0$. While the integrated irradiance distribution is dominated by the Gaussian peak, the overall peak width is broadened and there is significantly increased energy in the wings. For direct-write lithography of isolated guides, this integration of out-of-focus exposure leads to a small increase in guide width relative to the Gaussian beam waist. For closely spaced guides, the out-of-focus exposure leads to a sharp decrease in the index contrast between adjacent guides. Figure 5.13 demonstrates this problem for increasing guide counts from a single isolated guide up to a 9×9 array for Gaussian beams separated by $4w_0$. The plot shows cross sections of the integrated irradiance distribution, so for a material with a linear response the resulting index distribution would be proportional to these curves. Sublinear material response further exac-

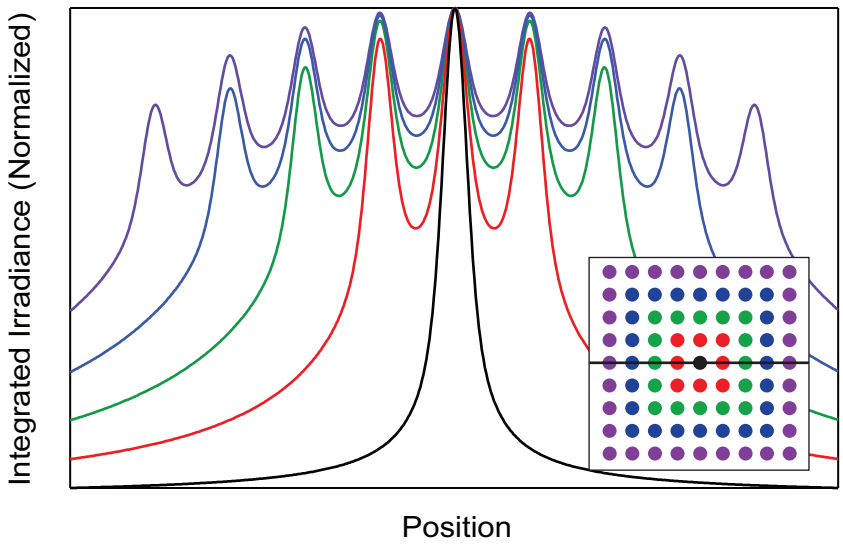

Figure 5.13: Cross section of integrated Gaussian irradiance profiles for a single Gaussian beam (black), a 3×3 array (red), a 5×5 array (green), a 7×7 array (blue), and a 9×9 array (violet). Gaussian beams comprising the arrays are incoherent with one another, and the beam separation is $4w_0$. Inset: the array geometries with a line indicating the plotting path.

erbates the contrast reduction, as does increasing the total array count.

Fabrication of dense 3D index structures by translating a photosensitive material through a 2D exposure pattern will always suffer from contrast reduction if the translation distance is large compared to the depth of field of the projection. One possible method for avoiding this problem is to use patterns based on nondiffracting light beams. One interpretation of the phenomenon of diffraction is to view any spatial light distribution as a superposition of modes. In a strict sense, a mode is a solution to the wave equation that propagates unchanged with only an accumulation of phase. In homogeneous media, solving the wave equation in Cartesian coordinates yields plane wave modes, and any transverse field distribution can be described as a superposition of these modes (the so-called angular spectrum of plane waves [117]). For monochromatic illumination, each plane wave in the superposition has a propagation vector $\mathbf{k}$ with the same magnitude,

$k = 2\pi n/\lambda_0$, but with a different component k_z along the optical axis of interest. Therefore, for a field distribution at a plane $z = 0$ propagating to another parallel plane a distance z away, each plane wave component will accumulate a different phase factor resulting in a different superposition and a modification of the transverse field distribution. Since each plane wave mode has a different z-component of its propagation vector, one can view diffraction as an effect of modal dispersion along the propagation direction z. Elimination of diffraction is therefore possible if one employs patterns that are modal solutions to the wave equation.

A solitary plane wave is not a very interesting pattern, and since it requires an infinite spatial extent it is also not a physically viable field distribution, though a collimated Gaussian beam provides a reasonable approximation. Alternatively, one might employ other modal solutions to the wave equation with more interesting transverse profiles. One such solution, first described by Durnin [192], is found by solving the wave equation for homogeneous, source-free media in cylindrical coordinates. This yields the following modal solution for the electric field:

$$E(x, y, z, t) = E_0 J_0(\alpha r) \exp\left[j(\omega t - \beta z)\right] \tag{5.30}$$

where $r^2 = x^2 + y^2$, $\beta^2 + \alpha^2 = k^2$, and J_0 is the zero-order Bessel function of the first kind. When β is real and $0 < \alpha \leq k$, the solution is a nondiffracting beam, which, unlike plane waves, contains a localized irradiance maximum, as shown in Fig. 5.14. These modes of homogeneous media, known as Bessel beams, do share important characteristics with plane waves, however. Both plane waves and Bessel beams are nondiffracting, and they are also both infinite in extent and carry infinite energy. Therefore, neither can be fully realized in a laboratory setting. Bessel beams with finite aperture have been shown to maintain their transverse profiles with limited diffraction over propagation distances up to [193]

$$z_{\max} = r\left[\left(\frac{2\pi}{\alpha}\lambda\right)^2 - 1\right]^{1/2}, \tag{5.31}$$

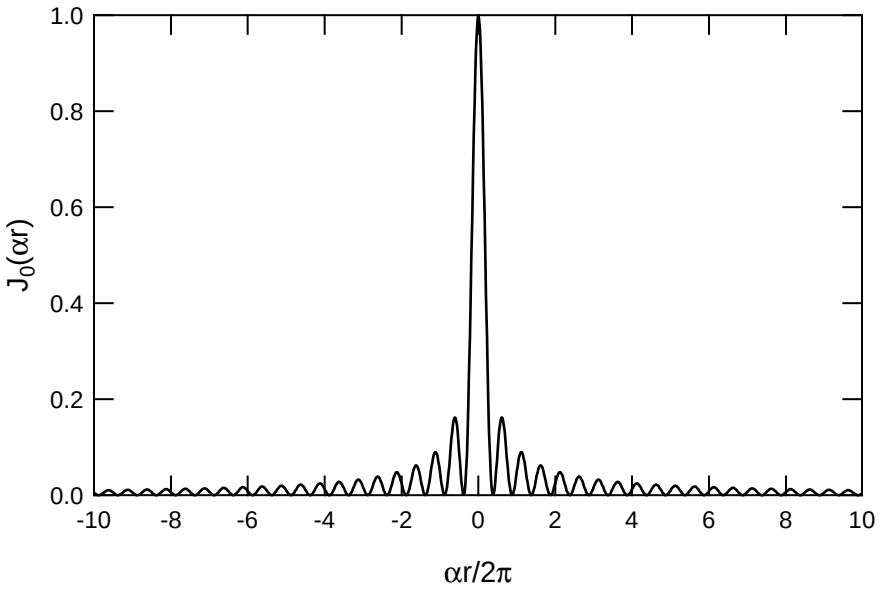

Figure 5.14: The irradiance profile of a Bessel beam.

where r is the radius of the aperture. This range can be significantly longer than the Rayleigh range of a Gaussian beam with a comparable spot radius. For example, to produce a FWHM central spot diameter of $5\,\mu$m at a wavelength of 532 nm ($\alpha = 0.45\,\mu\text{m}^{-1}$) with an undiffracted propagation length of 1 cm, the aperture needs to be only 0.76 mm in diameter.

While Bessel beams offer the intriguing property of diffraction-free propagation with a bright central spot, they still present challenges for producing illumination patterns for lithographic fabrication of waveguide arrays in volume photopolymers. Aside from the fact that the creation of a large array of Bessel beams would be a non-trivial task, the fact that significant power resides outside of the central maximum presents problems for assembling large arrays of Bessel beams while maintaining high contrast between maxima. Figure 5.15 illustrates this problem for a 9×9 array of Bessel beams, where the beam centers are separated by 2.6 times the spot radius. This separation was chosen as it represents an approximate local maximum in interguide contrast. The total irradiance pat-

tern of the 9×9 array is shown in Fig. 5.16. From these figures, it is clear that adding together large arrays of Bessel beams leads to an unacceptably high level of background exposure, despite the fact that each Bessel beam does not diffract as it propagates.

While Bessel beams may not be an ideal approach for fabricating waveguide arrays in volume photopolymer, they do provide insight into how one may synthesize illumination patterns that exhibit limited diffraction over large propagation distances. A Bessel beam itself can be described as a superposition of plane waves. The plane waves that are included in this superposition, though infinite in number, all share the same z-component of their propagation vector. For a J_0 beam, all of these plane wave components are in phase with one another. Introduction of an azimuthal phase factor yields higher order Bessel beams. Looking at non-diffracting Bessel beams as a superposition of plane waves with equal propagation constants in the z dimension suggests that other non-diffracting patterns can be generated by an appropriate superposition of plane waves. Since Bessel beams require an infinite superposition of plane waves, it is not feasible to directly synthesize them from their plane wave components. On the other hand, non-diffracting patterns that use a finite number of plane wave components can be directly synthesized. This approach is treated in the following section.

5.5 Holographic lithography

5.5.1 Introduction

Holographic, or interference, lithography refers to the process of generating a spatial irradiance distribution via interference, which is then used to expose a photosensitive material. For waveguide array fabrication, the use of holographic lithography with volume photopolymers has several advantages. First and foremost, it allows for broad-area exposures that create large numbers of waveguides

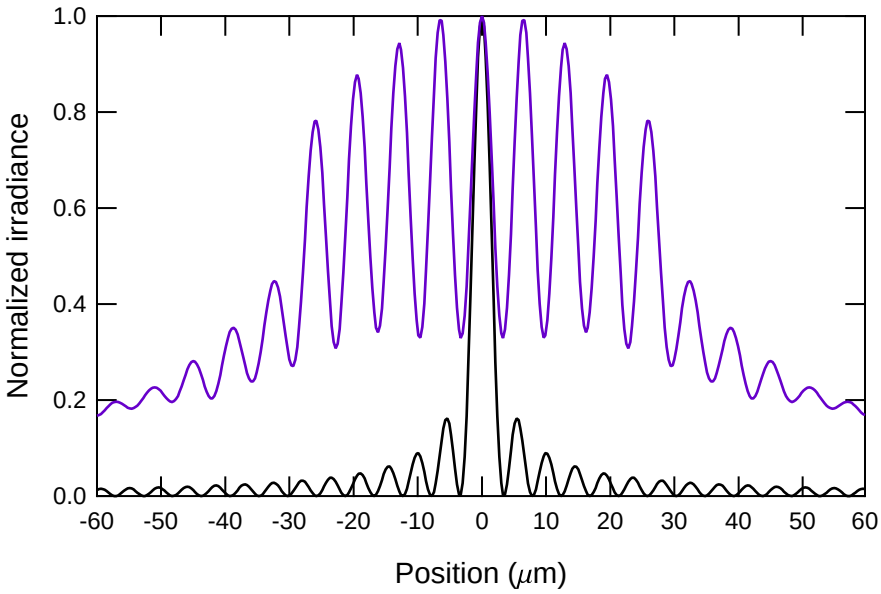

Figure 5.15: Cross section of integrated Bessel irradiance profiles for a single Bessel beam (black), and a 9×9 array (violet). The array geometry is the same as in Fig. 5.13.

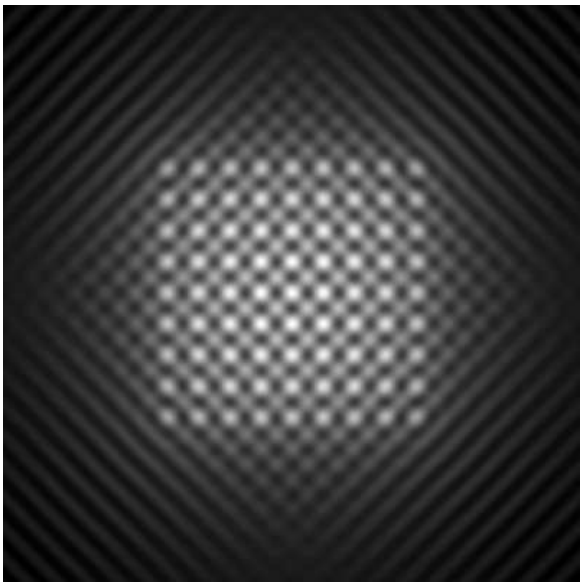

Figure 5.16: Irradiance distribution of a 9×9 array of Bessel beams.

simultaneously. This feature is key for practical fabrication of high-density waveguide arrays. Holography is also capable of producing spatially modulated irradiance patterns that have an extremely large depth of field. Furthermore, the guide-to-guide uniformity within an array can be extremely high, both in terms of physical size and index contrast. While holographic lithography cannot produce completely arbitrary illumination patterns in the same way projection lithography can, it does provide the ability to create a variety of periodic illumination patterns including both square and hexagonal arrays. The vast possibilities of pattern generation using holographic lithography is still an active area of research [194].

Holographic lithography has been widely employed in conjunction with traditional photoresists to produce broad area exposures of periodic patterns. Applications have included photonic crystal structures in two [195–197] and three dimensions [198–200], optical waveguides [201], microlens arrays [202], magnetic arrays [203] and metamaterials [204], sieves for microfiltration [205], and micropatterning of biopolymer surfaces [206,207]. These applications all exploit the ability of holographic lithography to produce highly regular arrays of period features. With the exception of 3D photonic crystals, these applications are all concerned with planar structures, and as such do not take advantage of the ability of holographic lithography to produce illumination patterns with large depth of field. 3D photonic crystal applications typically employ irradiance distributions that vary in all three dimensions, and thus also do not seek large depth of field, but rather utilize patterns that are periodic along the direction of propagation.

While the majority of applications for holographic lithography have not made use of extended depth of field, plane wave interference patterns are nevertheless capable of producing transverse irradiance distributions that propagate unchanged over macroscopic distances. One application that has made use of this phenomenon is the generation of optical lattices and waveguide arrays in photore-

fractive crystals as described in Sec. 5.1.1. The next section describes how large depth of field array patterns can be generated using multibeam interference.

5.5.2 Holographic irradiance pattern generation

Holographic lithography can produce essentially diffraction-free illumination patterns by interfering a finite number of plane waves that all have the same z-component of their propagation vector. These patterns are not truly diffractionless inasmuch as the plane wave components used to synthesize them are not truly plane waves, but rather Gaussian approximations with finite spatial extent. Within the region of beam overlap, however, the interference patterns can be translationally invariant along the z-axis.

The simplest pattern to create and record via holographic lithography is a sinusoidal grating in 1D. This pattern is formed by the interference of two equal-amplitude plane waves. The optical axis of such an exposure configuration is defined to bisect the angle between the wave vectors of the two plane waves, with the positive z axis in the direction of propagation. The wave vectors are taken to both lie in the xz plane. In this coordinate system, the two plane wave components are described by

$$\mathbf{E}_1(x,z) = E_0 e^{j[\omega t - k(x\sin\theta + z\cos\theta)]}\hat{\boldsymbol{\varrho}} \tag{5.32}$$

$$\mathbf{E}_2(x,z) = E_0 e^{j[\omega t - k(-x\sin\theta + z\cos\theta)]}\hat{\boldsymbol{\varrho}}, \tag{5.33}$$

where $\hat{\boldsymbol{\varrho}}$ is a polarization unit vector and θ is the angle each beam forms relative to the optic axis, as shown in Fig. 5.17. Where these two plane waves overlap, the resulting irradiance pattern will be

$$I(x,z) = |\mathbf{E}_1 + \mathbf{E}_2^*|^2$$

$$\Rightarrow \qquad I(x) = 2|E_0|^2\left[1 + \cos(2kx\sin\theta)\right], \tag{5.34}$$

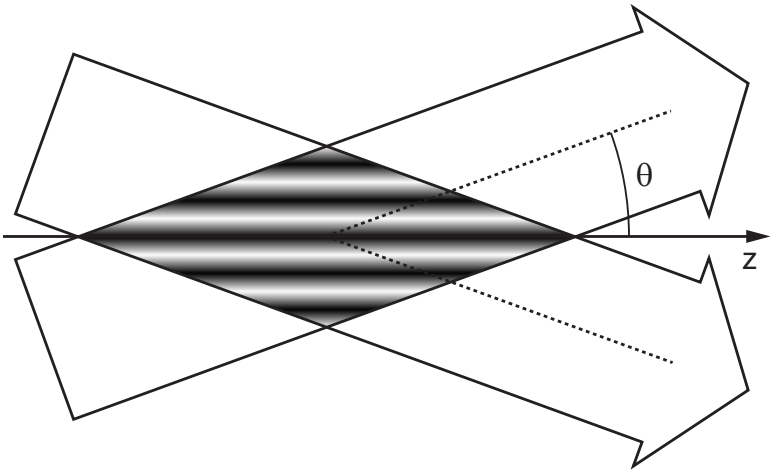

Figure 5.17: The geometry of plane wave interference to produce a sinusoidal grating pattern.

which no longer depends on z. Here the asterisk denotes complex conjugate. The spatial period Λ of the resulting sinusoidal pattern is

$$\Lambda = \frac{\pi}{k \sin\theta} = \frac{\lambda_0}{2n \sin\theta}. \tag{5.35}$$

For approximate, uniform-amplitude plane waves with a finite-aperture radius w that is large relative to the wavelength, the extent of the overlap region can be found by considering the geometrical ray optics picture shown in Fig. 5.18. For a desired exposure region with facets perpendicular to the optic axis and a transverse radius r, the maximum length L of the uniform exposure region is found by this geometric analysis to be

$$L = \frac{2(w - r)}{\tan\theta}. \tag{5.36}$$

For this simple two-beam case, Eq. 5.36 gives the maximum depth of a volume grating formed by holographic lithography in a volume photopolymer sample. By adding additional beams, interference patterns that are periodic in two transverse dimensions may be formed that are suitable for fabricating waveguide arrays. In this case, Eq. 5.36 describes the maximum length of the waveguide arrays for a given set of exposure parameters θ and w. The beam angle θ is determined by the

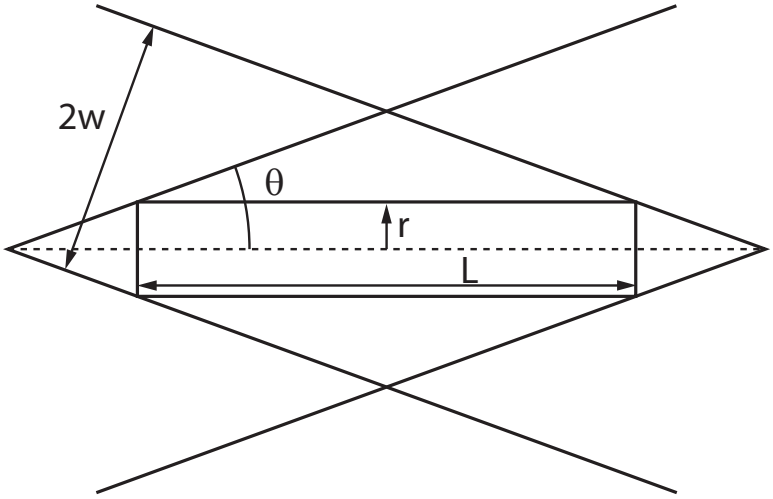

Figure 5.18: Geometry of a uniform exposure region with facets perpendicular to the optical axis for plane waves with finite aperture.

desired grating or waveguide array pitch, and the beam radius w is constrained by the physical size of the optical components used to construct the holographic lithography system.

One method to produce a translationally invariant, 2D irradiance pattern for waveguide array fabrication is to superimpose two orthogonal grating patterns formed by plane wave pairs. If this superposition is done incoherently, for example by producing the two grating patterns with orthogonally polarized light, a pattern like the one shown in Fig. 5.19 is produced.

The mathematical description of the resulting irradiance pattern follows directly from Eq. (5.34), and is given in normalized form by

$$\frac{I(x,y)}{I_0} = \frac{1}{2} + \frac{1}{4}\cos(2kx\sin\theta) + \frac{1}{4}\cos(2ky\sin\theta). \tag{5.37}$$

Here I have assumed that the angular separation θ of the beams that produce the grating with periodicity in x is the same as for the beams that produce the grating in y. This choice gives the resulting array pattern the same periodicity in both dimensions, but is not required. If the angular separations for the two sets of beams are different, then the periodicity in the x and y dimensions will also be

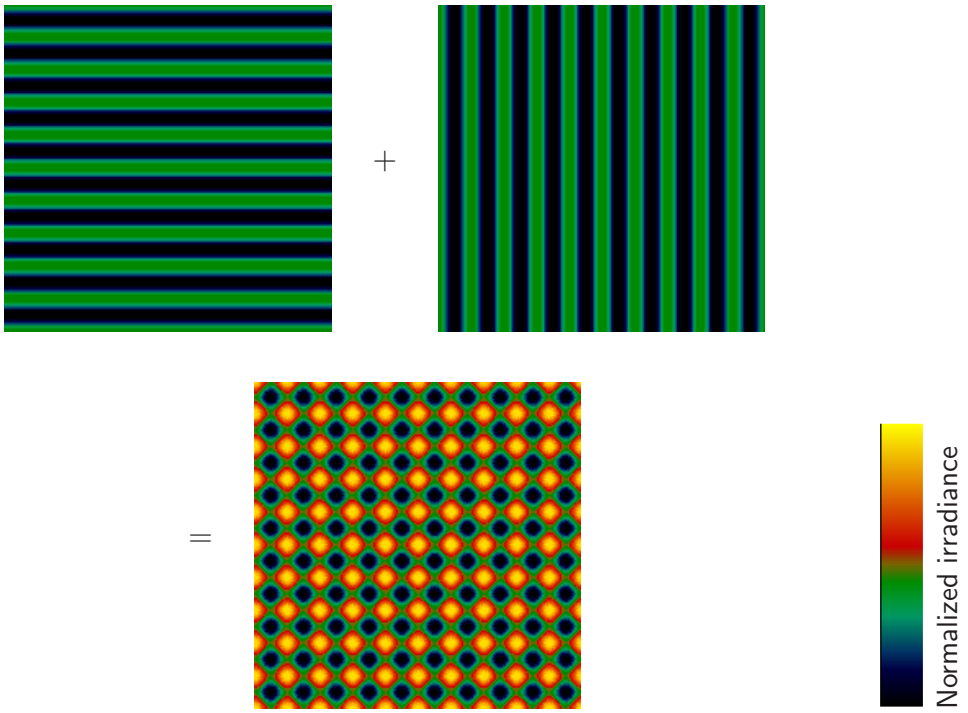

Figure 5.19: An incoherent sum of two coherent pairs of beams, each producing an orthogonal linear fringe pattern, produces a square array with incomplete isolation of the local maxima.

different, resulting in a rectangular array with the same general character as the array shown in Fig. 5.19.

Note that there is some ambiguity present in Eq. (5.37) and Fig. 5.19 with respect to the direction of propagation of the interfering beams. Both of the gratings in Fig. 5.19 can be produced by a beam pair that lies either in the plane of the paper or perpendicular to the plane of the paper. The result is that holographic lithography can be implemented using different exposure geometries in a manner similar to direct-write lithography. This is especially apparent in the context of waveguide array fabrication, since the desired spatial scales of the periodic exposure patterns require small angular separations between beam pairs. For example, to produce an irradiance pattern with a 10 μm pitch using 532 nm light, the required angular separation according to Eq. (5.35) is 1.52°

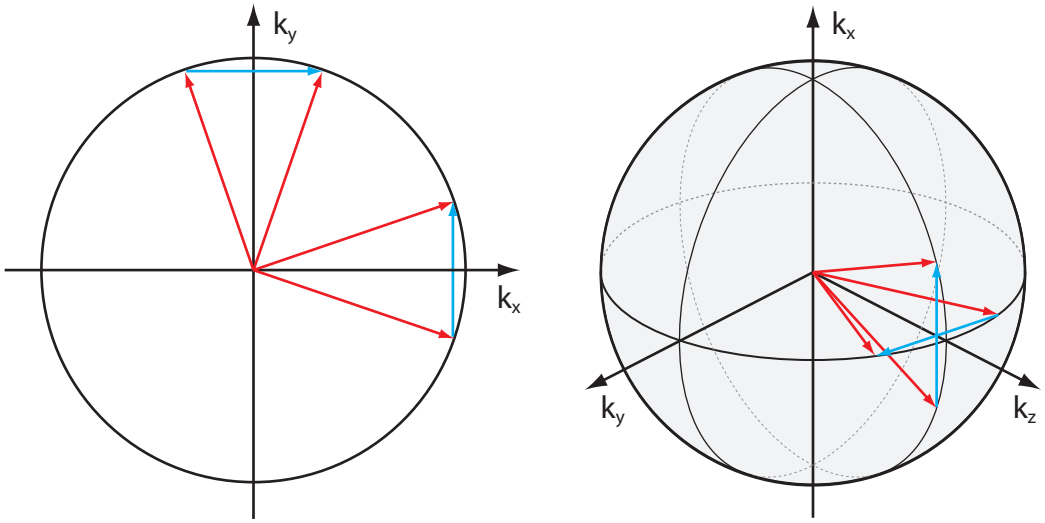

Figure 5.20: Beam configurations for producing square array patterns with beam incidence substantially (A) perpendicular and (B) parallel to the translationally invariant axis of the resulting irradiance pattern. Beam k-vectors are shown in red, and the resulting grating vectors are shown in blue.

in air. (Since the transverse component of the wave vector is conserved at the material boundary, interfering beams that produce a pitch Λ in air will produce the same pitch within material where $n \neq 1$, provided the angles of incidence are small and the interface is planar.) These geometries are best visualized using the k-space representations shown in Fig. 5.20. In Fig. 5.20(A) the two beam pairs are incident at angles symmetric about the x- and y-axes, respectively, and the result of the superposition is an array pattern that is translationally invariant along the z-axis out of the page. This geometry is referred to as a perpendicular exposure geometry, since the incident exposure axes are perpendicular to the axis of invariance in the resulting pattern. In Fig. 5.20(B) the two beam pairs are both incident substantially along the z-axis, which is also the axis along which the resulting irradiance pattern is constant. This arrangement is consequently referred to as a parallel exposure geometry.

While both parallel and perpendicular geometries can produce periodic 2D irradiance distributions with large depth of field, the parallel geometry is preferred for waveguide array fabrication applications in volume photopolymer. One reason for this preference is that the exposure light utilizes the same sample input and output facets as the resulting waveguide array. This means that only two sample facets are require optical surface quality. The perpendicular geometry would require at least four high-quality facets. Another important reason for choosing the parallel geometry is pattern monitoring. In the perpendicular geometry, the exposure beams rapidly diverge after passing through the sample because they are propagating along axes that are perpendicular to one another. The consequence is that the desired exposure pattern exists at the sample location only, and is difficult to accurately reproduce at another spatial location for monitoring purposes. In the parallel geometry, on the other hand, the exposure beams propagate closely spaced about a common axis. This facilitates collection of the beams following the overlap region to recreate the exposure pattern at another location along the z-axis. For incoherent summation of two individually coherent pairs, pattern monitoring is not especially important because the irradiance distribution does not depend strongly on small misalignments or relative phase shifts between beams. But for four mutually coherent beams, which as will be shown can produce superior irradiance pattern qualities for waveguide array fabrication relative to incoherent grating summation, small misalignments and relative beam phases become much more important. For this case, irradiance pattern monitoring is essential.

The pattern formed by incoherent grating addition described by Eq. (5.37) provides a square array of irradiance maxima, but plots of 1D slices through the irradiance pattern reveal that the maxima are not fully isolated. That is, the are directions along which the irradiance does not go to zero between adjacent

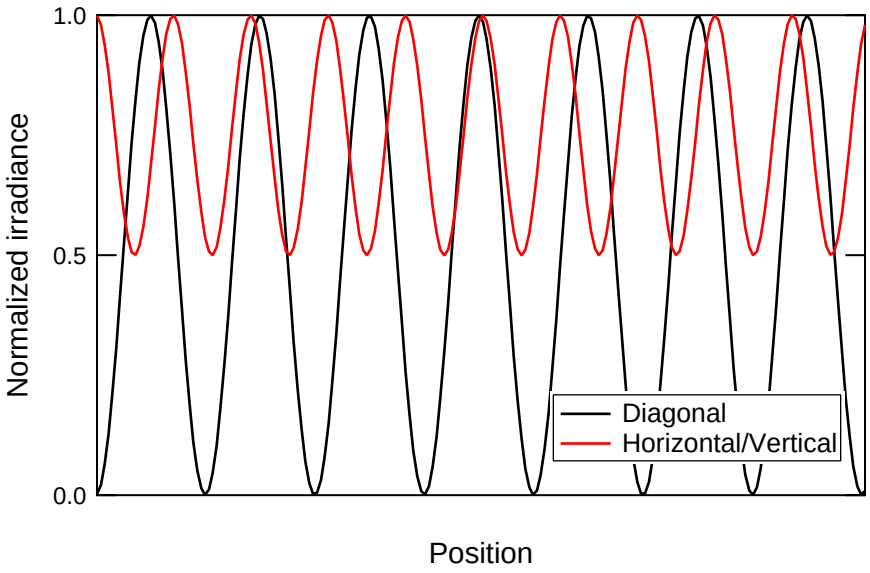

Figure 5.21: 1D slices through the irradiance pattern formed by incoherent summation of two orthogonal plane wave fringe patterns.

maxima. This is illustrated in Fig. 5.21 for the grating sum pattern as it is oriented in Fig. 5.19. Note that along the horizontal and vertical directions the irradiance drops to only half of the peak value between maxima, whereas the irradiance goes all the way to zero along the diagonals.

To make the best use of the dynamic range available in a given photopolymer material, the irradiance pattern should produce well-isolated irradiance maxima completely surrounded by a null region. This can be accomplished via interference of three or more mutually coherent, noncoplanar beams, depending on the desired pattern. Here I will derive a full-contrast square array irradiance patten that can be synthesized using four plane wave components. The required plane waves are in fact the same four plane waves illustrated in Fig. 5.20(B), but in this case they are all mutually coherent. These four plane waves can be expressed in terms of

their wave vector components $\mathbf{k} = (k_x, k_y, k_z)$ as

$$\mathbf{E}_1 = E_0 e^{j(\omega t + k_x x + k_y y + k_z z + \psi_1)} \hat{\boldsymbol{\varrho}}, \tag{5.38}$$

$$\mathbf{E}_2 = E_0 e^{j(\omega t + k_x x - k_y y + k_z z + \psi_2)} \hat{\boldsymbol{\varrho}}, \tag{5.39}$$

$$\mathbf{E}_3 = E_0 e^{j(\omega t - k_x x + k_y y + k_z z + \psi_3)} \hat{\boldsymbol{\varrho}}, \tag{5.40}$$

$$\mathbf{E}_4 = E_0 e^{j(\omega t - k_x x - k_y y + k_z z + \psi_4)} \hat{\boldsymbol{\varrho}}, \tag{5.41}$$

where $k_z = (k^2 - k_x^2 - k_y^2)^{1/2} > 0$. The wave vector components have the same magnitude for each beam, and differ only in sign. All four plane waves have equal amplitude, and each has an arbitrary phase offset, $\psi_{1\text{–}4}$. In the overlap region, the total normalized irradiance distribution is

$$I(x, y, z) \propto \left| \mathbf{E}_1 + \mathbf{E}_2 + \mathbf{E}_3 + \mathbf{E}_4 \right|^2 . \tag{5.42}$$

To simplify the notation in the following development, substitute the dimensionless position variables $X = 2k_x x$ and $Y = 2k_y y$ into the expressions for the four incident fields. Expressing the irradiance pattern as a normalized distribution and expanding the right hand side of Eq. (5.42) leads to

$$\begin{aligned} \frac{I(X,Y)}{I_0} = \frac{1}{2} + \frac{1}{8} \big[& e^{j(X + \psi_1 - \psi_3)} + e^{j(Y + \psi_1 - \psi_2)} + e^{j(X + Y + \psi_1 - \psi_4)} \\ & + e^{j(X + \psi_2 - \psi_4)} + e^{j(Y + \psi_3 - \psi_4)} + e^{j(X - Y + \psi_2 - \psi_3)} + \text{c.c.} \big] , \end{aligned} \tag{5.43}$$

where c.c. denotes the complex conjugate of the preceding terms inside the brackets. Note that the z dependence of the irradiance distribution has dropped out. The phase offsets for each beam have been included because for interference of more than two beams, the relative phases between the beams change the character of the resulting irradiance pattern. This is in contrast to two-beam interference (or the incoherent summation of two-beam interference) where the changes in the relative phases of the beams affects the resulting pattern only by shifting it. To demonstrate the effect of the relative beam phases, I will evaluate Eq. (5.43) for

two representative values of the beam phases that yield compact analytic expressions. Then I will show numerical calculations that illustrate the range of patterns that are formed for arbitrary beam phases.

The first case that I will address is where $\psi_1 = \pi$ and $\psi_2 = \psi_3 = \psi_4 = 0$. In this case, Eq. (5.43) becomes

$$\begin{aligned}\frac{I(X,Y)}{I_0} &= \frac{1}{2} + \frac{1}{8}\left[e^{j(X+\pi)} + e^{j(Y+\pi)} + e^{j(X+Y+\pi)} + e^{jX} + e^{jY} + e^{j(X-Y)} + \text{c.c.}\right] \\ &= \frac{1}{2} + \frac{1}{4}\left[\cos(X-Y) - \cos(X+Y)\right]. \end{aligned} \tag{5.44}$$

Introduction of an alternative transverse coordinate system (X', Y') that represents a 45° rotation, $\pi/2$ phase shift, and a $\sqrt{2}$ scaling of the original (X, Y) coordinate system, where

$$X = X' - Y' + \frac{\pi}{2} \tag{5.45}$$

$$Y = X' + Y' + \frac{\pi}{2} \tag{5.46}$$

results in the following expression for the normalized irradiance pattern:

$$\frac{I(X',Y')}{I_0} = \frac{1}{2} + \frac{1}{4}\left[\cos(X') + \cos(Y')\right]. \tag{5.47}$$

Note that the form of Eq. (5.47) is exactly the same as that of Eq. (5.37) for the case of incoherent summation of two two-beam fringe patterns. This irradiance pattern is plotted in Fig. 5.22, where it is apparent that both the minimum and maximum irradiance points lie at localized extrema, and four saddle points exist about each local maximum limiting the total contrast between maxima. This result shows that fully coherent four-beam interference can reproduce the same pattern as the pairwise coherent case, but with a 45° rotation of the pattern about the z-axis relative to the incident beam $\mathbf{k}$-vectors, along with a scaling factor and phase shift.

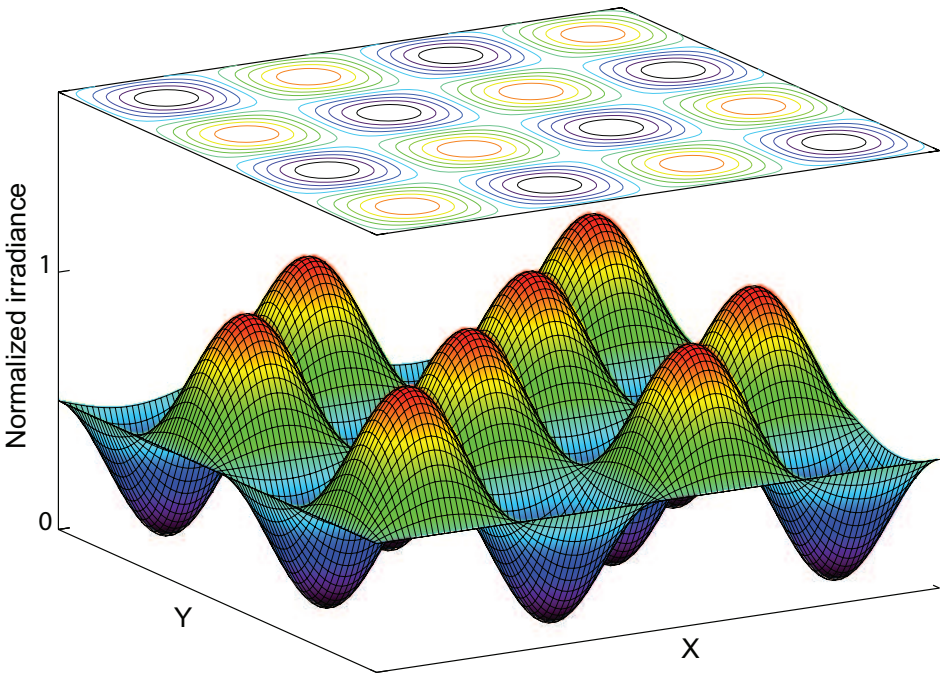

Figure 5.22: Surface and contour plots of the coherent four-beam irradiance pattern derived in Eq. (5.47) where one beam has a π phase shift relative to the other three.

Next, consider the case where the phase offsets for all four beams are zero ($\psi_1 = \psi_2 = \psi_3 = \psi_4 = 0$). In this case, Eq. (5.43) becomes

$$\frac{I(X,Y)}{I_0} = 1 + \frac{1}{4}\left[2e^{jX} + 2e^{jY} + e^{j(X+Y)} + e^{j(X-Y)} + \text{c.c.}\right]. \tag{5.48}$$

Again let's transform into a rotated and scaled coordinate system, but this time without the phase shift. To do so, take

$$X = X'' - Y'' \tag{5.49}$$

$$Y = X'' + Y''. \tag{5.50}$$

This yields

$$\begin{aligned}\frac{I(X,Y)}{I_0} &= 1 + \frac{1}{4}\left[2e^{j(X''-Y'')} + 2e^{j(X''+Y'')} + e^{j2X''} + e^{j2Y''} + \text{c.c.}\right] \\ &= 1 + \cos(X'' - Y'') + \cos(X'' + Y'') + \frac{1}{2}\cos 2X'' + \frac{1}{2}\cos 2Y''. \end{aligned} \tag{5.51}$$

Simplification using cosine sum and difference identities as well as the cosine half-angle formula results in

$$\begin{aligned}\frac{I(X,Y)}{I_0} &= 2\cos X''\cos Y'' + \cos^2 X'' + \cos^2 Y'' \\ &= (\cos X'' + \cos Y'')^2. \end{aligned} \tag{5.52}$$

This irradiance pattern is plotted in Fig. 5.23, showing complete irradiance nulls on all sides of each local maximum. This irradiance pattern therefore allows the full dynamic range of a volume photopolymer to be utilized for establishing index contrast in a 2D waveguide array structure. Without going through the details of an analytic derivation, note that a hexagonal array with high contrast can also be produced holographically, through the interference of three plane waves described by

$$\mathbf{E}_1 = E_0 e^{j(\omega t + k_{y1} y + k_z z + \psi_1)}\hat{\boldsymbol{\varrho}}, \tag{5.53}$$

$$\mathbf{E}_2 = E_0 e^{j(\omega t + k_x x - k_{y2} y + k_z z + \psi_2)}\hat{\boldsymbol{\varrho}}, \tag{5.54}$$

$$\mathbf{E}_3 = E_0 e^{j(\omega t - k_x x - k_{y2} y + k_z z + \psi_3)}\hat{\boldsymbol{\varrho}}. \tag{5.55}$$

when $k_x = \sqrt{3}k_{y1}/2$, $k_{y2} = k_{y1}/2$, and $k_z^2 = k^2 - k_{y1}^2 = k^2 - k_x^2 - k_{y2}^2$. This pattern is shown in Fig. 5.24.

In the case of the square array pattern, the relative phases of the four beams are important parameters for determining the resulting irradiance distribution. Equations Eq. (5.47) and Eq. (5.52) show that the relative phases can cause the four beam pattern to change from a sum of cosines to the square of a sum of cosines. For the hexagonal pattern, relative phase changes shift the pattern, but do not change its overall character. To demonstrate how the square array pattern changes for arbitrary beam phases, Fig. 5.25 shows the pattern progression as the phase of one beam is shifted relative to the other beams by varying amounts between zero and π. Shifting the phases of the other beams does not lead to

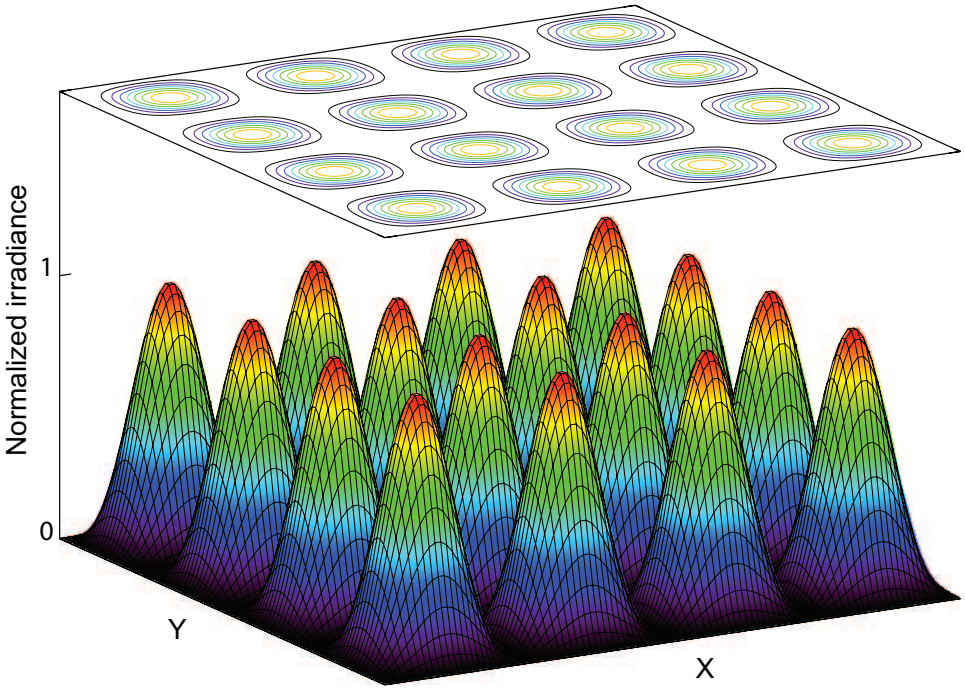

Figure 5.23: Surface and contour plots of the coherent four-beam irradiance pattern derived in Eq. (5.52) for producing a square array.

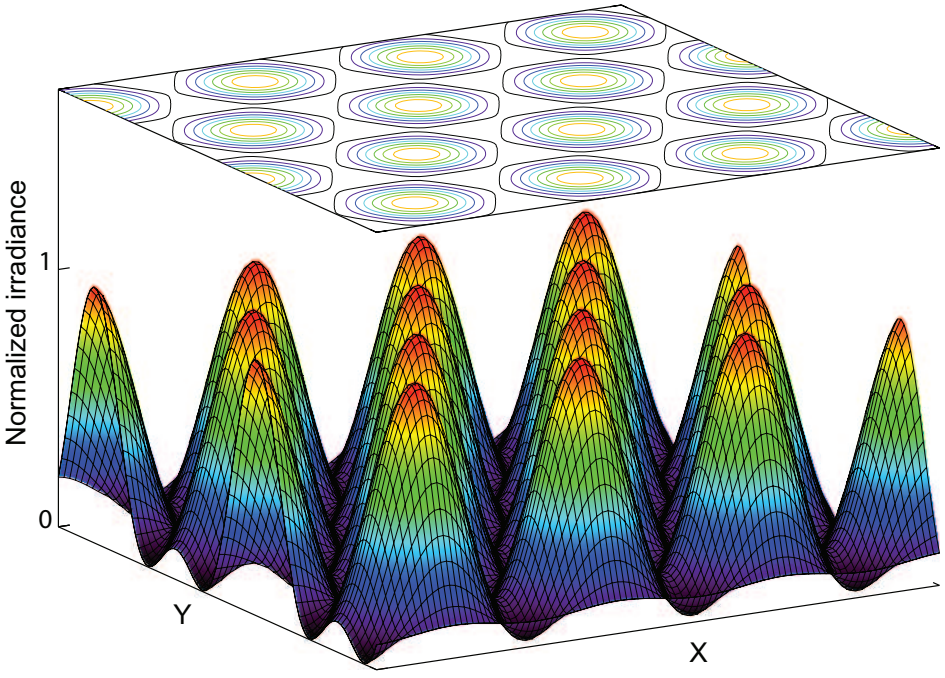

Figure 5.24: Surface and contour plots of a coherent three-beam irradiance pattern for producing a hexagonal array.

any additional patterns, but reproduces the patterns that result from a single beam phase shift with various amounts of shifting of the pattern in the x and y directions.

To produce holographic array patterns using multibeam interference in a practical holographic lithography system, it is apparent that the beam phases must be controlled in order to create the correct, desired pattern in the case of the four-beam case, and to maintain pattern stability and avoid contrast reduction due to shifting patterns for all holographic patterns. The other important consideration for a practical implementation is beam alignment. The calculated patterns such as the one shown in Fig. 5.23, were found using exact values for the transverse components of the wave vector. In a practical implementation, the transverse wave vector components are set through the angular alignment of each beam relative to the optical axis of the system. In the case of the square array pattern of Fig. 5.23, the transverse wave vector components k_x and k_y for each beam should all have the same magnitude with each combination of positive and negative signs represented throughout the four beams. Since the magnitudes of these values will not be exactly equal for a practical system, the tolerances on the angular alignment are best determined though numerical simulation based on Eqs. (5.38)–(5.41) and (5.42). This simulation reveals that slight beam misalignments cause the desired array pattern to experience phase rollovers across the field. An example of such a phase rollover is shown in Fig. 5.26. For a desired array size and pitch, simulation reveals the tolerances on the angular alignment to maintain a given contrast level. For example, for an array with a 10 μm pitch, a 0.001° misalignment results in a 6% contrast reduction along the diagonal over one thousand periods in one dimension. If the misalignment is increase to 0.002°, the contrast reduction increases to 25%. Therefore, for fabricating large area waveguide arrays, high angular tolerances on beam alignment must be achieved.

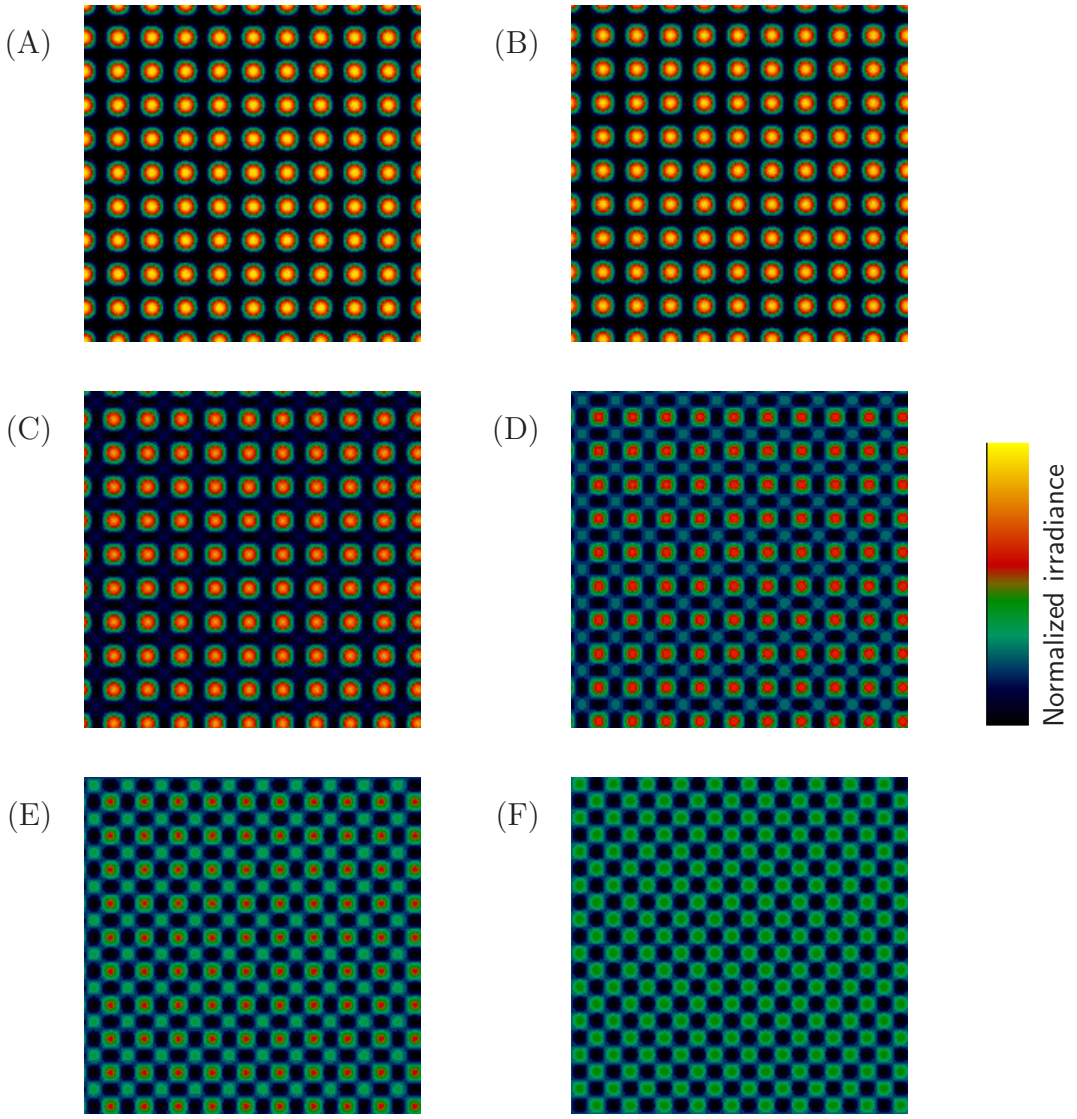

Figure 5.25: Four-beam interference patterns. (A) Four beams in phase. (B) One beam out of phase by $\pi/4$. (C) One beam out of phase by $\pi/2$. (D) One beam out of phase by $3\pi/4$. (E) One beam out of phase by $7\pi/8$. (F) One beam out of phase by π.

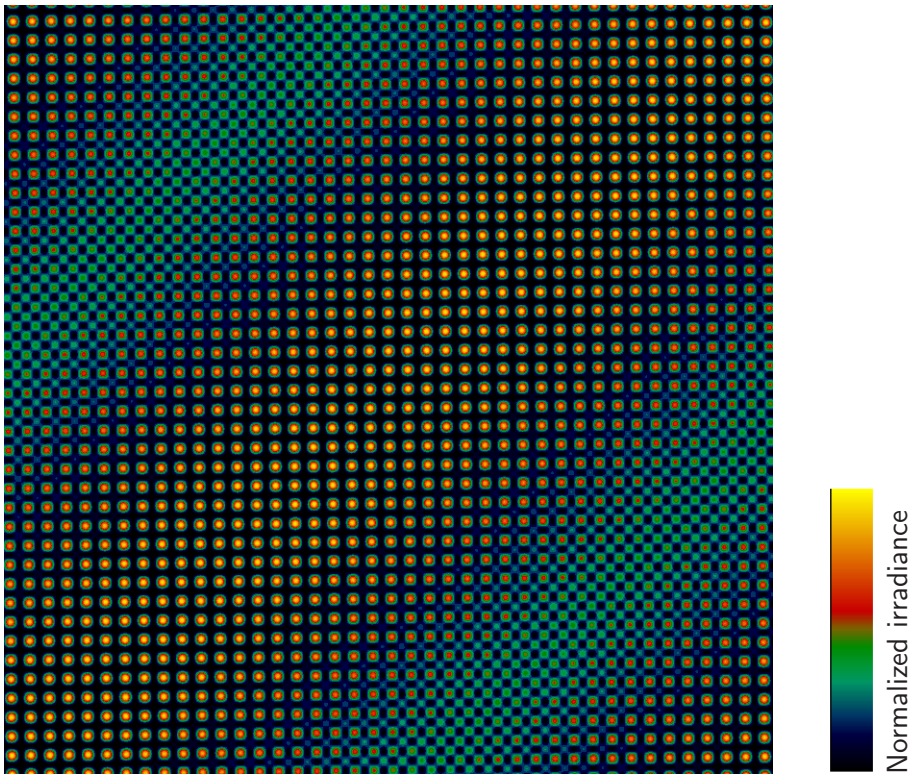

Figure 5.26: Calculated 10 μm pitch interference pattern with two beams misaligned by 0.07° in orthogonal directions.

5.5.3 Experimental holographic lithography system

5.5.3.1 System layout and overview

The goal of the design of the experimental holographic lithography system used for the work presented here was to provide a flexible and reconfigurable exposure system that would accommodate a broad range of sample geometries. This flexibility allows for control over exposure parameters so that a variety of exposure conditions can be explored. This flexibility comes at the expense of stability and ease of use. In Sec. **??** I provide some suggestions for system modifications that would change the balance of this design tradeoff. The system is designed for use with photopolymer materials that utilize initiators sensitive to green light (e.g., Irgacure 784) and that are largely insensitive to red light, since a HeNe laser is

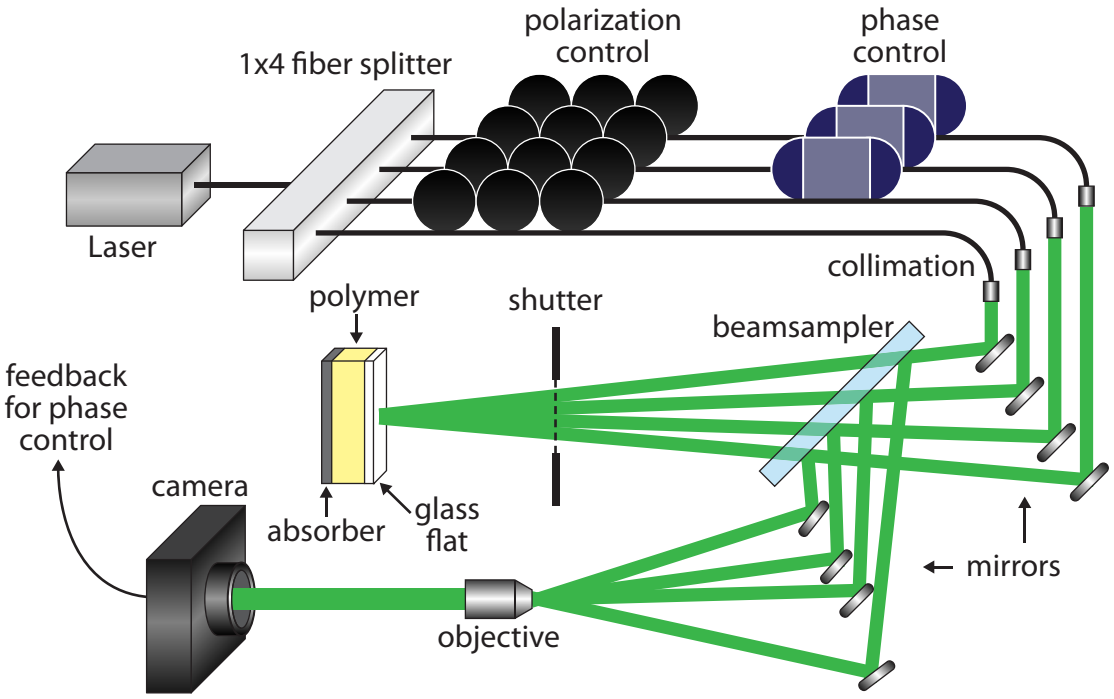

Figure 5.27: Diagram of the experimental holographic lithography system layout.

used to aid in sample alignment.

The experimental holographic lithography system is illustrated in Fig. 5.27. A diode-pumped solid-state laser (Coherent Compass) operating at 532 nm with a maximum output power of 100 mW is coupled into single-mode (SM) optical fiber (Nufern S460-HP). The fiber stage of the system is used to facilitate phase control and to provide spatial filtering. Coupling of the free-space laser beam into the SM fiber is accomplished using an aspheric lens with a focal length of 2.75 mm to match the laser beam size to the 3.4 μm mode field diameter of the SM fiber. The fiber is mounted on a 3-axis stage driven by piezoelectric actuators. Once coupled into the fiber, the light is split into four channels by a 1×4 fiber splitter. Each channel is equipped with a LeFevre loop polarization controller [208]. In three of the channels, these polarization controllers function to align the output polarization of the SM fiber to one of the principal axes of the polarization maintaining (PM)

fiber used in the next stage of the optical network. In the fourth channel, the polarization controller aligns the polarization of the free-space output of the SM fiber to match the polarization of the other four beams.

Three channels contain piezoelectric phase modulators (Canadian Instrumentation & Research Ltd. model 915B) to control the relative phases of three writing beams relative to the fourth. Phase control ensures irradiance pattern stability during exposure provided the phase modulators are driven by an appropriate control system. These phase modulators consist of PM fiber wrapped around a mandrel that includes a piezoelectric transducer. When a voltage is applied to the piezoelectric transducer, the mandrel expands, stretching the wrapped fiber and introducing an additional phase delay. The PM fiber prevents changes in the output polarization state as the transducer drive voltage is varied.

The outputs of the four fiber channels are collimated to produce 5 mm $1/e^2$ diameter beams using 10× microscope objectives. The polarization controllers and PM fiber outputs are oriented so that all four beams are linearly polarized in the vertical direction. Steering mirrors direct the beams to interfere with the appropriate **k**-vectors at the photopolymer sample. To achieve the alignment resolution necessary to meet the angular tolerances for broad area array exposures, the steering mirrors utilize kinematic mirror mounts equipped with piezoelectric actuators.

Prior to the point of interference, an uncoated glass beam sampler directs a small portion of each writing beam to a set of mirrors that cause the sampled beams to interfere with non-redundant angular spacings. This yields a linear fringe pattern that can be recorded using a camera and Fourier transformed in order to provide a measure of the relative phase of each beam relative to each other beam. This phase measurement provides feedback through a software control loop to stabilize the interference pattern using the piezoelectric phase controllers.

The polymer sample can be prepared in a variety of form factors. For the experiments presented here, the most commonly used form factors are glass fluorimetry cells and slide or coupon geometries where the photopolymer material is sandwiched between glass substrates. Here, the term "slide" refers to samples fabricated using standard microscope slides for substrates, and "coupon" refers to samples manufactured by InPhase Technologies using the Zerowave™ process that can produce optically flat sample facets. The material thickness for fluorimetry cell samples ranged from 5 to 10 mm, and for slides and coupons the thickness ranged from 0.5 to 8 mm. The photopolymer sample is oriented in the holographic lithography system so that its front facet is perpendicular to the central axis about which the four writing beams are distributed symmetrically. A HeNe alignment beam directed along this axis aids in proper alignment of the sample. The sample is positioned so that the plane of intersection of the four beams lies at the center of the sample. An absorbing filter is coupled to the back of the photopolymer sample using index matching fluid to suppress back reflections. Depending on the sample form factor, an uncoated glass flat is coupled to the front facet of photopolymer sample, also using index matching fluid. Slides and especially fluorimetry cells require the flat on the front interface to maintain the planar wavefronts of the writing beams. Otherwise, wavefront distortion due to curvature of the front facet can cause corruption of the desired irradiance pattern. Thinner coupon samples are generally sufficiently flat enough that the index-matched flat is not necessary. Coupon sample flatness degrades for thicker samples, so that the external flat may be required. The exposure time is controlled by an electronically activated shutter through which all four writing beams pass. Typical exposure conditions use 5 mW of optical power per writing beam and exposure times of 1 to 10 s.

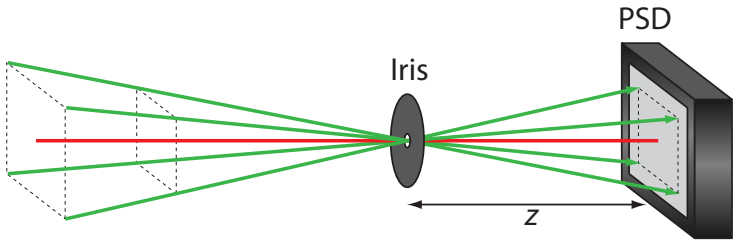

Figure 5.28: Layout for coarse alignment of writing beams using a position-sensitive detector.

5.5.3.2 Alignment procedure

To achieve the level of alignment precision necessary for broad area array exposures, the following two stage alignment procedure is employed. The first stage uses an iris placed at the beam intersection point and a position-sensitive detector (PSD) located a distance z to the right of the iris, as illustrated in Fig. 5.28. The collimated output of a HeNe laser is used to establish the optical axis of the system. Both the iris and the PSD are centered on the HeNe beam. The PSD output is a set of two voltage signals that indicate the (x, y) position of the centroid of a beam incident upon its active area. The PSD reading must be taken for a single beam at a time, so other beams are blocked when a PSD reading is made. With only the HeNe beam incident, the PSD output is zeroed to establish the $(0, 0)$ location on the optical axis.

It is convenient to describe the orientations of the writing beams in space in terms of the angles θ_x and θ_y as defined in Fig. 5.29. The z-axis represents the optical axis of the system, and corresponds to $\theta_x = \theta_y = 0$. In terms of these angles, the magnitudes of the transverse components of the wave vectors for the writing beams are $k_x = k_y = k \sin\theta$ where $\theta = \theta_x = \theta_y$. From Eq. 5.47, the pitch Λ of the square array irradiance pattern is related to θ (measured in air) by

$$\Lambda = \frac{\lambda_0}{2 \sin\theta}. \tag{5.56}$$

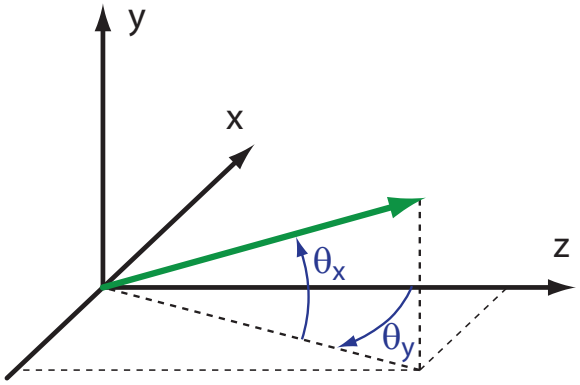

Figure 5.29: Geometry defining the angles that describe the writing beam orientations in space.

Each writing beam is sequentially aligned to produce angles $\theta_x = \pm\theta$ and $\pm\theta_y = \pm\theta$ by simultaneously centering the beam on the iris and locating the beam centroid on the PSD at $(\pm z \tan\theta, \pm z \tan\theta)$.

This coarse alignment procedure produces an array pattern with the desired pitch, but small alignment errors lead to phase rollovers across the irradiance pattern. These phase rollovers can be eliminated using a fine alignment procedure. For this procedure, the PSD is removed and replaced by an imaging system and a camera. The function of the imaging system is to convert the diverging set of plane waves to a converging set. Since the pitch of the irradiance pattern is generally on the same order as the pixel pitch of the camera, the imaging system is also designed to reduce the convergence angle of the plane waves so that a magnified version of the array pattern is produced on the camera. The imaging system consists of two lenses with focal lengths f_1 and f_2, as illustrated in Fig. 5.30. Typical values for f_1 and f_2 are 40 mm and 500 mm, respectively. Note that best performance using singlets is achieved with plano-convex lenses with the planar surface towards the center of the assembly, which is the opposite of a typical telescope arrangement. This is because the system is designed to transform input plane waves to output plane waves, rather than image points on an object.

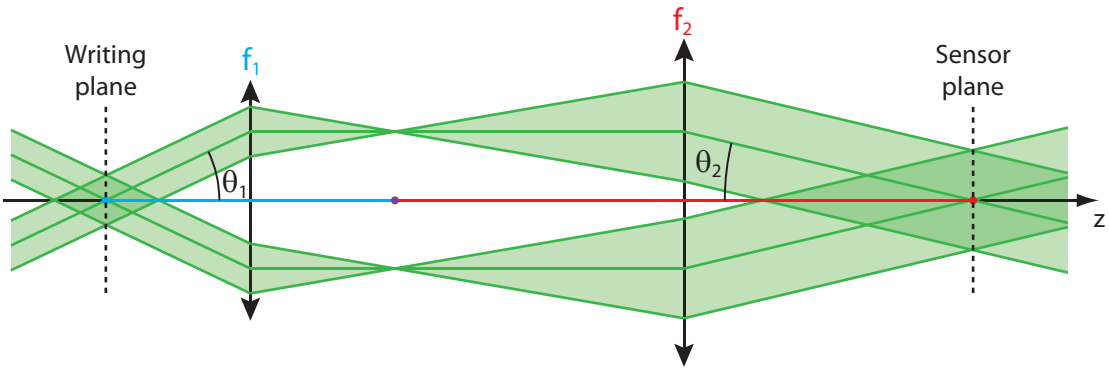

Figure 5.30: Ray picture of plane wave angle transformation using two lenses with focal lengths f_1 and f_2 arranged in a doubly telecentric configuration.

The fine alignment process is illustrated in Fig. 5.31. Adjacent pairs of beams are viewed on the camera sequentially. Each beam pair produces a sinusoidal grating pattern. When the beams are correctly aligned, beams 1 and 2 should produce the same grating pattern (as viewed by the camera) as beams 3 and 4. Similarly, beams 1 and 3 should produce the same grating pattern as beams 2 and 4. All four grating patterns should have the same period, and the grating vectors of the horizontal grating patterns should be precisely perpendicular to the grating vectors of the vertical grating patterns. For each pair of beams, the resulting grating pattern is analyzed by fitting sinusoids to each row or column of pixels along the direction of modulation. The period and phase offset of the sinusoidal fit is then determined for each row or column. The mean period provides feedback for adjusting the angular separation of the beam pair. The phase offset is plotted across columns or rows, and the slope of this phase plot provides feedback for adjusting the orientation of the beam pair. The goal is to produce phase plots with zero slope, which means that the grating patterns are precisely aligned to the horizontal or vertical directions, as set by the pixel layout of the camera. The alignment process begins with one pair, say beams 1 and 2, and adjustments are made to just one of the two beams, say beam 2. In this scenario,

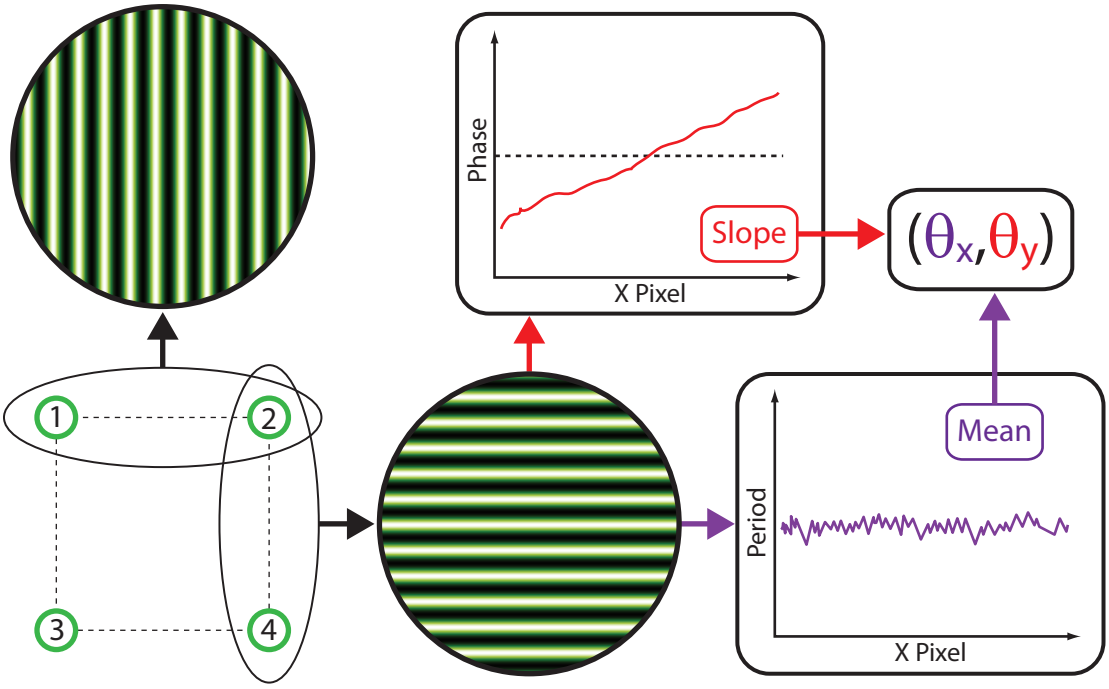

Figure 5.31: Process steps for fine alignment of the holographic writing beams. Two beams are unblocked at a time (lower left). Horizontal pairs yield vertical grating patterns (upper left), and vertical pairs yield horizontal gratings (lower center). For each grating pattern, a sinusoid is fit to each row (for vertical gratings) or column (for horizontal gratings) of pixels. The slope of the phase along rows or columns and the mean period of the sinusoid yield fine angular alignment adjustments.

beam 1 acts as the reference to which all other beams are aligned. After adjusting beam 2 to achieve the desired grating period and zero phase slope, then beam 1 is blocked and beam 4 is allowed to interfere with beam 2. During this step only beam 4 is adjusted to achieve the desired grating period and zero phase slope. Next, the interference pattern produced by beams 1 and 3 is used to align beam 3. The pattern produced by beams 3 and 4 provides redundant information, and may be used as a check of the procedure. The 1.3 megapixel cameras used in this work do not have sufficient resolution to view the entire field in order to evaluate the pattern quality and look for phase rollovers. The most convenient method of pattern quality inspection following the fine alignment procedure is to project the

pattern onto a screen with high magnification. This is easily accomplished using a single lens.

5.5.3.3 Phase control system

To ensure that the irradiance pattern produced by the interference of the four writing beams creates the desired pattern, i.e., the pattern of Fig. 5.23 and Fig. 5.25(A) described by Eq. (5.52) rather than one of the alternative four beam pattern such as those shown in Fig. 5.25(B)–(F), it is necessary to actively control the phases of the writing beams. This is because small changes in air currents and ambient temperature can cause relative phase changes among the beams, leading to pattern variation over time. The time scale of this pattern variation in ordinary laboratory conditions can be on the order of 1 s, even when the system is fully enclosed.

Phase control is accomplished using piezoelectric phase modulators in three of the four channels of the writing system The fourth channel acts as a phase reference. The phase modulators are driven using a feedback signal derived from an auxiliary interference pattern generated by picking off a small portion of each writing beam. These sampled beams are brought together to interfere in a configuration where the angular separation between each beam pair is unique. The pattern produced by this interference is captured using a camera, and the result is shown in Fig. 5.32. The 2D nature of this pattern is due to the fact that the interfering beams are not coplanar. Only one dimension of this interference pattern is required for phase control, however, and only a single row of camera pixels is used and can be selected arbitrarily. When the signal present on this pixel row is Fourier transformed, the result is a spatial frequency spectrum such as the one shown in Fig. 5.33. Because the beams interfere at a nonredundant set of angles, each beam pair produces a unique spatial frequency component in

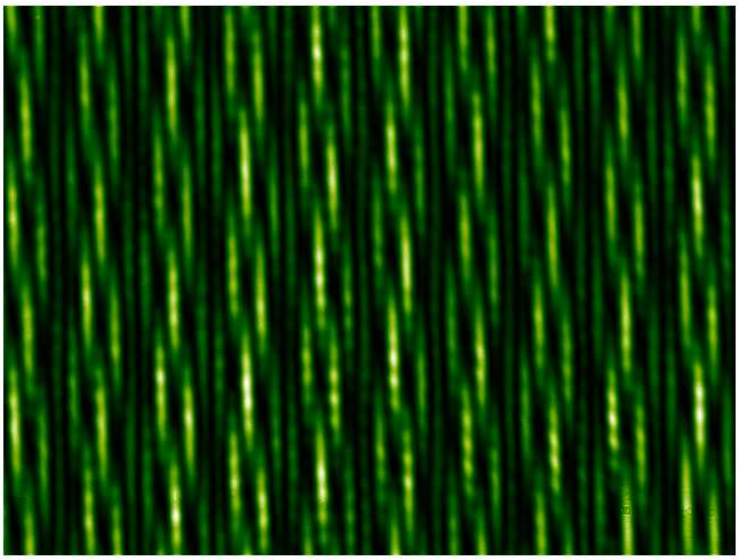

Figure 5.32: The interference pattern used for phase control.

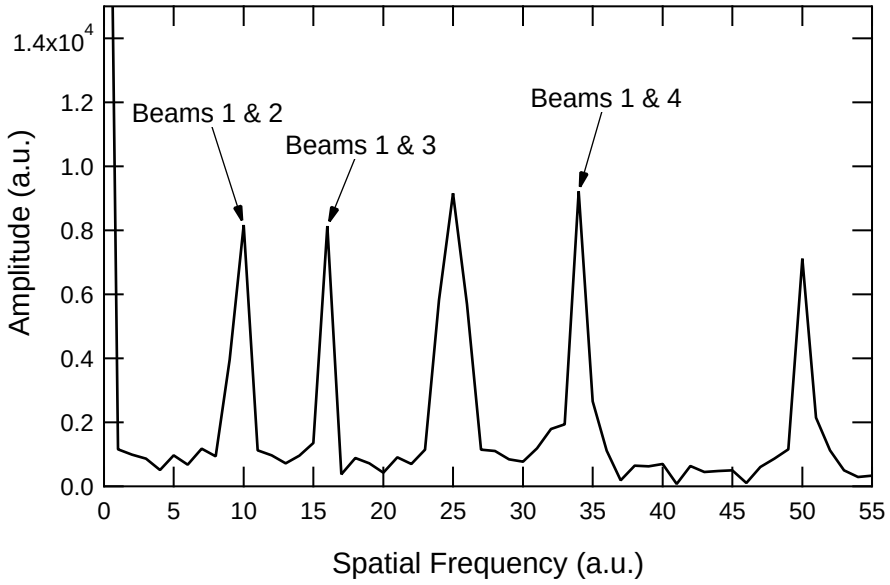

Figure 5.33: The amplitude of the Fourier transform of one row of pixels across the interference pattern used for phase control.

the interference pattern. These components yield distinct amplitude peaks in the Fourier spectrum. Each data point in the Fourier spectrum is complex, however, and the phase at the data array location of each peak provides a measure of the relative phase between the two beams of the pair. This phase measurement can therefore be used as a feedback signal for the phase control system.

One might be tempted to perform phase control using the four writing beams themselves after transmission through the photopolymer sample. This would have some advantages over using an auxiliary interference pattern. The foremost advantage is the common-path nature of this approach. When an auxiliary interference pattern is used, the potential exists for phase shifts to arise after the beam sampler, either in the writing arm or the phase control arm of the system. These differential phase shifts would not be compensated properly because the are not common to both arms, leading to errors in the writing pattern. Controlling phase directly using the writing light can avoid this problem. A second potential advantage is a small reduction in the overall complexity of the system since the auxiliary interference path could be eliminated. Unfortunately, there are two significant problems with this approach. First, phase control must be established prior to exposing the photopolymer sample to writing light to ensure that the irradiance pattern is correct and stable. If writing light transmitted by the sample is used for phase control, the control system will not be active until the shutter opens and exposes the sample. Second, the square array pattern used to expose the sample requires redundant angular spacings between the writing beams. This means that the relative phases of each beam pair cannot be extracted uniquely, even using a 2D Fourier transform of the pattern.

A functional block diagram of the implemented phase control system is illustrated in Fig. 5.34. The auxiliary interference pattern is formed by interfering the sampled beams at a convenient set of nonredundant angles ranging from 5 to

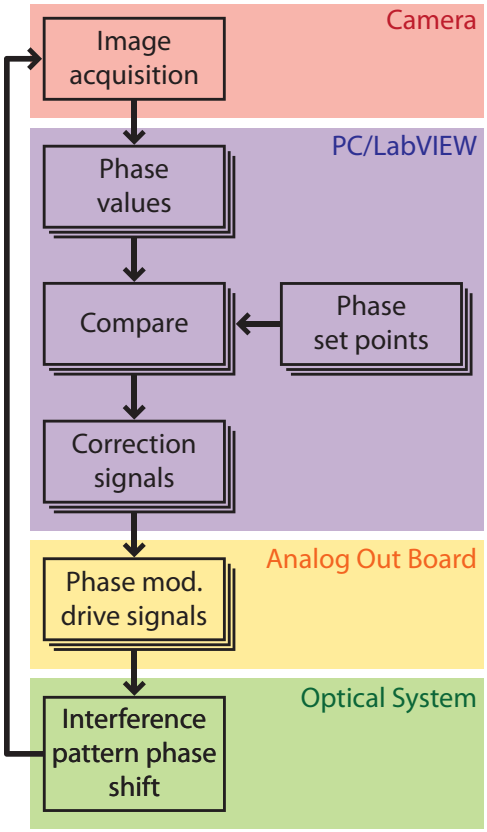

Figure 5.34: Block diagram of the phase control system for holographic lithography.

30 degrees. The interference pattern is magnified onto the camera using a 40× microscope objective. The camera is a Mightex MCE-B013-U CMOS camera. The camera sensor has a resolution of 1280 × 1024 pixels, but to increase the frame rate it is typically operated using a smaller resolution of 640 × 480 pixels when used in the phase control loop. The image collected on the camera is processed using a LabVIEW software utility called `PhaseControl.vi`. This utility performs a Fourier transform of a user-selectable row of pixels from the acquired image, and calculates the phase at three data array locations set by means of graph cursors in a plot of the amplitude of the Fourier transform. This utility also allows the user to specify a phase set point value between $-\pi$ and π for each of the three modulated channels. An error correction signal is determined from the measured phase

values and the set point values using a simple proportional algorithm. Integral and derivative contributions to the error correction signal did not yield appreciable performance increases and were thus dropped from the control algorithm. Manual loop tuning determined the optimal value for the proportional gain to be 0.15 V/rad. Based on the computed error correction signal, the software utility outputs a voltage signal in a ±5 V range through a Measurement Computing USB-3103 analog output board. This signal is converted by the phase modulator drive circuitry to produce a drive voltage in the range of ±50 V that is applied to the piezoelectric mandrels. The expansion and contraction of the piezoelectric mandrels then modulates the optical path in each channel by variable stretching of the wrapped optical fiber around each mandrel. This fiber stretching modulates the optical phase of each channel, which alters the interference pattern collected on the camera, thus closing the control loop.

The effect of the phase control system is shown in Fig. 5.35. The dashed curves show the relative phases for three beams as they wander on ∼1 s timescales due to small fluctuations in ambient environmental conditions. Activation of the phase control system locks the relative phases at the user-defined set points, which in the case of Fig. 5.35 were set to 1 rad, 0 rad, and −1 rad. Typical performance of the phase control system yields residual phase fluctuations with standard deviations on the order of 0.01 rad. The loss of contrast due to this amount of phase variation is on the order of 10^{-5}. The residual phase fluctuations are most likely due to vibrations or other sources of phase error that occur on timescales faster than the loop time of the phase control system. The speed of the control loop is limited by the frame rate of the camera to approximately 35 Hz.

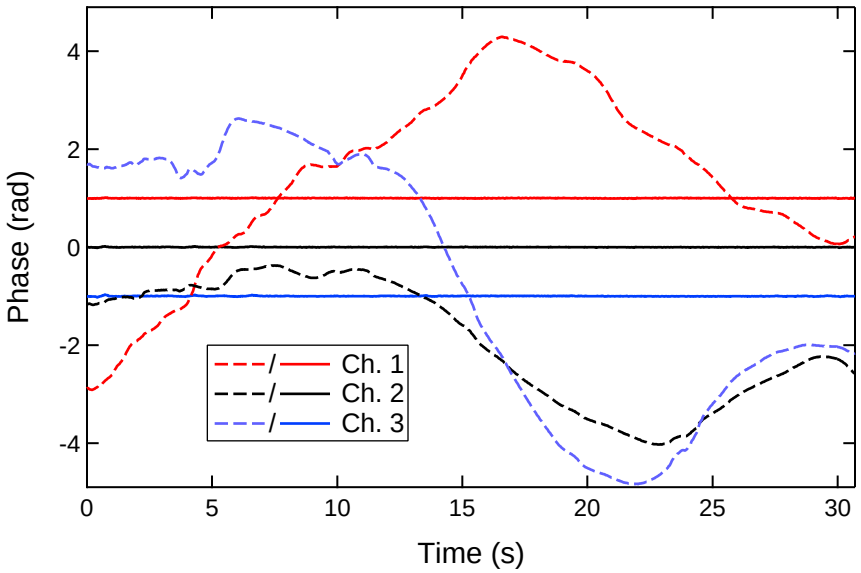

Figure 5.35: Measured phases for three beams relative to the reference beam when the phase control loop is on (solid) and off (dashed).

5.5.4 Fabricated holographic waveguide arrays

The holographic lithography system described here has been used to produce waveguide arrays in volume photopolymer material. Figure 5.36 shows results demonstrating the guidance capability of a 2D waveguide array fabricated using this system. For this array, the holographic exposure used 6.5 mW per beam over an exposure time of 4.0 s. The pitch of the array is approximately 28 μm, and the total length is 8 mm. The photopolymer material is HDS 3000 from InPhase Technologies with half of the standard photoinitiator concentration. The photoinitiator concentration was reduced from its standard value to decrease the total absorption by the sample in order to improve the front-to-back uniformity of the array. The exposure area is approximately 5 mm in diameter, resulting in an array of approximately 25,000 guides. To verify the light guiding properties of the array, an image pattern was projected on the array input and an image of the array output was collected onto a camera. The input image was created by

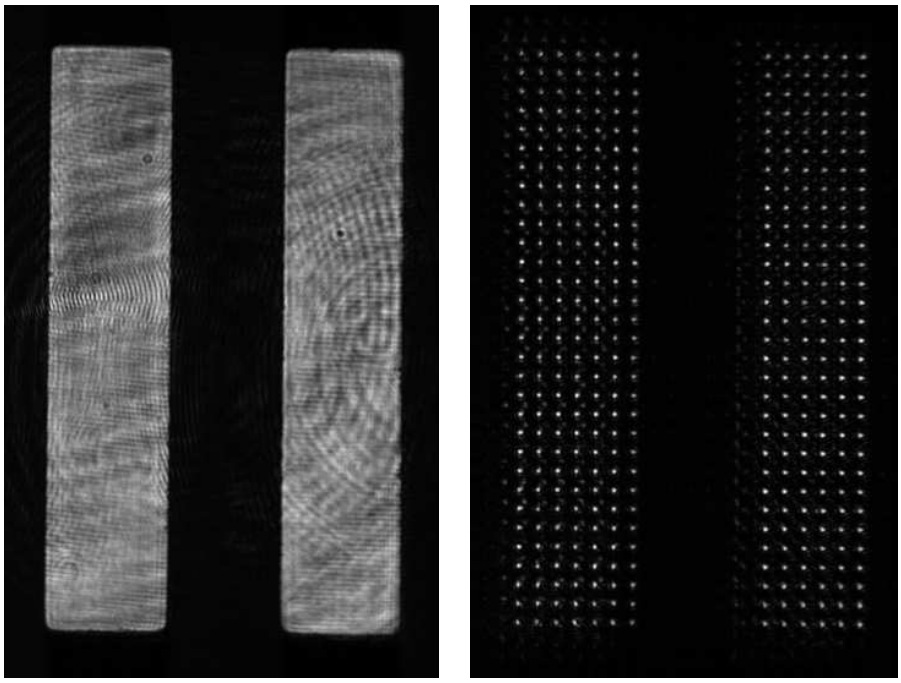

(A) (B)

Figure 5.36: (A) The input image projected onto the input facet of an 8 mm-long holographic waveguide array written in volume photopolymer. (B) An image of the waveguide array output showing a sampled version of the input image.

illuminating an chrome-on-glass Air Force resolution target with the collimated output of a HeNe laser. The light transmitted by the mask was imaged with 1:1 magnification onto the waveguide array input facet using a matched pair of aspheric lenses, each with a focal length of 11 mm (Thorlabs C220MP matched aspheric pair). An example of an input image is shown in Fig. 5.36(A), and the resulting array output showing a sampled version of the input image appears in Fig. 5.36(B). This test demonstrates the capability of holographic lithography to produce imaging waveguide arrays in volume photopolymer material.

Another image of an output signal from the 8 mm-long holographic photopolymer waveguide array is shown in Fig. 5.37(A). For this figure, the input image to the waveguide array was the numeral "3". Figure 5.37(B) and (C) show

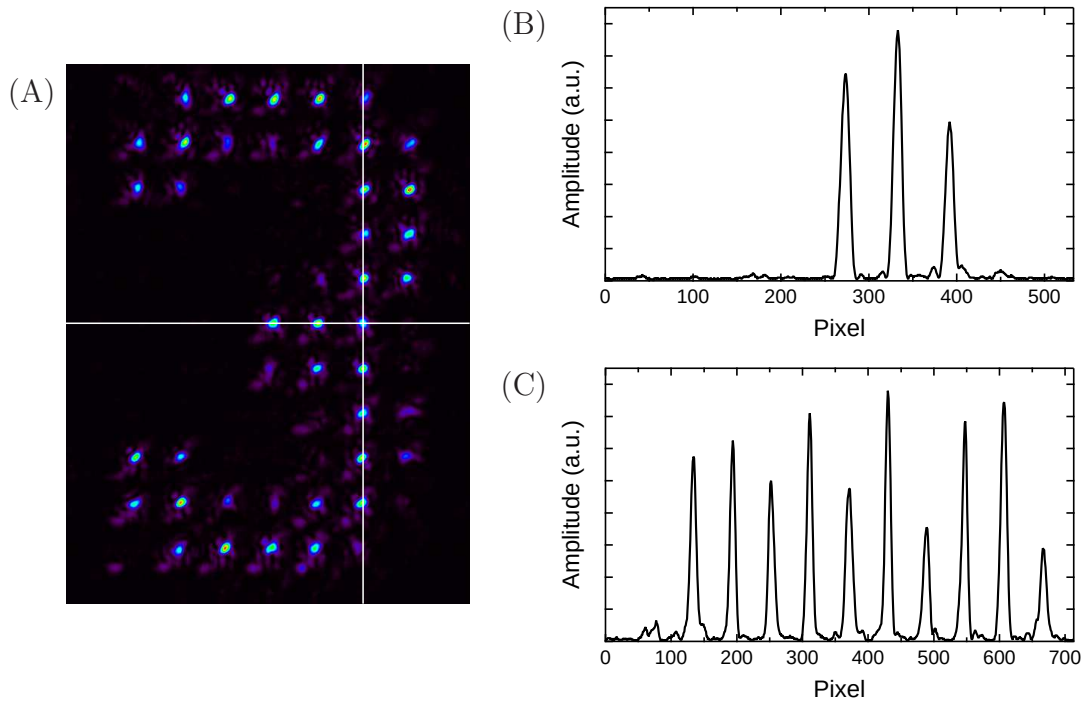

Figure 5.37: (A) Output image of an 8 mm-long holographic waveguide when an image of the numeral "3" is projected on the input. (B) A slice plot of the measured irradiance along the horizontal line shown in (A). (C) A slice plot of the measured irradiance along the vertical line shown in (A).

plots of the measured irradiance along the row and column of pixels indicated by white lines in Fig. 5.37(A). These plots show the irradiance maxima to be well localized within a single optical waveguide. Appreciable coupling between guides is not observed over the 8 mm length of the waveguide array.

The 8 mm waveguide array is useful for imaging demonstrations because it is long enough that the input image would be significantly defocused at the array output if no guiding structure exists. Another test for evaluating the index structure written in to the photopolymer material by the holographic lithography process is to view the index structure using DIC microscopy. The 8 mm waveguide array is too long to be imaged using DIC microscopy, however, so a 1 mm-thick structure was imaged instead. This structure has a pitch of 20 μm, and the result-

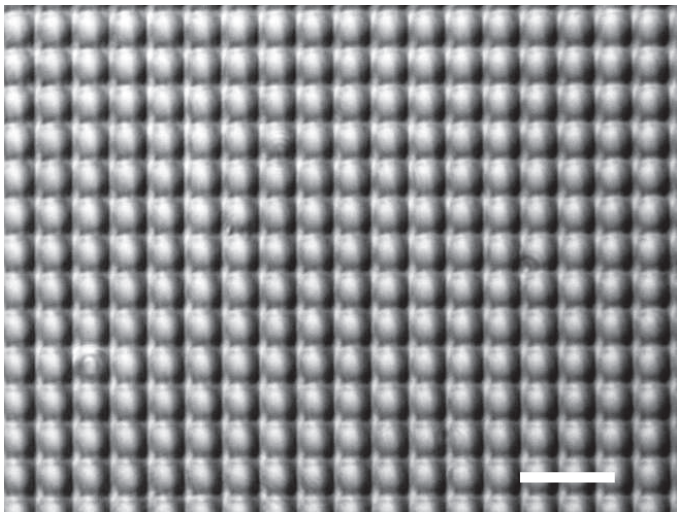

Figure 5.38: A phase contrast micrograph of a portion of a holographic waveguide array taken using a differential interference contrast microscope. The scale bar in the lower right represents 50 μm.

ing DIC microscope image is shown in Fig. 5.38. The 1 mm sample thickness is too large to make use of quantitative DIC methods for quantifying the refractive index variation, but this image gives a qualitative view of the shape and uniformity of the index structure. It appears that the peaks of the index structure are broadened relative to the valleys, but this is difficult to confirm using the qualitative DIC picture. Quantitatively understanding the shape and magnitude of the index structures that result from holographic lithography is important for tuning the process to achieve the waveguide array performance desired for particular applications. Chapter 6 presents an SWI system capable of providing such spatially resolved quantitative index contrast measurements.

The results presented here demonstrate that holographic lithography in volume photopolymers can effectively produce large, 2D optical waveguide arrays using a single exposure with moderate laser power. The work described here represents a proof of principle only, however, and more research is required in order to fully characterize the resulting arrays and tune the material and exposure parame-

ters in order to engineer waveguide arrays having specific functionality. The number and type of experiments undertaken during this work were significantly limited by the availability of suitable photopolymer samples. Two types of photopolymer samples were used: commercial photopolymer manufactured by InPhase Technology, and "Burlap" photopolymer manufactured in the McLeod lab at CU. While the Burlap material showed good sensitivity, high scatter and phase nonuniformity in thick samples prevented the fabrication of viable 2D waveguide arrays. The InPhase photopolymer showed good phase uniformity in 1 mm thick samples, but uniformity degraded for thicker samples. Phase nonuniformities in thick samples used in holographic lithography lead to differential phase shifts among and within the writing beams, resulting in a corruption of the writing pattern. The cause of the phase nonuniformity is most likely shrinkage during the thermal cure of the matrix component. Furthermore, the financial instability and eventual closing of InPhase significantly limited access to their photopolymer. Thus, continued research on 2D waveguide array fabrication in volume photopolymers requires further material development research to develop optical photopolymers that can be cast in thick volumes with a high degree of phase uniformity throughout.

5.6 Summary and conclusions

Volume photopolymers are a promising material platform for integrated optics applications generally, and specifically for optical waveguide arrays. These materials respond to incident illumination with a local increase in index of refraction within the volume of the material. Index structure formation is driven by local monomer depletion resulting in concentration gradients that drive monomer diffusion. This allows volume photopolymers to be patterned in 3D using only a single processing step. The index structures written into volume photopolymers can be fixed using a simple flood cure using incoherent light. This post-cure step

converts all remaining monomer to polymer without inducing any concentration gradients, so no mass transport occurs as the material is rendered insensitive to further illumination.

Volume photopolymers are attractive candidates for fabricating arrays of optical waveguides, which are widely used in applications such as endoscopic imaging and optical interconnects for data transmission. Waveguide arrays can be fabricated in volume photopolymers using a variety of methods. Three methods presented in this chapter are direct write lithography, projection lithography, and holographic lithography. Advantages of direct write lithography include the ability to write arbitrary arrays, including arrays with defects. A major drawback of the direct write approach is its sequential nature, which means that fabrication times for large arrays can be inconveniently or prohibitively long. Also, dense arrays written by direct write lithography must contend with changes in material response over the course of multiple waveguide exposures. A precure step can mitigate this problem in materials where the response variation is primarily due to the consumption of oxygen, which can diffuse into the material from the atmosphere and inhibit the photopolymerization reaction.

Because of the high sensitivity of volume photopolymers, index structure formation does not rely on the high irradiance of focused beams and so low power cw sources can be used to form many index structures at once using projection lithography. This method is an extension of direct write lithography, where the polymer sample is translated through a region in space occupied by a real optical image, rather that just a single focused beam. For waveguide array fabrication, this approach allows for multiple waveguides to be fabricated in parallel. The primary drawback of projection lithography is integration of out-of-focus light. Because volume photopolymers respond to incident illumination with a linear or sublinear response, consumption of monomer occurs not only at the high-irradiance focal

plane, but also in all planes before and after the focus. The out-of-focus exposure can be negligible for short, sparse arrays, but severely limits the index contrast that can be achieved for longer, dense arrays.

Holographic lithography overcomes the problem of out-of-focus exposure while maintaining the ability to write many waveguides in parallel by forming patterns that do not diffract over a large depth of field. This is accomplished by synthesizing illumination patterns using a finite set of plane waves that all have wave vectors with z components of the same magnitude. This results in diffractionless patterned illumination beams, because each plane wave component accumulates the same phase with varying distance in z. Since a practical implementation necessarily utilizes finite-aperture approximations of plane waves, the resulting patterns are not truly diffraction free. Use of well-collimated Gaussian beams provides good plane wave approximations, yielding high-contrast array patterns throughout the overlap region, which can easily be a centimeter or longer. The holographic approach limits the types of waveguide array distributions that can be written, but regular square and hexagonal array patterns can be readily produced.

Optical waveguide arrays fabricated using holographic lithography have been demonstrated for sample thicknesses of up to 8 mm. The holographic lithography system employed a four-beam interference pattern with dynamic phase stabilization to ensure pattern stability. The guiding properties of the arrays have been verified by image transmission, and the index structure has been examined using DIC microscopy.

While the principle of waveguide array fabrication via holographic lithography in photopolymers has been demonstrated, additional research is necessary to achieve the ability to tune the material and exposure parameters in order to exert fine control over the performance characteristics of the resulting waveguide

arrays. One important capability that will help enable this step is quantitative measurements of the index contrast of the waveguide array structures. Not only is a measure of the peak contrast required, but also spatially resolved measurements of the shape of the index structures in order to better understand the mechanism of index structure formation in volume photopolymer materials. The following chapter presents one method to perform spatially resolved quantitative index contrast measurements using SWI. Another challenge that must be overcome to further refine holographic lithography of volume photopolymers is the effective packaging of photopolymer materials that maintain good phase uniformity throughout thick volumes. The number and types of experiments undertaken during the work described here was largely limited by the availability of suitable photopolymer material samples. A more complete discussion of future challenges remaining in the field of waveguide array fabrication in volume photopolymers is presented in Ch. 7.

Chapter 6

Index Contrast Measurement

6.1 Introduction

In this chapter I present a novel implementation of swept-wavelength interferometry (SWI) in the form of an SS-OCT system for performing quantitative and spatially resolved measurements of refractive index contrast. The primary motivation for developing this measurement technology is the characterization of photosensitive polymers and polymer optical devices, such as the 2D polymer waveguide arrays described in the preceding chapter.

Specifically, volume photopolymers used for holographic data storage and hybrid integrated optics applications require quantitative characterization of refractive index structures to help advance physical models of index structure formation, as well as to provide feedback for the development and optimization of lithographic processes for fabricating devices in these materials. Other applications of spatially resolved quantitative index contrast measurements include characterization optical fiber and components such as GRIN lenses and phase microscopy of biological samples.

This chapter begins with a discussion of traditional and emerging methods for measuring refractive index and visualizing microscopic phase objects. This discussion will provide a framework for placing the innovation described here within

the context of other measurement techniques. Next, I will introduce the concept of refractive index measurement via Fresnel reflectivity, which is the fundamental mechanism by which the SS-OCT system performs refractive index measurements. This general approach to index measurement has a long history, but the sensitivity and depth-resolved measurement capability of SWI provides significant improvements over prior methods. The chapter then proceeds to describe how SWI can be employed to perform precise measurements of amplitude reflectivity, before describing the experimental SS-OCT system in detail. This system is based on the principles of SWI developed in Chapter 2, and is capable of quantitative measurements of index contrast as small as 10^{-4} on spatial scales on the order of $10\,\mu$m. Finally, measurement results are presented for gratings and waveguide arrays in volume photopolymers, as well as for commercial optical fibers. This method of index contrast measurement, together with the phase-stabilized holographic lithography system described for grating and waveguide array fabrication, provide a complete toolkit for studying index formation in diffusion-mediated photopolymers.

6.2 Overview of refractive index measurement

Most conventional methods for measuring refractive index, such as minimum deviation, critical angle, autocollimation, and ellipsometry are well suited for measuring the index of bulk samples or thin films of homogeneous solids or liquids [209]. In general, however, these methods are not well suited for measuring variations of refractive index that occur on length scales below 10^{-2} to $10^{-3}\,$m. For example, the autocollimation method performs a measurement of refractive index by determining the angle at which a mirrored prism precisely retroreflects an incident beam [210]. Thus, this method typically requires a bulk sample fashioned in a prism geometry and a broad area illumination region. The critical

angle method determines refractive index using the angle of emergence of critically refracted rays from a grazing incidence illumination along an interface [211]. Bulk samples are required due to the broad interfacial region required by grazing incidence. Ellipsometry is capable of performing measurements of refractive index and thickness of thin films by analyzing the change in polarization state upon reflection of an off-normally incident illumination beam. Ellipsometry can be performed in an imaging configuration to achieve spatially resolved measurements [212], but it requires off-normal incidence that limits the lateral resolution of the measurement.

For characterization of transparent objects with index variations on small length scales, various methods of phase microscopy are typically used. Traditional techniques such as Zernike phase-contrast microscopy and Nomarski differential interference contrast (DIC) microscopy render transparent phase structures visible, but do not offer a quantitative measure of the refractive index. In recent years, numerous efforts have been made to add quantitative measurement capabilities to phase microscopy. These efforts include quantitative DIC microscopy [213], structured-illumination phase microscopy [214], digital holography [215, 216], and optical coherence tomography [130]. Depending on the particular application, one drawback of these phase microscopy techniques is that they measure relative variations in optical path length (OPL) rather than provide a direct measurement of refractive index on microscopic scales. The optical path length depends not only on the local refractive index, but on the thickness of the sample and the refractive index at all points along the path of a ray. For applications such as the characterization of integrated optical devices, fiber measurements, and development of holographic materials, a direct measurement of refractive index variations is needed. Additionally, for the characterization of volume photopolymer materials and optical devices fabricated in these materials, an index contrast measurement that

can be made through a transparent substrate is essential. This chapter presents a novel application of SS-OCT that meets these needs for direct measurement of index contrast on spatial scales on the order of 10 μm.

6.3 Index contrast from Fresnel reflectivity

The index contrast measurement using SS-OCT presented in this chapter is based on a measurement of the reflectivity variations at an interface between two materials. In general, the reflection at such an interface depends on the refractive indices on either side of the interface, as well as the angle of incidence and polarization of the incident light. The Fresnel equations that describe these dependencies for nonmagnetic materials are [217]

$$r_{\parallel} = \frac{n_t \cos\theta_i - n_i \cos\theta_t}{n_i \cos\theta_t + n_t \cos\theta_i}, \tag{6.1}$$

$$r_{\perp} = \frac{n_i \cos\theta_i - n_t \cos\theta_t}{n_i \cos\theta_i + n_t \cos\theta_t}, \tag{6.2}$$

where $r_{\parallel}$ is the amplitude reflection coefficient for light polarized parallel to the plane of incidence, and $r_{\perp}$ is for light polarized perpendicular to the plane of incidence. In these expressions, n and θ refer to refractive index and angle relative to the interface normal, respectively, and the subscripts i and t likewise refer to the incident and transmitted side of the interface. The angles θ_i and θ_t are related by Snell's law: $n_i \sin\theta_i = n_t \sin\theta_t$. For normal incidence, the polarizations become degenerate and the amplitude reflection coefficient reduces to

$$r_{\parallel} = -r_{\perp} = \frac{n_t - n_i}{n_t + n_i}. \tag{6.3}$$

The minus sign arises because to maintain a right-handed coordinate system upon reflection, one of the transverse dimensions requires a sign flip while the other does not. If the index of one material at the interface is known, a measurement of reflectivity therefore allows the other refractive index to be determined. This

approach to index measurement has a long history, and has been employed for spatially resolved index measurements particularly in the context of optical fibers using direct detection of the reflected light [218]. In the present work, Fresnel reflectivity is measured via SWI to provide a highly sensitive and depth resolved measurement of reflectivity that has significant benefits over the traditional direct detection approach. The most important of these benefits for the primary application of photopolymer material and device characterization are:

- The reflectivity measurement is depth-resolved, allowing for the characterization of index structures buried beneath a transparent substrate. Also, reflectivity from planes beyond the focus are automatically rejected as well. This capability is especially important for *en face* characterization of waveguide devices, where direct detection suffers from strong contributions from distal reflections due to guidance.

- Coherent detection provides a direct measurement of the amplitude reflection coefficient, r, rather then a measurement of the power reflectivity $|r|^2$. This provides higher sensitivity and dynamic range, allowing for reflectivity measurements at interfaces that are nearly index-matched as well as at air/material interfaces.

For clarity going forward, let us define two types of index contrast. The first is the contrast at the interface between n_i and n_t. Define Δn as the difference between these two indices:

$$\Delta n = n_t - n_i. \tag{6.4}$$

The second type of index contrast is the one that ultimately is the goal of the measurement; that is, the index contrast that results from the spatial dependence of n_t on the transverse coordinates, x and y. Thus we can define an index contrast

δn relative to a reference location (x_0, y_0) as

$$\delta n(x, y) = n_t(x_0, y_0) - n_t(x, y). \tag{6.5}$$

The latter definition of index contrast is typically the desired quantity for characterization of photopolymer devices and optical fiber index profiling. The maximum value of δn gives the total contrast for a particular device, such as the core/cladding index contrast in an optical fiber, or the dynamic range of a volume photopolymer material. A measurement of $\delta n(x, y)$ can be performed via a spatially resolved Fresnel reflectivity measurement according to

$$\delta n(x, y) = n_i \left(\frac{1 \pm r(x_0, y_0)}{1 \mp r(x_0, y_0)} - \frac{1 \pm r(x, y)}{1 \mp r(x, y)} \right), \tag{6.6}$$

where the upper sign is for $n_i < n_t$, and the lower sign is for $n_i > n_t$. The SS-OCT for index contrast measurement relies on just such a spatially resolved measurement of the Fresnel reflectivity.

The transverse resolution of the index contrast measurement is achieved by focusing the probe beam to a diffraction-limited spot at the interface of interest. The development above for the case of normal incidence is valid for the case of the focused probe beam as well, provided it is uniformly polarized. This is because for given polarization, the focused beam includes a range of angles of incidence such that there are equal portions of the beam polarized parallel and perpendicular to the local plane of incidence. As the angle of incidence increases, $r_{\parallel}$ increases while $r_{\perp}$ decreases until the Brewster angle is reached. For a focused Gaussian beam, most of the power is concentrated at small angles, even at high NA, due to the Gaussian power distribution. Figure 6.1 illustrates the variation with NA of the effective reflection amplitude coefficient for a Gaussian beam incident on an interface with $n_i = 1$ and $n_t = 1.5$. The effective reflection amplitude coefficient is calculated by first taking the Fourier transform of a Gaussian irradiance

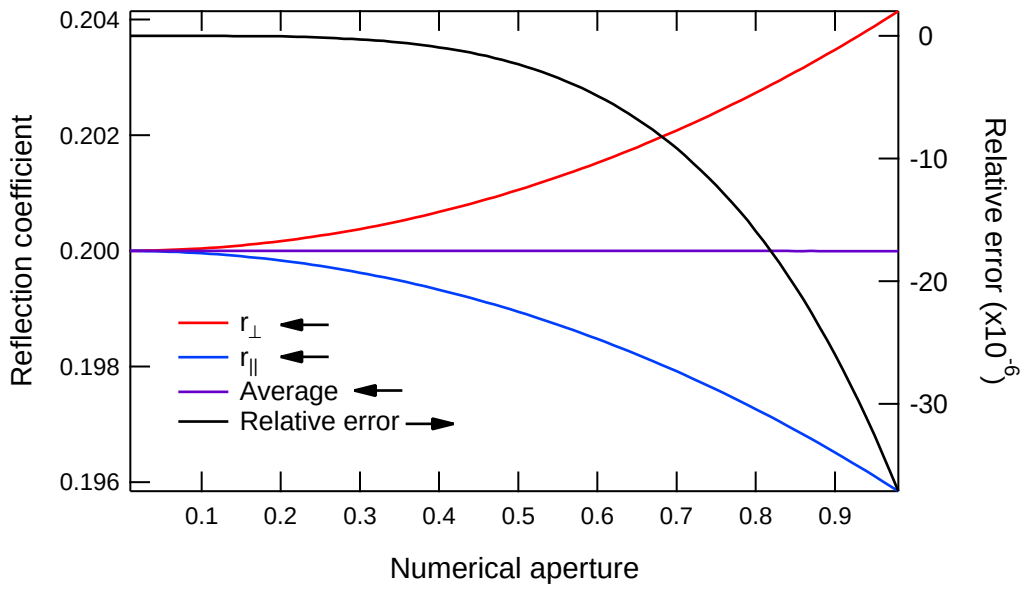

Figure 6.1: A plot of the effective Fresnel reflection coefficients versus numerical aperture for a focused Gaussian beam incident on a material with a refractive index of 1.5 from a material with a refractive index of 1. The black curve is the relative error when the polarization averaged reflection coefficient is compared to the value for a plane wave at normal incidence.

distribution at a waist:

$$\mathcal{F}\{E(x,y;z=0)\} = \iint E_0 e^{-(x^2+y^2)/w_0^2} e^{-2\pi j(k_x x + k_y y)} dx\, dy \tag{6.7}$$

$$\Rightarrow \qquad \mathcal{E}(k_x,k_y;z=0) = \sqrt{\pi} w_0 E_0 e^{-\pi^2 w_0^2 (k_x^2+k_y^2)}. \tag{6.8}$$

The angles of incidence and transmittance in the Fresnels equations can also be written in terms of the wave vector components k_x and k_y as

$$\cos\theta_{i,t} = \left(1 - \frac{k_x^2 + k_y^2}{k_{i,t}^2}\right), \tag{6.9}$$

where the wave vector magnitudes k_i and k_t in the incident and transmitted medium are $k_{i,t} = 2\pi n_{i,t}/\lambda_0$. By substituting Eq. (6.9) into Eqs. (6.1) and (6.2) for the reflection amplitude coefficients, multiplying the result by Eq. 6.8, and integrating over propagating wave vectors $k_x^2 + k_y^2 < k_i^2$ in the incident material, the total reflected amplitude is computed. Performing the same integral

without multiplying by the reflection amplitude coefficients gives a measure of the incident amplitude. The ratio yields the total effective reflection amplitude coefficient plotted in Fig. 6.1. The NA is related to the Gaussian waist w_0 by $\mathrm{NA} = \lambda_0/\pi n w_0$ [219]. Because of the conical distributions of incident angles, for a focused Gaussian beam to be polarized completely parallel or perpendicular to the local plane of incidence would require a radially or azimuthally polarized beam. For linear or elliptical polarization, both parallel and perpendicular polarizations are present, leading to a cancelation of the effect of components incident at angles away from the interface normal. Therefore, the Fresnel expression for normal incidence may be used to convert reflectivity to refractive index contrast using a focused Gaussian beam, even though the beam contains components that are incident off-normal.

6.4 Amplitude reflectivity measurement using SWI

Since quantitative characterization of index contrast can be accomplished via a measurement of Fresnel reflectivity, SWI provides a highly sensitive and depth-resolved means for performing such an analysis. The reflectivity measurement can be framed in terms of scalar device characterization as presented in Sec. 2.6. In the present case, the device transfer function is

$$\mathbf{H} = \begin{bmatrix} r_{\parallel} & 0 \\ 0 & r_{\perp} \end{bmatrix}, \tag{6.10}$$

or, since we are interested only in normal incidence where the polarizations are degenerate,

$$\mathbf{H} = r\mathbf{I}, \tag{6.11}$$

where $\mathbf{I}$ is the identity matrix. In this case, the contribution to the interference fringe pattern due to the reflection at the interface of interest is

$$\tilde{U}(\nu) = 2rU_0 \cos\left(2\pi\nu\tau_0 + \psi\right) \tag{6.12}$$

assuming copolarization. In the experimental system, polarization diverse detection is employed to avoid polarization fading of the fringe amplitude. A Fourier transform of the fringe pattern includes a contribution due to the interface of interest given by

$$\mathcal{U}(\tau) = rU_0 \left\{ \mathcal{W}(\tau) \otimes [\delta(\tau - \tau_0) + \delta(\tau + \tau_0)] \right\} \tag{6.13}$$

where $\mathcal{W}(\tau)$ is the Fourier transform of a windowing function $W(\nu)$ that is multiplied by the frequency domain interferogram prior to performing the Fourier transform, and the symbol $\otimes$ indicates convolution. Here a constant phase factors due to ψ has been dropped. If no explicit windowing function is used, $W(\nu)$ represents the spectrum of the tunable laser source, which, if assumed to be constant, yields a rect function in the frequency domain and a sinc function in the time domain. For precise amplitude measurements of a single tone, a flat-top window is preferred for the best noise performance [220], at the expense of broader peaks and reduced resolution in the time domain. For the experimental work that follows, a fifth order flat-top window has been used to multiply the frequency domain data, which, for a N-point data set indexed by i, is given by

$$W_i = g_0 - g_1 \cos(2\pi i/N) + g_2 \cos(4\pi i/N) - g_3 \cos(6\pi i/N) + g_1 \cos(8\pi i/N) \tag{6.14}$$

where $g_0 = 0.21557895$, $g_1 = -0.41663158$, $g_2 = 0.277263158$, $g_3 = -0.083578947$, and $g_4 = 0.006947368$. Once the window function is applied and the data is transformed to the time domain, the amplitude of the reflection at τ_0 is determined by the amplitude of the peak located at $\tau = \tau_0$ in the time domain data set. The system is calibrated by performing a measurement using an interface between materials of known refractive indices to determine the scaling between time domain peak magnitude and absolute amplitude reflectivity.

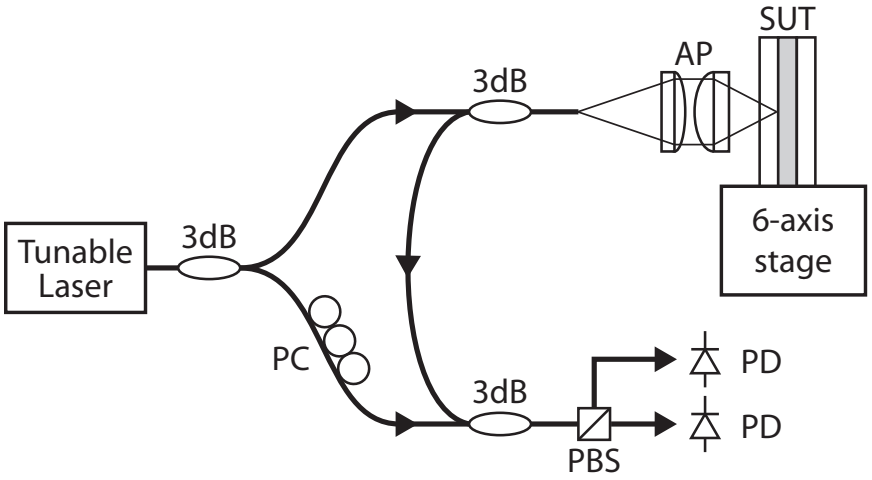

Figure 6.2: Schematic diagram of the SS-OCT system for index contrast measurement. 3dB, 3dB fiber coupler; AP, aspheric lens pair; PBS, polarization beam splitter; PC, polarization controller; PD, photodetector; SUT, sample under test. Not shown is the auxiliary interferometer implementing the frequency sampling method.

6.5 Experimental SS-OCT system for index contrast measurement

6.5.1 Hardware design

The experimental scanning SS-OCT system for index contrast measurement is illustrated in Fig. 6.2. The laser source is an Agilent 81680A tunable laser capable of continuous mode-hop-free wavelength tuning over the range from 1460 to 1580 nm. To account for fluctuations in the tuning rate, an auxiliary interferometer is used as a frequency clock to trigger data acquisition. The relative delays of the trigger interferometer and the measurement interferometer are chosen such that the slow tuning approximation is valid, so higher order correction of sampling errors is not necessary. For this system, the trigger interferometer delay is $\tau_t = 63.9410$ ns. In the measurement interferometer, a 3 dB coupler splits the input light between a reference path and a test path. The reference path is transmissive, and includes a polarization controller that is configured to split the

reference path light equally between the two polarization diverse detector channels. In the test path, another 3dB coupler serves as a circulator, delivering light to the sample under test (SUT) and collecting the reflected signal. The light directed towards the SUT leaves the fiber by way of a polished and anti-reflection (AR)-coated fiber connector. A pair of aspheric lenses (Thorlabs 230260P-C) with a focal ratio of 3.4 images the 10.4 μm diameter mode field of the fiber output to a diffraction-limited 3 μm diameter spot on the surface of the SUT at a depth of 1.6 mm in glass. This depth was chosen to correspond to the thickness of the N-BK7 windows used for calibration samples, which are described in Sec. 6.5.4. Diffraction limited performance at this depth of material was verified via modeling using Zemax optical design software.

The depth sectioning capability of SWI provides a unique capability for optical system assembly based on system modeling. The Zemax model for the free-space probe optics yields a value for the distance between the fiber end facet and the first lens that yields diffraction limited performance at a material depth of 1.6 mm. The depth-sectioning capability of the SS-OCT system provides the convenient capability to precisely measure and set lens separations during system assembly with an accuracy of approximately 50 μm. (The precision ranging technique of Ch. 4 could be employed to improve this figure by several orders of magnitude, but such high accuracy is not needed in this case as it would greatly exceed the tolerances of the model.) The -80 dB (power) sensitivity of the system allows the AR coated lens interfaces to be located even when they are strongly confocally excluded by the diverging probe light and the small SM fiber core. After the lens separation was set to the optimal distance determined by the Zemax model, performance was verified by scanning a reflecting interface axially, and recording the reflected signal as a function of axial position. The separation between the fiber end facet and the first lens was finely adjusted to maximize the

peak reflection signal for an axial scan. This process is equivalent to maximizing the Strehl ratio of the probe beam.

The SUT is mounted on a high-resolution six-axis motorized stage manufactured by Segura Sekei. The resolution of the stage in the linear dimensions is 40 nm. This stage is used to align the interface of interest to the focal plane of the aspheric lens pair and to scan the sample transversely for measurements of reflectivity variations as a function of position. The reflected light from the SUT is coupled back into the single mode fiber and passes through the 3dB coupler that serves as a circulator. This light then interferes with the reference path light at the two polarization-diverse detection channels. The photodetectors are two Thorlabs PDA10CS amplified InGaAs detectors. The detector signals are digitized by a National Instruments PCI-6115 DAQ card. Data processing and user control are accomplished using a LabVIEW software application, described below in Sec. 6.5.3. The reflectivity is found by determining the magnitude of the time domain peak that corresponds to the reflection from the peak of interest in software.

6.5.2 Confocal rejection and surface tracking

Within the subsystem that includes the fiber output facet and the aspheric lens pair, the SM fiber core functions as a confocal pinhole, rejecting reflected light except when the reflector is located at the focus of the objective lens. A traditional confocal microscope makes use of this out-of-focus rejection in order to perform depth-resolved measurements. The SS-OCT system instead gets depth information from the swept-wavelength interference signal, as illustrated in Fig. 6.3 for a single *A*-scan of photopolymer sample packaged as a coupon with a photopolymer layer between two glass substrates. Because the goal is to determine index contrast through a precise reflectivity measurement, the confocal rejection becomes

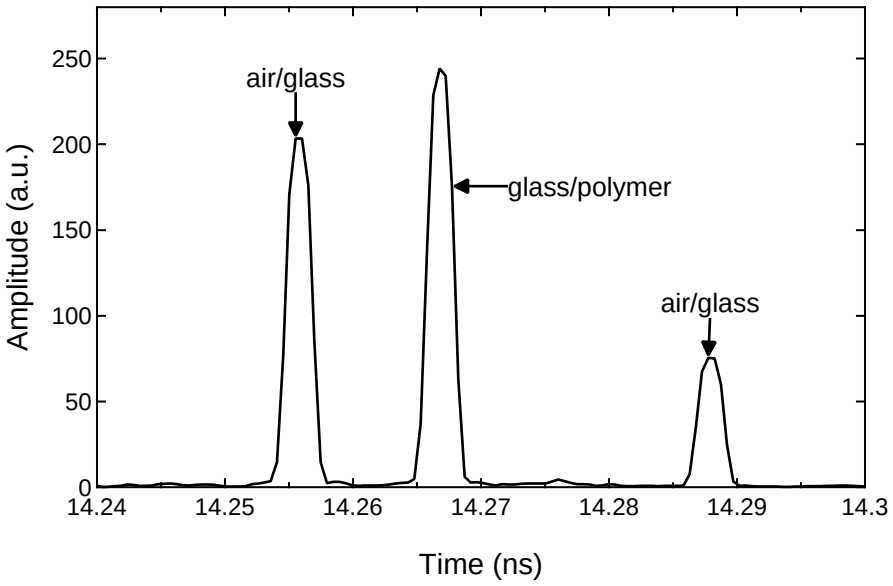

Figure 6.3: An *A*-scan of a polymer volume phase grating between glass substrates. The reflections from the substrate/air interfaces are apparent despite being partially confocally rejected. All three layers are approximately 1 mm thick.

more of a hindrance than a feature, because it means that an accurate reflectivity measurement depends on the interface of interest being located precisely at the focus of the objective lens. If the interface is displaced axially, the signal level falls off, and this is indistinguishable from a decrease in reflectivity due to a decrease in index contrast at the interface. Such axial displacements can occur during scanning if the interface of interest is not perfectly orthogonal to the optical axis of the system, or if the interface is not planar. One way to deal with this issue is to perform an axial scan in z at each (x, y) coordinate during a scan in order to determine the peak reflectivity. The problem with this approach is that such an axial scan adds significant time to the measurement. Because each data point requires the laser to be swept over a bandwidth of several nm, and the maximum sweep rate of the Agilent 81680A laser is 40 nm/s, each point requires ~ 1 s or more to acquire depending on the specific sweep bandwidth and whether or not

any averaging is used. Therefore, implementing an axial scan of 10 to 100 points at each transverse location would result in prohibitively long measurement times.

An alternative approach that solves the problem of confocal rejection masquerading as refractive index variations without the need for a large number of additional measurements is to employ a precise range measurement using the phase-sensitive SS-OCT technique described in Ch. 4. Using the fiber output facet as a reference, the optical path delay to an interface positioned precisely at the objective lens focus can be determined using a single axial scan. Use of digital filtering and phase slope determination for both the fiber end facet and the interface of interest allows this delay to be determined with an uncertainty on the order of 100 as. This value is somewhat higher than that reported in Ch. 4 due to the decreased mechanical stability associated with mounting the sample on a 6-axis stage stack. After performing an axial scan to determine the optical path delay, the path delay can then be monitored for each measurement throughout a 2D scan. If the path delay deviates from the optimal value, it can be corrected by moving the sample axially. In this manner, the problem of confocal rejection can be solved with only a single additional measurement when necessary, rather than via a full axial scan at each transverse coordinate.

6.5.3 Software interface

The data processing and user interface functions of the SS-OCT system have been implemented as a LabVIEW software application. The software interface has been designed to flexibly allow the system to be used as a general purpose OFDR instrument, as well as perform spatially resolved index contrast measurements. The user interface is shown in Fig. 6.4. This section will describe the basic functionality of the software, but is not intended to provide user instruction. The interface is organized into the following seven main functional areas:

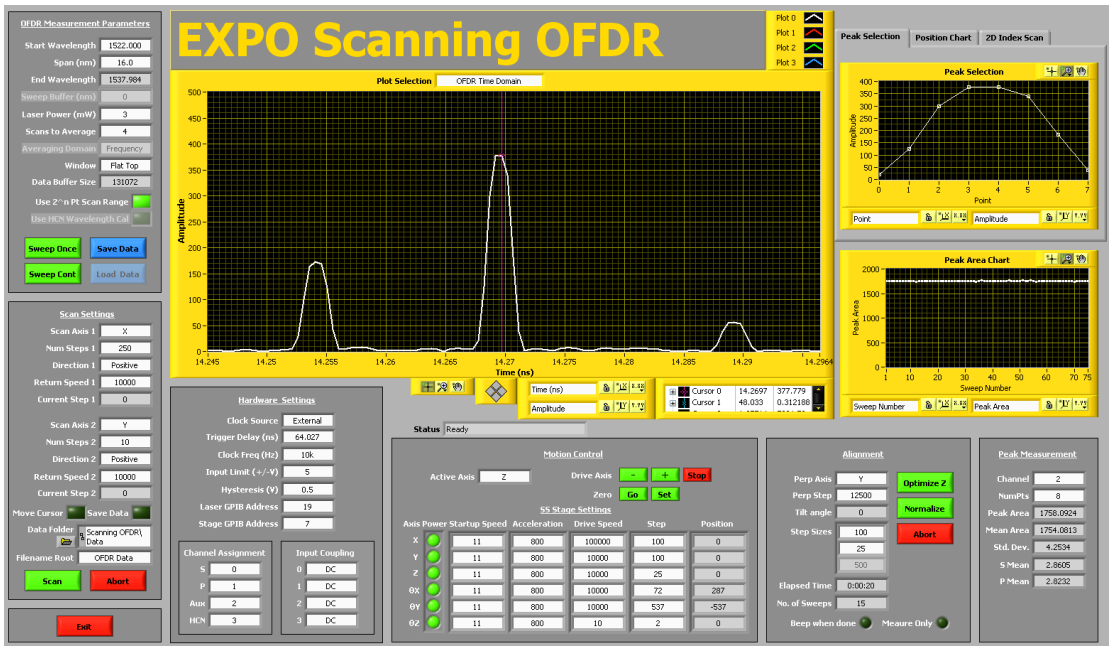

Figure 6.4: The graphical user interface for the SS-OCT system for index contrast measurement.

Hardware Settings This area contains the low-level hardware parameters for the SS-OCT system. The user can select between internally triggered data using the sampling clock available on the DAQ card, or externally trigged data using the trigger interferometer fringe pattern as a frequency clock. For externally triggered data, the user must specify the trigger interferometer delay, and for internally triggered data the user can select a desired clock speed up to the 10 MS/s limit of the DAQ card. This control area also includes settings for the GPIB addresses of the tunable laser and translation stages, the input voltage range setting for the DAQ card, analog input channel assignments and input coupling settings, and a hysteresis level for use with an external clock.

OFDR Measurement Parameters This area contains the controls that allow the user to set the hardware parameters that define a single *A*-scan, including the start and end wavelengths, the laser power, and whether or not multiple *A*-scans should be averaged. It also allows the user to select a windowing function that is

applied to the frequency domain data prior to the Fourier transform. Currently supported windows include a Hanning window for optimal range resolution, and a flat-top window for improved peak amplitude measurement performance. Controls for saving data and for initiating a single *A*-scan or a continuous sequence of *A*-scans are included in this area as well. Greyed-out controls have not yet been implemented in the current software version.

Motion Control This area contains provides the user control over the Segura Sekei translation stage stack. Each of the six axes can have an independent setting for the initial startup speed, acceleration, drive speed, and step size. The step size is given in units of 40 nm "ticks". These settings are used for interactive control of whichever axis is selected as the active axis, as well as for programmatic stage control during scanning.

Scan Settings This area contains the settings for positional scanning of the SUT. Scanning may be performed in one or two dimensions, and the *A*-scans data acquired at each coordinate may be optionally saved.

Alignment This area provides control over the routine that orients the sample perpendicularly to the optic axis of the SS-OCT probe beam. The routine operates by moving the sample a user-specified distance in both the positive and negative directions along the chosen axis, and performing a precision ranging measurement to the interface of interest at each point using the method described in Ch. 4. The two range measurements along with the transverse distance between them allows the orientation angle of the sample to be computed. The corresponding angular stage axis then reorients the sample so that it is perpendicular to the optic axis.

Peak Measurement This area is primarily for indicators associated with the interface reflectivity measurement. Rather than simply gauge the height of a reflection peak, the software uses the area under the peak for improved noise

performance. The number of points used for this peak area calculation is set in this area. The resulting value for the peak area, as well as the average and standard deviation of recent measurements are reported. Also, the mean signal level on the two polarization diverse detection channels is reported for purposes of monitoring the reference path polarization state.

Plot Areas This area is not specifically labeled, but comprises the three graphs including the large main graph and the two smaller graphs at right. The main graph displays the amplitude of the current *A*-scans data. The user may also select to view the raw fringe data acquired on the analog input channels of the DAQ card. When *A*-scans data is displayed, a graph cursor is used to specify the reflection peak that corresponds to the interface of interest. The selected peak is plotted in the small graph in the upper right. The graph on the lower right keeps a running tally of each peak area measurement until it is cleared by the user.

6.5.4 Calibration

To calibrate the refractive index measurement I used calibration samples that each include a planar interface between two regions of known index. These samples were assembled using a front window made from N-BK7 optical glass, which has a refractive index of 1.50091 at a wavelength of 1529.6 nm [221]. The other side of each calibration interface is a calibrated refractive index fluid manufactured by Cargille Labs. The fluid is contained in a 0.5 ml "microbeaker", with an outer diameter of 12 mm. The 12.7 mm diameter N-BK7 optical window is affixed to the filled microbeaker using 5-minute epoxy, forming a sealed glass capsule containing the calibrated refractive index fluid that conveniently fits in a 0.5 inch diameter optic mount. A total of eight calibration samples have been assembled. The eight Cargille fluids used and their indices at 1530 nm are summarized in Table 6.1.

Table 6.1: The refractive index fluids used to calibrate the index contrast measurement.

Cargille Series	n_D at 25° C	Index at 1530 nm and 25° C
AA	1.4000	1.3897
AA	1.4400	1.4300
A	1.4600	1.4497
A	1.4700	1.4587
A	1.4720	1.4605
A	1.4800	1.4677
A	1.4820	1.4695
A	1.4900	1.4767

Because the measured reflection peak amplitudes are proportional to the Fresnel amplitude reflection coefficient, the peak amplitudes $P(n_i, n_t)$ for the eight calibration samples are fit to the Fresnel reflectivity relation according to

$$P = \mathcal{C}|r| = \mathcal{C}\left(\frac{n_t - n_i}{n_t + n_i}\right), \tag{6.15}$$

where $\mathcal{C}$ is the calibration constant of proportionality between peak amplitude and amplitude reflectivity. The measured peak amplitudes for the eight calibration samples along with a curve fit of Eq. (6.15) are shown in Fig. 6.5. These measured values result in a value for $\mathcal{C}$ of 146,767. Over time, the calibration drift slightly with changes in laser power. This can be compensated for by referencing the peak amplitude measurement to a reference power measurement made by picking off a small portion of the laser output with a fiber tap. Alternatively, the calibration needs to be performed regularly. The calibration was found to be stable for time periods on the order of a few days. To recalibrate, measurements of all calibration samples are not required. A measurement of a single calibration sample is sufficient to find a scaling factor to adjust the value of the calibration constant, $\mathcal{C}$.

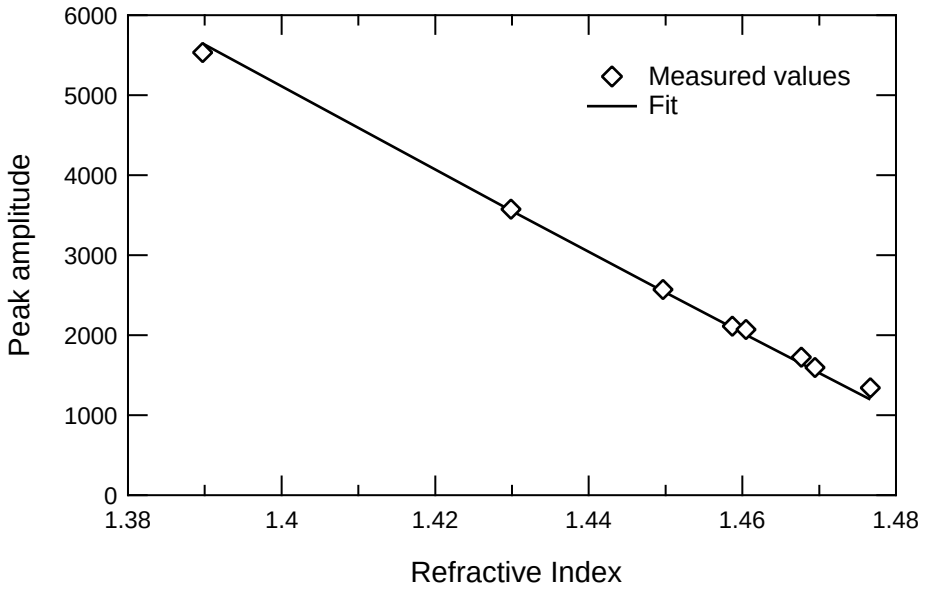

Figure 6.5: Measured reflection peak amplitudes for eight calibration samples of known index contrast, along with a curve fit to the Fresnel reflectivity relation.

6.5.5 Resolution and noise performance

Based on the 12-bit ADC performed by the PCI-6115 DAQ card, one would expect to be able to measure variations in the reflection amplitude coefficient to one part in 10^4. This is because the 12-bit ADC yields 36 dB of dynamic range, and the upper and lower limits of this dynamic range can be configured by adjusting the photodetector gain and the input voltage range on the DAQ card. For typical operation, the dynamic range is configured such that a 4% back reflection fills 11 bits so that the ADC does not saturate. Because the SS-OCT system employs coherent detection, the amplitude of the fringe pattern is directly proportional to the amplitude reflectivity, not the power reflectivity. Thus the full 36 dB dynamic range is available for amplitude measurements, and power measurements may be performed with a 72 dB dynamic range. An amplitude coefficient of $r = 0.2$ spread over 11 bits means that $0.2/2048 \approx 10^{-4}$ is the best resolution that one might expect. Converting this resolution figure for the amplitude reflection coefficient to

an index contrast value using Eq. (6.6) yields an index contrast resolution on the same order. From the calculations presented in Sec. 2.9, the quantization noise due to the ADC is expected to be the dominant noise source in the measurement.

6.6 Index contrast measurement results

The experimental SS-OCT system described above has been used to characterize a variety of refractive index structures, including commercial optical fibers and holographic structures in volume photopolymer materials. To verify the technique, the first measurement was a determination of the core/cladding index contrast of Corning SMF28 optical fiber. This is a standard telecommunication fiber that is well known and well characterized. The SS-OCT measurement of the index contrast yielded a value of $0.366 \pm 0.020\%$, which compares favorably to the specified contrast of 0.36%. Another measurement to test the validity of the SS-OCT index contrast measurement method was performed on Corning 62.5/125 gradient index multimode fiber. The results of this measurement are shown in Fig. 6.6. The peak measured index contrast is in good agreement with the specified index contrast for this fiber of 2%. For both of these fiber measurements, the fiber was prepared by cleaving the fiber end. The fiber was mounted so that the SS-OCT probe beam was normally incident on the cleaved fiber end facet. In the case of the SM fiber, the $8.2\,\mu$m diameter core was located by monitoring the amount of light coupled into the core by directing the back end of the fiber to an optical power meter. A transverse scan across the fiber end facet that includes both cladding and core reflectivity measurements yields a value for the index contrast. For the multimode fiber, the large core area did not require active alignment, and two transverse scans, one horizontal and one vertical, are sufficient to locate the center of the core. The data in Fig. 6.6 is for a third transverse scan across the full fiber end facet and passing through the center of the core.

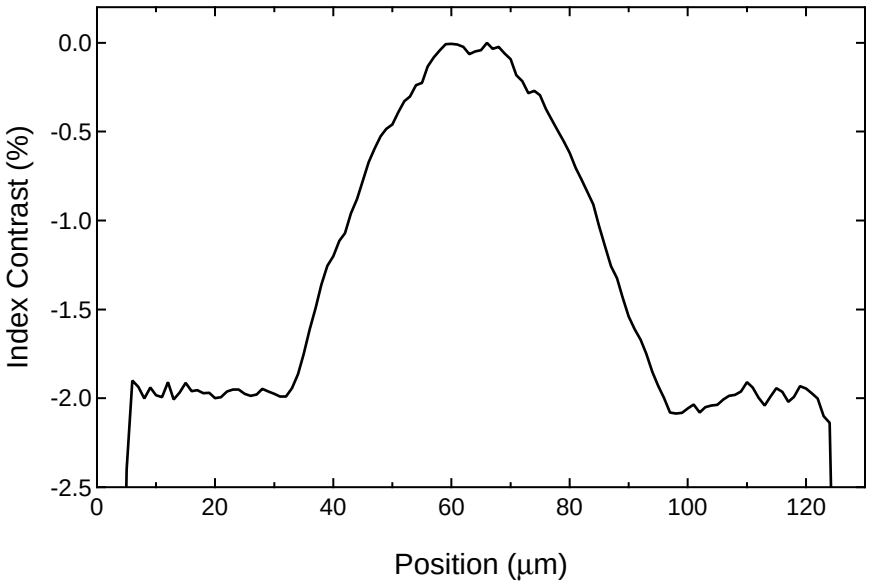

Figure 6.6: Index contrast measurement for Corning 62.5/125 gradient index optical fiber. The index contrast is normalized to the peak reflectivity. The index contrast specified by the manufacturer is 2%.

The primary limitation for this method of characterizing optical fibers is the surface quality of the cleaved end facet. Depending on the quality of the cleave, various amounts of surface roughness and local surface curvature may exist. End facet contamination by dust or dirt is also a concern. Generally, poor surface quality leads to a reduction in the received reflection signal due to scattering or lensing effects. Surface contaminants may also take the form of strong point reflectors that increase the reflection signal at discrete locations. Variable surface quality causes point-to-point measurement noise in the index contrast measurement that can be greater than the intrinsic performance of the SS-OCT system. The variation in the index contrast value for the cladding regions and at the center of the core of the multimode fiber shown in Fig. 6.6 is most likely due to surface imperfections.

One of the key advantages of the SS-OCT approach surface reflectivity measurements is the ability to perform depth-resolved measurements. This allows for

the mitigation (though not necessarily elimination) of the surface quality issue for certain types of test samples. For example, volume photopolymer samples are often cast under or between glass substrates. By choosing a substrate with high optical quality, the resulting substrate/polymer interface will also be of high quality, provided no delamination occurs. For the subsequent results presented for index contrast measurements of volume photopolymers, glass substrates and containers of varying quality were used, so some point-to-point measurement noise due to imperfect surface quality exists in these measurements. For future measurements, attention to the surface quality of the substrates can lead to improved results if high-quality optical windows are used.

Measurement of index contrast in volume photopolymer materials is one of the primary motivations for developing the experimental SS-OCT system. Eleven repetitions of one such measurement for a plane-wave holographic grating written in volume photopolymer appear in Fig. 6.7. The photopolymer material in this sample is InPhase HDS-3000 with half of the standard photoinitiator concentration, packaged as a 1 mm layer between glass microscope slides. The grating was fabricated using the holographic lithography system described in Sec. 5.5.3 by blocking two of the four writing beams. The exposure power was 6.8 mW per beam and the exposure time was 2 s. The grating pitch is 20 μm. Repetition of the index contrast measurement shows that the standard deviation of the measured index contrast values at each point (plotted at the top of Fig. 6.7) is generally less than 10^{-4}, which is in good agreement with the expected measurement resolution from the arguments of Sec. 6.5.5. This measurement immediately indicates that the material response to incident illumination is not linear, since the grating index structure displays marked deviation from the sinusoidal exposure pattern. The broadening of the peaks and narrowing of the valleys relative to a pure sinusoidal tone is indicative of sublinear material response. Additionally, a small dip

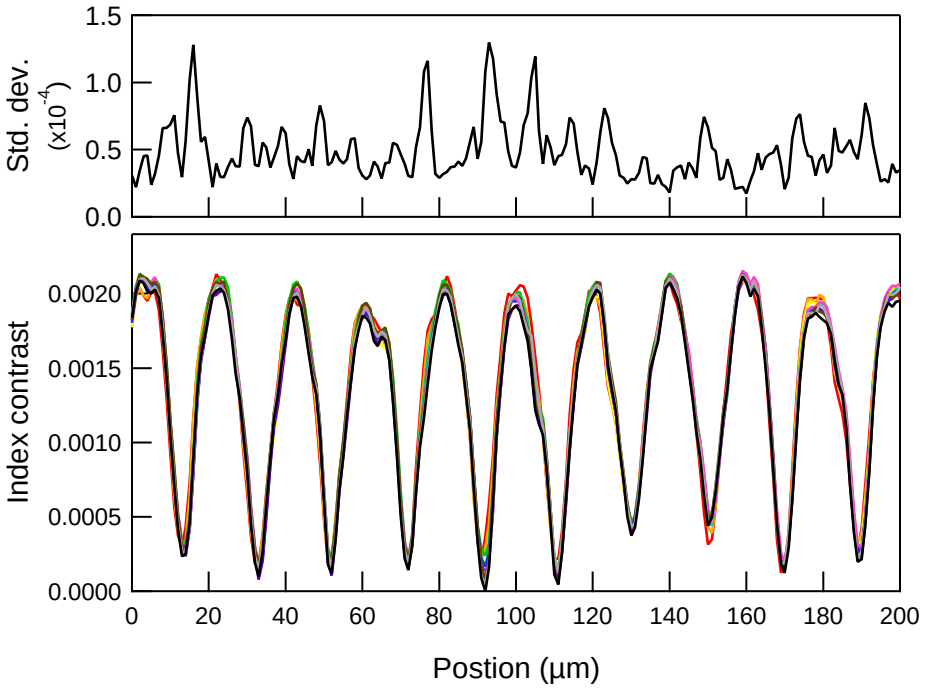

Figure 6.7: Eleven repeated measurements of the index contrast over a 200 μm region of a holographically written grating in volume photopolymer. At top is the standard deviation of the eleven measurements at each spatial location.

is visible at the top of several index contrast peaks. While these features are at this limit of the transverse spatial resolution of the system, they are repeatable as indicated by the eleven repetitive measurements. While they could be caused by surface roughness or contamination of the substrate prior to sample assembly, they could also be due to incomplete monomer diffusion into the high-irradiance regions of exposure pattern* [176].

Because the holographic exposure used Gaussian beams, various locations across the grating received differing irradiance levels during the exposure. The

*Similar measurements of index contrast in holographic phase gratings in volume photopolymer have been performed by Keith Kamysiak, whereby the Fresnel reflectivity is measured using direct detection with an autobalancing photodetector. While this approach does not offer depth resolved measurements like SS-OCT and requires high-index substrates due to reduced sensitivity relative to SS-OCT, it has the advantage of operating at visible wavelengths yielding improved transverse resolution. These measurements have confirmed the existence of regular index contrast dips at the peak of 20 μm pitch gratings in HDS 3000.

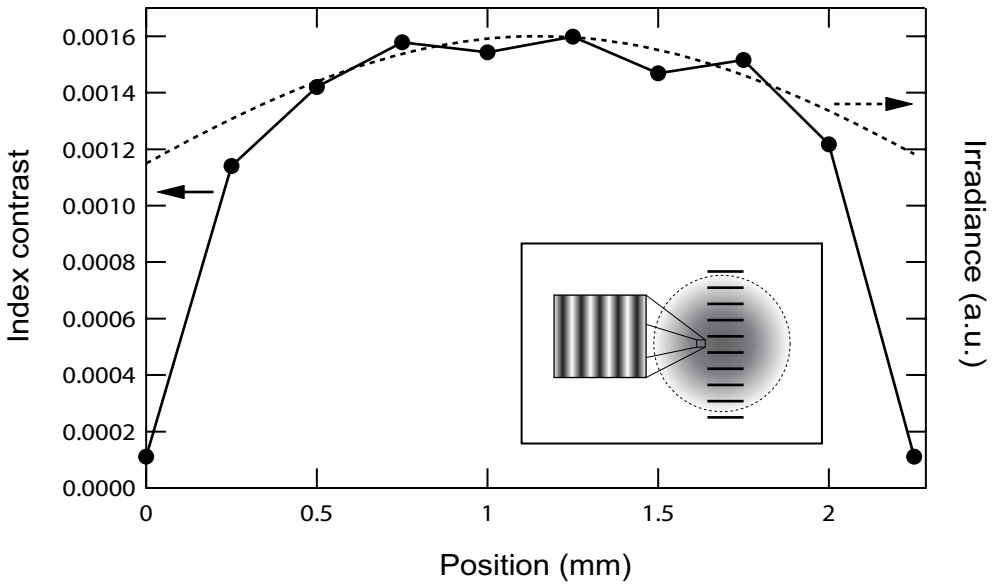

Figure 6.8: A plot of the index contrast present at various locations across a plane-wave holographic grating written in volume photopolymer (solid curve). Each data point corresponds to the peak-to-peak index contrast of the grating as a function of position as determined by a 250 mum linear SS-OCT scan. The dotted curve is the approximate irradiance envelope of the exposure used to fabricate the grating, normalized to the peak height of the index contrast plot. Note that the grating has much sharper edges than the Gaussian irradiance profile. Inset: The location of the 1D scans relative to the exposure region and the orientation of the grating structure.

SS-OCT system can probe the index contrast spatially across the grating area to characterize the material response to the different irradiance levels. Figure 6.8 shows the results of ten linear scans performed across the grating regions at different positions. The inset shows the scan locations relative to the exposed grating region and the orientation of the grating index structure. The index contrast value plotted on the vertical axis is the peak-to-peak index contrast of the fundamental sinusoidal tone of the grating. Note that the index contrast across the exposure region is relatively constant, and falls off sharply at the edges. For comparison purposes, a Gaussian of approximately the same width as the envelope of the exposure pattern is plotted as well. The index contrast of the grating falls off

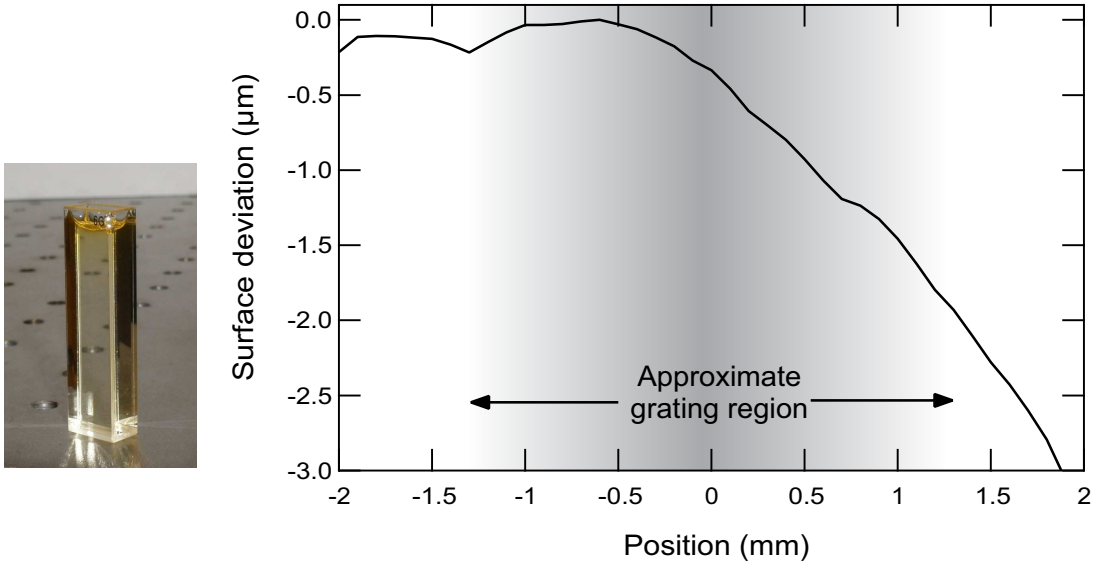

(A) (B)

Figure 6.9: (A) A photograph of a volume photopolymer sample packaged in a glass fluorimetry cell. (B) The surface profile of the glass/polymer interface of the sample in (A) over a region where a holographic grating has been written.

significantly more sharply than the Gaussian irradiance distribution used to fabricate it. This plot indicates that a threshold level exists in the index structure formation process, which can be advantageous for producing broad area structures with good uniformity.

To demonstrate the ability of the SS-OCT system to track a non-planar surface during a measurement scan, the system was used to measure the surface profile of a photopolymer sample packaged in a glass fluorimetry cell. A photograph of the sample is shown in Fig. 6.9(A). When the liquid polymer precursors cure to form a solid matrix polymer inside the fluorimetry cell, shrinkage along with surface adhesion to the glass causes the cell facets to bow inward. After lithographic exposure to create index structures in the sample, a small amount of additional shrinkage occurs. Because of confocal rejection of reflected light by SM fiber coupling in the SS-OCT system, measurement errors will occur if the focus of

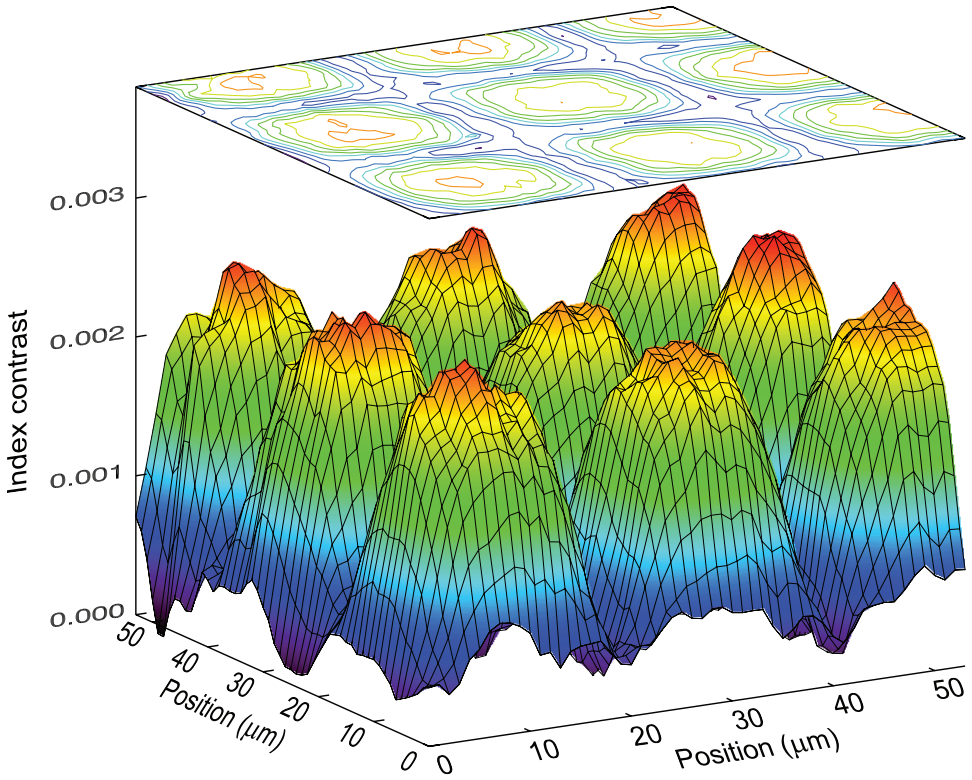

Figure 6.10: Surface and contour plots of measured index contrast data for a holographically written 2D waveguide array in volume photopolymer.

the objective lens does not track the glass polymer surface during a measurement. The surface profile of the polymer sample in a region where a holographic grating has been written is shown in Fig. 6.9(B). Note the bowing of the surface, coupled with a small additional bowing in the grating region. This surface tracking ability allows the SS-OCT system to effectively perform index contrast measurements of non-planar samples.

A final example of an index contrast measurement performed with the SS-OCT system is shown in Fig. 6.10. This is a quantitative index contrast measurement for the 2D waveguide array structure shown in the DIC microscope image in Fig. 5.38. Whereas the DIC image provided a qualitative view of the waveguide array index structure, the SS-OCT measurement provides a quantitative value of 0.002 for the peak index contrast. Also, this measurement provides a quantitative

picture of the shape of the index structure that forms each guide, showing them to be broader than the irradiance peaks of the exposure pattern (Fig. 5.23). The narrow valleys are indicative of a sublinear material response to incident irradiance, and the broad peaks with small central dips are consistent with diffusion-limited index structure formation. Depending of the specific application, characteristics such as these may or may not be desirable. This type of quantitative index measurement is a key capability for further understanding of index structure formation in volume photopolymers and for designing and optimizing lithographic processes for producing high quality, functional optical devices in these materials.

6.7 Summary and conclusions

This chapter has presented a novel application of SWI in the form of a SS-OCT system for performing quantitative measurements of refractive index and refractive index contrast based on Fresnel reflectivity. This method provides a direct measurement of refractive index variations on spatial scales as small as $10\,\mu$m. The depth sectioning capability of SS-OCT allows precise Fresnel reflectivity measurements from buried interfaces with a higher degree of signal isolation from other reflections that may be present than can be achieved using confocal rejection alone. The SS-OCT system has been implemented as a laboratory instrument including a graphical user interface suitable for use by anyone interested in performing spatially resolved reflectivity measurements with a moderate amount of user instruction. To verify the accuracy of the instrument, measurements of core/cladding index contrast were performed on commercial optical fibers. The instrument has also been used to measure phase gratings and optical waveguide arrays written in volume photopolymers. The resolution of the index contrast measurement in approximately 10^{-4}, and is limited by the quantization noise intrinsic to the 12-bit ADC used in the instrument. Point-to-point variation in the

measured reflectivity is also dependent on the quality of the interface of interest. For poor surface qualities, this becomes the limiting factor for the resolution of the index contrast measurement. Another significant limitation of this SS-OCT system is the slow measurement speed, which limits 2D scans to small areas. The slow speed results from the sweep capabilities of the swept-wavelength optical source, which has a maximum sweep rate of 40 nm/s. Also, the transverse spatial resolution is limited by the NA of the focusing lens and the relatively long C-band wavelength range. Improved speed and resolution would make this instrument even more useful for its target application of quantitative index contrast characterization of optical devices fabricated in volume photopolymer. Suggestions for further system improvements are given in Ch. 7. Even without further improvement, the SS-OCT system described here will be a valuable tool for use in optical photopolymer material development and for providing quantitative feedback in the design and optimization process for lithographic device fabrication methods in volume photopolymers.

Chapter 7

Conclusions and Future Work

7.1 Summary

Optical interferometry using swept-wavelength sources has proven to be a valuable measurement technique that has undergone impressive growth since it was first introduced in the early 1980s. The relative maturity of swept sources has led to the introduction of several commercial instruments based on SWI over the past decade. The widespread interest in OCT imaging, along with continuing extension of OCT concepts to applications beyond biomedicine, continues to drive research and innovation in spectral interferometry. This thesis has presented several advancements to the state of the art in SWI technology for performing precision measurements.

Chapter 1 provided an historical introduction to SWI and a description of its development over the past thirty years in the context of the major applications for which it has been used. Beginning as a method for characterizing reflectivity in optical fibers and fiber network components, the application base of SWI has grown to include amplitude, phase, and polarization measurements for telecommunication applications, as well as free space ranging via FMCW lidar, fiber optic sensing using OFDR, full-field surface profilometry, and biomedical imaging with SS-OCT.

Chapter 2 is intended as a theoretical and practical introduction to SWI for future graduate students who may continue and build on the work of this thesis, as well as others who for whom such an introduction may prove useful. To my knowledge, there is currently no text that provides a comprehensive introduction to the practical implementation of SWI, and my hope is this chapter can play a small part in filling this void. The only text that concentrates solely on swept-wavelength techniques is the book by Zheng [52], but this volume focuses primarily on sensing applications and completely omits references to OCT, OFDR, and optical component testing. Key concepts such as a discussion of source tuning characteristics are missing from Zheng's analysis. The only other notable text is Brezinski's treatment of OCT [129], which is dominated by discussions of TD-OCT and specific applications of OCT in medicine.

Continued advancements in swept-wavelength optical sources providing faster sweep rates and increased coherence have led to practical SWI systems for which interferometric monitoring of the instantaneous frequency of the source are subject to higher-order errors in the frequency measurement. The work presented in Ch. 3 represents the first in-depth analysis of the effect of tuning rate fluctuations since Glombitza and Brinkmeyer presented the first complete description of an interferometric trigger in 1993 [22], when available source tuning rates and coherence lengths made the validity of the slow tuning approximation a foregone conclusion. I have shown here that sampling errors resulting from a breakdown of the slow tuning approximation can be balanced through another source of sampling errors, namely finite delays in optical and electronic hardware that exist for each data acquisition channel in an SWI system. These results are applicable to SWI systems independent of application whenever fast sweep rates and/or long interferometer delays are required. A majority of the content in Ch. 3 was the subject of an article published in the journal *Optics Express* in 2008 [115].

One of the most exciting recent developments in spectral interferometry including SWI has been the use of phase information for sub-nanometer measurements of relative displacement. Relative displacements down to 39 pm have been reported [109]. Chapter 4 describes three important developments that allow for the extension of phase-sensitive SWI to absolute ranging. The first is the use of digital filtering and phase-slope estimation to yield quantitative, high-resolution depth measurement adjustments to within a factor of 5×10^{-5} of the transform-limited depth resolution of the system. The second is the use of self-referenced ranging measurements to cancel environmental noise and errors due to sweep-to-sweep variations in the tunable source output. The third contribution is a quantitative analysis of the time domain sampling grid accuracy, along with a description of accurate sampling grid calibration using a wavelength calibration artifact. These developments are the subject of a paper that has been accepted for publication in *Optics Express* in 2011 [222].

An area where SWI holds great promise for contributing needed measurement capabilities that are not currently available is in the characterization of volume photopolymer materials. Because these materials are optically addressable at the micron scale in bulk volumes, characterization of the resulting index structures necessitates new measurement capabilities since current methods for refractometry and phase microscopy generally require uniform bulk material or thin samples, respectively. Chapter 5 examines one application of volume lithography in photopolymers that has motivated much of the SWI development presented in this thesis. This application is the fabrication of 2D arrays of optical waveguides. Because of their high sensitivity and ability to be cast in a variety of form factors, waveguide arrays in photopolymers are an interesting potential avenue for applications such as VCSEL array coupling, studies of wave propagation in periodic media, and components for endoscopic imaging. After discussing the relative mer-

its of three approaches to waveguide array fabrication in volume photopolymers — direct write lithography, projection lithography, and holographic lithography — I present an experimental realization of a holographic exposure system and demonstrate the fabrication of imaging waveguide arrays. Novel components of this system include a fiber-based active phase stabilization system and a precision alignment process to produce broad-area holographic exposures with high contrast. A summary of the experimental holographic lithography work appears in the proceedings of the Optical Society of America *Frontiers in Optics* conference for 2010 [223], and a full description of this work will be the subject of a future publication.

Chapter 6 presents one implementation of an SWI system that provides the needed quantitative index contrast measurement capability that has been noted in the context of volume photopolymer lithography. This measurement technique can also be valuable for material characterization of polymers for holographic data storage applications, as well as for testing other types of optical devices that rely on spatially varying refractive index, such as optical fiber and GRIN lenses. The system uses the sensitivity intrinsic to SWI measurements to detect spatial variations in refractive index through a transversely scanned measurement of Fresnel reflectivity. The ability of SWI to distinguish optical paths with different propagation delays allows the measurement of refractive index structures that are buried beneath transparent substrates. High sensitivity enables accurate measurements even when the substrate and the structure of interest are nearly index-matched. The analysis of reflectivity data based on the Fresnel equations for normal incidence are shown to be valid for focused Gaussian beams despite their finite angular spectrum provided that they are uniformly polarized. The resolution of the index contrast measurement is 10^{-4}, and is limited by the 12-bit quantization in the DAQ hardware. The system has been used to successfully perform quan-

titative refractive index contrast measurements for a range of devices including commercial optical fibers, as well as gratings and optical waveguide arrays written in volume photopolymers. A summary of this work is included in the proceedings of the Optical Society of America *Frontiers in Optics* conference for 2010 [224], and a more complete description in a future publication is planned.

While SWI has matured over the past decade to the point where it is the basis for multiple commercial instruments and it has been used in clinical medical applications, it is still a fertile ground for further research and innovation. This thesis has presented several such innovations, and the opportunity exists for many more exciting developments. The following section provides some suggestions for future directions that build on the work presented in this thesis.

7.2 Future directions

7.2.1 Sampling error correction

While the work presented in Ch. 3 has theoretically and experimentally established the principle of sampling error correction and the extension of the frequency sampling method to the regime beyond the slow tuning approximation, the experimental demonstration was limited to a single path in the measurement interferometer. Because of the potential for frequency dependent delays in the photodiode amplifiers and data acquisition electronics, implementation of sampling error correction by matching delays for an instrument that must operate over an extended depth range will probably require either a frequency dependent delay line or careful engineering of a flat group delay response of the system electronics. While a solution that involves a dispersive optical delay is conceivable, a more practical approach is most likely to be an exercise in electronic circuit design.

7.2.2 Applications of existing SWI hardware

The system presented in Ch. 4 for precision absolute ranging and the system described in Ch. 6 for quantitative index contrast measurements are fundamentally the same system, with small differences in ancillary hardware and software, such as the 6-axis stage stack and phase-slope processing algorithms. In its current form, this system is a suitable foundation for further research into the applications of phase-sensitive precision ranging the characterization of refractive index structures.

One natural extension to the work on precision ranging is to utilize the translation stage stack to implement a scanning surface and thickness profilometry system. The resolution of the system could allow for thickness profiling of silicon wafers down to the level of a single atomic monolayer. By adding a high NA objective lens to the system for micron-level transverse resolution, the system could be used for quantitative surface profilometry of lithographically fabricated structures and micro-optical components.

The scanning system for index contrast measurement can be extended by adding a measurement of dispersion. The Fresnel reflectivity measurement using SWI has the capability to distinguish between the dispersion exhibited by the two materials on either side of the reflecting interface. The dispersion due to material on the incident side of the interface will manifest in the phase of the measured signal. Material with finite first-order dispersion will yield a parabolic rather than a linear phase response versus optical frequency. This is because the different spectral components that compose the optical frequency sweep will accumulate different amounts of phase progression as they double-pass through the incident material upon reflection. The reflected light is never transmitted through the second material, thus its dispersion does not contribute to the phase of the detected signal. However, the amplitude of the Fresnel reflection will vary with the value of

the phase index across the sweep bandwidth. Thus, the dispersion of the material on the transmitted side of the interface is contained in the spectral variation of the amplitude reflectivity. By appropriately processing both the phase and amplitude of the reflected signal, the dispersion of both media can be determined.

Another possible extension of the existing index contrast measurement system capability is to increase the sensitivity by shifting the 72 dB dynamic range of the 12-bit DAQ to span lower reflectivity values for measurement of index structures buried beneath substrates with closely matched indices. This would improve the resolution of the index contrast measurement enabling the characterization of weaker index structures. This can be accomplished by increasing the photodetector gain and AC coupling the analog inputs to the DAQ card. A shorter trigger delay may be necessary for operation with increased gain settings because the bandwidth of the current Thorlabs PDA10CS photodetectors decreases for higher gain settings. Also, the back reflection from the fiber end facet may require reduction so that it does not saturate the measurement. A combination of an angle cleave with an AR coating could solve this problem.

7.2.3 SWI system alterations and improvements

7.2.3.1 Increased speed via a fast swept source

One of the biggest drawbacks to the current SS-OCT system for measuring spatial refractive index variations is the speed of the measurement. The maximum tuning rate setting of the Agilent 81680A laser is 40 nm/s, which, coupled with sequential GPIB control of the laser wavelength sweep and translation of the sample using the Seruga Seiki stages, results in measurement rates of 1 Hz or slower. This slow measurement speed severely limits the ability of the system to perform high-resolution 2D scans in reasonable time periods. Also, slow measurement times allow environmental noise to couple into measurements, limiting the precision of

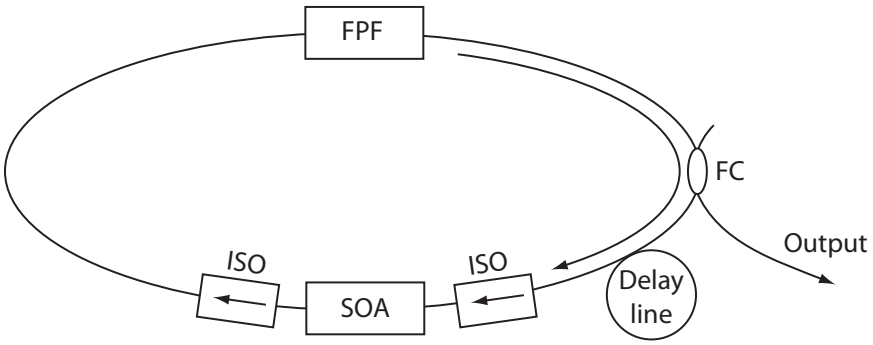

Figure 7.1: Diagram illustrating the layout of a Fourier domain mode locked laser. FPF, fiber Fabry-Perot filter; FC, fiber coupler; ISO, isolator; SOA, semiconductor optical amplifier. Figure adapted from Ref. [98].

absolute optical path length measurements performed using phase-sensitive SWI. The utility of the experimental SWI system could be substantially improved by increasing the measurement speed.

A measurement speed increase of several orders of magnitude can be implemented in a relatively straightforward fashion by leveraging technological advances that have accompanied the widespread interest in optical coherence tomography in over the past two decades. As described in Ch. 1, OCT was originally introduced as a means to perform depth-resolved imaging by combining time-domain low-coherence interferometry with a raster-scanning system [64], with the frequency domain methods SD-OCT [67] and SS-OCT [66] being introduced shortly thereafter. In 2003 two groups [68,69] published work demonstrating an intrinsic sensitivity advantage of the frequency domain approaches, stimulating research in SS-OCT and the associated swept-wavelength sources. Among the recent developments in high-speed swept sources, FDML lasers are of particular interest. They achieve high sweep rates by including a fast, electronically addressable wavelength filter (typically a tunable fiber Fabry-Perot filter) within a fiber ring cavity, as shown in Fig. 7.1. The pass band of the filter is swept at a rate equal to the optical circumnavigation rate of the ring cavity while the gain medium is pumped

to achieve a population inversion. Provided group velocity dispersion is properly managed within the cavity, this configuration causes the phases of the longitudinal cavity modes to become locked such that modal interference at the filter location results in constructive interference at the instantaneous filter pass band wavelength, and destructive interference at all other wavelengths. Thus light of one optical frequency passed by the filter propagates around the cavity and reencounters the filter again with its pass band tuned to the same frequency. In this way, a complete frequency sweep is stored within the laser cavity, and the output is a train of continuous wavelength sweeps with a repetition rate given by the optical transit time of the ring cavity. This type of mode-locked operation allows cavity modes for all spectral components to be simultaneously active within the cavity. This is in contrast to typical swept-wavelength laser operation, where lasing at each wavelength throughout a sweep must build up sequentially from amplified spontaneous emission. FDML lasers are analogous to traditional mode locked lasers, where all cavity modes have constant phase leading to constructive interference at a single spatio-temporal location within the laser cavity and resulting in a train of short pulses at a repetition rate determined by the cavity round-trip transit time. In an FDML laser, the cavity modes are also locked, but with a different phase relationship.

Initial demonstrations of FDML lasers used an electrically pumped SOA with a peak gain near 1310 nm as the gain medium together with a cavity constructed using Corning SMF28e optical fiber, which has a zero dispersion wavelength between 1310 and 1324 nm. These choices make additional dispersion management components unnecessary [97]. The frequency sweep can be made moderately linear by optimizing the waveform used to drive the tunable filter [101], but for phase measurements an interferometric trigger or data resampling is necessary. Because the sweep rate can be so high (sweep repetition rates up to 370 kHz

have been demonstrated for a 120 nm range at center wavelength of 1300 nm [98]), limitations on data acquisition speeds significantly reduce the overall measurable depth relative to the slowly swept laser used in the experiments described in this thesis. For example, a 100 kHz sweep repetition rate for a 100 nm range about 1300 nm corresponds to a frequency sweep rate of 1.775×10^6 THz/s, which when coupled with data acquisition hardware capable of 1 GS/s yields a Nyquist criterion for the maximum interferometer path length difference of 8.45 cm (see Sec. 2.5.1.1). The coherence length of FDML laser demonstrations are also on the order of centimeters, so a system implementation incorporating an FDML laser would have a more limited depth range, though it would be sufficient for index contrast and profilometry applications.

7.2.3.2 Increased speed via multiplexing

The speed of multi-point measurements using the existing Agilent 81680A tunable laser can be improved by exploiting the high coherence of the laser to multiplex multiple measurements in the time domain. The current SWI system uses a trigger interferometer with a relative delay of approximately 64 ns, yielding a double-pass distance range of roughly 6.5 m. The coherence of the source and the acquisition speed capability of the National Instruments PCI-6115 DAQ card would support the extension of this distance range to 100 m or more. For index contrast measurement or profilometry applications, the distance range needed for any single point measurement is only a few millimeters or perhaps a centimeter at most. This means that the 100 m depth range of the system could be divided into as many as 10,000 individual depth bins, each corresponding to a different probe path. For a reflection system, each probe path would require an independent fiber as shown in Fig. 7.2, so 10,000 may be beyond the range of practicality, though perhaps 100 independent probes would be feasible. In this case, the total measure-

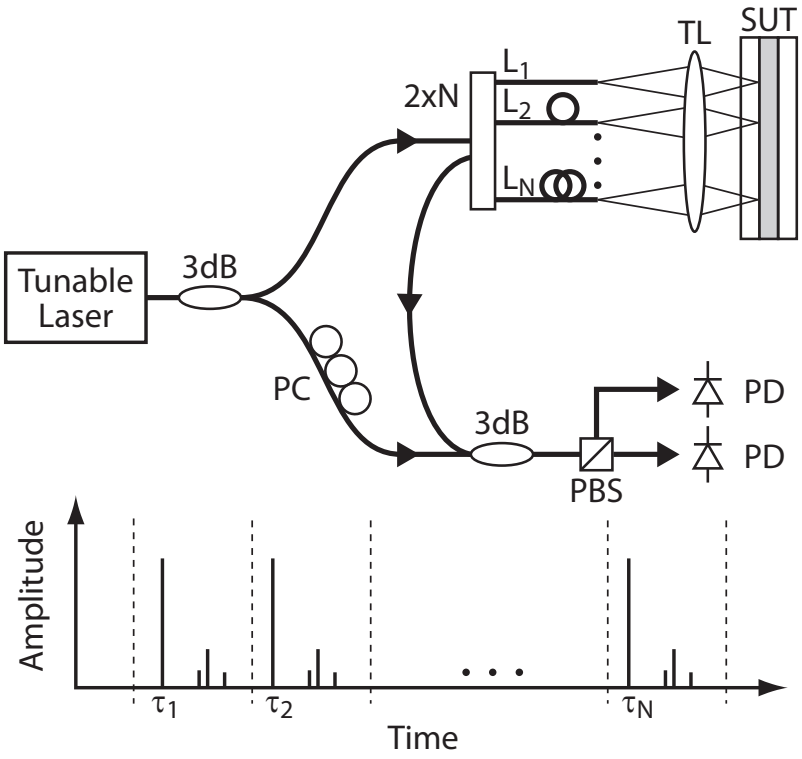

Figure 7.2: Conceptual diagram for time-domain-multiplexed SWI measurements. At top, the optical network for a multiplexed measurement of spatially resolved reflectivity. The system has N fiber probes, each with a different path length from L_1 through L_N. At bottom, the time domain plot for a single laser sweep, showing the reflectivity measurement for each probe in a distinct temporal bin. 1xN, $1\times N$ fiber coupler; 3dB, 3dB fiber coupler; PBS, polarization beam splitter; PC, polarization controller; PD, photodetector; SUT, sample under test; TL, telecentric lens.

ment could have up to 1 m of range. By appropriately selecting the relative delay of each probe path, the signal due to each probe will appear within a different designated bin in the time domain. Therefore, a system with N probe paths is capable of performing N spatially resolved reflectivity measurements simultaneously using a single sweep of the tunable source and a single polarization-diverse detection subsystem. This would enable spatially resolved reflectivity measurements without scanning, or transverse scanning could be employed to probe a finer spatial scale than the probe distribution, requiring only $1/N$ as many scan steps to produce a measurement with the same number of points as a system with a single probe. If additional laser power is required to provide sufficient power to each probe, an optical amplifier could be employed to amplify the tunable laser output. This concept is equally applicable to multiplexed imaging of biological samples using SS-OCT.

7.2.3.3 Quantitative transmission phase microscopy

The SS-OCT system presented in Ch. 6 provides a quantitative measure of index contrast at an interface, but it does not probe the volume of the material. An alternative approach is to use the capabilities offered by the precision ranging techniques of Ch. 4 to perform quantitative measurements of optical path length in either a transmission or reflection geometry. Figure 7.3 illustrates a potential transmission geometry that employs a Mach-Zehnder configuration for the swept-wavelength interferometer. Alternatively, the existing reflection geometry could be used to double-pass the sample if it is placed on a reflecting substrate, or if a reference mirror is placed closely following the sample under test. In either geometry, a phase-sensitive measurement of optical delay as a function of transverse position would yield a phase contrast image of the SUT. In the reflection geometry, this is essentially the group refractive index measurement of Ch. 4, but the

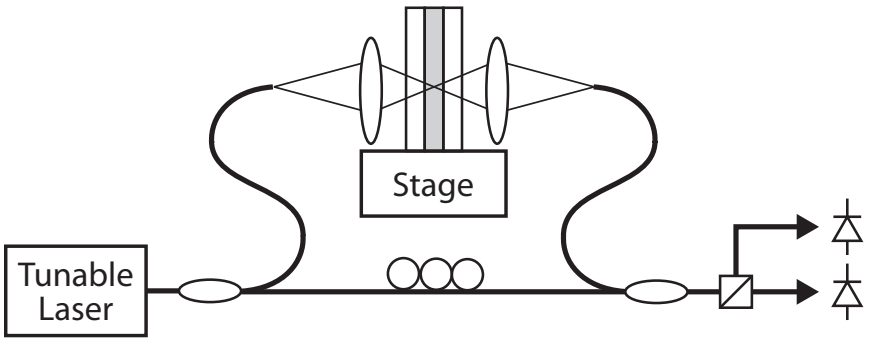

Figure 7.3: Conceptual diagram for a transmission phase microscopy system using SWI.

addition of a focusing objective lens would provide a spatially resolved measurement in the transverse dimensions. The reflecting method offers the possibility of separating the index and thickness, but the requirement of a reference reflector presents a challenge either in terms of transverse spatial resolution, in the case where the reflector is displaced from the sample by a finite distance, or with thin samples, if the reference reflector is in contact with the sample. In the latter case, the challenge arises if the sample is thinner than the transform-limited resolution of the SWI measurement (i.e, the reflection peak width), in which case the front and rear sample reflections cannot be independently filtered for phase slope estimation. A potential solution to this issue is that if two reflections are assumed, the expected phase response can be determined as a function of separation, and a nonlinear curve fit can determine this separation. In either case, whether a reflection or transmission geometry is used, the transverse spatial variation in the optical path length through the sample can be determined by variation of the phase slope of the interference beat signal. The results of Ch. 4 indicate that this measurement can be accomplished to better than $\lambda/1000$. With SWI, no 2π ambiguity exists as in traditional interferometry, so thick samples can be accommodated. The multiplexing approach described above could also be applied to transmission phase microscopy.

7.2.3.4 Volume phase tomography

Both the method of using Fresnel reflectivity to measure index contrast and transmission phase microscopy leave something yet to be desired, namely a complete map of refractive index in depth. A depth-resolved reconstruction of 3D phase structures could be accomplished through the use of SWI to perform phase sensitive optical diffraction tomography (ODT). ODT performs a reconstruction of a spatially varying refractive index distribution through a measurement of the diffracted field or intensity as a function of both input angle and output angle [187]. For measurements of diffracted intensity, a degree of *a priori* knowledge about the SUT is generally required in order to accurately perform the tomographic reconstruction. In an SWI implementation of ODT, the electric field would be measured directly, including both amplitude and phase, so that any refractive index distribution could be reconstructed without prior knowledge. Also, measurement of the field yields high sensitivity and dynamic range, allowing for the detection of weak diffracted signals that would be difficult to detect directly. Furthermore, time domain multiplexing could be employed to acquire all required data during a single laser sweep, avoiding the need to rotate the sample. A conceptual illustration of an SWI system for this purpose is shown in Fig. 7.4. In this multiplexing scheme, each combination of N inputs and N outputs would require a unique path length, resulting in N^2 temporal bins in the time domain data set. Since each probe path experiences a loss of $1/N^2$ relative to a single point system, a high power source or optical amplifier may be necessary depending on the number of ports. The use of a multipath Mach-Zehnder interferometer geometry allows for short duration temporal bins, since each bin will contain only a single transmission peak. A multipath Michelson geometry, on the other hand, would need to accommodate transmissive and reflective paths, such as fiber end facet reflections. The Mach-Zehnder geometry allows the entire available time domain range to be

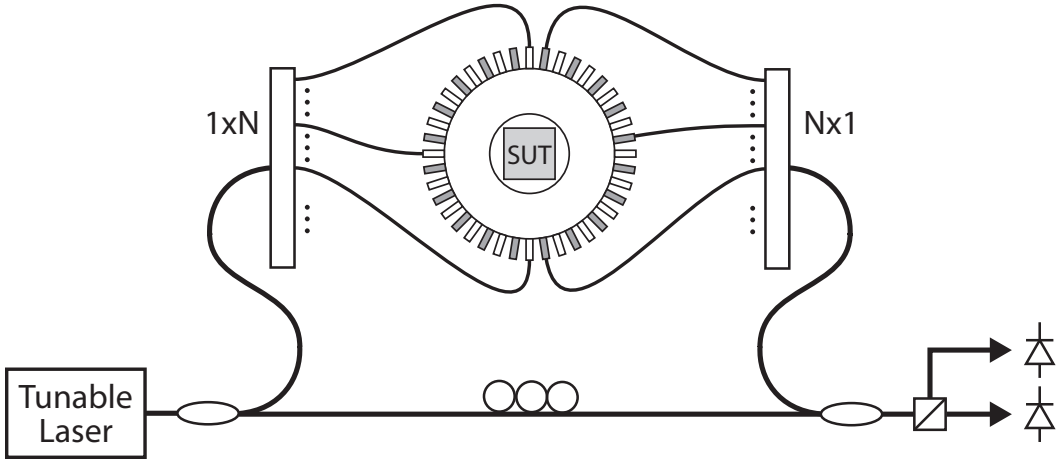

Figure 7.4: Conceptual diagram for single-scan phase-sensitive optical diffraction tomography using SWI. The sample under test is placed in a cylindrical chamber surrounded by input (white) and output (grey) fiber ports, each outfitted with a collimation optic. For clarity, only three input and three output fibers are drawn. The path lengths are chosen such that each combination of input and output port yields a unique path length.

divided up into a nonredundant set of delay bins. The sample is positioned in a cylindrical chamber with alternating input and output fiber ports distributed about the perimeter. A collimating optic on such as a GRIN lens on each fiber port is used to provide plane wave illumination by the input ports, as well as more efficient plane wave sampling by the output ports. With an appropriate calibration of the system delays and detected amplitude response, such a system should be able to produce high-resolution, depth-resolved tomograms of a 2D slice of the SUT. By translating the sample (out of the page in Fig. 7.4), or through the use of additional out-of-plane multiplexed fiber ports, a full 3D reconstruction could be accomplished.

7.2.4 Volume lithography of photopolymers

The work presented in Ch. 5 provided an initial demonstration of the ability of holographic lithography to produce 2D arrays of optical waveguides in volume

photopolymer. The extent of this work was largely limited by the availability of volume photopolymer samples of sufficient optical quality. Therefore, one of the most important extensions to this work is ongoing development of optical photopolymer materials. The tools presented in this thesis, particularly the phase-stabilized holographic lithography system and the SS-OCT for quantitative index contrast measurements, provide the fabrication and testing capabilities to support an active program of volume photopolymer material development. Now that InPhase Technologies no longer provides volume photopolymers commercially, academic development of materials is even more important. Attempts at "home-made" materials during the course of this thesis work yielded good sensitivity, but exhibited high levels of scatter and poor phase uniformity, especially in thick samples. For holographic lithography of waveguide arrays, solving the problem of matrix phase uniformity in thick volumes is likely to present the biggest challenge.

Provided a steady supply of material, the current holographic lithography system is well suited for ongoing studies of material response to various exposure conditions, such as exposure power and duration and array pitch, as well as variation of material parameters such as photoinitiator and writing monomer concentration. Such studies should allow for the precise engineering of waveguide arrays for specific applications by exerting control over the index contrast and the array pitch. It was my hope to demonstrate both imaging and coupled arrays and to observe discrete diffraction effects in holographically written waveguide array in volume photopolymer; perhaps a future student will achieve this demonstration. There also exist several possibilities for extension to different types of waveguide array devices. For example, by embedding a mirror in the photopolymer sample at 45° relative to the exposure system axis, a waveguide array incorporating a 90° bend could be fabricated. Another possible extension would be to produce a

tapered fanout waveguide array through the interference of spherical waves rather than plane waves.

The experimental holographic lithography system described in this thesis provides a high degree of versatility at the expense of ease of use. This is an acceptable trade off for initial research demonstrations, but future implementations may be driven by different priorities. To increase the stability of the system and make it easier to use, the four discrete writing beams could be replaced by a single diffractive optical element. This would drastically simplify the system, transferring the complexity to the design and implementation of the diffractive element. Both the phase stabilization system and the precision alignment procedure would no longer be necessary. If a change in the exposure pattern was desired, however, a different diffractive element would be needed.

Bibliography

[1] A. A. Michelson and E. W. Morley, "On the relative motion of the Earth and the luminiferous ether," *Am. J. Sci.*, vol. 34, no. 203, pp. 333–345, 1887. [Online]. Available: http://www.aip.org/history/gap/PDF/michelson.pdf xiv, 1, 2

[2] P. Hariharan, *Optical Interferometry, 2nd ed.* Academic Press, 2003. 1, 2

[3] T. H. Maiman, "Stimulated optical radiation in ruby," *Nature*, vol. 187, pp. 493–494, 1960. 1

[4] D. N. Keep, "Frequency-modulation radar for use in the mercantile marine," *Proc. IEE B Radio Electron. Eng.*, vol. 103, no. 10, pp. 519–523, 1955. 4

[5] W. Eickhoff and R. Ulrich, "Optical frequency domain reflectometry in single-mode fiber," *Appl. Phys. Lett.*, vol. 39, pp. 693–695, 1981. 4

[6] S. A. Kingsley and D. E. N. Davies, "OFDR diagnostics for fibre and integrated-optic systems," *Electron. Lett.*, vol. 21, pp. 434–435, 1985. 4, 5

[7] D. Uttam and B. Culshaw, "Precision time domain reflectometry in optical fiber systems using a frequency modulated continuous wave ranging technique," *J. Lightwave Technol.*, vol. LT-3, no. 5, pp. 971–977, 1985. 4, 57

[8] M. K. Barnoski and S. M. Jensen, "Fiber waveguides: a novel technique for investigating attenuation characteristics," *Appl. Opt.*, vol. 15, no. 9, pp. 2112–2115, 1976. 4

[9] R. I. MacDonald, "Frequency domain optical reflectometer," *Appl. Opt.*, vol. 20, no. 10, pp. 1840–1844, 1981. 5

[10] H. Ghafoori-Shiraz and T. Okoshi, "Fault location in optical fibers using optical frequency domain reflectometry," *J. Lightwave Technol.*, vol. LT-4, no. 3, pp. 316–322, 1986. 5

[11] J. Nakayama, K. Iizuka, and J. Nielsen, "Optical fiber fault locator by the step frequency method," *Appl. Opt.*, vol. 26, no. 3, pp. 440–443, 1987. 5

[12] H. Barfuss and E. Brinkmeyer, "Modified optical frequency domain reflectometry with high spatial resolution for components of integrated optic systems," *J. Lightwave Technol.*, vol. 7, pp. 3–10, 1989. 5, 9

[13] S. Moon and D. Y. Kim, "Ultra-high-speed optical coherence tomography with a stretched pulse supercontinuum source," *Opt. Express*, vol. 14, no. 24, pp. 11 575–11 584, 2006. 5, 10

[14] D. W. Dolfi, M. Nazarathy, and S. A. Newton, "5-mm-resolution optical-frequency-domain reflectometry using a coded phase-reversal modulator," *Opt. Lett.*, vol. 13, no. 8, pp. 678–680, 1988. 5

[15] W. V. Sorin, D. K. Donald, S. A. Newton, and M. Nazarathy, "Coherent FMCW reflectometry using a temperature tuned Nd:YAG ring laser," *IEEE Photon. Technol. Lett.*, vol. 2, pp. 902–904, 1990. 5

[16] K. Shimizu, T. Horiguchi, and Y. Koyamada, "Measurement of rayleigh backscattering in single-mode fibers based on coherent OFDR employing a DFB laser diode," *IEEE Photon. Technol. Lett.*, vol. 3, pp. 1039–1041, 1991. 5

[17] R. Passy, N. Gisin, and J. P. von der Weid, "High-sensitivity-coherent optical frequency-domain reflectometry for characterization of fiber-optic network components," *IEEE Photon. Technol. Lett.*, vol. 7, pp. 667–669, 1995. 5, 6

[18] G. Mussi, N. Gisin, R. Passy, and J. P. von der Weid, "-152.5 dB sensitivity high dynamic-range optical frequency-domain reflectometry," *Electron. Lett.*, vol. 32, pp. 926–927, 1996. 5

[19] K.-Y. Huang and G. M. Carter, "Coherent optical frequency domain reflectometry (OFDR) using a fiber grating external cavity laser," *IEEE Photon. Technol. Lett.*, vol. 6, pp. 1466–1468, 1994. 5, 18

[20] J. P. von der Weid, R. Passy, and N. Gisin, "Mid-range coherent optical frequency domain reflectometry with a DFB laser diode coupled to an external cavity," *J. Lightwave Technol.*, vol. 13, pp. 954–960, 1995. 5

[21] L.-T. Wang, K. Iiyama, F. Tsukada, N. Yoshida, and K.-I. Hayashi, "Loss measurement in optical waveguide devices by coherent frequency-modulated continuous-wave reflectometry," *Opt. Lett.*, vol. 18, pp. 1095–1097, 1993. 6, 18

[22] U. Glombitza and E. Brinkmeyer, "Coherent frequency-domain reflectometry for characterization of single-mode integrated-optical waveguides," *J. Lightwave Technol.*, vol. 11, pp. 1377–1384, 1993. 6, 11, 19, 70, 80, 96, 222

[23] J. P. von der Weid, R. Passy, G. Mussi, and N. Gisin, "On the characterization of optical fiber network components with optical frequency domain reflectometry," *J. Lightwave Technol.*, vol. 15, pp. 1131–1141, 1997. 6, 57

[24] M. Froggatt, B. Soller, D. Gifford, and M. Wolfe, "Correlation and keying of Rayleigh scatter for loss and temperature sensing in parallel optical networks," in *Optical Fiber Communication Conference*, OSA Technical Digest Series. Optical Society of America, 2004, paper PDP17. 6

[25] M. Froggatt, T. Erdogan, J. Moore, and S. Shenk, "Optical frequency domain characterization (OFDC) of dispersion in optical fiber Bragg gratings," in *Bragg Gratings, Photosensitivity, and Poling in Glass Waveguides*, OSA Technical Digest Series. Optical Society of America, 1999, pp. 176–178. 6

[26] M. Yoshida, K. Nakamura, and H. Ito, "A new method for measurement of group velocity dispersion of optical fibers by using a frequency-shifted feedback fiber laser," *IEEE Photon. Technol. Lett.*, vol. 13, pp. 227–229, 2001. 6

[27] M. Froggatt, E. Moore, and M. Wolfe, "Interferometric measurement of dispersion in optical components," in *Optical Fiber Communication Conference*, OSA Technical Digest Series. Optical Society of America, 2002, pp. 252–253, paper WK1. 6

[28] T.-J. Ahn, Y. Jung, K. Oh, and D. Y. Kim, "Optical frequency-domain chromatic dispersion measurement method for higher-order modes in an optical fiber," *Opt. Express*, vol. 13, pp. 10 040–10 047, 2005. 6

[29] B. J. Soller, D. K. Gifford, M. S. Wolfe, and M. E. Froggatt, "High resolution optical frequency domain reflectometry for characterization of components and assemblies," *Opt. Express*, vol. 13, pp. 666–674, 2005. 6, 26

[30] M. Froggatt, B. Soller, D. Gifford, and M. Wolfe, "Vibration tolerant swept wavelength interferometry," in *Optical Fiber Communication Conference and Exposition and the National Fiber Optic Engineers Conference*, Technical Digest (CD). Optical Society of America, 2005, paper PDP8. 6, 11

[31] M. Froggatt, "Distributed measurement of the complex modulation of a photoinduced bragg grating in an optical fiber," *Appl. Opt.*, vol. 35, pp. 5162–5164, 1996. 6

[32] J. Skaar, "Measuring the group delay of fiber Bragg gratings by use of end-reflection interference," *Opt. Lett.*, vol. 24, no. 15, pp. 1020–1022, 1999. 6

[33] M. Froggatt, J. Moore, and T. Erdogan, "Full complex transmission and reflection characterization of a Bragg grating in a single laser sweep," in *Optical Fiber Communication Conference*, OSA Technical Digest (CD). Optical Society of America, 2000, paper WB1. 6

[34] H. Rosenfeldt, C. Knothe, J. Cierullies, and E. Brinkmeyer, "Evolution of amplitude and dispersion spectra during fiber Bragg grating fabrication," in *Bragg Gratings, Photosensitivity, and Poling in Glass Waveguides*, OSA Technical Digest Series. Optical Society of America, 2001. 6, 18, 70

[35] B. J. Soller and M. E. Froggatt, "Polarization diverse optical frequency domain interferometry: all coupler implementation," in *OSA Special Meeting on Bragg Gratings, Photosensitivity, and Poling in Glass Waveguides*, OSA Technical Digest Series. Optical Society of America, 2003, paper MB4. 6

[36] O. H. Waagaard, "Spatial characterization of strong fiber bragg gratings using thermal chirp and optical-frequency-domain reflectometry," *J. Lightwave Technol.*, vol. 23, pp. 909–914, 2005. 6, 18

[37] G. M. H. Flockhart, G. A. Cranch, and C. K. Kirkendall, "Rapid characterization of the ultraviolet induced fiber Bragg grating complex coupling coefficient as a function of irradiance and exposure time," *Appl. Opt.*, vol. 46, no. 34, pp. 8237–8243, 2007. 6

[38] B. Huttner, J. Reecht, N. Gisin, R. Passy, and J. P. von der Weid, "Local birefringence measurements in single-mode fibers with coherent optical frequency-domain reflectometry," *IEEE Photon. Technol. Lett.*, vol. 10, pp. 1458–1460, 1998. 6

[39] M. Yoshida, T. Miyamoto, N. Zou, K. Nakamura, and H. Ito, "Novel PMD measurement method based on ofdr using a frequency-shifted feedback fiber laser," *Opt. Express*, vol. 9, pp. 207–211, 2001. 6

[40] M. Wegmuller, M. Legré, and N. Gisin, "Distributed beatlength measurement in single-mode fibers with optical frequency-domain reflectometry," *J. Lightwave Technol.*, vol. 20, pp. 800–807, 2002. 6

[41] M. Zou, M. Yoshida, Y. Namihira, and H. Ito, "PMD measurement based on delayed self-heterodyne OFDR and experimental comparison with itu-t round robin measurements," *Electron. Lett.*, vol. 38, pp. 115–116, 2002. 6

[42] B. J. Soller, M. Wolfe, and M. E. Froggatt, "Polarization resolved measurement of rayleigh backscatter in fiber-optic components," in *Optical Fiber Communication Conference and Exposition and the National Fiber Optic Engineers Conference*, Technical Digest (CD). Optical Society of America, 2005, paper NWD3. 6

[43] M. E. Froggatt, D. K. Gifford, S. Kreger, M. Wolfe, and B. J. Soller, "Characterization of polarization-maintaining fiber using high-sensitivity optical-frequency-domain reflectometry," *J. Lightwave Technol.*, vol. 24, pp. 4149–4154, 2006. 6

[44] T.-J. Ahn, S. Moon, Y. Youk, Y. Jung, K. Oh, and D. Y. Kim, "Mode analysis and modal delay measurement of few modes fiber by using optical frequency domain reflectometry based on 1550 nm TLS," in *Conference on Lasers and Electro-Optics/Quantum Electronics and Laser Science and Photonic Applications Systems Technologies*, Technical Digest (CD). Optical Society of America, 2005, paper JThE5. 6

[45] T.-J. Ahn and D. Y. Kim, "High-resolution differential mode delay measurement for a multimode optical fiber using a modified optical frequency domain reflectometer," *Opt. Express*, vol. 13, pp. 8256–8262, 2005. 6

[46] T.-J. Ahn, S. Moon, Y. Youk, Y. Jung, K. Oh, and D. Y. Kim, "New optical frequency domain differential mode delay measurement method for a multimode optical fiber," *Opt. Express*, vol. 13, pp. 4005–4011, 2005. 6

[47] M. Wegmuller, P. Oberson, O. Guinnard, B. Huttner, L. Guinnard, C. Vinegoni, and N. Gisin, "Distributed gain measurements in Er-doped fibers with high resolution and accuracy using an optical frequency domain reflectometer," *J. Lightwave Technol.*, vol. 18, no. 12, pp. 2127–2132, 2000. 6

[48] M. Wegmuller, F. Scholder, A. Fougères, and N. Gisin, "Evaluation of measurement techniques for characterization of photonic crystal fibers," in *Conference on Lasers and Electro-Optics/Quantum Electronics and Laser Science and Photonic Applications Systems Technologies*, Technical Digest (CD). Optical Society of America, 2002, paper JThA4. 6

[49] G. D. VanWiggeren, A. R. Motamedi, and D. M. Baney, "Single-scan interferometric component analyzer," *IEEE Photon. Technol. Lett.*, vol. 15, no. 9, pp. 263–265, 2003. 6, 40

[50] G. D. VanWiggeren, , and D. M. Baney, "Swept-wavelength interferometric analysis of multiport components," *IEEE Photon. Technol. Lett.*, vol. 15, no. 9, pp. 1267–1269, 2003. 6

[51] D. K. Gifford, B. J. Soller, M. S. Wolfe, and M. E. Froggatt, "Optical vector network analyzer for single-scan measurments of loss, group delay, and polarization mode dispersion," *Appl. Opt.*, vol. 44, pp. 7282–7286, 2005. 6, 40, 46

[52] J. Zheng, *Optical Frequency-Modulated Continuous-Wave (FMCW) Interferometry*. Springer, 2005. 6, 222

[53] R. J. Espejo and S. D. Dyer, "Transverse-stress fiber Bragg grating sensor with high spatial resolution and temperature stability," *J. Lightwave Technol.*, vol. 25, no. 7, pp. 1777–1785, 2007. 6

[54] A. M. Abdi, S. Suzuki, A. Schülzgen, and A. R. Kost, "Strain measurements using fiber Bragg grating array," in *Frontiers in Optics*, OSA Technical Digest (CD). Optical Society of America, 2005, paper FWO5. 6

[55] M. Froggatt and J. Moore, "High-spatial-resolution distributed strain measurement in optical fiber with Rayleigh backscatter," *Appl. Opt.*, vol. 37, pp. 1735–1740, 1998. 6

[56] M. Froggatt, D. Gifford, S. Kreger, M. Wolfe, and B. Soller, "Distributed strain and temperature discrimination in unaltered polarization maintaining fiber," in *Optical Fiber Sensors*, OSA Technical Digest (CD). Optical Society of America, 2006, paper ThC5. 6

[57] A. K. Sang, M. E. Froggatt, D. K. Gifford, S. T. Kreger, and B. D. Dickerson, "One centimeter spatial resolution temperature measurements in a nuclear reactor using rayleigh scatter in optical fiber," *IEEE Sens. J.*, vol. 8, no. 7, pp. 1375–1380, 2008. 6

[58] M. Jiang, D. Chen, and S. He, "Multiplexing scheme of long-period grating sensors based on a modified optical frequency domain reflectometry," *IEEE Photon. Technol. Lett.*, vol. 20, no. 23, pp. 1962–1964, 2008. 6

[59] E. C. Burrows and K.-Y. Liou, "High resolution laser LIDAR utilising two-section distributed feedback semiconductor laser as a coherent source," *Electron. Lett.*, vol. 26, pp. 577–579, 1990. 6

[60] A. Dieckmann, "FMCW-LIDAR with tunable twin-guide laser diode," *Electron. Lett.*, vol. 30, no. 4, pp. 308–309, 1994. 6

[61] C. J. Karlsson, F. Å. A. Olsson, D. Letalick, and M. Harris, "All-fiber multifunction continuous-wave coherent laser radar at 1.55 μm for range, speed, vibration, and wind measurements," *Appl. Opt.*, vol. 39, no. 21, pp. 3716–3726, 2000. 6

[62] S. H. Yun, G. J. Tearney, J. F. de Boer, N. Iftimia, and B. E. Bouma, "High-speed optical frequency-domain imaging," *Opt. Express*, vol. 11, pp. 2953–2963, 2003. 7, 94

[63] M. Brezinski, *Optical Coherence Tomography Principles and Applications*. Elsevier, 2006. 7

[64] D. Huang, E. A. Swanson, C. P. Lin, J. S. Schuman, W. G. Stinson, W. Chang, M. R. Hee, T. Flotte, K. Gregory, C. A. Puliafito, and J. G. Fujimoto, "Optical coherence tomography," *Science*, vol. 254, pp. 1178–1181, 1991. 7, 228

[65] R. C. Youngquist, S. Carr, and D. E. N. Davies, "Optical coherence-domain reflectometry: a new optical evaluation technique," *Opt. Lett.*, vol. 12, pp. 158–160, 1987. 7, 94

[66] S. R. Chinn, E. A. Swanson, and J. G. Fujimoto, "Optical coherence tomography using a frequency-tunable optical source," *Opt. Lett.*, vol. 22, pp. 340–342, 1997. 7, 94, 96, 228

[67] A. F. Fercher, C. K. Hitzenberger, G. Kamp, and S. Y. El-Zaiat, "Measurement of intraocular distances by backscattering spectral interferometry," *Opt. Commun.*, vol. 117, no. 1, pp. 43–48, 1995. 7, 228

[68] R. Leitgeb, C. K. Hitzenberger, and A. F. Fercher, "Performance of Fourier domain vs. time domain optical coherence tomography," *Opt. Express*, vol. 11, no. 8, pp. 889–893, 2003. 8, 228

[69] M. A. Choma, M. V. Sarunic, C. Yang, and J. A. Izatt, "Sensitivity advantage of swept source and Fourier domain optical coherence tomography," *Opt. Express*, vol. 11, no. 18, pp. 2183–2189, 2003. 8, 228

[70] B. Liu and M. E. Brezinksi, "Theoretical and practical considerations on detection performance of time domain, Fourier domain, and swept source optical coherence tomography," *J. Biomed. Opt.*, vol. 12, no. 4, p. 044007, 2007. 8

[71] K. Zheng, B. Liu, C. Huang, and M. E. Brezinski, "Experimental confirmation of potential swept source optical coherence tomography performance limitations," *Appl. Opt.*, vol. 47, no. 33, pp. 6151–6158, 2008. 8

[72] B. Povazay, K. Bizheva, A. Unterhuber, B. Hermann, H. Sattmann, A. Fercher, W. Drexler, A. Apolonski, W. Wadsworth, J. Knight, P. S. J. Russel, M. Vetterlein, and E. Scherzer, "Submicrometer axial resolution optical coherence tomography," *Opt. Lett.*, vol. 27, pp. 1800–1802, 2002. 8, 95

[73] J. G. Fujimoto, "Optical coherence tomography for ultrahigh resolution *in vivo* imaging," *Nat. Biotechnol.*, vol. 21, pp. 1361–1367, 2003. 8

[74] W. Drexler, "Ultrahigh-resolution optical coherence tomography," *J. Biomed. Opt.*, vol. 9, pp. 47–74, 2004. 8

[75] R. A. Leitgeb, W. Drexler, A. Unterhuber, B. Hermann1, T. Bajraszewski, T. Le, A. Stingl, and A. F. Fercher, "Ultrahigh resolution fourier domain optical coherence tomography," *Opt. Express*, vol. 12, no. 10, pp. 2156–2165, 2004. 8

[76] M. Wojtkowski, "High-speed optical coherence tomography: basics and applications," *Appl. Opt.*, vol. 49, no. 16, pp. D30–D61, 2010. 8

[77] S. Kuwamura and I. Yamaguchi, "Wavelength scanning profilometry for real-time surface shape measurement," *Appl. Opt.*, vol. 36, no. 19, pp. 4473–4482, 1997. 8

[78] A. Yamamoto and I. Yamaguchi, "Surface proflometry by wavelength scanning Fizeau interferometer," *Opt. Laser Technol.*, vol. 32, pp. 261–266, 2000. 8

[79] I. Yamaguchi, A. Yamamoto, and M. Yano, "Surface topography by wavelength scanning interferometry," *Opt. Eng.*, vol. 39, no. 1, pp. 40–46, 2000. 8

[80] A. Yamamoto, C.-C. Kuo, K. Sunouchi, S. Wada, I. Yamaguchi, and H. Tashiro, "Surface shape measurement by wavelength scanning interferometry using an electronically tuned Ti:sapphire laser," *Opt. Rev.*, vol. 8, no. 1, pp. 59–63, 2001. 8

[81] D. S. Mehta, M. Sugai, H. Hinosugi, S. Saito, T. K. Mitsuo Takeda, H. Takahashi, M. Ando, M. Shishido, and T. Yoshizawa, "Simultaneous three-dimensional step-height measurement and high-resolution tomographic imaging with a spectral interferometric microscope," *Appl. Opt.*, vol. 41, no. 19, pp. 3874–3885, 2002. 8, 10

[82] A. Yamamoto and I. Yamaguchi, "Profilometry of sloped plane surfaces by wavelength scanning interferometry," *Opt. Rev.*, vol. 9, no. 3, pp. 112–121, 2002. 8

[83] D. S. Mehta, S. Saito, H. Hinosugi, M. Takeda, and T. Kurokawa, "Spectral interference Mirau microscope with an acousto-optic tunable filter for three-dimensional surface profilometry," *Appl. Opt.*, vol. 42, no. 7, pp. 1296–1305, 2003. 8

[84] T. Amano, H. Hiro-Oka, D. Choi, H. Furukawa, M. T. M. N. K. S. Fumiyoshi Kano, and K. Ohbayashi, "Optical frequency-domain reflectometry with a rapid wavelength-scanning superstructure-grating distributed bragg reflector laser," *Appl. Opt.*, vol. 44, no. 5, pp. 808–816, 2005. 8

[85] T. Anna, C. Shakher, and D. S. Mehta, "Simultaneous tomography and topography of silicon integrated circuits using full-field swept-source optical coherence tomography," vol. 11, pp. 1–9, 2009. 8

[86] X. Jiang, K. Wang, F. Gao, and H. Muhamedsalih, "Fast surface measurement using wavelength scanning interferometry with compensation of

environmental noise," *Appl. Opt.*, vol. 49, no. 15, pp. 2903–2909, 2010. 8, 10, 11

[87] M. V. Sarunic, S. Weinberg, and J. A. Izatt, "Full-field swept-source phase microscopy," *Opt. Lett.*, vol. 31, no. 10, pp. 1462–1464, 2006. 8, 95

[88] S. K. Dubey, D. S. Mehta, A. Anand, and C. Shakher, "Simultaneous topography and tomography of latent fingerprints using full-field swept-source optical coherence tomography," vol. 10, p. 015307, 2008. 8

[89] T. Day, M. Brownell, and I.-F. Wu, "Widely tunable external cavity diode lasers," *Proc. SPIE*, vol. 2378, p. 35, 1995. 9

[90] R. Huber, M. Wojtkowski, J. G. Fujimoto, J. Y. Jiang, and A. E. Cable, "Three-dimensional and C-mode OCT imaging with a compact, frequency-swept laser source at 1300 nm," *Opt. Express*, vol. 13, no. 26, pp. 10 523–10 538, 2005. 9

[91] S.-W. Lee, C.-S. Kim, and B.-M. Kim, "External line-cavity wavelength-swept source at 850 nm for optical coherence tomography," *IEEE Photon. Technol. Lett.*, vol. 19, no. 13, pp. 176–178, 2007. 9

[92] V. J. Srinivasan, R. Huber, I. Gorczynska, J. G. Fujimoto, J. Y. Jiang, P. Reisen, and A. E. Cable, "High-speed, high-resolution optical coherence tomography retinal imaging with a frequency-swept laser at 850 nm," *Opt. Lett.*, vol. 32, no. 4, pp. 361–363, 2007. 9

[93] C. Chong, A. Morosawa, and T. Sakai, "High-speed wavelength-swept laser source with high-linearity sweep for optical coherence tomography," *IEEE J. Sel. Topics Quantum Electron.*, vol. 14, pp. 235–242, 2008. 9, 10, 18

[94] S. H. Yun, C. Boudoux, G. J. Tearney, and B. E. Bouma, "High-speed wavelength-swept semiconductor laser with a polygon-scanner-based wavelength filter," *Opt. Lett.*, vol. 28, no. 20, pp. 1981–1983, 2003. 9

[95] M. A. Choma, K. Hsu, and J. A. Izatt, "Swept source optical coherence tomography using an all-fiber 1300-nm ring laser source," *J. Biomed. Opt.*, vol. 10, no. 4, p. 044009, 2005. 9

[96] H. Lim, J. F. de Boer, B. H. Park, E. C. W. Lee, R. Yelin, and S. H. Yun, "Optical frequency domain imaging with a rapidly swept laser in the 815-870 nm range," *Opt. Express*, vol. 14, no. 13, pp. 5937–5944, 2006. 9

[97] R. Huber, M. Wojtkowski, and J. G. Fujimoto, "Fourier domain mode locking (FDML): A new laser operating regime and application for optical coherence tomography," *Opt. Express*, vol. 14, no. 8, pp. 3225–3237, 2006. 10, 229

[98] R. Huber, D. C. Adler, and J. G. Fujimoto, "Buffered Fourier domain mode locking: unidirectional swept laser sources for optical coherence tomography imaging at 370,000 lines/s," *Opt. Lett.*, vol. 31, no. 20, pp. 2975–2977, 2006. 10, 228, 230

[99] M. Y. Jeon, J. Zhang, Q. Wang, and Z. Chen, "High-speed and wide bandwidth Fourier domain mode-locked wavelength swept laser with multiple SOAs," *Opt. Express*, vol. 16, no. 4, pp. 2547–2554, 2008. 10

[100] K. Iiyama, L.-T. Wang, and K. ichi Hayashi, "Linearizing optical frequency-sweep of a laser diode for FMCW reflectometry," *J. Lightwave Technol.*, vol. 14, pp. 173–178, 1996. 10, 18

[101] C. M. Eigenwillig, B. R. Biedermann, G. Palte, and R. Huber, "K-space linear Fourier domain mode locked laser and applications for optical coherence tomography," *Opt. Express*, vol. 16, no. 12, pp. 8916–8937, 2008. 10, 18, 229

[102] M. Kobayashi, K. Takada, and J. Noda, "Optical-frequency encoder using polarization-maintaining fiber," *J. Lightwave Technol.*, vol. 8, pp. 1697–1702, 1990. 10

[103] E. Brinkmeyer and U. Glombitza, "High-resolution coherent frequency-domain reflectometry using continuously tuned laser diodes," in *Optical Fiber Communication Conference*, vol. 4, OSA Technical Digest Series. Optical Society of America, 1991, p. 129, paper WN2. 10, 19, 68

[104] R. Passy, N. Gisin, J. P. von der Weid, and H. H. Gilgen, "Experimental and theoretical investigations of coherent OFDR with semiconductor laser sources," *J. Lightwave Technol.*, vol. 12, no. 9, pp. 1622–1630, 1994. 11, 55, 57

[105] R. Huber, M. Wojtkowski, K. Taira, and J. G. Fujimoto, "Amplified, frequency swept lasers for frequency domain reflectometry and oct imaging: design and scaling principles," *Opt. Express*, vol. 13, no. 9, pp. 3513–3528, 2005. 11, 18

[106] A. Cordes, G. Xavier, G. V. de Faria, and J. von der Weid, "High axial resolution swept source for optical coherence tomography," *Electron. Lett.*, vol. 46, pp. 27–29, 2010. 11

[107] M. A. Choma, A. K. Ellerbee, C. Yang, T. L. Creazzo, and J. A. Izatt, "Spectral-domain phase microscopy," *Opt. Lett.*, vol. 30, no. 10, pp. 1162–1164, 2005. 11, 95

[108] M. V. Sarunic, S. Weinberg, and J. A. Izatt, "Full-field swept-source phase microscopy," *Opt. Lett.*, vol. 31, no. 10, pp. 1462–1464, 2006. 11

[109] D. C. Adler, R. Huber, and J. G. Fujimoto, "Phase-sensitive optical coherence tomography at up to 370,000 lines per second using buffered Fourier domain mode-locked lasers," *Opt. Lett.*, vol. 32, no. 6, pp. 626–628, 2007. 11, 69, 95, 223

[110] B. J. Vakoc, S. H. Yun, J. F. de Boer, G. J. Tearney, and B. E. Bouma, "Phase-resolved optical frequency domain imaging," *Opt. Express*, vol. 13, no. 14, pp. 5483–5493, 2005. 11, 95

[111] K. Tsuji, K. Shimizu, T. Horiguchi, and Y. Koyamada, "Spatial-resolution improvement in long-range coherent optical frequency domain reflectometry by frequency-sweep linearisation," *Electron. Lett.*, vol. 33, pp. 408–410, 1997. 18

[112] T.-J. Ahn, J. Y. Lee, and D. Y. Kim, "Suppression of nonlinear frequency sweep in an optical frequency-domain reflectometer by use of Hilbert transformation," *Appl. Opt.*, vol. 44, pp. 7630–7634, 2005. 18, 97

[113] K. Takada, "High-resolution OFDR with incorporated fiber-optic frequency encoder," *IEEE Photon. Technol. Lett.*, vol. 4, pp. 1069–1072, 1992. 19

[114] D. C. Adler, Y. Chen, R. Huber, J. Schmitt, J. Connolly, and J. G. Fujimoto, "Three-dimensional endomicroscopy using optical coherence tomography," *Nat. Photonics*, vol. 1, no. 12, pp. 709–716, 2007. 19

[115] E. D. Moore and R. R. McLeod, "Correction of sampling errors due to laser tuning rate fluctuations in swept-wavelength interferometry," *Opt. Express*, vol. 16, pp. 13 139–13 149, 2008. 19, 97, 101, 222

[116] M. Born and E. Wolf, *Principles of Optics, 7th ed.* Cambridge University Press, 1999. 22

[117] J. W. Goodman, *Introduction to Fourier Optics, 2nd ed.* McGraw-Hill, 1996. 23, 74, 98, 152

[118] G. P. Agrawal, *Fiber-Optic Communication Systems, 2nd ed.* Wiley-Interscience, 1997. 40, 121, 137

[119] B. L. Heffner, "Automated measurement of polarization mode dispersion using Jones matrix eigenanalysis," *IEEE Photon. Technol. Lett.*, vol. 4, no. 9, pp. 1066–1069, 1992. 46

[120] B. E. A. Saleh and M. C. Teich, *Fundamentals of Photonics.* Wiley-Interscience, 1991. 53

[121] J. A. Armstrong, "Theory of interferometric analysis of laser phase noise," *J. Opt. Soc. Am.*, vol. 56, no. 8, pp. 1024–1031, 1966. 57

[122] P. B. Gallion and G. Debarge, "Quantum phase noise and field correlation in single frequency semiconductor laser systems," *IEEE J. Quantum Electron.*, vol. QE-20, no. 4, pp. 343–349, 1984. 57, 59

[123] M.-C. Amann, "Phase noise limited resolution of coherent lidar using widely tunable laser diodes," *Electron. Lett.*, vol. 28, no. 18, pp. 1694–1696, 1992. 57

[124] S. Venkatesh and W. V. Sorin, "Phase noise considerations in coherent optical FMCW reflectometry," *J. Lightwave Technol.*, vol. 11, no. 10, pp. 1694–1700, 1993. 57, 58, 59, 62

[125] H. Nguyen and E. Shwedyk, *A First Course in Digital Communications*. Cambridge University Press, 2009. 66

[126] J. Geng, C. Spiegelberg, and S. Jiang, "Narrow linewidth fiber laser for 100-km optical frequency domain reflectometry," *IEEE Photon. Technol. Lett.*, vol. 17, no. 9, pp. 1827–1829, 2005. 69

[127] D. K. Gifford, M. E. Froggatt, M. S. Wolfe, S. T. Kreger, and B. J. Soller, "Millimeter resolution reflectometry over two kilometers," in *Proc. 33rd European Conference on Optical Communication*. VDE Verlag GMBH, 2007, paper Tu.3.6.1. 69

[128] T.-J. Ahn and D. Y. Kim, "Analysis of nonlinear frequency sweep in high-speed tunable laser sources using a self-homodyne measurement and Hilbert transformation," *Appl. Opt.*, vol. 46, pp. 2394–2400, 2007. 72

[129] M. E. Brezinkski, *Optical Coherence Tomography: Principles and Applications*. Elsevier, 2006. 94, 222

[130] C. Joo, T. Akkin, B. Cense, B. H. Park, and J. F. de Boer, "Spectral-domain optical coherence phase microscopy for quantitative phase-contrast imaging," *Opt. Lett.*, vol. 30, no. 16, pp. 2131–2133, 2005. 95, 195

[131] M. A. Choma, A. K. Ellerbee, S. Yazdanfar, and J. A. Izatt, "Doppler flow imaging of cytoplasmic streaming using spectral domain phase microscopy," *J. Biomed. Opt.*, vol. 11, no. 2, p. 024014, 2006. 95

[132] W. V. Sorin and D. F. Gray, "Simultaneous thickness and group index measurement using optical low-coherence reflectometry," *IEEE Photon. Technol. Lett.*, vol. 4, no. 1, pp. 105–107, 1992. 95

[133] H.-C. Cheng and Y.-C. Liu, "Simultaneous measurement of group refractive index and thickness of optical samples using optical coherence tomography," *Appl. Opt.*, vol. 49, pp. 790–797, 2010. 96

[134] J. Na, H. Y. Choi, E. S. Choi, C. Lee, and B. H. Lee, "Self-referenced spectral interferometry for simultaneous measurements of thickness and refractive index," *Appl. Opt.*, vol. 48, no. 13, pp. 2461–2467, 2009. 96, 100

[135] W. C. Swann and S. L. Gilbert, "Accuracy limits for simple molecular absorption based wavelength references," in *Technical Digest: Symposium on Optical Fiber Measurements, 2004.* NIST, 2004, pp. 15–18. 102

[136] P. E. Ciddor, "Refractive index of air: new equations for the visible and near infrared," *Appl. Opt.*, vol. 35, no. 9, pp. 1566–1573, 1996. 111, 264, 269

[137] P. E. Ciddor and R. J. Hill, "Refractive index of air. 2. group index," *Appl. Opt.*, vol. 38, no. 9, pp. 1663–1667, 1999. 111, 265

[138] D. B. Leviton and B. J. Frey, "Temperature-dependent absolute refractive index measurements of synthetic fused silica," *Proc. SPIE*, vol. 6273, p. 62732K. 113, 269

[139] R. Liang, *Optical Design for Biomedical Imaging.* SPIE Press, 2010. 118

[140] Y. S. Sabharwal, A. R. Rouse, L. Donaldson, M. F. Hopkins, and A. F. Gmitro, "Slit-scanning confocal microendoscope for high-resolution *in vivo* imaging," *Appl. Opt.*, vol. 38, no. 34, pp. 7133–7144, 1999. 119

[141] J. Knittel, L. Schnieder, G. Messerschmidt, and T. Messerschmidt, "Endoscope-compatible confocal microscope using a gradient index-lens system," *Opt. Commun.*, vol. 188, no. 5–6, pp. 267–273, 2001. 119

[142] M. Scepanovic, J. E. Castillo, J. K. Barton, D. Mathine, R. K. Kostuk, and A. Sato, "Design and processing of high-density single-mode fiber arrays for imaging and parallel interferometer applications," *Appl. Opt.*, vol. 43, no. 21, pp. 4150–4156, 2004. 119, 122

[143] T. Xie, D. Mukai, S. Guo, M. Brenner, and Z. Chen, "Fiber-optic-bundle-based optical coherence tomography," *Opt. Lett.*, vol. 30, no. 14, pp. 1803–1805, 2005. 119

[144] H. F. Ghaemi, Y. Li, T. Thio, and T. Wang, "Fiber image guide with subwavelength resolution," *Appl. Phys. Lett.*, vol. 72, no. 10, pp. 1137–1139, 1998. 119

[145] D. V. Plant and A. G. Kirk, "Optical interconnects at the chip and board level: challenges and solutions," *Proc. IEEE*, vol. 88, no. 6, pp. 806–818, 2000. 119

[146] D. Christodoulides, F. Lederer, and Y. Silberberg, "Discretizing light behaviour in linear and nonlinear waveguide lattices," *Nature*, vol. 424, pp. 817–823, 2003. 119

[147] S. Longhi, "Quantum-optical analogies using photonic structures," *Laser & Photonics Rev.*, vol. 3, no. 3, pp. 243–261, 2009. 119, 121

[148] H. S. Eisenberg, Y. Silberberg, R. Morandotti, and J. S. Aitchison, "Diffraction management," *Appl. Phys. Lett.*, vol. 85, no. 9, pp. 1864–1866, 2000. 120

[149] T. Pertsch, T. Zentgraf, U. Peschel, A. Brauer, and F. Lederer, "Anomalous refraction and diffraction in discrete optical systems," *Phys. Rev. Lett.*, vol. 88, no. 9, pp. 93 901–93 901, 2002. 120

[150] T. Pertsch, U. Peschel, F. Lederer, J. Burghoff, M. Will, S. Nolte, and A. Tünnermann, "Discrete diffraction in two-dimensional arrays of coupled waveguides in silica," *Opt. Lett.*, vol. 29, no. 5, pp. 468–470, 2004. 120, 124

[151] H. S. Eisenberg, Y. Silberberg, R. Morandotti, A. R. Boyd, and J. S. Aitchison, "Discrete spatial optical solitons in waveguide arrays," *Phys. Rev. Lett.*, vol. 81, no. 16, pp. 3383–3386, 1998. 120

[152] J. W. Fleischer, M. Segev, N. K. Efremidis, and D. N. Christodoulides, "Observation of two-dimensional discrete solitons in optically induced nonlinear photonic lattices," *Nature*, vol. 422, pp. 147–150, 2003. 120, 123

[153] A. S. Davydov and N. I. Kislukha, "Solitary excitons in one-dimensional molecular chains," *Phys. Status Solidi B*, vol. 59, no. 2, pp. 465–470, 1973. 120

[154] A. Trombettoni and A. Smerzi, "Discrete solitons and breathers with dilute bose-einstein condensates," *Phys. Rev. Lett.*, vol. 86, no. 11, pp. 2353–2356, 2001. 120

[155] W. Królikowski and Y. S. Kivshar, "Soliton-based optical switching in waveguide arrays," *J. Opt. Soc. Am. B*, vol. 13, no. 5, pp. 876–887, 1996. 121

[156] D. N. Christodoulides and E. D. Eugenieva, "Blocking and routing discrete solitons in two-dimensional networks of nonlinear waveguide arrays," *Phys. Rev. Lett.*, vol. 87, no. 23, p. 233901, 2001. 121

[157] K. Nishioka, K. Ono, and M. Shiraiwa, "Image fiber," U.S. Patent 5,479,550, Dec. 26, 1995. 122

[158] X. Chen, K. L. Reichenback, and C. Xu, "Experimental and theoretical analysis of core-to-core coupling on fiber bundle imaging," *Opt. Express*, vol. 16, no. 26, pp. 21 598–21 607, 2008. 122

[159] U. Röpke, H. Bartelt, S. Unger, K. Schuster, and J. Kobelke, "Two-dimensional high-precision fiber waveguide arrays for coherent light propagation," *Opt. Express*, vol. 15, no. 11, pp. 6894–6899, 2007. 122

[160] Y. Li, J. Ai, and J. Popelek, "Board-level 2-d data-capable optical interconnection circuits using polymer fiber-image guides," *Proc. IEEE*, vol. 88, no. 6, pp. 794–805, 2000. 122

[161] J. Ai and Y. Li, "Polymer fiber-image-guide-based embedded optical circuit board," *Appl. Opt.*, vol. 38, no. 2, pp. 325–332, 1999. 122

[162] T. Maj, A. G. Kirk, D. V. Plant, J. F. Ahadian, C. G. Fonstad, K. L. Lear, K. Tatah, M. S. Robinson, and J. A. Trezza, "Interconnection of a two-dimensional array of vertical-cavity surface-emitting lasers to a receiver array by means of a fiber image guide," *Appl. Opt.*, vol. 39, no. 5, pp. 683–689, 2000. 122

[163] S. D. Mukherjee, G. R. Hadley, K. M. Geib, K. D. Choquette, T. R. Carter, A. J. Fischer, M. Robinson, and C. T. Sullivan, "Critical parameters for parallel interconnects using vcsel arrays and fiber image guides," *Proc. SPIE*, vol. 4942, pp. 292–305, 2003. 122

[164] J.-S. Kim and J.-J. Kim, "Stacked polymeric multimode waveguide arrays for two-dimensional optical interconnects," *J. Lightwave Technol.*, vol. 22, no. 3, pp. 840–844, 2004. 122

[165] N. K. Efremidis, S. Sears, D. N. Christodoulides, J. W. Fleischer, and M. Segev, "Discrete solitons in photorefractive optically induced photonic lattices," *Phys. Rev. E*, vol. 66, p. 046602, 2002. 123

[166] Z. Chen and H. Martin, "Waveguides and waveguide arrays formed by incoherent light in photorefractive materials," *Opt. Mater.*, vol. 23, pp. 235–241, 2003. 123

[167] B. Terhalle, A. S. Desyatnikov, C. Bersch, D. Träger, L. Yang, J. Imbrock, Y. S. Kivshar, and C. Denz, "Anisotropic photonic lattices and discrete solitons in photorefractive media," *Appl. Phys. B Lasers Opt.*, vol. 86, pp. 399–405, 2007. 123

[168] M. Klotz, H. Meng, G. J. Salamo, M. Segev, and S. R. Montgomery, "Fixing the photorefractive soliton," *Opt. Lett.*, vol. 24, no. 2, pp. 77–79, 1999. 123

[169] K. M. Davis, K. Miura, N. Sugimoto, and K. Hirao, "Writing waveguides in glass with a femtosecond laser," *Opt. Lett.*, vol. 21, no. 21, pp. 1729–1731, 1996. 124

[170] A. Szameit, D. Bloemer, J. Burghoff, T. Pertsch, S. Nolte, and A. Tünnermann, "Hexagonal waveguide arrays written with fs-laser pulses," *Appl. Phys. B Lasers Opt.*, vol. 82, no. 4, pp. 507–512, 2006. 124

[171] K. Curtis, L. Dhar, A. J. Hill, W. L. Wilson, and M. R. Ayres, *Holographic Data Storage: From Theory to Practical Systems.* John Wiley & Sons, 2010. 125

[172] J. William J. Gambogi, A. M. Weber, and T. J. Trout, "Advances and applications of dupont holographic photopolymers," *Proc. SPIE*, vol. 2043, pp. 2–13, 1994. 125

[173] D. A. Waldman, R. T. Ingwall, P. K. Dhal, M. G. Horner, E. S. Kolb, H.-Y. S. Li, R. A. Minns, and H. G. Schild, "Cationic ring-opening photopolymerimization methods for volume hologram recording," *Proc. SPIE*, vol. 2689, pp. 127–141, 1996. 125

[174] L. Dhar, A. Hale, H. E. Katz, M. L. Schilling, M. G. Schnoes, and F. C. Schilling, "Recording media that exhibit high dynamic range for digital holographic data storage," *Opt. Lett.*, vol. 24, no. 7, pp. 487–489, 1999. 125

[175] A. C. Sullivan, M. W. Grabowski, and R. R. McLeod, "Three-dimensional direct-write lithography into photopolymer," *Appl. Opt.*, vol. 46, no. 3, pp. 295–301, 2007. 125, 134, 143

[176] G. Zhao and P. Mouroulis, "Diffusion model of hologram formation in dry photopolymer materials," *J. Mod. Opt.*, vol. 41, no. 10, pp. 1929–1939, 1994. 126, 215

[177] V. L. Colvin, R. G. Larson, A. L. Harris, and M. L. Schilling, "Quantitative model of volume hologram formation in photopolymers," *J. Appl. Phys.*, vol. 81, no. 9, pp. 5913–5923, 1997. 126

[178] J. T. Sheridan and J. R. Lawrence, "Nonlocal-response diffusion model of holographic recording in photopolymer," *J. Opt. Soc. Am. A*, vol. 17, no. 6, pp. 1108–1114, 2000. 126

[179] J. R. Lawrence, F. T. O'Neill, and J. T. Sheridan, "Photopolymer holographic recording material parameter estimation using a nonlocal diffusion based model," *J. Appl. Phys.*, vol. 90, no. 7, pp. 3142–3148, 2001. 126

[180] G. Odian, *Principles of Polymerization, 4th ed.* Wiley-Interscience, 2004. 128

[181] R. R. Gattass and E. Mazur, "Femtosecond laser micromachining in transparent materials," *Nat. Photonics*, vol. 2, pp. 219–225, 2008. 134

[182] R. R. McLeod, M. S. Kirchner, and A. C. Sullivan, "3D micro-optic circuits in holographic photopolymers," in *Controlling Light with Light: Photorefractive Effects, Photosensitivity, Fiber Gratings, Photonic Materials and More*, OSA Technical Digest (CD). Optical Society of America, 2007, paper TuC2. 134

[183] C. D. Anderson, R. R. McLeod, M. W. Grabowski, and A. C. Sullivan, "Photopolymer waveguide to fiber coupling via 3D direct-write lithography," in *Integrated Photonics Research and Applications/Nanophotonics*, OSA Technical Digest (CD). Optical Society of America, 2006, paper ITuD4. 135

[184] C. Ye and R. R. McLeod, "Grin lens and lens array fabrication with diffusion-driven photopolymer," *Opt. Lett.*, vol. 33, no. 22, pp. 2575–2577, 2008. 135

[185] A. C. Sullivan and R. R. McLeod, "3D tapered waveguides in volume photopolymers," in *Integrated Photonics and Nanophotonics Research and Applications*, OSA Technical Digest (CD). Optical Society of America, 2007, paper ITuA7. 135

[186] M. W. Grabowski and R. R. McLeod, "Low loss ring resonator waveguides in self processing photopolymers," in *Conference on Lasers and Electro-Optics/Quantum Electronics and Laser Science Conference and Photonic Applications Systems Technologies*, OSA Technical Digest (CD). Optical Society of America, 2008, paper JTuA32. 135

[187] A. C. Sullivan, "Tomographic characterization of volume photopolymers for integrated optics," Ph.D. dissertation, University of Colorado at Boulder, 2008. 136, 234

[188] J. T. Verdeyen, *Laser Electronics, 3rd ed.* Prentice Hall, 1995. 136, 150

[189] H. Kogelnik, "Theory of dielectric waveguides," in *Topics in Applied Physics, Vol. 7: Integrated Optics*, T. Tamir, Ed. Springer-Verlag, 1995. 137

[190] M. Ams, G. D. Marshall, D. J. Spence, and M. J. Withford, "Slit beam shaping method for femtosecond laser direct-write fabrication of symmetric waveguides in bulk glasses," *Opt. Express*, vol. 13, no. 15, pp. 5676–5681, 2005. 138

[191] M. Pluta, *Advanced Light Microscopy, Vol. 2: Specialized Methods.* Elsevier, 1989. 139

[192] J. Durnin, "Exact solutions for nondiffracting beams. I. The scalar theory," *J. Opt. Soc. Am. A*, vol. 4, no. 4, pp. 651–654, 1987. 153

[193] J. Durnin, J. J. J. Miceli, and J. H. Eberly, "Diffraction-free beams," *Phys. Rev. Lett.*, vol. 58, no. 15, pp. 1499–1501, 1987. 153

[194] G. M. Burrow and T. K. Gaylord, "Constrained parametric optimization of point geometries in multi-beam-interference lithography," in *Frontiers in Optics*, OSA Technical Digest (CD). Optical Society of America, 2010, paper FWS3. 157

[195] I. B. Divliansky, A. Shishido, I.-C. Khoo, T. S. Mayera, D. Pena, S. Nishimura, C. D. Keating, and T. E. Mallouk, "Fabrication of two-dimensional photonic crystals using interference lithography and electrodeposition of CdSe," *Appl. Phys. Lett.*, vol. 79, no. 21, pp. 3392–3394, 2001. 157

[196] L. Prodan, T. G. Euser, H. A. G. M. van Wolferen, C. Bostan, R. M. de Ridder, R. Beigang, K.-J. Boller, and L. Kuipers, "Large-area two-dimensional silicon photonic crystals for infrared light fabricated with laser interference lithography," *Nanotechnology*, vol. 15, pp. 639–642, 2004. 157

[197] F. Quiñónez, J. W. Menezes, L. Cescato, V. F. Rodriguez-Esquerre, H. Hernandez-Figueroa, and R. D. Mansano, "Band gap of hexagonal 2D photonic crystals with elliptical holes recorded by interference lithography," *Opt. Express*, vol. 14, no. 11, pp. 4873–4879, 2006. 157

[198] I. Divliansky, T. S. Mayer, K. S. Holliday, and V. H. Crespi, "Fabrication of three-dimensional polymer photonic crystal structures using single diffraction element interference lithography," *Appl. Phys. Lett.*, vol. 82, no. 11, pp. 1667–1669, 2003. 157

[199] C. K. Ullal, M. Maldovan, E. L. Thomas, G. Chen, Y.-J. Han, and S. Yang, "Photonic crystals through holographic lithography: Simple cubic, diamond-like, and gyroid-like structures," *Appl. Phys. Lett.*, vol. 84, no. 26, pp. 5434–5436, 2004. 157

[200] V. Ramanan, E. Nelson, A. Brzezinski, P. V. Braun, and P. Wiltzius, "Three dimensional silicon-air photonic crystals with controlled defects using interference lithography," *Appl. Phys. Lett.*, vol. 92, no. 17, p. 173304, 2008. 157

[201] W. W. Ng, C.-S. Hong, and A. Yariv, "Holographic interference lithography for integrated optics," *IEEE T. Electron Dev.*, vol. ED-25, no. 10, pp. 1193–2000, 1978. 157

[202] C. S. Lim, M. H. Hong, Q. X. Y. Lin, B. S. Lukyanchuk, A. S. Kumar, and M. Rahman, "Microlens array fabrication by laser interference lithography for super-resolution surface nanopatterning," *Appl. Phys. Lett.*, vol. 89, no. 19, p. 191125, 2006. 157

[203] M. Zheng, M. Yu, Y. Liu, R. Skomski, S. H. Liou, D. J. Sellmyerb, V. N. Petryakov, Y. K. Verevkin, N. I. Polushkin, and N. N. Salashchenko, "Magnetic nanodot arrays produced by direct laser interference lithography," *Appl. Phys. Lett.*, vol. 79, no. 16, pp. 2606–2608, 2001. 157

[204] N. Feth, C. Enkrich, M. Wegener, and S. Linden, "Large-area magnetic metamaterials via compact interference lithography," *Opt. Express*, vol. 15, no. 2, pp. 501–507, 2007. 157

[205] C. J. M. van Rijn, W. Nijdam, S. Kuiper, G. J. Veldhuis, H. van Wolferen, and M. Elwenspoek, "Microsieves made with laser interference lithography for micro-filtration applications," *J. Micromech. Microeng*, vol. 9, pp. 170–172, 1999. 157

[206] F. Yu, P. Li, H. Shenc, S. Mathurc, C.-M. Lehrb, U. Bakowskyd, and F. Mücklicha, "Laser interference lithography as a new and efficient technique for micropatterning of biopolymer surface," *Biomaterials*, vol. 26, pp. 2307–2312, 2005. 157

[207] F. Yu, F. Mücklich, P. Li, H. Shen, S. Mathur, C.-M. Lehr, and U. Bakowsky, "In vitro cell response to a polymer surface micropatterned by laser interference lithography," *Biomacromolecules*, vol. 6, pp. 1160–1167, 2005. 157

[208] H. C. LeFevre, "Single-mode fibre fractional wave devices and polarisation controllers," *Electron. Lett.*, vol. 16, no. 20, pp. 778–780, 1980. 173

[209] S. Singh, "Refractive index measurement and its applications," *Physica Scripta.*, vol. 65, pp. 167–180, 2002. 194

[210] I. K. Ilev, "Simple autocollimation laser refractometer with highly sensitive, fiber-optic output," *Appl. Opt.*, vol. 34, no. 10, pp. 1741–1743, 1995. 194

[211] E. Moreels, C. de Greef, and R. Finsy, "Laser light refractometer," *Appl. Opt.*, vol. 23, no. 17, pp. 3010–3013, 1984. 195

[212] G. Jin, R. Jansson, and H. Arwina, "Imaging ellipsometry revisited: Developments for visualization of thin transparent layers on silicon substrates," *Rev. Sci. Instrum.*, vol. 67, no. 8, pp. 2930–2936, 1996. 195

[213] S. V. King, A. Libertun, R. Piestun, C. J. Cogswell, and C. Preza, "Quantitative phase microscopy through differential interference imaging," *J. Biomed. Opt.*, vol. 13, p. 024020, 2008. 195

[214] S. R. P. Pavani, A. R. Libertun, S. V. King, and C. J. Cogswell, "Quantitative structured-illumination phase microscopy," *Appl. Opt.*, vol. 47, pp. 15–24, 2008. 195

[215] E. Cuche, F. Bevilacqua, and C. Depeursinge, "Digital holography for quantitative phase-contrast imaging," *Opt. Lett.*, vol. 24, pp. 291–293, 1999. 195

[216] G. Zito, A. Finizio, and S. De Nicola, "Spatially resolved refractive index profiles of electrically switchable computer-generated holographic gratings," *Opt. Express*, vol. 17, no. 21, pp. 18 843–18 851, 2009. 195

[217] E. Hecht, *Optics, 3rd. ed.* Addison-Wesley, 1998. 196

[218] W. J. Stewart, "Optical fiber and preform profiling technology," *IEEE J. Quantum Electron.*, vol. QE-18, no. 10, pp. 1451–1466, 1982. 197

[219] P. C. D. Hobbs, *Building Electro-Optical Systems: Making It All Work, 2nd ed.* John Wiley & Sons, 2009. 200

[220] G. DAntona and A. Ferrero, *Digital Signal Processing for Measurement Systems Theory and Applications.* Springer, 2008. 201

[221] "Optical glass data sheets," Schott North America, Inc., Jan. 2011. [Online]. Available: www.us.schott.com/advanced_optics/english/download/schott_optical_glass_jan_2011_us.pdf 209

[222] E. D. Moore and R. R. McLeod, "Phase-sensitive swept-source interferometry for absolute ranging with application to measurements of group refractive index and thickness," *Opt. Express*, Submitted for publication. 223

[223] ——, "Permanent holographic waveguide arrays," in *Frontiers in Optics*, OSA Technical Digest (CD). Optical Society of America, 2010, paper FWS4. 224

[224] ——, "Index contrast measurement using scanning optical frequency domain reflectometry," in *Frontiers in Optics*, OSA Technical Digest (CD). Optical Society of America, 2010, paper JWA38. 225

[225] "Temperature coefficient of the refractive index," Schott North America, Inc., Technical Information TIE-19, Jul. 2008. [Online]. Available: http://www.us.schott.com/advanced_optics/english/download/schott_tie-19_temperature_coefficient_of_refractive_index_v2d_july_2008_us.pdf 269, 270

[226] "Lithosil synthetic fused silica product broshure," Schott North America, Inc., Jan. 2010. [Online]. Available: www.us.schott.com/advanced_optics/english/download/schott_fused_silica_jan_2010_us.pdf 269

Appendix A

Abbreviations and Symbols

Table A.1: Abbreviations.

1D	One-dimensional
2D	Two-dimensional
3D	Three-dimensional
ADC	Analog to Digital Conversion
CCD	Charge-Coupled Device
CD	Chromatic Dispersion
CGH	Computer Generated Hologram
CMOS	Complementary Metal Oxide Semiconductor
cw	continuous wave
DAQ	Data Acquisition
DGD	Differential Group Delay
DIC	Differential Interference Contrast
DUT	Device Under Test
ECDL	External Cavity Diode Laser
FDML	Fourier Domain Mode Locked
FFT	Fast Fourier Transform
FIG	Fiber Image Guide
FMCW	Frequency Modulated Continuous Wave
FRM	Faraday Rotator Mirror
FWHM	Full Width at Half Maximum
GD	Group Delay
IDL	Interactive Data Language
lidar	light detection and ranging
NA	Numerical Aperture
OCT	Optical Coherence Tomography

Table A.1: Abbreviations (cont.)

ODT	Optical Diffraction Tomography
OFDR	Optical Frequency Domain Reflectometry
OPL	Optical Path Length
OTDR	Optical Time Domain Reflectometry
PBS	Polarizing Beam Splitter
PDI	Polarization Delay Interferometer
PDL	Polarization Dependent Loss
PM	Polarization-Maintaining
PMD	Polarization Mode Dispersion
PSD	Position-Sensitive Detector
RIN	Relative Intensity Noise
SM	Single-Mode
SS-OCT	Swept-Source Optical Coherence Tomography
SUT	Sample Under Test
SWI	Swept-Wavelength Interferometry
TD-OCT	Time Domain Optical Coherence Tomography
VCSEL	Vertical-Cavity Surface-Emitting Laser

Table A.2: Roman symbols.

a	Absorption coefficient
a, b, c, d	Transfer function matrix elements
A	Electronic signal amplitude
b	Number of bits
B	Power equivalent bandwidth
c	Speed of light $(299,792,458\,\mathrm{m/s})$
C_1, C_2	Proportionality constants
$\mathcal{C}$	Calibration constant
d	Waveguide separation distance
e	Base of the natural logarithm (2.718282)
e	Fundamental electron charge $(1.602176 \times 10^{-19}\,\mathrm{C})$
E	Electric field (scalar)
$\mathbf{E}$	Electric field (vector)
E_0	Electric field amplitude
f	Focal length
f	Frequency
f_ε	Probability density function for ε

Table A.2: Roman symbols (cont.)

$\mathcal{F}$	Fourier transform operator
h	Planck's constant (6.626076×10^{-34} J·s)
H	Scalar transfer function
$\mathbf{H}$	Vector transfer function
i	array or sampling index
$\bar{i}$	Mean photocurrent
I	Irradiance
I	Photoinitiator
I_0	Peak irradiance
$\mathbf{I}$	Identity matrix
I_0	Initial or peak irradiance
$\mathcal{I}_0$	Photons per second per volume
j	$\sqrt{-1}$
J_0	Zero-order Bessel function of the first kind
$\mathbf{k}$	Wave vector
k	Wave vector magnitude
k_x, k_y, k_z	Cartesian wave vector components
K	Number of reflectors
l	Waveguide width
L	Length or thickness
m	Array index
M	Monomer
$[M]$	Monomer concentration
$M\bullet$	Monomer radical
$[M\bullet]$	Monomer radical concentration
n	Index of refraction
n	Summation index
$\bar{n}$	Mean number of photons
n_g	Group refractive index
n_r	Phase refractive index relative to air
N	Number of data points
p	Number of fringes
$\hat{\boldsymbol{p}}$	P polarization unit vector
P	Power
P_0	Initial or peak power
Q	Number of quantization levels
r	Amplitude reflection coefficient
r	Aperture radius

Table A.2: Roman symbols (cont.)

$r_{\parallel}$	Parallel amplitude reflection coefficient
$r_{\perp}$	Perpendicular amplitude reflection coefficient
R	Relative power loss (i.e., reflectivity)
$R_{min,q}$	Shot noise floor
$R_{min,Q}$	Quantization noise floor
$R_{min,R}$	RIN noise floor
R_U	Normalized autocorrelation
$R\bullet$	Radical
$[R\bullet]$	Radical concentration
$\mathbf{R}$	Polarization rotation matrix
$\Re$	Real part
$\mathcal{R}_i$	Initiation rate
$\mathcal{R}_p$	Polymerization rate
$\mathcal{R}_t$	Termination rate
$\hat{\boldsymbol{s}}$	S polarization unit vector
S	Sampling rate
$\mathcal{S}$	Power spectral density
t	Time
T	Total process time
u	Uncertainty
U	Signal voltage
$\tilde{U}$	Oscillating portion of a signal
$\mathcal{U}$	Fourier transform of U
U_0	Peak signal voltage
U^f	Filtered signal data
U^p	Processed signal data
U_p	Signal on P polarization channel
U_s	Signal on S polarization channel
U_t	Trigger interferometer signal
$\hat{U}_i$	Quantized signal levels
v	Velocity
V	Normalized frequency
V	Voltage
$\mathcal{V}$	Energy per unit area
w	Beam radius
w_0	Gaussian beam waist
W	Window function
$\mathcal{W}$	Fourier transform of W

Table A.2: Roman symbols (cont.)

x, y, z	Cartesian coordinates
X, Y	Dimensionless coordinates
z_0	Rayleigh range
Z	Inhibitor
$[Z]$	Inhibitor concentration

Table A.3: Greek symbols.

α	Bessel beam parameter
α	Photopolymer parameter
β	Propagation constant
β_1, β_2	Eigenvalues of $\mathbf{H}$
γ	Laser sweep rate
Γ	Slow tuning parameter
δ	Dirac delta function
δn	Refractive index contrast
δt	Sampling interval in t
$\delta\nu$	Fringe period or sampling interval in ν
$\delta\tau$	Sampling interval in τ
Δ	Quantization level spacing
Δn	Refractive index contrast
$\Delta\nu$	Range of ν
$\Delta\nu_c$	Calibration optical frequency range
$\Delta\nu_{\mathrm{FWHM}}$	FWHM line width
$\Delta\tau$	Time domain range
$\Delta\omega$	Angular frequency range
ε	Quantization error
η	Photodetector quantum efficiency
η^I	Intrinsic sampling error
η^D	Sampling error due to DAQ delay
θ	Angle of incidence
Θ	Transfer function phase
κ_p	Polymerization rate constant
κ_t	Termination rate constant
κ_z	Inhibition rate constant
λ	Wavelength
λ_0	Free space wavelength

Table A.3: Greek symbols (cont.)

Λ	Spatial period
ν	Optical frequency
ν_0	Initial optical frequency
ν_c	Sweep center optical frequency
ξ	Phase offset
π	3.141593
ρ	Cylindrical radial coordinate
$\hat{\boldsymbol{\varrho}}$	Polarization unit vector
σ	Proportionality constant between $\lvert\mathbf{E}\rvert^2$ and U
σ	Standard deviation
τ	Delay (generally)
τ_0	Relative delay between two paths of an interferometer
$\tau_{0,q}$	Coarse estimation of τ_0
$\tau_{0,p}$	Precise adjustment to $\tau_{0,q}$
τ_c	Coherence time
τ_D	DAQ delay
τ_m	Relative delay of a measurement interferometer
τ_p	Relative delay of a PDI
τ_t	Relative delay of a trigger interferometer
τ_w	Filter window duration
ϕ	Phase
ϕ_d	Deterministic phase
ϕ_r	Stochastic phase
Φ	Measured phase
φ	Polymerization quantum yield
ψ	Phase offset
ω	Angular frequency

Appendix B

Refractive Index Models

B.1 The group refractive index of air

The high accuracy and precision of the self-referenced, phase-sensitive SS-OCT system described in Ch. 4 allows for measurements of group refractive index with uncertainties on the order of 10^{-6}. Because the sample under test is surrounded by air, the measured group index is necessarily referenced to that of air. An accurate measurement of the group index of the sample therefore requires an accurate determination of the group index of the surrounding air at the time of the measurement. At this level of precision, the variations in temperature, air pressure, and relative humidity have significant effects on the refractive index of air. The group index measurement experiment was conducted in Boulder, Colorado, at an elevation of approximately 5375 feet* above sea level, where the refractive index of air differs from that at sea level by approximately 5×10^{-5}.

The current state-of-the-art model for calculating the phase refractive index of the atmosphere was published by Ciddor in 1996 [136], wherein the author cites agreement of the model with measured data to the order of 10^{-8}. Later, Ciddor and Hill published an updated discussion on calculating the group refractive index

*This is the approximate elevation of the first floor of the Engineering Center on the University of Colorado campus, as determined from the 2011 Boulder 7.5 minute quadrangle published by the U.S. Geological Survey.

of air [137]. The general approach for calculating the phase index is to determine the refractive index for dry air and water vapor independently at a set of standard conditions, and then determine their partial densities relative to their densities at the standard conditions. The standard refractive indices are multiplied by the relative densities to yield partial refractive indices, and the partial indices are then combined. Ciddor compares two methods for performing the combination, simple summation and summation using the Lorentz-Lorenz relation, and finds that the agreement between the two methods is on the order of 10^{-9} or better. The group refractive index is found by differentiation of the Lorentz-Lorenz relation.

To enable accurate measurements of group refractive index of optical samples using SWI, I implemented the group refractive index model of Ciddor and Hill using Interactive Data Language (IDL)[†] in a procedure called `airindex`. This procedure calls one subroutine, `compress`, for calculating the compressibility of moist air. The code implementing the procedure `airindex` and the function `compress` is listed below.

B.1.1 Listing of the procedure `airindex`

```
1  PRO airindex
2  ;---------------------------------------------------------------------
3  ;  Procedure to calculate the refractive index of air following
4  ;  Ciddor and Hill.
5  ;
6  ;  Author:  Eric Moore
7  ;  Date:  Dec. 2, 2010
8  ;---------------------------------------------------------------------
9
10 ;*********************************************************************
11 ; Inputs
12 ;*********************************************************************
13 TC = 25.0D                          ; Temperature in Celsius
14 pk = 83.5D                          ; Air pressure in kPa
15 h = 0.20D                           ; Relative humidity (0 - 1)
16 WL1 = 1.5D0                         ; Start wavelength in um
```

[†]IDL is a trademark of ITT Visual Information Solutions.

```
WL2 = 1.564172                          ; End wavelength in um
xc = 450.D                              ; CO2 concentration in ppm

;*****************************************************************
; Contants and derived quantities
;*****************************************************************
WL = ABS(WL2+WL1)/2D0                   ; Center wavelength in um
sigma = 1D/WL                           ; Wavenumber
p = pk * 1000.D                         ; Air pressure in Pa
TK = TC + 273.15D                       ; Temperature in Kelvin
Mw = 0.018015D                          ; Molar mass of water vapor
R = 8.314510D                           ; Ideal gas constant

; Molar mass of dry air
Ma = (28.9635D + (12.011D * 1D-6 * (xc-400.D))) * 1D-3

; Constants for saturation vapor pressure formula
A = 1.2378847D-5
B = -1.9121316D-2
C = 33.93711047D
D = -6.3431645D3

; Saturation vapor pressure
svp = EXP(A*TK^2 + B*TK + C + D/TK)

; Constants for enhancement factor formula
alpha = 1.00062D
beta = 3.14D-8
gamma = 5.6D-7

; Enhancement factor of water vapor in air
f = alpha + beta*p + gamma*TC

; Molar fraction of water
xw = f*h*svp/p

; Sellmeier coefficients for standard air
k0 = 238.0185D
k1 = 5792105D
k2 = 57.362D
k3 = 167917.D

; Refractive index of standard air
nas = 1D-8*(k1/(k0-sigma^2) + k3/(k2-sigma^2)) + 1.D

; Refractive index corrected for CO2
```

```
63 naxs = (nas-1D)*(1.D + 0.534D*1D-6*(xc-450.D))+1.D
64
65 ; Polynomial coefficients for the index of water vapor
66 w0 = 295.235D
67 w1 = 2.6422D
68 w2 = -0.032380D
69 w3 = 0.004028D
70
71 ; Refractive index of standard water vapor
72 nws = 1D-8*1.022D*(w0 + w1*sigma^2 + w2*sigma^4 + w3*sigma^6)+1.D
73
74 ; Compressibility of dry air
75 Za = compress(101325.D, 288.15D, 0.D)
76
77 ; Compressibility of water vapor
78 Zw = compress(1333.D, 293.15D, 1.D)
79
80 ; Density of standard dry air
81 rhoaxs = (101325.D*Ma/(Za*R*288.15D))
82
83 ; Density of standard water vapor
84 rhows = (1333.D*Mw/(Zw*R*293.15D))
85
86 ; Compressibility of air under experimental conditions
87 Z = compress(p,TK,xw)
88
89 ; Partial density of dry air
90 rhoa = p*Ma*(1D -xw)/(Z*R*TK)
91
92 ; Partial density of water vapor
93 rhow = p*Mw*xw/(Z*R*TK)
94
95 ; Phase index of air, method 1
96 nprop = 1.D + (rhoa/rhoaxs)*(naxs-1.D) + (rhow/rhows)*(nws-1.D)
97
98 ; Lorentz-Lorenz relation for air
99 La = (naxs^2-1D)/(naxs^2+2D)
100
101 ; Lorentz-Lorenz relation for water vapor
102 Lw = (nws^2-1D)/(nws^2+2D)
103
104 ; Total Lorentz-Lorenz relation
105 L = (rhoa/rhoaxs)*La + (rhow/rhows)*Lw
106
107 ; Phase index of air, method 2
108 nLL = SQRT((1D + 2D*L)/(1D - L))
```

```
109
110 ; Derivative of phase index for standard air
111 dnas = -2D*sigma*( (k1/(k0-sigma^2)^2) + $
112                   (k3/(k2-sigma^2)^2) )*1D-8
113
114 ; Derivative of phase index for standard water vapor
115 dnws = -1.022D*1D-8*(2D*w1*sigma + 4D*w2*sigma^3 + 6D*w3*sigma^5)
116
117 ; Pick one phase index
118 n = nLL
119
120 ; The group index of air under experimental conditions
121 ng = n - sigma*(((n^2+2D)^2)/n) * $
122      ( (naxs/(naxs^2+2D)^2)*(rhoa/rhoaxs)*dnas + $
123        (nws/(nws^2+2D)^2)*(rhow/rhows)*dnws )
124
125 print, 'Group index:', ng
126
127 END
```

B.1.2 Listing of the function `compress`

```
1  FUNCTION compress, p, t, xw
2  ;---------------------------------------------------------------------
3  ;  Function to calculate the compressibility of moist air
4  ;  p = Air pressure in pascals
5  ;  t = Temperature in Kelvin
6  ;  xw = Molar fraction of water
7  ;
8  ;  Author:  Eric Moore
9  ;  Date:  Dec. 2, 2010
10 ;---------------------------------------------------------------------
11
12 tc=t-273.15D                          ; Temperature in Celsius
13
14 ; Constants for compressibility formula
15 a0 = 1.58123D-6
16 a1 = -2.9331D-8
17 a2 = 1.1043D-10
18 b0 = 5.707D-6
19 b1 = -2.051D-8
20 c0 = 1.9898D-4
21 c1 = -2.376D-6
22 d = 1.83D-11
23 e = -0.765D-8
24
```

```
; Compressibility of moist air
z = 1D - (p/t)*(a0 + a1*tc + a2*tc^2 + (b0+b1*tc)*xw + $
    (c0+c1*tc)*xw^2) + (p/t)^2*(d+e*xw^2)

RETURN, z
END
```

B.2 The group refractive index of fused silica

To verify the measurement of the group refractive index of silica in Sec. 4.4 I turned to literature published by the manufacturer (Schott AG) in order to compare the measured value with an accepted value. In reviewing the Schott literature, I discovered that the refractive index values supplied by Schott for their optical glasses are not in fact the absolute refractive indices, but are rather reported as relative values with respect to the refractive index of air at a temperature of 20° C and a pressure of 101.33 kPa [225]. Thus, the Sellmeier coefficients provided by Schott yield a value $n_r = n/n_{\text{air}}$, where n is the absolute refractive index and n_{air} is the refractive index of air. This means that a correct calculation of the group index of silica requires a chain-rule differentiation incorporating the Sellmeier formulae for both silica and air. The reference calculation is further complicated by the fact that the model for the temperature dependence of the refractive index of silica provided by Schott is valid only up to a wavelength of 1060 nm. Fortunately, Leviton and Frey [138] published tabulated values of the thermo-optic coefficient of fused silica over a range of temperatures from 30 K to 300 K and wavelengths from 400 nm to 2.6 μm.

To perform the reference calculation for the group index of fused silica, I employed the following resources. I began with the Sellmeier coefficients provided by Shott, which give the phase index of silica relative to air at 20° C and 101.33 kPa [226]. I then employed the Sellmeier coefficients provided by Ciddor [136] to find the phase index of standard air, n_{air}. Then, because standard air as reported

by Ciddor is at a temperature of 15° C, I used a simple temperature model for standard air provided by Schott [225] rather than the rigorous Ciddor model to convert the index of standard air to the index at 20° C. This value then allows the absolute index of fused silica to be determined at 20° C. An interpolated value for the thermo-optic coefficient using the data of Leviton and Frey is then used to find the absolute phase index of fused silica at the temperature of interest. The group index n_g is then found from this value of the phase index and by differentiating the Sellmeier equations for both fused silica and air according to

$$n_g = n - \lambda \frac{dn}{d\lambda} \tag{B.1}$$

$$= n - \lambda \frac{d}{d\lambda}(n_r n_{\text{air}}) \tag{B.2}$$

$$= n - \lambda \frac{dn_r}{d\lambda} - \lambda \frac{dn_{\text{air}}}{d\lambda}. \tag{B.3}$$

These calculations have been implemented in the IDL procedure `ngSilica`.

B.2.1 Listing of the procedure `ngSilica`

```
PRO ngSilica
;---------------------------------------------------------------------
;  Procedure to calculate the phase and group indices of fused
;  silica using Sellmeier coefficients from the Schott literature
;  and interpolated temperature coefficient data from Leviton and
;  Frey.
;
;  Author:  Eric Moore
;  Date:  December 8, 2010
;---------------------------------------------------------------------

;*********************************************************************
; Inputs
;*********************************************************************
T = 25.0D                       ; Temperature in C
WL1 = 1.5D                      ; Start wavelength in um
WL2 = 1.564172                  ; End wavelength in um
WL = abs(WL1+WL2)/2D0

;*********************************************************************
; Constants and derived quantities
```

```
;*****************************************************************
; Sellmeier coefficients for fused silica
B1 = 0.6694226D0
B2 = 0.4345839D0
B3 = 0.8716947D0
C1 = 4.480112D-3
C2 = 1.328470D-2
C3 = 95.34148D0

; Phase index relative to standard air at 20 deg. C
nprs=sqrt(1+((B1*WL^2)/(WL^2-C1)) + ((B2*WL^2)/(WL^2-C2)) $
     + ((B3*WL^2)/(WL^2-C3)));

; Derivative of phase index with respect to wavelength
A1=-( (B1*WL^3) / ((WL^2-C1)^2) ) + ( (B1*WL)/(WL^2-C1) );
A2=-( (B2*WL^3) / ((WL^2-C2)^2) ) + ( (B2*WL)/(WL^2-C2) );
A3=-( (B3*WL^3) / ((WL^2-C3)^2) ) + ( (B3*WL)/(WL^2-C3) );
dndl = (A1+A2+A3)/nprs

; Phase index relative to air at temperature T
npr = nprs ;+ DT*dndt
npr1 = nprs1 ;+ DT*dndt1
npr2 = nprs2 ;+ DT*dndt2

; Sellmeier coefficients for standard air from Ciddor
k0 = 238.0185D
k1 = 5792105D
k2 = 57.362D
k3 = 167917.D

; Phase index of standard air (101.33 kPa, 15 deg. C)
sigma = 1/WL
nas = 1D-8*(k1/(k0-sigma^2) + k3/(k2-sigma^2)) + 1.D

; Derivative of phase index of standard air with respect to
; temperature from Schott T.I.E. 19
dnadt = -0.0037D0*((nas-1D0)/(1D0+0.0037D0*T))

; Phase index of air at 101.33 kPa, 20 deg. C
na = nas - dnadt*5D0

; Absolute phase index of fused silica
np0 = npr * na

; Interpolate temp coeff from Leviton and Frey data for the range
;1500 - 1600 nm
```

```
dndt1500295 = 8.45D-6    ; dn/dt at 1500 nm and 295 K
dndt1500300 = 8.57D-6    ; dn/dt at 1500 nm and 300 K
dndt1600295 = 8.29D-6    ; dn/dt at 1600 nm and 295 K
dndt1600300 = 8.41D-6    ; dn/dt at 1600 nm and 300 K

dndt1500T = dndt1500295 + (dndt1500300-dndt1500295)*((T-21.85)/5D0)
dndt1600T = dndt1600295 + (dndt1600300-dndt1600295)*((T-21.85)/5D0)

dndtWL = dndt1500T + (dndt1600T-dndt1500T)*((WL-1.5D0)/1D0)
dndt = dndtWL

; Absolute phase index of fused silica at temperature T
np = np0 + DT*dndt

; Derivative of the phase index of air with respect to wavelength
dnadl = -2D0*1D-8*sigma*((k1/(k0-sigma^2)^2) + (k3/(k2-sigma^2)^2))

; Group index of fused silica
ng = np - WL*na*dndl + sigma*np*dnadl;

print, ng

END
```